The University of Sheffield

Novel Sensorless Control for Permanent Magnet Synchronous Machines Based on Carrier Signal Injection

Peilin Xu

A thesis submitted for the degree of Doctor of Philosophy

Department of Electronic and Electrical Engineering

The University of Sheffield

3 Solly Street, Sheffield, S1 4DE, UK

June 2017

Abstract

In this thesis, the carrier signal injection methods are in focus for the sensorless control of permanent magnet synchronous machines (PMSMs), utilising alternative types of carrier responses, i.e., the carrier current and zero sequence carrier voltage, respectively.

For the carrier current sensing based carrier signal injection methods, this study investigates the combined effects of signal processing delays and HF resistance, which generates large position estimation errors. Accordingly, a new compensation strategy by modifying the phase angle of the demodulation signal is proposed. The influence of machine parameter asymmetries on the conventional carrier injection methods is also investigated. The 2nd harmonic position estimation errors will arise due to the asymmetries. To mitigate the resistance asymmetry, the selection of the proper injection frequency is discussed. Besides, a new dual frequency injection strategy is also proposed for inductance asymmetry suppression.

Furthermore, a novel carrier signal injection strategy with zero sequence carrier voltage sensing is proposed. This injection strategy is performed on the estimated reference frame, anti-rotating at twice the estimated electrical speed of the rotor. It combines the synergies of both the zero sequence method (i.e., high bandwidth and stability) and the pulsating injection (i.e., high accuracy and fast dynamic response). Then, the proposed anti-rotating injection strategy is further applied for the square-wave signal injection. The anti-rotating square-wave injection with zero sequence voltage sensing can also integrate the merits of both zero sequence voltage sensing and square-wave injection.

In addition, magnetic polarity identification using the zero sequence voltage responses is also performed. The amplitude variation-based polarity detection method using the zero sequence voltage has a higher detection sensitivity than the conventional method using the carrier current. The secondary harmonic based detection method using the zero sequence voltage has the advantages of simple signal demodulation, fast response, and a large signal-to-noise (S/N) ratio. Considering that the secondary harmonics of the zero sequence voltage contain the actual magnetic polarity information and have less distortion, they are directly utilised to estimate the rotor position. This removes the time-consuming process of the polarity detection, and enhances the robustness and stability of the estimation.

The final part of the thesis presents full comparisons for the different carrier signal injection methods with alternative types of carrier responses sensing. The influence of signal processing delays, the cross-coupling magnetic saturation effects, inverter nonlinearity effects, and multiple saliency effects, etc., will be investigated.

Acknowledgements

Content

Nomenclatures

B_{HF} Flux density at carrier injection frequency

B_{LF} Flux density at fundamental frequency

f_e Fundamental frequency

f_h Injection frequency

i_a Phase A current

i_b Phase B current

i_c Phase C current

i_{dh} D-axis HF carrier current

I_{pos} Carrier current response after signal demodulation in the positive sequence frame

i_{qh} Q-axis HF carrier current

I_α Carrier current response after signal demodulation in α-axis

$i_{\alpha h}$ Carrier current in α-axis

I_β Carrier current response after signal demodulation in β-axis

$i_{\beta h}$ Carrier current in β-axis

L_0 DC component of phase self-inductance

L_2 2nd harmonic component of phase self-inductance

L_4 4th harmonic of phase inductance

L_{aa} Phase A self-inductance

L_{avg} Average inductance

L_{bb} Phase B self-inductance

L_c 2nd harmonic self-inductance for cross-coupling saturation effect

L_{cc} Phase C self-inductance

L_d Incremental d-axis inductance

L_{dif} Half of the difference of d-axis and q-axis inductances

L_{dif-k}	The kth harmonic inductive saliency
L_{dq}	Incremental d-/q-axis mutual inductance
L_{fh+fe}	HF inductance harmonic at the frequency of (f_h+f_e)
L_{fh-fe}	HF inductance harmonic at the frequency of (f_h-f_e)
L_q	Incremental q-axis inductance
M_0	DC component of mutual self-inductance
M_2	2nd harmonic component of mutual self-inductance
M_{ab}/M_{ba}	Mutual inductance between Phases A and B
M_{ac}/M_{ca}	Mutual inductance between Phases A and C
M_{bc}/M_{cb}	Mutual inductance between Phases B and C
M_c	2nd harmonic mutual-inductance for cross-coupling saturation effect
N	Number of turns per phase
r_a	Resistance of Phase A
r_{avg}	Average resistance
r_b	Resistance of Phase B
r_c	Resistance of Phase C
r_d	D-axis HF resistance
r_{dif}	Half of the difference of d-axis and q-axis resistances
r_{dif-k}	The kth harmonic resistive saliency
r_{dq}	D-/q-axis HF mutual resistance
r_q	Q-axis HF resistance
U	Injection amplitude
U_{AN}	Phase A voltage to the machine neutral point N
U_{AO}	Phase A voltage to the capacitor mid-point O
U_{AR}	Phase A voltage to the resistor network central point R
U_{BN}	Phase B voltage to the machine neutral point N
U_{BO}	Phase B voltage to the capacitor mid-point O

U_{BR}	Phase B voltage to the resistor network central point R
U_{CN}	Phase C voltage to the machine neutral point N
U_{CO}	Phase C voltage to the capacitor mid-point O
U_{CR}	Phase C voltage to the resistor network central point R
u_{dh}	D-axis HF carrier voltage
u_{qh}	Q-axis HF carrier voltage
U_{RN}	Zero sequence voltage from resistor network central point R to neutral point N
$u_{RN\text{-}sum}$	Zero sequence voltage response after signal demodulation
$U_{RN\alpha}$	Zero sequence voltage response in α-axis after signal demodulation
$U_{RN\beta}$	Zero sequence voltage response in β-axis after signal demodulation
U_{RO}	Voltage from resistor network central point R to the capacitor mid-point O
γ_{neg}	Negative sequence current distortion ratio due to inverter nonlinearity
γ_q	Estimated q-axis distortion ratio due to inverter nonlinearity
γ_{zeq}	Zero sequence voltage distortion ratio due to inverter nonlinearity
$\Delta i_{\alpha h}$	Differentiation of α-axis carrier current
$\Delta i_{\beta h}$	Differentiation of β-axis carrier current
ΔL	Asymmetry in self-inductance
ΔM	Asymmetry in mutual-inductance
$\delta_{q/neg}$	Relative distortion ratio of estimated q-axis current to negative sequence current
δ_r	Phase angle due to resistance asymmetry
Δu_{dh}	D-axis distorted voltage due to inverter nonlinearity
Δu_{qh}	Q-axis distorted voltage due to inverter nonlinearity
$\delta_{zeq/neg}$	Relative distortion ratio of zero sequence voltage to negative sequence current
$\Delta\theta$	Position estimation error
θ_e	Actual rotor position in electrical period
θ_m	Phase shift due to dq-axis inductance
θ_{m1}	Phase shift due to dq-axis resistance

θ_{s1}	2nd harmonic phase shift in self-inductance for cross-coupling saturation effect
θ_{s2}	2nd harmonic phase shift in mutual-inductance for cross-coupling saturation effect
θ_{s3}	Zero sequence voltage phase shift for cross-coupling saturation effect
μ_0	Permeability of the air
μ_r	Relative permeability
μ_{r_a}	Average relative permeability in Phase A flux path
μ_{r_b}	Average relative permeability in Phase B flux path
μ_{r_c}	Average relative permeability in Phase C flux path
φ	Phase shift in carrier current response
φ_d	Phase shift due to signal processing delay
φ_{Lk}	Phase shift in the kth harmonic inductive saliency
φ_{rk}	Phase shift in the kth harmonic resistive saliency
Ψ_A	Flux-linkage of Phase A
ω_h	Injection angular frequency
$\hat{u}_{2d}$	Carrier voltage injected in d_2-axis for anti-rotating injection
$\hat{u}_{2q}$	Carrier voltage injected in q_2-axis for anti-rotating injection
$\hat{u}_{dh}$	HF carrier voltage in the estimated synchronous d-axis
$\hat{u}_{qh}$	HF carrier voltage in the estimated synchronous q-axis
$\Delta\vec{u}_h$	Distorted voltage due to inverter nonlinearity
$\hat{L}_{dif}$	Total inductive saliency
$\hat{i}_{dh}$	HF carrier current in the estimated synchronous d-axis
i_d^m	D_m-axis current in the 45° shift estimated reference frame
$\hat{i}_{qh}$	HF carrier current in the estimated synchronous q-axis
i_q^m	Q_m-axis current in the estimated synchronous reference frame with 45° shift
$\hat{r}_{dif}$	Total resistive saliency
$|B|$	Amplitude of flux-density

$\lvert H \rvert$	Amplitude of flux-intensity
$\lvert i_{dh} \rvert$	D-axis carrier current amplitude
$\lvert U_{2nd} \rvert$	Secondary harmonic amplitude of zero sequence voltage
$\lvert u_{RN} \rvert$	Zero sequence voltage amplitude
$\lvert Z \rvert$	HF total impedance

Abbreviation List

AC	Alternating current
BLAC	Brushless AC
BLDC	Brushless DC
BPF	Band-pass-filter
DC	Direct current
EKF	Extended Kalman filter
EMF	Electromotive force
FE	Finite element
FP	Frozen permeability
HF	High frequency
HPF	High-pass-filter
INFORM	Indirect flux detection by on-line reactance measurements
IPM	Interior permanent magnet
LPF	Low-pass-filter
MRAS	Model reference adaptive system
MMF	Magneto-motive force
PI	Proportional integral
PLL	Phase locked loop
PM	Permanent magnet
PMSMs	Permanent magnet synchronous machines
PWM	Pulse width modulation
S/N	Signal-to-noise
SMO	Sliding mode observer
SPM	Surface-mounted permanent magnet
SRFF	Synchronous reference frame filter
SVPWM	Space vector pulse width modulation
THD	Total harmonic distortion
VC	Vector control
ZCC	Zero current clamping

1 General Introduction

1.1 Introduction

In recent decades, electrical machines have been applied into many new fields, e.g., electrical vehicles, aircrafts, and more. Accordingly, higher requirements are now demanded of electrical machine systems, hence electrical machines should offer excellent performance in terms of high torque and power density, high efficiency, high reliability, and so on [ZHU07]. Among the various types of electrical machines, permanent magnet synchronous machines (PMSMs) have been widely employed due to their significantly higher torque density and efficiency, and hence, the weight and size of PMSMs are significantly reduced, compared to the conventional dc and induction machines. On the other hand, with the developments of power electronics and high precision digital controllers, the machine drive techniques have also been greatly improved with higher efficiency and reliability. The topic of PM machine drives has therefore been an appealing area for academic research in recent years.

For high performance control of PMSMs, accurate rotor position information is essentially required. In general, the rotor position is obtained by a precise sensor, such as Hall sensor, encoder, and resolver, which is normally installed on the rotor shaft, as shown in Fig. 1.1(a). Clearly, this will require additional volume and cost, as well as presenting noise problems and related reliability issues. Besides, the working capability of these position sensors is also limited under extremely harsh conditions (e.g., high temperature, high pressure, etc.).

To eliminate the need for position sensors, position sensorless (self-sensing) control techniques have been researched for many years (see Fig. 1.1(b)). The basic idea of sensorless control is to estimate the rotor position from certain machine parameter or variable (e.g., phase back-EMF, saliency inductance, etc.), which contain the actual rotor position information [ACA06]. Accordingly, in order to track these machine parameters, the machine terminal voltages/currents are normally utilised for the online estimation, based on the PM machine mathematical model.

In this chapter, the alternative PM machine topologies will be introduced first, followed by the state-of-the-art sensorless control techniques. Lastly, the scope of the research and the major contributions in this thesis will be also outlined.
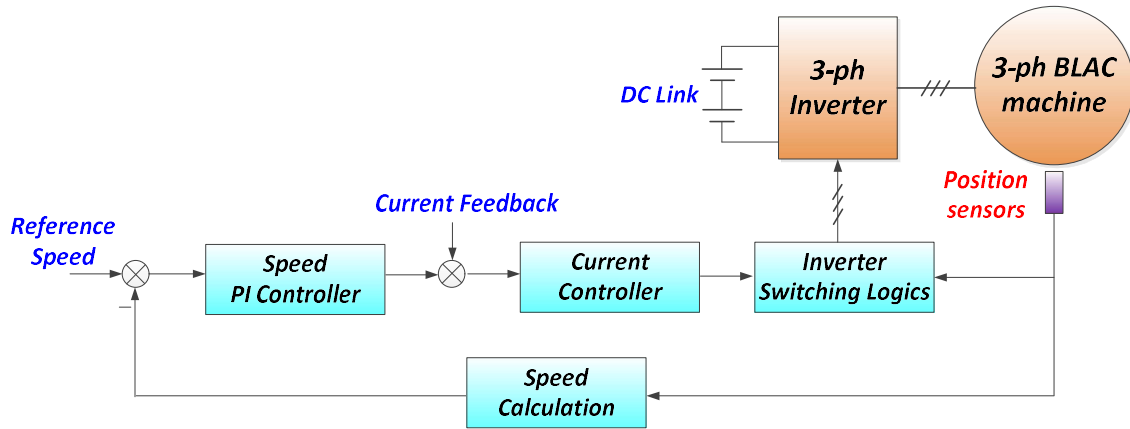
(a) Sensored mode
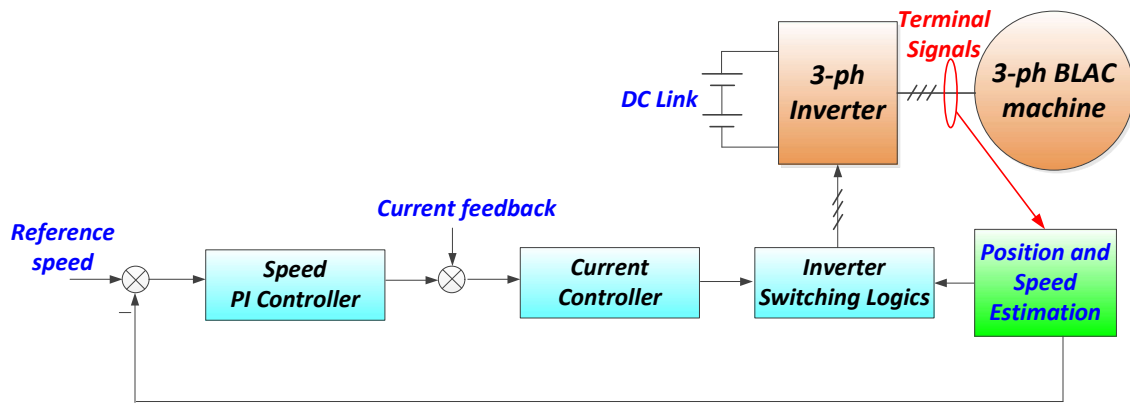
(b) Sensorless mode

Fig. 1.1 PM machine control system in senored/sensorless modes.

1.2 Categories of Permanent Magnet Synchronous Machines Topologies

Within the last few decades, there has been much research into the various aspects of PMSMs. The different classifications for the PM machines are summarized in Fig. 1.2 [CHE99] [ZHU07]. Specifically, in Fig. 1.2, from the type of air-gap fields, the PM machines can be divided into the radial-field, axial-field, transverse-flux, and hybrid-fields machines, respectively. Compared to the radial-field PM machines, the axial-field and transverse-flux PM machines can have higher torque and power density [SIT01] [GUO06] [LIU16]. The complex manufacturing processes restrict the further applications of the axial-field and transverse-flux PM machines, however. Then, in terms of stator winding configurations, the PM machines can be mainly grouped into two categories: the fractional-slot machine with the non-overlapping concentrated windings as shown in Fig. 1.3(a), and the integral-slot machine

with the overlapping distributed windings in (Fig. 1.3(b)). Compared to the distributed windings, the concentrated windings have the advantages of shorter end-windings and a higher slot packing factor, leading to the reduction of total machine mass and copper losses, [ISH06] [ZHU07] [REF10]. Consequently, the machine's overall efficiency and torque density are improved. However, compared to the integral-slot machines, the fractional-slot PM machines suffer from the high contents of stator magneto-motive force (MMF) harmonics, which could cause increased PM eddy current losses, localised magnetic saturation, acoustic noises and vibrations, etc., [WAN14a] [DAJ14]. To reduce the MMF harmonics for the fractional-slot PM machine, considerable research on the multilayer windings, two slot-pitches windings, multiphase machines, etc., has been performed in recent years [ALB13] [WAN14a] [DAJ11] [LEV08] [CHE16a].
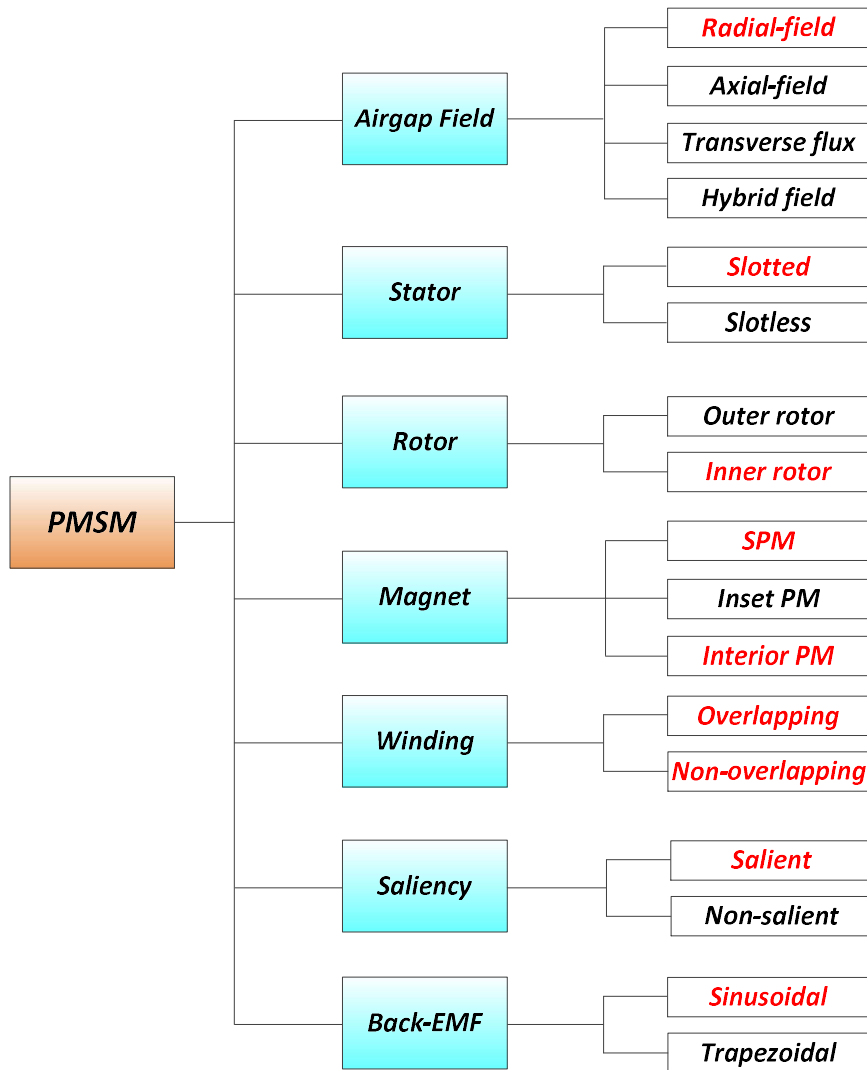
Fig. 1.2 Summary for various PM machine topologies.

(a) Non-overlapping Windings   (b) Overlapping Windings
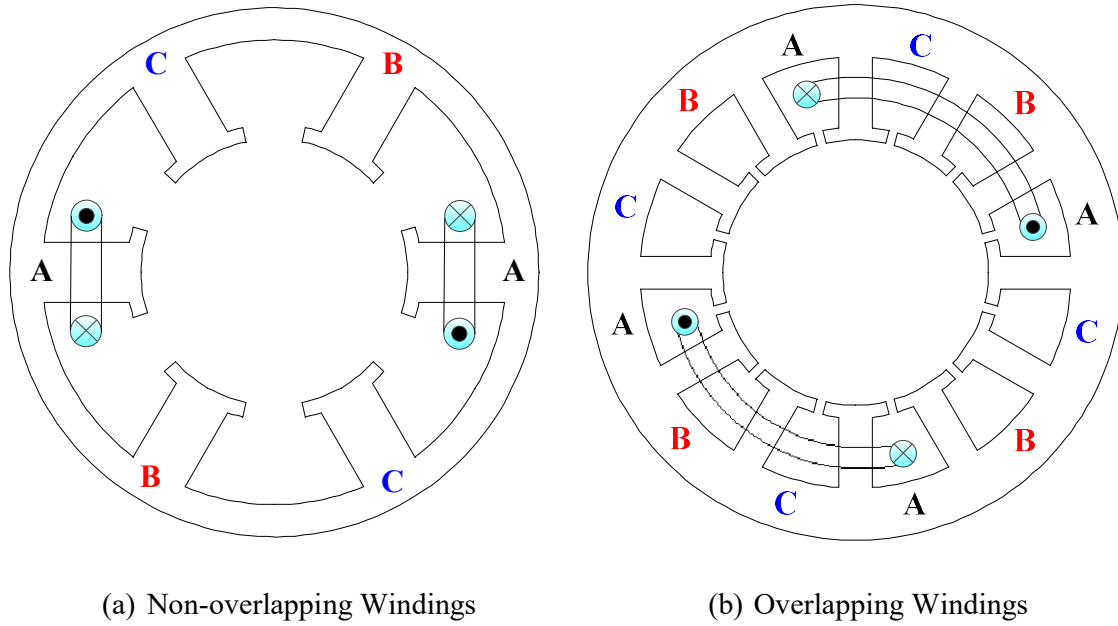
Fig. 1.3 Various winding configurations for the PM machines.

On the other hand, the rotor structures of PM machines can be mainly classified into four types: (a) surface-mounted PM, (b) inset PM, (c) interior circumferential PM, and (d) interior radial PM, as shown in Fig. 1.4(a)-(d), respectively. Among these PM machines, the surface-mounted PM (SPM) machine is the most widely used topology. The SPM machine has the advantages of a simple structure and low manufacturing cost. Moreover, the magnet shape can be easily optimised to incorporate more sinusoidal-distributed flux density in the air-gap [WAN14b]. However, on the other hand, due to direct exposure to the armature reaction field, the magnets may suffer from irreversible demagnetization risk [ZHU07]. Compared to the SPM machine, the inset PM machine has considerable rotor saliency due to the high permeability iron steels between the PMs, (Fig. 1.4(b)). Accordingly, it can utilise the reluctance torque to increase the torque density. In contrast, the other two interior PM (IPM) structures, (Fig. 1.4(c)-(d)), have the merits of high rotor saliency, good flux-weakening capability, and low risk of PM demagnetization. Furthermore, the circumferential IPM rotor structure in Fig. 1.4(c) can also easily realise the flux focusing effects, resulting in increased air-gap flux density. There are drawbacks to the IPM machines, however. The leakage flux through the rotor ribs is relatively large and the rotor's mechanical strength at high speed is poor.

(a) Surface-mounted PM   (b) Inset PM

(c) Interior circumferential PM   (d) Interior radial PM
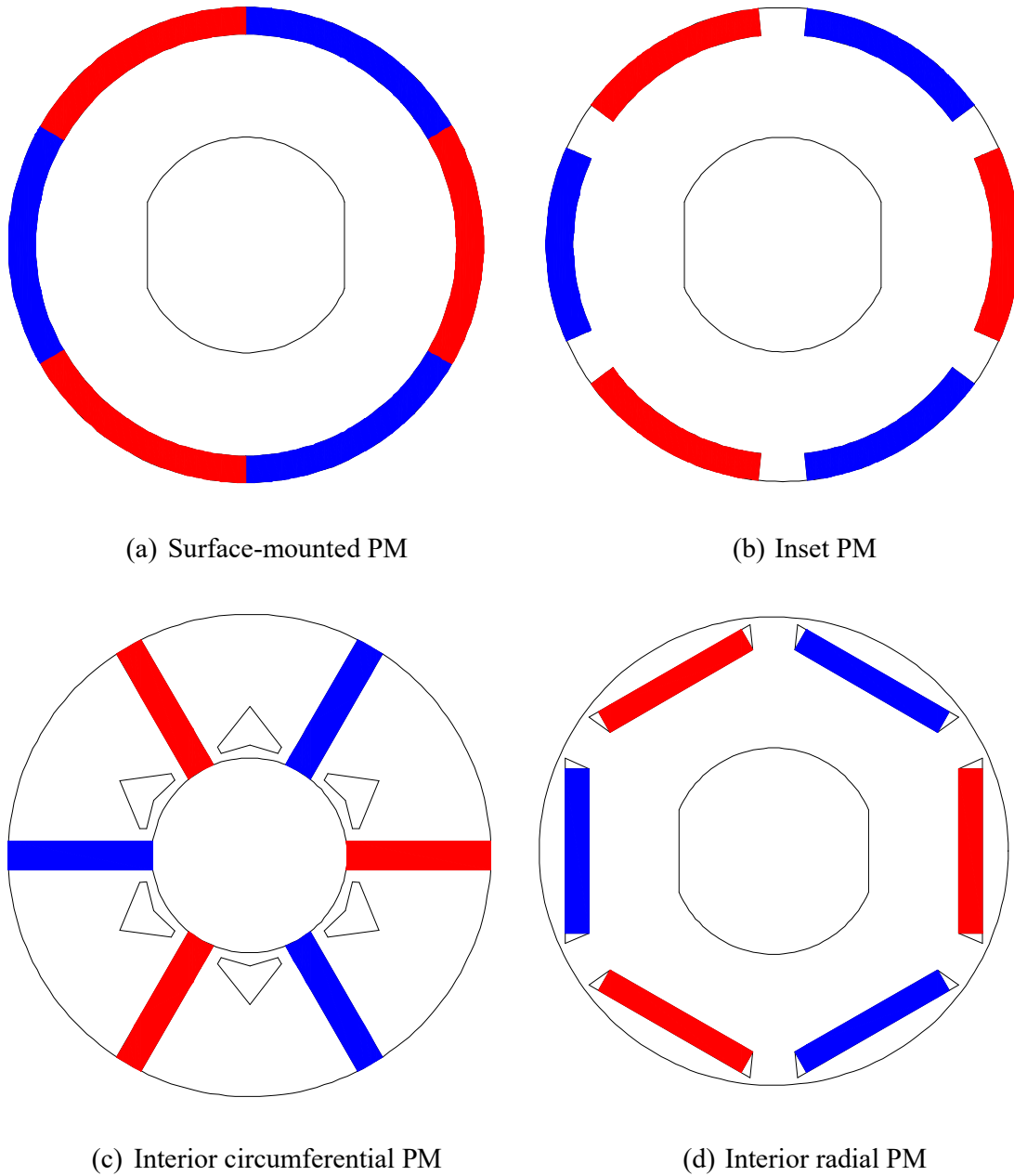
Fig. 1.4 Various rotor PM structures for PM machines.

Then, with the rotation of the rotor PMs, the back-EMF in the stator windings can be generated. The PM machines can be also classified according to their type of back-EMF waveforms as brushless DC (BLDC) machines with trapezoidal phase back-EMF, and brushless AC (BLAC) machines with sinusoidal phase back-EMF (Fig. 1.5(a)-(b)). Normally, BLDC machines are fed by square-wave currents (e.g., 120°) as shown in Fig. 1.5(a), to produce the smooth electromagnetic torque. However, practically, due to the current distortions during the commutation, the torque pulsations may still exist in the BLDC

machines [JAH96]. Besides, due to the rich harmonics in the back-EMF and input square-wave currents, the iron and PM losses may be very large in the BLDC machines. In contrast, BLAC machines fed by sinusoidal currents can also generate a smooth torque output, while the resultant PM losses are expected to be small. Additionally, the control strategy for BLAC machines can easily realize the constant power operation based on the dq-axis theory [ZHU07]. The BLAC control system will be focused in this thesis.
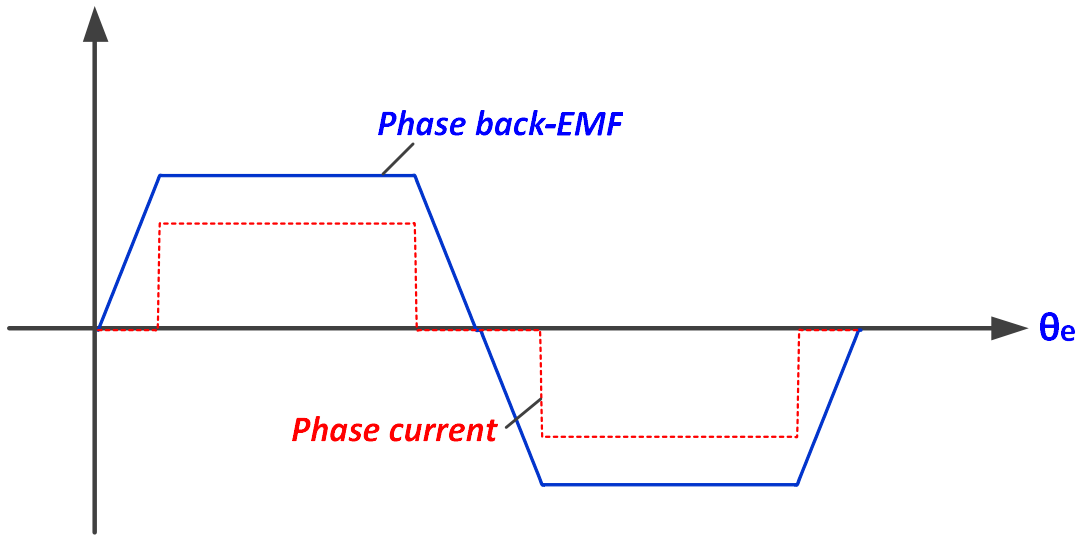
(a) Brushless DC machine
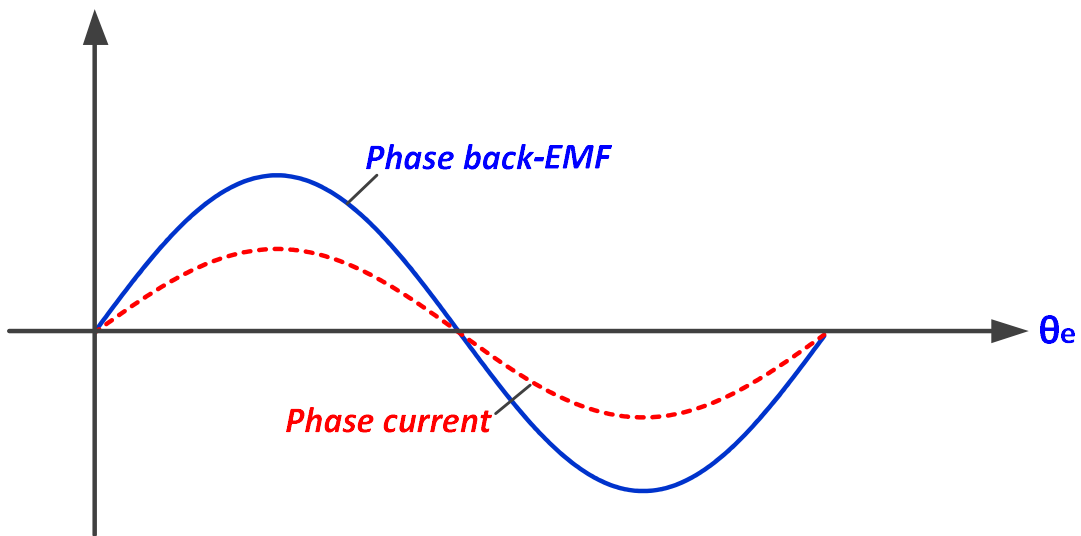
(b) Brushless AC machine

Fig. 1.5 Phase currents and back-EMFs for Brushless DC and AC machines.

1.3   Sensorless Control of Permanent Magnet Synchronous Machines

Several types of PM machine topologies were introduced in the previous section. For the high performance control of these PM machines, obtaining accurate rotor position information is vital. As mentioned in section 1.1, the position sensors increase the cost and volume of the system, and reduce its reliability, etc. To overcome these issues, sensorless (self-sensing) control strategies have been investigated as an alternative for PM machines. Generally, for PM machines operating in BLAC/BLDC modes, the main sensorless control methods can be categorized as the back-EMF/flux-linkage (fundamental model) based and machine saliency based techniques, as demonstrated in Fig. 1.6, [BET14]. Clearly, this is due to either the phase back-EMF or saliency inductance/resistance varying with the rotor position. Then, by tracking these rotor-position-dependent machine parameters, the online rotor position estimation can be realised.
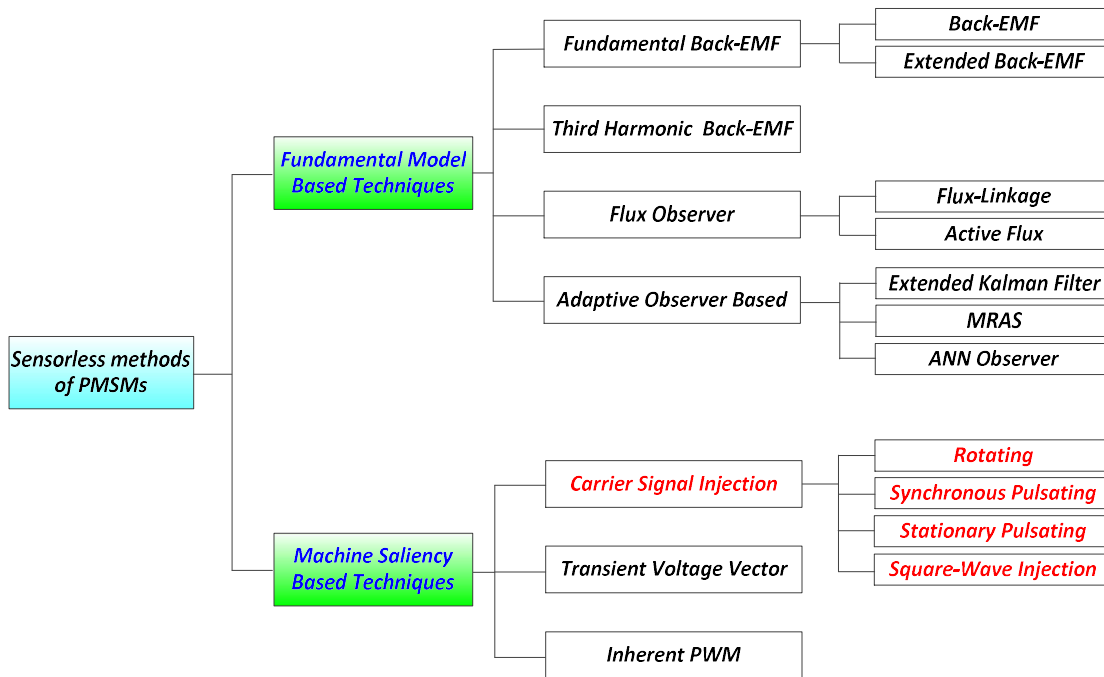
Fig. 1.6 Summary of sensorless control methods for PM machines.

Back-EMF based sensorless methods can produce excellent position estimation performances in the middle- and high-speed region [MOR02] [LI07] [CHE03]. However, since the back-EMF amplitudes are proportional to the rotor speed, the signal-to-noise (S/N) ratio for the back-EMF signals will significantly deteriorate in the low-speed region. Alternatively, machine saliency based position estimation methods can perform well in the

low-speed and even zero-speed regions. This is due to the saliency amplitude (e.g., saliency inductance amplitude) not being related to the rotor speed. Then, with additional signals superimposed on the fundamental excitations and interacted with the saliency at zero- and low-speed, the rotor-position-dependent responses can be generated and then used for the online position estimation [JAN95] [SCH96] [RAU07] [LEI11] [BRI11]. Saliency based position estimation methods may be also degraded at higher rotor speed, however, due to disturbance from the back-EMF signals, voltage margin issues, etc. These two major types of sensorless control methods will be specifically illustrated in the following sections.

1.3.1 Back-EMF/flux-linkage based sensorless methods

As shown in Fig. 1.5, the machine back-EMF varies with the rotor position. The position information can therefore be obtained by estimating the back-EMF/flux-linkage signals. Normally, the open-loop calculation or closed-loop observers can be utilised to track these back-EMF signals. Besides, based on the fundamental model, the adaptive observers, e.g., the extended Kalman filter (EKF), and the model reference adaptive system (MRAS), etc., can be also directly utilised for the rotor position/speed estimation.

1.3.1.1 Fundamental back-EMF based sensorless control methods

Firstly, for the non-salient PM machines, the mathematical model in the synchronous rotating reference frame neglecting the cross-coupling magnetic saturation effects can be described as

$$\begin{bmatrix} u_d \\ u_q \end{bmatrix} = \begin{bmatrix} r_s + Lp & -\omega_e L \\ \omega_e L & r_s + Lp \end{bmatrix} \begin{bmatrix} i_d \\ i_q \end{bmatrix} + \omega_e \begin{bmatrix} 0 \\ \psi_{pm} \end{bmatrix} \tag{1.1}$$

where r_s is the phase resistance, L is the inductance, ω_e is the rotor electrical angular speed, p is the differential operator, Ψ_{pm} is the PM flux-linkage, u_d and u_q are the d- and q-axis voltages, i_d and i_q are the d- and q-axis currents, respectively. However, since the actual d- and q-axes are unknown in the sensorless control mode, the mathematical model in the estimated d-/q-axis frame should be deduced instead. Accordingly, with the transformation of the coordinates, the fundamental model in the estimated d-/q-axis reference frame can be described as

$$\begin{bmatrix} \hat{u}_d \\ \hat{u}_q \end{bmatrix} = \begin{bmatrix} r_s + Lp & -\omega_e L \\ \omega_e L & r_s + Lp \end{bmatrix} \begin{bmatrix} \hat{i}_d \\ \hat{i}_q \end{bmatrix} + \omega_e \psi_{pm} \begin{bmatrix} -\sin(\Delta\theta) \\ \cos(\Delta\theta) \end{bmatrix} \qquad (1.2)$$

From (1.2), only the back-EMF due to the PM excitation ($\omega_e \psi_{pm}$) contains the rotor position information for the non-salient PM machine. Then, according to (1.1)-(1.2), the rotor position can be estimated from the voltage difference between the reference voltage and the model-predicted voltage [MAT96] [LEE15]. It is noted, however, that the above model cannot be applied to the salient pole machine, because not only the back-EMF and also the saliency inductance contain the rotor position information. Alternatively, the extended back-EMF method can be used for the sensorless control of salient pole machines [MOR02] [CHE03]. The voltage model can be described as

$$\begin{bmatrix} \hat{u}_d \\ \hat{u}_q \end{bmatrix} = \begin{bmatrix} r_s + L_d p & -\omega_e L_q \\ \omega_e L_q & r_s + L_d p \end{bmatrix} \begin{bmatrix} \hat{i}_d \\ \hat{i}_q \end{bmatrix} + E_{ex} \begin{bmatrix} -\sin(\Delta\theta) \\ \cos(\Delta\theta) \end{bmatrix} \qquad (1.3)$$

where E_{ex} presents the extended back-EMF, and can be expressed as

$$E_{ex} = \omega_e \psi_{pm} + \omega_e (L_d - L_q) i_d + p(L_q - L_d) i_q \qquad (1.4)$$

Thus, based on (1.3)-(1.4), the rotor position estimation for the salient pole machine can be also realised. The extended back-EMF based method can be further improved by considering the cross-coupling magnetic saturation effects [LI07].

Although the open-loop calculation for the back-EMF signals is simple and easy to implement, the drawback is that it is easily affected by the uncertainty of machine parameters [LEE15]. Alternatively, the close-loop observers can be utilised for the more precise estimation of the back-EMF signals. By way of example, as shown in Fig. 1.7(a), the disturbance observer has been used for the back-EMF estimation, which has proven effective for the sensorless control [SEN95] [CHE03] [PAR14] [XIA16]. The sliding-mode based back-EMF observer is also presented as an alternative, as shown in Fig. 1.7(b) [CHI09] [WAN14] [KIM11] [SON16], having the advantages of simple structure, the immunity to the machine parameter variations, and great dynamic performances.
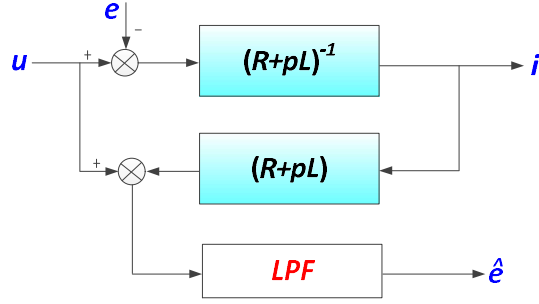
(a) Disturbance observer based
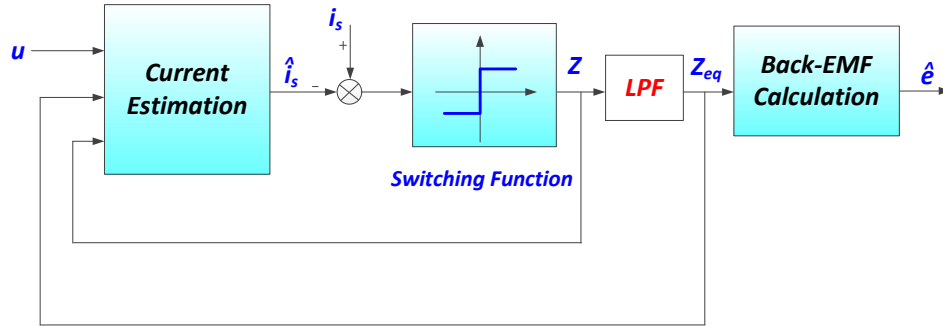
(b) Sliding-mode observer based

Fig. 1.7 Close-loop back-EMF observers for the rotor position estimation.

1.3.1.2 Third harmonic back-EMF based sensorless control methods

It is not just the fundamental back-EMF in the positive sequence frame that contains the rotor position information. The 3rd harmonic back-EMF in the zero sequence frame can be also used to estimate rotor position [MOR96] [SHE04] [LIU14a]. In Fig. 1.8, the 3rd harmonic back-EMF can be obtained from the resistor central point R to the machine neutral point N. The relationships between the fundamental and 3rd harmonic back-EMFs with the rotor position variation are shown in Fig. 1.9.

Then, with the integration of the 3rd harmonic back-EMF, the zero-crossing points of the 3rd harmonic flux-linkage can be detected to determine the commutation instants for the BLDC machines [SHE04]. For the BLAC operation, the continuous rotor position can be also obtained with the integration of the estimated rotor speed [SHE06] [LIU14a]. However, due to the estimated speed being calculated using two adjacent zero-crossing points, and not being fast enough to reflect the change in the actual rotor speed, the dynamic sensorless performance is deteriorated [LIU14a]. Accordingly, the continuous 3rd harmonic signal rather than the discontinuous zero-crossing points is utilised as a reference to reduce the speed and

position estimation errors, as shown in Fig. 1.10 [LIU14a].

Compared to the fundamental back-EMF sensorless methods, the 3rd harmonic back-EMF method is relatively simple and potentially low-cost to implement, not relied on the machine parameters, less sensitive to the distortions, etc. It also has several drawbacks, however, such as (a) the PM machine should be non-salient type, (b) access to the machine's neutral point is required, and (c) the PM machine should contain the 3rd harmonic back-EMF, [SHE06].
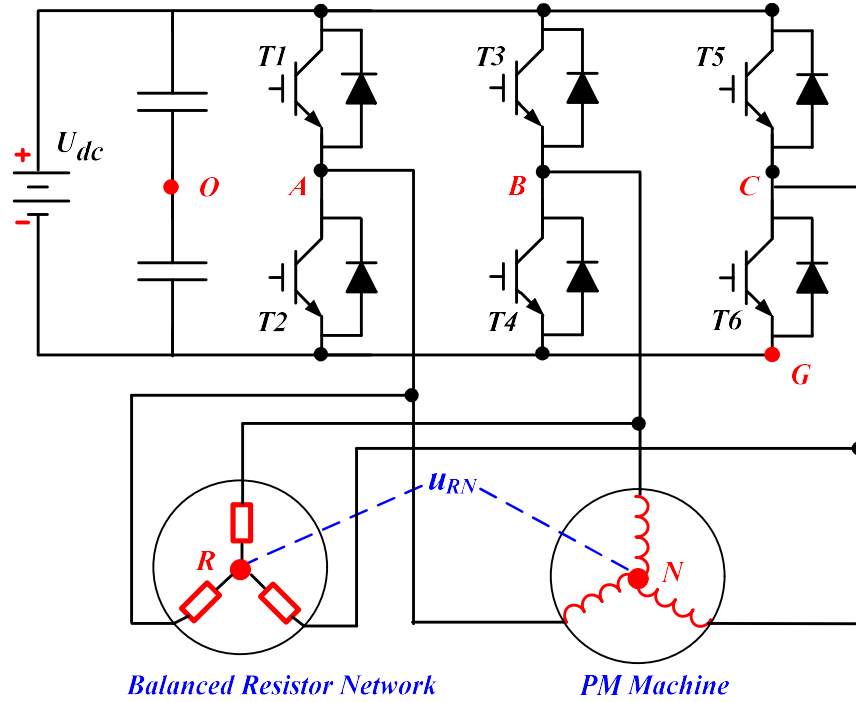
Fig. 1.8 Measurement of 3rd harmonic back-EMF of PM machines.
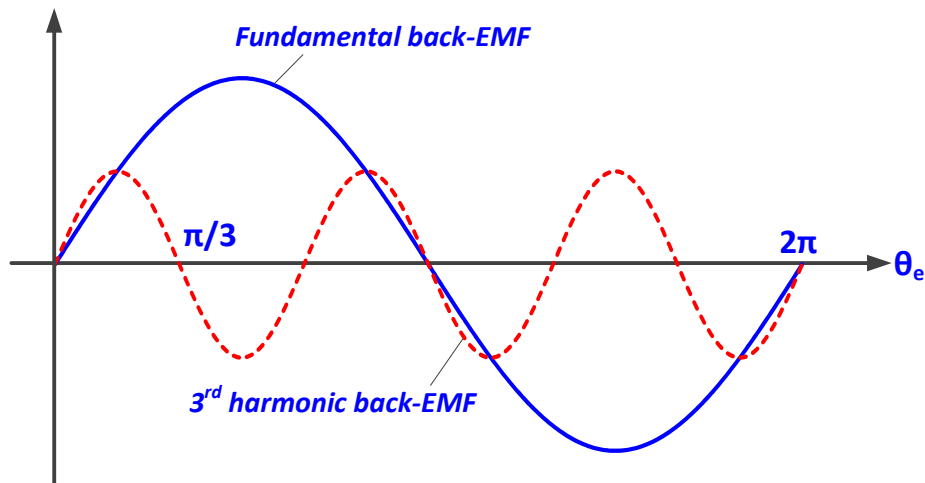
Fig. 1.9 Relationships of fundamental and 3rd harmonic back-EMFs with rotor position.
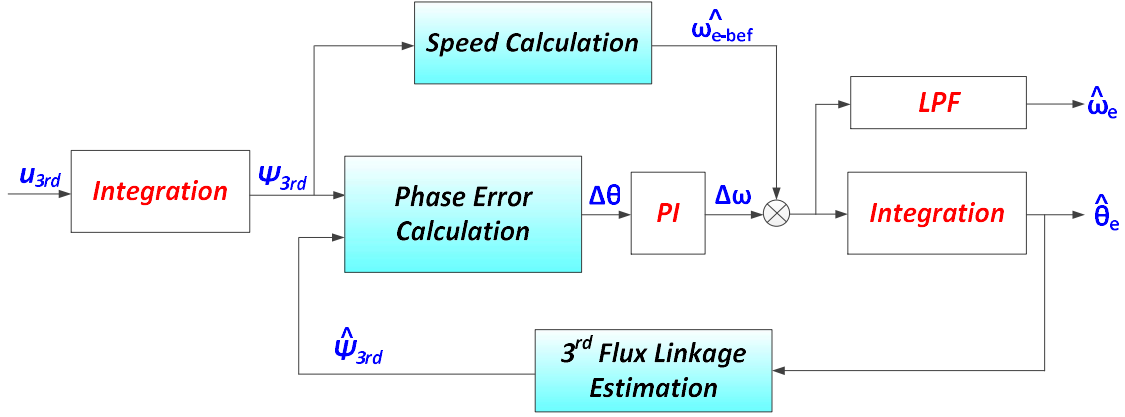
Fig. 1.10 Compensation for speed estimation error under dynamic conditions for 3rd harmonic back-EMF based sensorless control.

1.3.1.3 Flux-linkage based sensorless control methods

Alternatively, the flux-linkage in the machine fundamental model can be also used for the rotor position estimation of PM machines [WU91] [HU98] [SHE02] [PEL10], as shown in Fig. 1.11. The basic idea of the flux-linkage based sensorless control method can be described as

$$
\begin{aligned}
\psi_{s\alpha} &= \int (u_{s\alpha} - r_s i_{s\alpha}) dt \\
\psi_{s\beta} &= \int (u_{s\beta} - r_s i_{s\beta}) dt
\end{aligned}
\tag{1.5}
$$

where $\psi_{s\alpha}$, $\psi_{s\beta}$, $i_{s\alpha}$, $i_{s\beta}$, $u_{s\alpha}$, $u_{s\beta}$ are the stator flux-linkages, currents and voltages in the α- and β-axes, respectively. Normally, the stator voltages in (1.5) can adopt the reference voltages, which do, however, suffer from inverter nonlinearity effects, e.g., dead time, voltage drop of the power switches, switching delay, etc., [HAR00] [TER01] [PEL10]. Accordingly, with the offline measurements or the self-commissioning procedures, the inverter nonlinearity effects can be suppressed for online rotor position estimation, as shown in Fig. 1.12 [PEL10]. Besides, it is also noted that the open-loop calculation for the flux-linkages in (1.5) is also easily affected by the stator resistance variations and integration drift [WU91] [SHE02]. To improve these issues, several close-loop observation methods for the flux-linkage are also presented in [HU98] [YOO09] [FOO10].
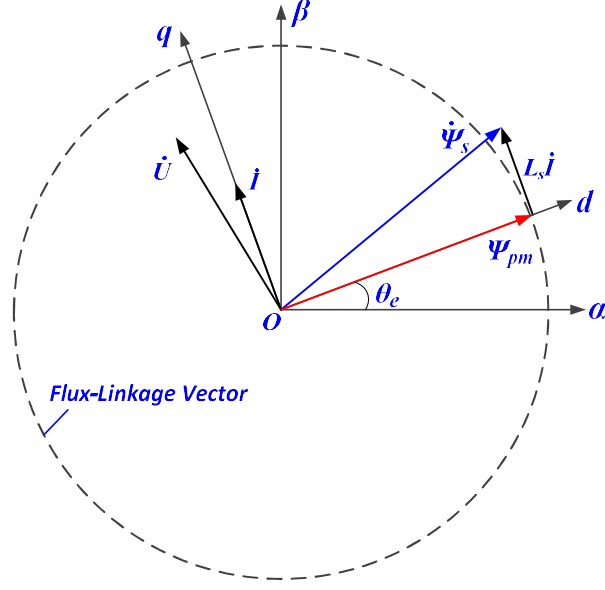
Fig. 1.11 Flux-linkage phasor diagram for the PM machines.
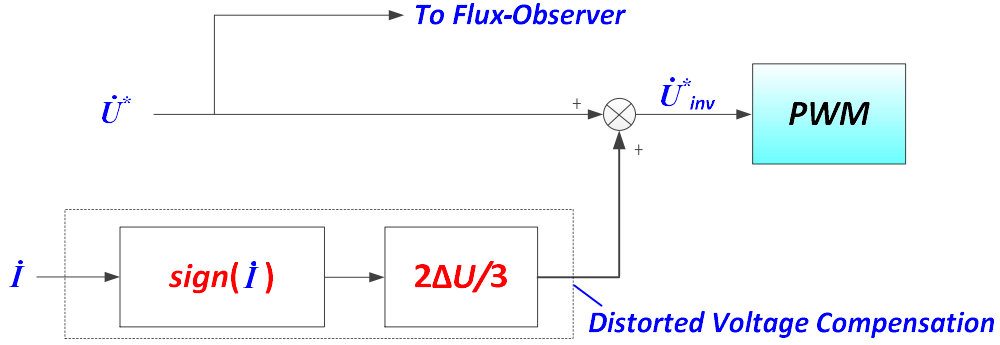
Fig. 1.12 Compensation of inverter nonlinearity effects for flux observer sensorless method.

However, the conventional flux observer based sensorless method cannot be applied to the salient pole PM machines. Accordingly, similar to the extended back-EMF method, the active flux method is presented to transform the salient pole machine to a non-salient pole counterpart [BOL09] [ZHA15]. Specifically, the active flux can be described as

$$\psi_d^a = \psi_{pm} + (L_d - L_q)i_d \tag{1.6}$$

where Ψ_d^a is the active flux, Ψ_{pm} is the PM flux-linkage, L_d and L_q are the apparent d- and q-axis inductances, i_d is the d-axis current, respectively. With (1.6), the mathematical model in the rotor reference frame can be re-described as

$$\vec{u} = r_s\vec{i} + (s + j\omega_e)L_q\vec{i} + (s + j\omega_e)\vec{\psi}_d^a \qquad (1.7)$$

where u and i are the complex voltage and current vectors, ω_e is the electrical angular frequency, respectively. From (1.7), the salient pole PM machine model has become the non-salient type. Besides, the active flux position is the same as the rotor PM flux position, which therefore can greatly simplify the estimation of rotor position and speed [BOL09]. In order to obtain the active flux, from Fig. 1.13, it can be described as

$$\vec{\psi}_d^a = \vec{\psi}_s - L_q\vec{i}_s \qquad (1.8)$$

From (1.8), the active flux can be easily obtained in the stationary reference frame, and then the rotor position and speed can be estimated based on the arctangent operation [BOL09].
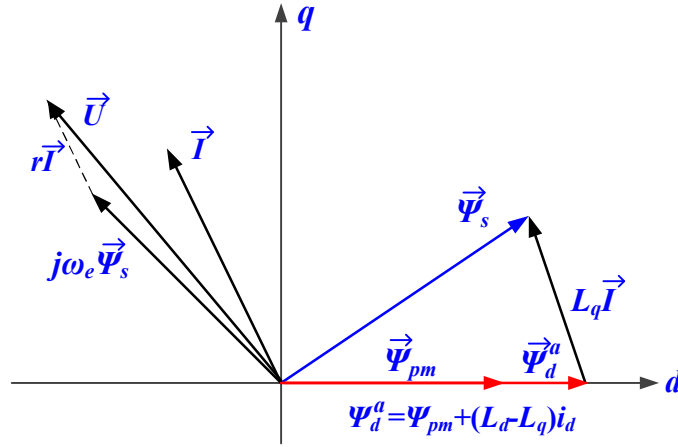
Fig. 1.13 Active flux phasor diagram for the salient PM machines.

1.3.1.4 Other observer based sensorless methods

Besides, based on the PM machine mathematical model, the adaptive observers, e.g., the EKF and MRAS, etc., are also utilized for the estimation of rotor position and speed [LEV02] [BAE03a] [QUA14] [PII08] [GAD10] [VER14]. These adaptive observers are shown to have the merits of fast convergence, good robustness, insensitivity to machine parameter variations, etc.

By way of example, the basic idea of the MRAS based sensorless method is to utilise one adjustable model to track the reference model. The estimation errors between the two models will then be used for the correction of the adjustable model. When the adjustable model behaves in the same way as the reference model, the rotor position and speed information can

then be obtained [BAE03b] [GAD10]. One specific example for the MRAS based sensorless method, as shown in Fig. 1.14 [BAE03b], is to use the output from the d-axis current controller as the input estimation error signal. In Fig. 1.14, the feed-forward voltage u_{ds_ff} predicted from the adjustable model can be described as

$$u_{ds\_ff} = r_s i_d - L_s \hat{\omega}_e i_q \qquad (1.9)$$

Then, the actual applied voltage in the reference model, i.e., the d-axis voltage command u_d^*, can be described as

$$u_{ds\_ff} = r_s i_d - L_s \omega_e i_q + \omega_e \psi_{pm} \sin(\Delta\theta) \qquad (1.10)$$

The estimation error Δu_d between the above two models can thus be expressed as

$$\Delta u_d \approx \omega_e \psi_{pm} \Delta\theta \qquad (1.11)$$

Then, with the position observer in Fig. 1.14, the estimated rotor position and speed can be obtained.
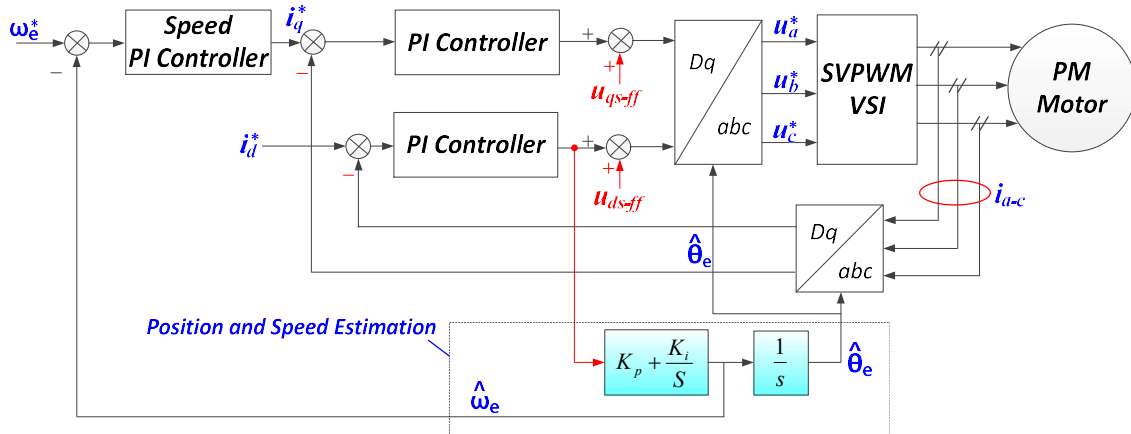
Fig. 1.14 Sensorless vector control based on MRAS method.

1.3.2 Saliency based sensorless methods

The back-EMF/flux-linkage based sensorless methods presented above offer excellent performances in the middle- and high-speed regions. However, they lose the effectiveness for rotor position estimation at standstill and in low-speed regions due to the significantly reduced signal amplitudes. Alternatively, the machine saliency detection based sensorless techniques can be employed in this operation mode, because the amplitude of the machine

saliency (e.g., the 2nd harmonic phase inductance) is not related to the rotor speed.

Machine saliency can be divided into the two categories, i.e., the inductive saliency [KAN10] [YAN11] [GRA15] and resistive saliency [YAN12a] [GRA15]. Specifically, the inductive saliency is generated due to the non-uniform distribution of the airgap permeance, Fig. 1.15, resulting in the unequal magnetic paths for the d- and q-axis armature reactions. In Fig. 1.15, for certain phase, the flux-paths always change with the rotation of the salient pole, and consequently the phase inductance varies with the rotor position. Different from the back-EMF signals varying once during one electrical period, the inductance varies twice, Fig. 1.15, due to that the armature flux paths are exactly the same when rotor stopping at either north-pole or south-pole.
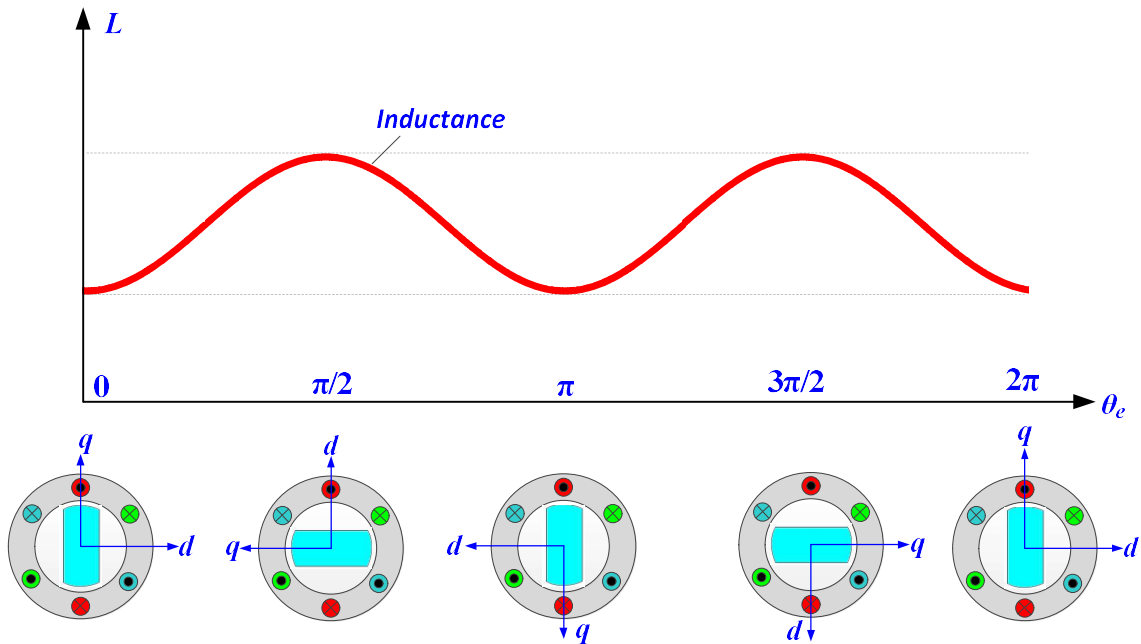
Fig. 1.15 Saliency inductance variation with rotor position.

On the other hand, resistive saliency is generated due to the spatial variation of total eddy-current losses, i.e., the eddy-current-reflected saliency [YAN12a]. This can be explained by the fact that the flux-lines penetrating the irons and PMs always vary from d-axis to q-axis, as shown in Fig. 1.17(a)-(b). Accordingly, the induced eddy-current losses are featured with the spatial variation, i.e., the resistive saliency, in Fig. 1.17 [YAN12a]. The major advantage of resistive saliency is that even in a non-salient SPM machine without sufficient stator saturation, the variations of the eddy current loss can be obtained with carrier signal injections [YAN12a]. However, similar to the inductive saliency, the resistive saliency also

undergoes two cycles during one electrical period, resulting in the uncertain magnetic polarity [YAN12b].

(a) Injection at d-axis   (b) Injection at q-axis

$(i_a=1.0$ A, $i_b=-0.5$ A, $i_c=0.5$ A) $(i_a=0$ A, $i_b=-0.866$A, $i_c=0.866$ A)
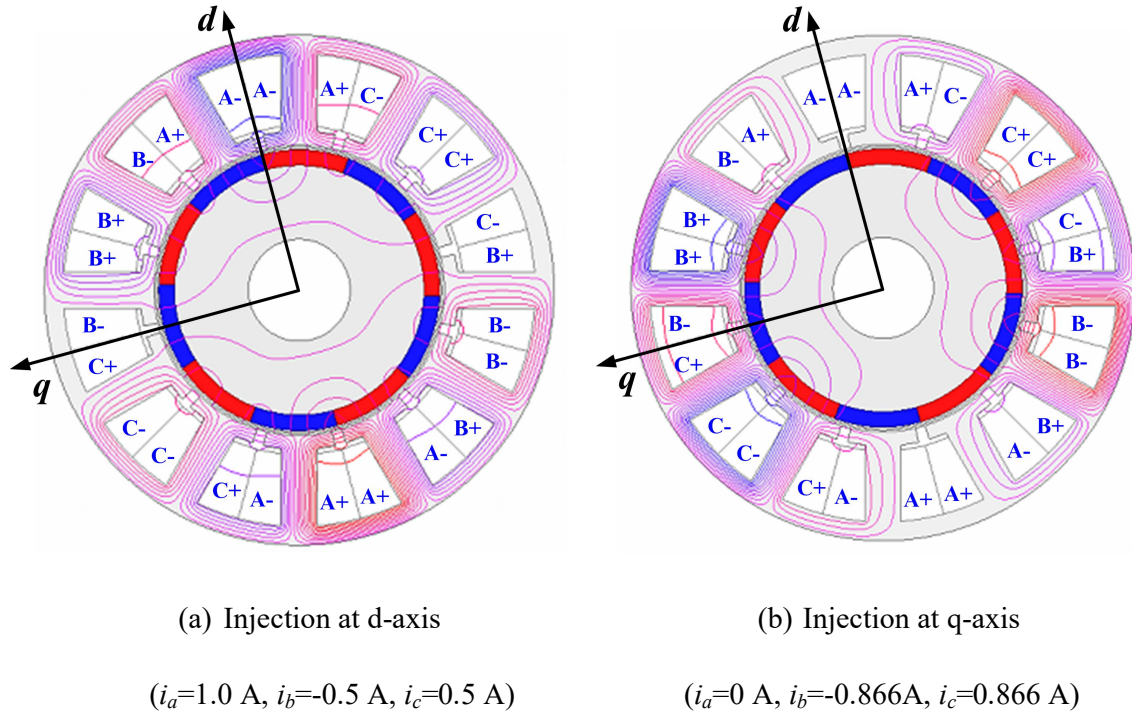
Fig. 1.16 D-axis and q-axis armature flux distributions of the PM machine.

Then, by exploiting these machine saliencies at standstill and in low-speed regions, the rotor position and speed information can be potentially obtained using high frequency (HF) signal excitations [JAN95] [SCH96] [RAU07] [LEI11] [BRI11]. The basic principle is that with the interaction between the HF excitations and machine saliency, the rotor-position-dependent carrier responses can be generated. Then, with the appropriate signal demodulation and position observers, the rotor position and speed can be estimated from these carrier responses. Currently, there are mainly three types of HF excitations, i.e., the continuous carrier signal injection, transient voltage vector injection, and inherent PWM excitations, which will be introduced in the following sections, respectively.

(a) Injection at d-axis   (b) Injection at q-axis
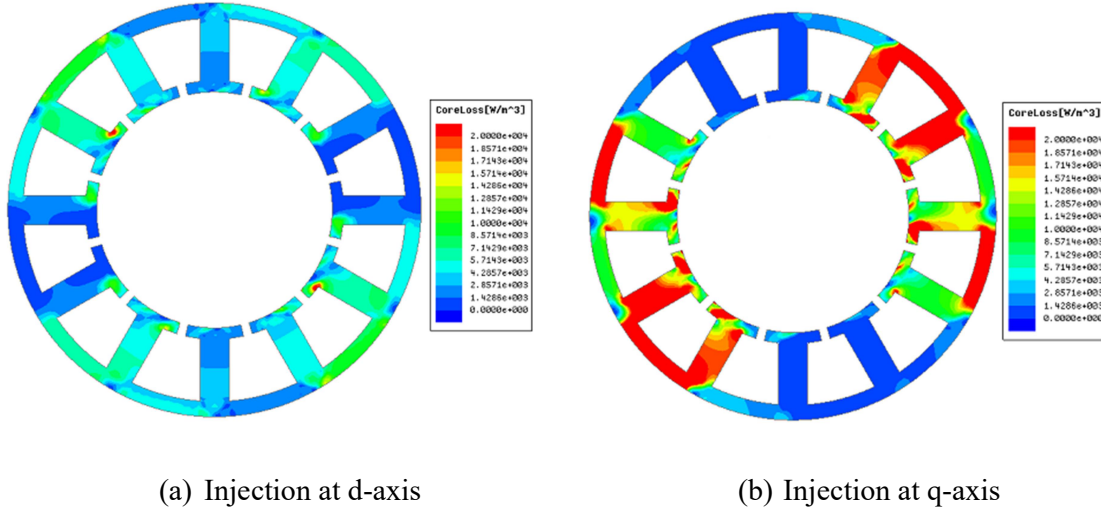
Fig. 1.17 Iron loss density distribution for the PM machine due to carrier signal injection.

1.3.2.1 Continuous carrier signal injection methods

Continuous carrier signal injection methods can be mainly classified into three types: rotating injection on the stationary reference frame [JAN95] [DEG98] [GAR07] [RAC08a] and pulsating injection on the estimated synchronous reference frame [COR98] [JAN03] [YOO11], and pulsating injection on the stationary reference frame [LIU14b] [CHE16c] [TAN16].

Specifically, for the rotating injection method, the three phase balanced carrier voltages are injected on both the α- and β-axes of the stationary reference frame, as shown in Fig. 1.18(a),

$$\begin{bmatrix} u_\alpha \\ u_\beta \end{bmatrix} = U \begin{bmatrix} \cos \omega_h t \\ \sin \omega_h t \end{bmatrix} \tag{1.12}$$

where u_α and u_β are the injected voltages in the α- and β-axes, U is the injection amplitude, ω_h is the injection angular frequency, respectively. Then, based on the HF injection model, the carrier currents can be derived as [JAN95]

$$i_\alpha + j i_\beta = \frac{U}{2\omega_h L_d L_q} [(L_d + L_q)e^{j(\omega_h t - \pi/2)} + (-L_d + L_q)e^{j(-\omega_h t + 2\theta_e + \pi/2)}] \tag{1.13}$$

where i_α and i_β are the current responses in the α- and β-axes, L_d and L_q are the incremental d- and q-axis self-inductances, respectively. It is noted that the incremental inductance describes the ratio of the variation of flux-linkage ($\Delta\Psi$) to the current variation (Δi), i.e., $\Delta\Psi/\Delta i$ [LI09]. In contrast, the apparent inductance directly describes the ratio of the flux-linkage (Ψ) to the

current (i), i.e., Ψ/i. From (1.13), it can be seen that the negative sequence carrier current contains the rotor position information [JAN95] [DEG98], and its amplitude is related to the machine saliency level. Accordingly, with the signal demodulation (synchronous reference frame filter, etc.) and rotor position observer, the rotor position and speed can be estimated [RAC08c]. In contrast, for the pulsating injection in the estimated synchronous reference frame in Fig. 1.18(b), the injection voltages can be described as

$$\begin{bmatrix} \hat{u}_d \\ \hat{u}_q \end{bmatrix} = U \begin{bmatrix} \cos\omega_h t \\ 0 \end{bmatrix} \quad (or \ U \begin{bmatrix} 0 \\ \cos\omega_h t \end{bmatrix}) \tag{1.14}$$

Then, the carrier current response for the pulsating injection can be obtained as (assuming the injection is performed at the estimated d-axis) [JAN03]

$$\hat{i}_{qh} = \frac{U}{2\omega_h L_d L_q}(-L_d + L_q)\sin(\omega_h t)\sin(2\Delta\theta) \tag{1.15}$$

Accordingly, the estimated q-axis current response in (1.15) can be utilised for the rotor position estimation. The idea for the pulsating injection is that once the estimated d-axis aligns with the actual rotor d-axis, the estimated q-axis carrier current response in (1.15) will become zero, due to the natural decoupling of the actual d- and q-axes. Just by controlling the estimated q-axis carrier current to be zero, the estimated d-axis will hence accurately track the actual rotor position. Actually, the major difference between the rotating injection in (1.13) and the pulsating injection in (1.15) is that the former is a phase-modulation technique to track the saliency position, while the latter is an amplitude-modulation technique [KIM04a] [RAC08a] [RAC08c].

The pulsating injection in the stationary reference frame is also proposed in [LIU14b], as shown in Fig. 1.18(c). Accordingly, the carrier injection voltages can be expressed as [LIU14b]

$$\begin{bmatrix} u_\alpha \\ u_\beta \end{bmatrix} = U \begin{bmatrix} \cos\omega_h t \\ 0 \end{bmatrix}(or \ U \begin{bmatrix} 0 \\ \cos\omega_h t \end{bmatrix}) \tag{1.16}$$

Then, the carrier current responses in the α- and β-axes can be derived as (assuming the voltage injection is performed in the α-axis) [LIU14b]

$$\begin{bmatrix} i_\alpha \\ i_\beta \end{bmatrix} = \frac{U}{2\omega_h L_d L_q} \begin{bmatrix} (L_d + L_q) + (-L_d + L_q)\cos(2\theta_e) \\ (-L_d + L_q)\sin(2\theta_e) \end{bmatrix} \sin \omega_h t \qquad (1.17)$$

This type of injection method is simple to implement, and also quite reliable due to the injection axis being in the stationary reference frame. However, from (1.17), it requires the machine parameter information in the starting period, which may require the offline measurements and therefore increase the signal demodulation complexity. The comparisons for the above three types of carrier signal injection methods are given in Table 1.1[LIU13].

(a) Rotating injection

(b) Pulsating injection in the estimated d-/q-axis

(a) Pulsating injection in the stationary reference frame
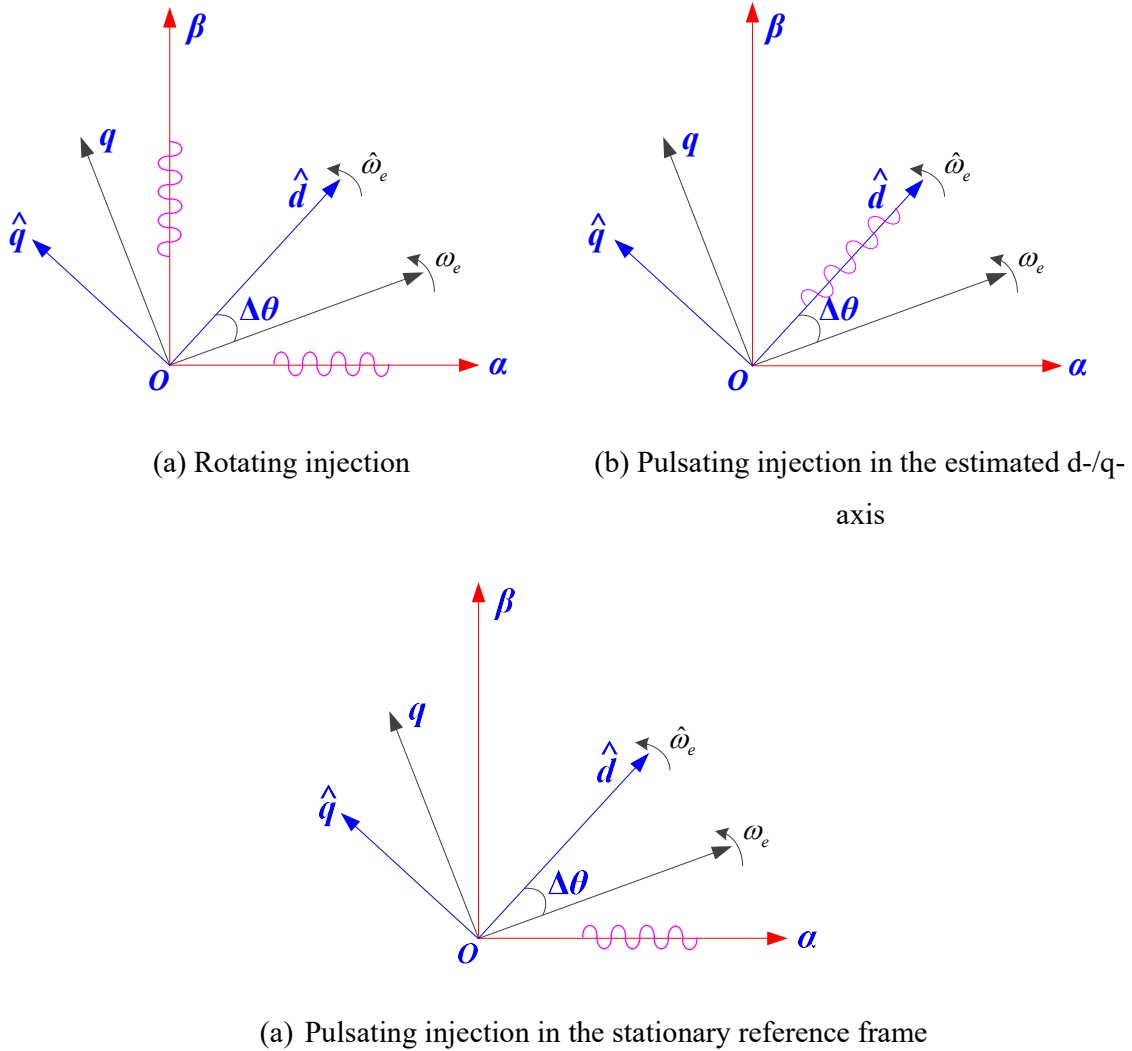
Fig. 1.18 Different continuous carrier signal injection methods.

To improve the accuracy of these carrier signal injection methods, the influences of cross-coupling magnetic saturation [GUG06] [REI08] [LI09], inverter nonlinearity [GON11] [GUE05] [CHO08] multiple saliency [DEG98], and resistances [REI10], etc. have been

investigated. The cross-coupling magnetic saturation effects between the d- and q-axes have been shown to cause the phase shift in the carrier responses, resulting in the position estimation errors [LI09]. Accordingly, the neural network structure [REI08] or offline measurements [LI09] [LIU14b], etc., have been used for the online compensation and have shown great effectiveness. The inverter nonlinearity effects on the carrier signal injection methods are also investigated, and the parasitic capacitance and dead time effects are shown to be the two major distortion sources [GUE05] [GON11]. Various compensation techniques, such as the pre-compensation with online distorted voltage estimation [CHO06] or available datasheet parameters [SAL11], positive sequence carrier current responses [GON11], etc., have been utilised to suppress the inverter nonlinearity. The multiple saliency effect is another type of distortion for the carrier signal injection methods [DEG98] [RAC08c] [CHE16b]. Magnetic saturation, asymmetric distribution of three phase stator windings, and slotting effects, etc., will possibly contribute to the multiple saliency effects [DEG98]. Consequently, the machine's spatial saliency will not be purely sinusoidal-distributed (unlike in Fig. 1.15). Accordingly, the offline measurements [DEG98] [BRI02], multi-signal injection [CHE14], adaptive notch filter [CHE16b], etc., have been utilised to decouple the multiple saliency effects online. Besides, in carrier signal injection based methods, the purely inductive model is generally employed for simplified analysis. In [REI10], the effects of the high-frequency resistances on saliency tracking-based sensorless control methods are also presented, with potential sources of errors in the estimated position due to the resistances being also suppressed.

Table 1.1 Comparative Results of Different Carrier Signal Injection Strategies

	Rotating	Synchronous Pulsating	Stationary Pulsating
Reference frame	Stationary	Estimated synchronous	Stationary
Carrier current response	Phase-modulation	Amplitude-modulation	Amplitude-modulation
Stability of signal injection	Good	Medium	Good
Signal demodulation	Medium	Simple	Complex
Torque ripple	Large	Small	Medium
Cross-coupling	Same	Same	Same

The effectiveness evaluation for the carrier signal injection methods is also investigated, with the use of the anisotropy ratio [GUG06] [SER12], feasible region [BIA07] [BIA15] and sensorless safety operation area (SSOA) [ZHU11] [LIN15], respectively. In [BIA07], the feasible region accounting for the machine saliency level in the dq-plane is introduced, which is bounded by the curve $L_{dif}=0$ (L_{dif} being the difference between d- and q-axis inductances). The effect of stator and rotor saturation on the feasible region is further investigated in [BIA13]. In [ZHU11], the SSOA is also proposed to define the working area in which the sensorless operation can be guaranteed with the consideration of practical issues, namely A/D resolution and signal to noise (S/N) ratio. Furthermore, the proper injection frequency and voltage can be selected according to the SSOA [ZHU11] [LIN15].

On the other hand, in terms of injected signal waveforms, carrier signal injection methods can be classified into sinusoidal-wave [JAN95] [JAN03] and square-wave signal injection [YOO11] [LEI08] [NI16]. Generally, the sinusoidal-wave signal injection strategy is easy and simple for implementation [JAN03]. However, due to the limited PWM switching frequency, the injection frequency cannot be too high, which makes the separation between fundamental and carrier signals very difficult, eventually resulting in limited system bandwidths [LIU14c] [YOO11]. In contrast, the square-wave injection strategy can adopt higher injection frequency, and accordingly the system bandwidths can be significantly enhanced because the low pass filters (LPFs) used for signal demodulation are completely eliminated [YOO11] [YOO14] [LIU14c]. However, the conventional square-wave injection methods may also have two main disadvantages. The first is that the carrier injection voltage needs to be much higher with the increase of injection frequency to maintain the reasonable signal-to-noise (S/N) ratio [SUN11] [LIU14c], while the carrier voltage is restricted to the available bus voltage for control [BRI01] [SUN11]. To reduce the injection voltage in square-wave injection strategy, the additional capacitor is added to the inverter output to suppress the inverter nonlinearity effects [KWO15]. In [KIM16], the injected voltage magnitude is regulated to suppress the induced HF current ripples, and accordingly under the constraint of the same RMS value of the current ripple, the average injection voltage is reduced. The second disadvantage for the square-wave injection methods is that generally the resultant carrier responses used for rotor position estimation require differentiation processing (i.e., $\Delta i/\Delta t$) [YOO11] [YOO14] [XIE16], which however increases the signal demodulation complexity compared to conventional sinusoidal signal injection methods [RAC08c]. Moreover, the differentiation of the carrier current signals is sensitive to current measurement

noises, and consequently may result in low S/N ratio [XIE16]. To improve the S/N ratio, over-sampling of the carrier current signals may be suggested [XIE16].

Furthermore, for carrier voltage signal injection methods, it is noted that apart from the carrier current responses, the zero sequence voltage responses can be also used for sensorless control [BRI05] [GAR07] [CON06]. Measuring the zero sequence carrier voltage, as with the 3rd harmonic back-EMF, requires a balanced resistor network and access to the machine neutral point are also required, as shown in Fig. 1.8. Compared to carrier current sensing based methods, it is found that zero sequence carrier voltage is less sensitive to injection distortions [BRI04] [GAR07]. Moreover, it has been observed that the system bandwidth can be significantly enhanced using zero sequence voltage. Consequently, position estimation accuracy and stability are improved [GAR07]. However, the conventional zero sequence carrier voltage sensing method is based on rotating signal injection [BRI05] [CON06], and the resultant position information signal is phase-modulated by machine saliency [BRI05]. Any signal processing delays (e.g., digital delay, sampling circuit delay, etc.) which affect the phase shift of zero sequence voltage can therefore give rise to errors in the estimated position [RAC08a] [RAC08c]. Additionally, as with the 3rd harmonic back-EMF method, the access to the machine neutral point is essentially required for the zero sequence voltage sensing methods [GAR07]. The comparisons between the conventional carrier current and zero sequence voltage sensing based sensorless techniques are summarized in Table 1.2 [BRI04] [GAR07] [RAC08a] [RAC08c] [KIM04a].

Table 1.2 Comparison of Different Carrier Injection Methods with Alternative Carrier Responses

	Pulsating injection with current sensing	Rotating injection with current sensing	Rotating injection with zero sequence voltage sensing
Access to machine neutral point	Not required	Not required	Required
Bandwidth	Medium	Medium	High
Sensitivity to injection distortion	Medium	High	Low
Reliablity	Medium	Medium	High
Carrier response	Amplitude-modulation	Phase-modulation	Phase-modulation
Signal Demodulation	Simple	Complex	Complex
Accuracy	High	Medium	Medium

Lastly, it should be noted that although the carrier signal injection methods have shown great effectiveness for rotor position self-sensing, they also suffer from several issues, such as, losses [YAN12a] [REI11] [LIM11], noises and vibration [WAN16a] [WAN16b], torque ripple [LIU13], and etc. The temperature issues for carrier signal injection methods are investigated in [REI11], and it is found that the rotating injection has the highest increase of temperature due to the overall highest losses. Besides, in order to reduce the noises and vibrations produced by carrier signal injection, one type of pseudo-random carrier injection strategy is presented in [WAN16a]. Specifically, as shown in Fig. 1.19 [WAN16a], carrier voltages with two different frequencies are randomly injected cycle by cycle, and consequently the power spectrum density distribution can be extended rather than remaining at a fixed frequency, resulting in reduced audible noises.
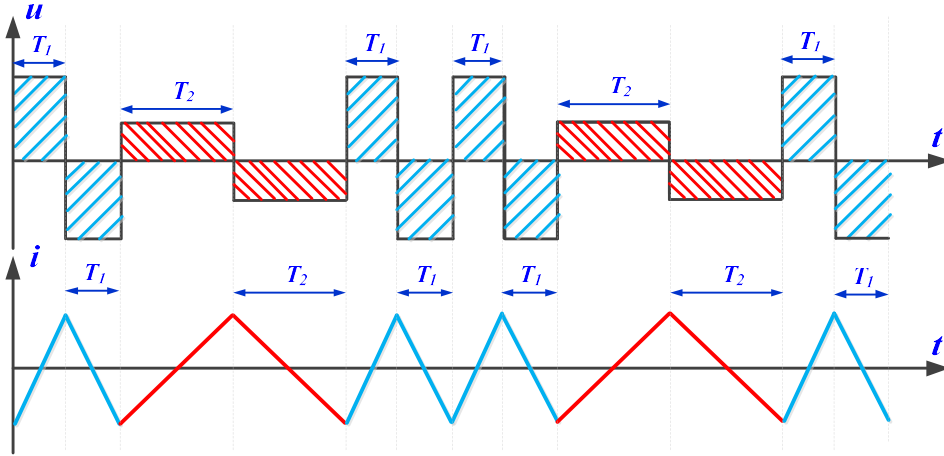
Fig. 1.19 Pseudo-random carrier voltage injection strategy.

1.3.2.2 Transient voltage vector injection methods

In the zero- and low-speed region, apart from the continuous carrier signal injection methods, the transit voltage vector injection in the PWM periods can be also utilised for the machine saliency detection [ROB04] [XIE16]. To use the voltage vector injection method, the PWM switching patterns should be modified, so the resultant current variations can be detected and demodulated for rotor position estimation. By way of example, for the INFORM (indirect flux detection by on-line reactance measurement) method, the transient vectors are injected during the zero vector dwelling of the PWM as shown in Fig. 1.20 [SCH96] [ROB04] [XIE15]. Three pairs of voltage vectors are injected within three continuous PWM periods, and then the rotor position information can be obtained by demodulating the current variations.

However, due to the INFORM method being performed in a very short period of time, it may increase the implementation complexity for the practical voltage injection and current sampling, etc., [XIE16]. Besides, the current response may also be sensitive to the parameter variations, measurement delay and noises, etc., [YOO11]. Additionally, as with the continuous carrier signal injection methods, the current distortions will also contribute to torque ripples, noises and vibrations. The double transient injection based modified INFORM method is thus proposed to improve the current waveforms in [ROB04].
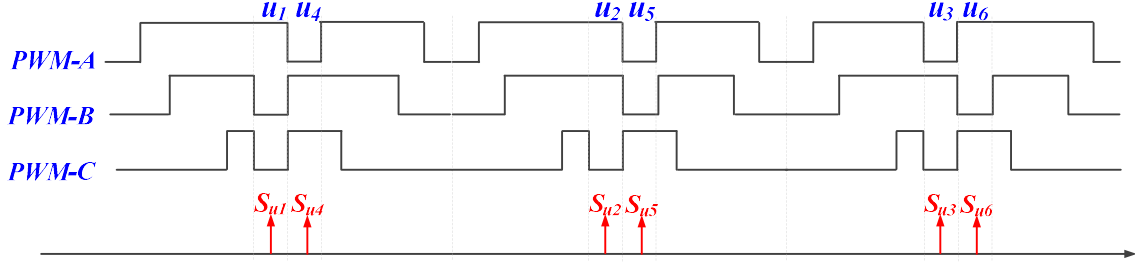
Fig. 1.20 Transit voltage vector injection based on INFORM method.

1.3.2.3 Inherent PWM based methods without additional signal injection

Under normal machine operation, the voltage vectors in the inherent PWM switching patterns can be also directly utilised to estimate the rotor position. Inherent PWM methods do not need to inject any additional signals, resulting in reduced switching losses, noises, and torque ripples compared with continuous carrier signal injection and transit voltage vector injection methods [RAU07] [RAU11].

In [RAU07], the zero vector current derivative (ZVCD) method during one PWM period is used to estimate rotor position. Specifically, the current derivative of the estimated d-axis current during the zero vector dwelling period in Fig. 1.21 can be described as

$$\left.\frac{d\hat{i}_d}{dt}\right|_{u_0/u_7} = -\frac{r_s}{2}\left(\frac{1}{L_q} - \frac{1}{L_d}\right)\hat{i}_q \sin(2\Delta\theta) - \frac{\omega\psi_{pm}}{L_q}\sin(\Delta\theta) \qquad (1.18)$$

Then, from (1.18), the estimated rotor position and speed can be obtained from the inductive saliency information by neglecting the back-EMF signals in the zero- and low-speed regions. Similarly, the current derivatives can be also measured from other voltage vectors in one PWM period to reconstruct the rotor position information [HOL05] [GAO07] [BOL11] [HUA11].
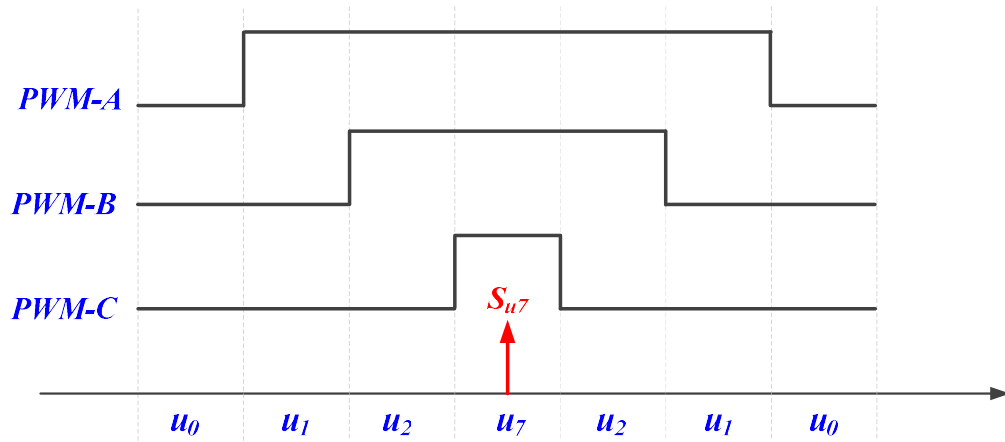
Fig. 1.21 Zero vector current derivative method in one PWM period.

Apart from the carrier current responses in the stationary and synchronous reference frames, the carrier responses in the zero sequence reference frame due to PWM excitations can be also utilised for rotor position estimation [LEI11] [HOL98]. In [HOL98] [IWA16], the zero sequence carrier voltage due to the inherent PWM is used for machine saliency tracking. It is noted that the zero sequence voltage sensing method due to PWM works on the same principle as that due to the continuous carrier signal injection [BRI05], while the major differences are in the implementation procedures [BRI05] [BRI04]. Alternatively, with the analog filter connected in the zero sequence current paths in Fig. 1.22, the zero sequence current responses can be also used for the rotor position estimation [LEI11]. However, the analog filter should be well designed to eliminate the zero sequence currents around the fundamental frequency (e.g., 3rd harmonic current), while leaving only the zero sequence responses around PWM frequency.
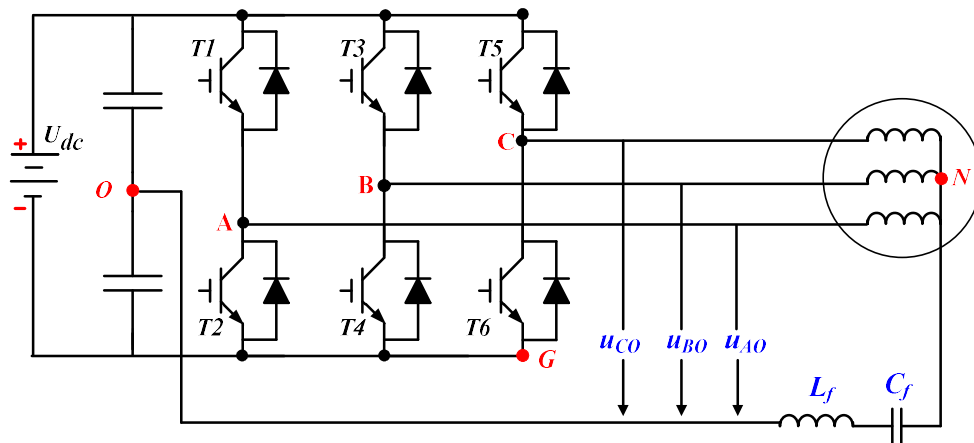
Fig. 1.22 Zero sequence current detection based on standard SVPWM.

From the above analyses, the comparisons for the above saliency detection based sensorless strategies are summarized in Table 1.3 [GON12].

Table 1.3 Comparative Results of Machine Saliency Based Position Estimation Methods

	Carrier signal injection	Transient voltage vector	Inherent PWM
Implementation complexity	Simple	Medium	Medium
Additional injection	Required	Required	Not Required
Excitation frequency	Low	Medium	High
Dynamic response	Slow	Medium	Fast
Current measurement cost	Low	High	High
Wide speed operation	Poor	Medium	Good
Current sampling frequency	Medium	High	High

1.3.2.4   Magnetic polarity identification

Although the above HF excitation methods exploiting the machine saliencies have shown the good effectiveness for rotor position estimation, they cannot detect the actual magnetic polarity. This is due to the inductive (resistive) saliency undergoing two cycles during one electrical period, as shown in Fig. 1.15 [GON13]. Clearly, the back-EMF based sensorless methods do not require any identification of magnetic polarity. Accordingly, for saliency detection based methods, many efforts have been taken to investigate the magnetic polarity detection, which can mainly be divided into transit short pulses [HOL08] [NOG98] [HAQ03] [WAN12], secondary current harmonics [JEO05] [KIM04b] [ZHA14] [RAC08b], and amplitude variation of carrier current due to saturation changes [GON13]. Among the three types of methods, in terms of signal-to-noise (S/N) ratio, short pulses and the amplitude variation based methods are superior [GON13]. The basic principle for the two types of methods is to apply different d-axis excitations in the estimated rotor direction. Then, by observing the carrier response variations produced by the changes of d-axis inductance, the magnetic polarity ambiguity can be cleared [GON13]. It is noted, however, that the

convergence for these two methods is not as fast as that of the secondary harmonic methods [GON13]. This is due to the secondary harmonic method not needing the further step to change the magnetic saturation with additional signals. However, the disadvantage for the secondary harmonic method is the reduced S/N ratio [JEO05] [GON13]. This can be improved by increasing carrier injection voltage, which does, however, increase the noises and vibration at the same time [JEO05]. The comparisons of the above different magnetic polarity identification strategies are listed in Table 1.4 [GON13].

Table 1.4 Comparative Results of Different Magnetic Polarity Identification Methods

	Short pulses	Current amplitude variations	Secondary current harmonics
Concept complexity	Simple	Simple	Complex
S/N ratio	High	High	Low
Robustness	High	High	Low
Response	Slow	Slow	Quick
Computation burden	Light	Light	Medium
Integration with sensorless algorithm	No	Yes	Yes

1.4   Scope and Contributions of the Thesis

In this chapter, the main sensorless control strategies for the PM machines have been introduced and reviewed. The research focus of this thesis is continuous carrier signal injection methods, utilising alternative types of carrier responses (i.e., the carrier current and zero sequence carrier voltage). The research scope of this thesis is illustrated in Fig. 1.23.
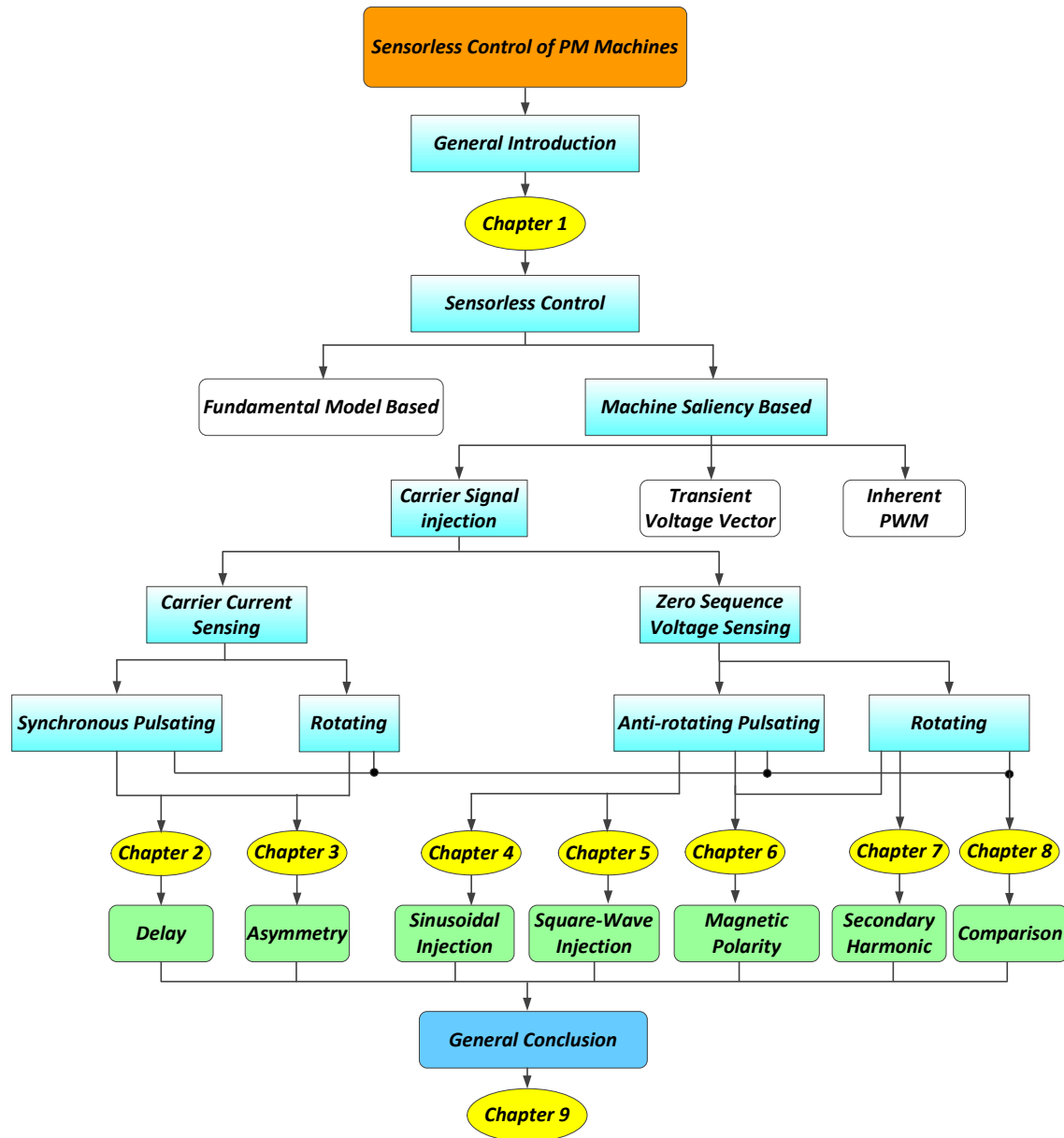
Fig. 1.23 Research scope.

The thesis is structured as follows.

Chapter 2 discusses the combined effects of signal processing delay and HF resistance for the two conventional carrier signal injection methods, i.e., the rotating injection in the stationary reference frame and pulsating injection in the estimated synchronous reference frame. Accordingly, a new compensation strategy based on modifying the demodulation signal phase angle is also developed for the online compensation of the position estimation errors.

Chapter 3 investigates the influence of asymmetric machine parameters on the two conventional carrier signal injection methods. Errors in the position estimation due to the resistance and inductance asymmetries are analytically derived and compared for the rotating and pulsating signal injection methods. Moreover, the online compensation strategies for such asymmetries are also developed for the two injection methods.

Chapter 4 proposes a novel sinusoidal-wave signal injection strategy for the rotor position estimation utilising the zero sequence carrier voltage response. In contrast to the conventional rotating injection in the stationary reference frame and pulsating injection in the estimated synchronous reference frame, the proposed method is injected on the estimated reference frame anti-rotating at twice the rotor's estimated electrical speed. The proposed method combines both the synergies of zero sequence voltage sensing and pulsating injection.

Chapter 5 proposes a novel square-wave signal injection strategy utilising the zero sequence carrier voltage response for the rotor position estimation. The square-wave signal is also injected on the estimated reference frame anti-rotating at twice the rotor's estimated electrical speed. The proposed square-wave injection method will demonstrate the merits of both zero sequence sensing and square-wave injection.

Chapter 6 investigates the initial rotor position estimation and magnetic polarity identification utilising the zero sequence carrier voltage responses. Two types of magnetic polarity detection methods, i.e., the amplitude variation due to saturation changing and secondary zero sequence carrier voltage harmonics, respectively, will be examined for the carrier signal injection methods.

Chapter 7 proposes a novel position estimation method without the need for magnetic polarity identification, which is based on the modulated HF saliency. The mechanism of the modulated HF saliency containing the real magnetic polarity information will be clearly described, and then the carrier signal responses (secondary harmonics) from the interaction between the HF field and the modulated HF saliency will also be derived. Accordingly, with these secondary harmonic responses, the actual rotor position can be estimated without any ambiguity of magnetic polarity.

Chapter 8 presents the full comparisons for the different carrier signal injection methods, considering alternative carrier responses. Specifically, the influence of signal processing delays, the cross-coupling magnetic saturation effects, inverter nonlinearity effects, multiple

saliency effects, and the iron and PM losses due to carrier injection, will be investigated.

Chapter 9 summarizes the research work in this thesis and discusses potential future work in this area.

The major contributions of the research work in this thesis include

- With the analyses on the combined effects of signal processing delays and HF resistance, a new online compensation strategy is proposed to suppress the position estimation errors via tracking the phase shift due to the delays. This contribution has been published in [XU17a].

- The position estimation errors in the carrier signal injection methods due to machine parameter asymmetries are systematically and analytically derived. To suppress the position errors, guidelines for the injection frequency selection are provided for resistance asymmetry, while a dual frequency injection strategy is also presented for inductance asymmetry. This contribution has been published in [XU16a].

- A novel anti-rotating sinusoidal-wave signal injection strategy is proposed to combine the merits of zero sequence voltage sensing and the amplitude-modulation technique. This contribution has been published in [XU16b].

- The novel anti-rotating signal injection strategy is further applied for the square-wave signal injection to combine the synergies of the zero sequence voltage sensing square-wave injection. This contribution has been published in [XU16c].

- Magnetic polarity identification methods using the zero sequence voltage responses are proposed. The amplitude variation based polarity detection method using the zero sequence voltage is found to have a higher detection sensitivity. Besides, for rotating injection, the secondary harmonic based polarity detection method using the zero sequence voltage has the advantages of simple signal demodulation, fast response, and moreover a large S/N ratio. This contribution has been published in [XU17b].

- A novel position estimation method that exploits the modulated HF saliency is proposed and the estimated rotor position does not have the ambiguity of magnetic

polarity. This contribution has been published in [XU16d].

- The systematic comparisons are also performed between different carrier signal injection methods considering alternative carrier responses. The comparative results provide more physical understandings about how the carrier injection method works and how it is affected by the nonlinear behaviours of the PM machine or inverter.

It is noted that in this thesis, totally two prototype PM machines have been used for the experimental verifications. Specifically, a 600 W interior PM (IPM) machine is used in chapters 2 and 3. Then, from chapter 4 to chapter 8, a 230 W surface-mounted PM (SPM) machine with the access to the winding neural point is used.

The publications on the Ph.D. research topic are given in Appendix A.

2 Carrier Signal Injection Based Sensorless Control for Permanent Magnet Synchronous Machines with Tolerance of Signal Processing Delays and High Frequency Resistances

2.1 Introduction

As introduced in chapter 1, the carrier signal injection methods have shown good effectiveness for rotor position estimation of PMSMs in the zero- and low-speed range [JAN95] [JAN03]. However, they suffer from several issues, e.g., losses [YAN12a] [REI11], noises [KOC09], voltage margin for the injection [BRI01], and moreover the limited system bandwidths due to the use of filters for the separation of carrier and fundamental frequency signals [BRI01] [GAR07] [YOO11]. Particularly, in order to improve the bandwidth issue, higher injection frequency is suggested for the carrier injection methods [BRI01] [SUN11], and then the filters for signal separation can be selected weaker leading to reduced delays [YOO11].

However, the increase of carrier injection frequency is not costless since larger injection voltage is then required to maintain the reasonable signal amplitude for the carrier currents, while the injection voltage is intrinsically limited to the available voltage for machine control [BRI01] [SUN11]. Normally, it is the case especially for low resolution A/D occasions where the signal amplitude has great effect on the position estimation performances [BRI01] [ZHU11]. Whereas for high resolution A/D converter cases, e.g., the 16-bit A/D converter utilised for experiments in this chapter, several milli-ampere current sensing can be fulfilled. Therefore, under such cases, with the carrier voltage maintained, the injection frequency can be increased to some extent (>1/10 PWM switching frequency), leading to enhanced system bandwidths.

However, it should be noted that when higher carrier frequency is injected, on one hand, signal processing delays including PWM updating delay [BAE03b] and inverter delay become prominent, which can significantly deteriorate the position estimation performances as analysed in [CUP12] [MOG13] [KOC09]. These delays can cause additional phase shift between the carrier voltage and current, which is originally assumed to be 90 degrees for purely inductive components [MOG13] [KOC09]. On the other hand, with the increase of injection frequency, the HF resistance components may be enlarged by the eddy-current

losses, etc., [WAN14e] [REI10] [YAN12a].

Then, accordingly, with the typical signal demodulation for rotor position estimation, it will be shown that the useful inductive components (especially the primary inductive saliency component) will be reduced significantly, while the undesirable HF resistive component will be simultaneously enlarged due to the delay effects. Consequently, the position estimation performances are severely degraded at higher injection frequencies, caused by the combined effects of digital delay and HF resistance, particularly for the pulsating signal injection method.

Since the parasitic HF resistance effect is difficult to be suppressed, the delay effect can be alternatively compensated to improve the position estimation performance [CUP12] [MOG13] [SAT11] [HA03]. In [CUP12], the look-up (LUT) table technique is utilised, which however requires time-consuming offline tests and furthermore takes the memory of digital controller. In [MOG13], for the pulsating injection, the carrier current responses in the positive and negative reference frame are extracted, respectively, to suppress the position errors caused by the delay effects. Although the method in [MOG13] shows good effectiveness, it is more computationally intensive compared to the classical signal demodulation method for the pulsating injection [RAC08c], and consequently may degrade the dynamic responses. In [SAT11] [HA03], the 45 degrees rotation based control strategy is utilised for the delay effect suppression and also has shown great effectiveness. However, since the HF resistance effect is not considered, the position estimation performance at higher injection frequency is compromised, which will also be illustrated and compared in this chapter. Besides, the method proposed in [SAT11] [HA03] may not be applicable for the rotating signal injection strategy.

Therefore, in this chapter, firstly, the carrier signal injection methods at higher injection frequency will be analysed, and it will be shown that position estimation errors will become unacceptable due to the combined effects of HF resistance and digital delay. Then, based on the above analyses, a new compensation strategy utilising PI controller is proposed to suppress the position errors due to signal processing delay and HF resistance effects. Specifically, by modifying the demodulation signal phase angle, the amplitude of inductive saliency part used for position tracking is significantly increased while the HF resistance part is suppressed. Finally, the effectiveness of proposed compensation methods for the two carrier injection methods is verified experimentally on a prototype IPM machine.

The major new results of this chapter have been published in [XU17a].

2.2 Carrier Signal Injection Model Considering Signal Processing Delay and HF Resistance Effects

Generally, the carrier signal injection method assumes the phase shift between the carrier voltage and current is 90 degrees for purely inductive components. However, the phase differences over 90 degrees are observed as shown in Fig. 2.1, which can be attributed to the HF resistance [REI10] [GON11] [WAN14], inverter on/off delay [GUE05] [RAC08c], PWM duty cycle updating delay and analog circuit delays [BAE03b] [CUP12] [MOG13], etc. By way of example, due to the PWM updating delay, the actual voltage applied to the windings may already have a delay angle with the reference injection voltage, resulting in the phase angle delay of carrier current as shown in Fig. 2.1.

With the increase of carrier signal injection frequency, the additional phase shift φ will be significantly increased as illustrated in Fig. 2.2, from which over one sampling delay is clearly observed. On the other hand, the HF resistance effect will also be enlarged at higher injection frequencies [WAN14] [REI10]. These effects on the position estimation performance will be modelled and analysed as follows.
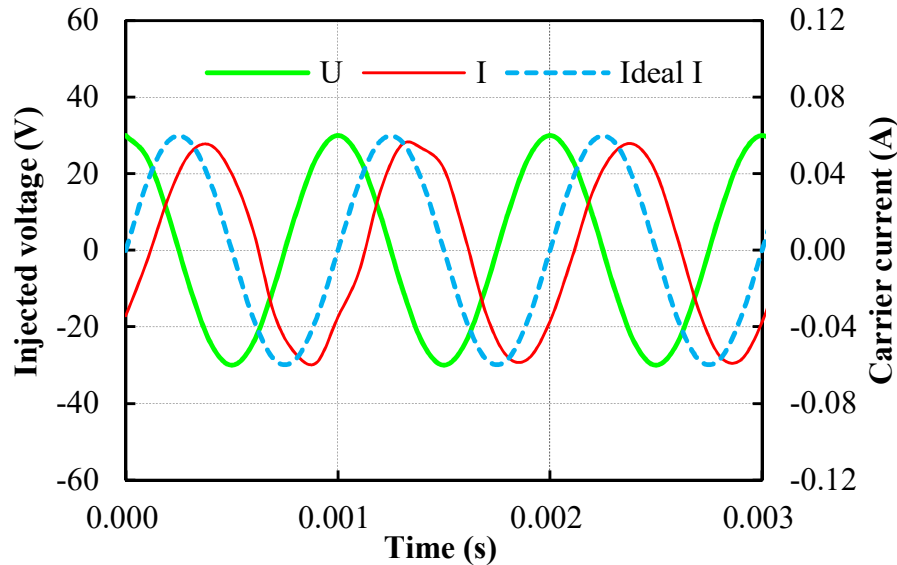
Fig. 2.1 Measured phase shift between carrier voltage and current at 30 V/1 kHz injection (PWM switching frequency 10 kHz).
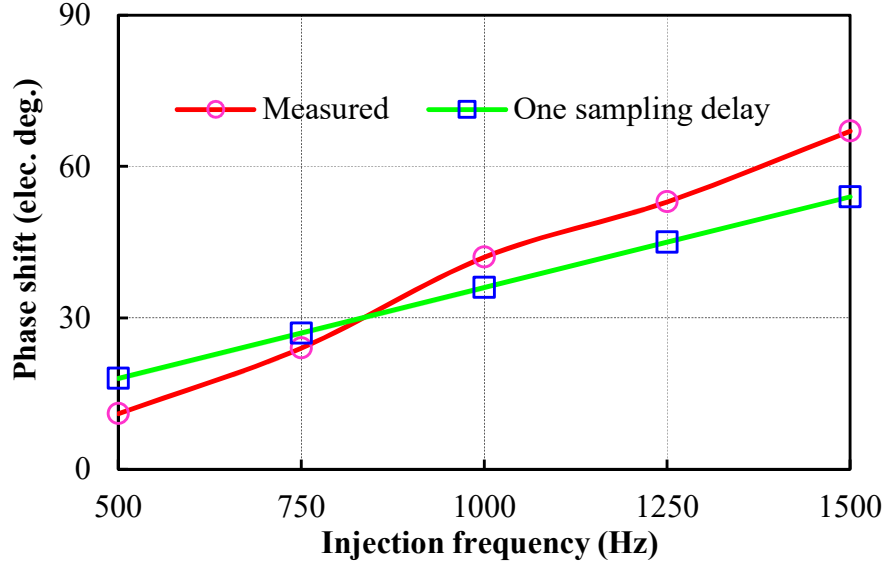
Fig. 2.2 Measured additional phase angle φ (PWM switching frequency 10 kHz).

2.2.1 HF signal injection model

According to [REI10], the HF model for PMSMs in the rotor d-/q-axis reference frame is described as

$$
\begin{bmatrix} u_{dh} \\ u_{qh} \end{bmatrix} = \begin{bmatrix} r_d & r_{dq} \\ r_{qd} & r_q \end{bmatrix} \begin{bmatrix} i_{dh} \\ i_{qh} \end{bmatrix} + \begin{bmatrix} L_d & L_{dq} \\ L_{qd} & L_q \end{bmatrix} p \begin{bmatrix} i_{dh} \\ i_{qh} \end{bmatrix}
\tag{2.1}
$$

where L_d and L_q are the HF incremental d- and q-axis self-inductances, L_{dq} and L_{qd} are the d-/q-axis mutual inductances related to magnetic cross-saturation effects, r_d, r_q and r_{dq} (r_{qd}) are the HF resistances in the d/q-axis plane, respectively.

Then, with the coordinate transformation from the actual to the estimated synchronous reference frame, the HF model in (2.1) can be further expressed as

$$
\begin{bmatrix} \hat{u}_{dh} \\ \hat{u}_{qh} \end{bmatrix} = T(\Delta\theta) \begin{bmatrix} r_d & r_{dq} \\ r_{qd} & r_q \end{bmatrix} T^{-1}(\Delta\theta) \begin{bmatrix} \hat{i}_{dh} \\ \hat{i}_{qh} \end{bmatrix} + T(\Delta\theta) \begin{bmatrix} L_d & L_{dq} \\ L_{qd} & L_q \end{bmatrix}
$$
$$
\cdot T^{-1}(\Delta\theta) p \begin{bmatrix} \hat{i}_{dh} \\ \hat{i}_{qh} \end{bmatrix}
\tag{2.2}
$$

where

$$T(\Delta\theta) = \begin{bmatrix} \cos\Delta\theta & -\sin\Delta\theta \\ \sin\Delta\theta & \cos\Delta\theta \end{bmatrix} \tag{2.3}$$

For the pulsating injection on the estimated d-/q-axis reference frame as shown in Fig. 2.3, the carrier voltage can be expressed as [JAN03]

$$\begin{aligned} \hat{u}_{dh} &= U\cos\omega_h t \\ \hat{u}_{qh} &= 0 \end{aligned} \tag{2.4}$$
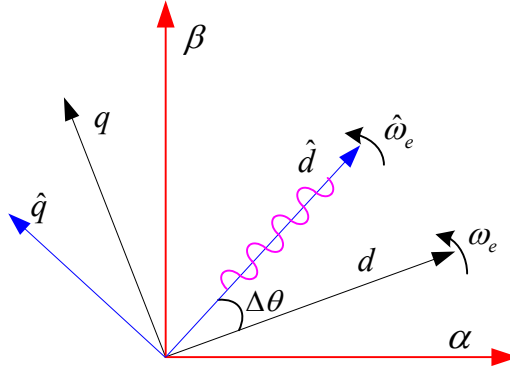
Fig. 2.3 The pulsating signal injection method in the estimated synchronous reference frame.

where U and ω_h are the carrier voltage and angular frequency. According to (2.1)-(2.4), by considering the delay and HF resistance effects, the estimated q-axis carrier current used for rotor position tracking can be derived as

$$\hat{i}_{qh} \approx \frac{U}{|Z|}\{\cos(\omega_h t - \varphi)[r_{dif}\sin(2\Delta\theta) - r_{dq}\cos(2\Delta\theta)] + \omega_h\sin(\omega_h t - \varphi)[L_{dif}\sin(2\Delta\theta) \\ -L_{dq}\cos(2\Delta\theta)]\} \tag{2.5}$$

where L_{dif} is the d-/q-axis inductance difference, i.e., $L_{dif} = (-L_d + L_q)/2$, r_{dif} is the d-/q-axis resistance difference, i.e., $r_{dif} = (-r_d + r_q)/2$, and

$$|Z| \approx \omega_h^2 L_d L_q \tag{2.6}$$

$$\varphi \approx -\arctan\frac{2r_{avg}L_{avg}}{\omega_h(L_d L_q - L_{dq}^2)} + \varphi_d \tag{2.7}$$

where $r_{avg} = (r_d + r_q)/2$ and $L_{avg} = (L_d + L_q)/2$, respectively. In (2.7), the phase shift φ contains two terms, the first term of which is due to the existence of HF resistance (including stator resistance), and the other term φ_d is related to signal processing delays, e.g., PWM updating

delay, etc., as reported in [CUP12] [MOG13] [BAE03b]. Since higher injection frequency is assumed in this chapter, the resultant phase shift φ is dominated by the signal processing delays, i.e.,

$$\varphi \approx \varphi_d \tag{2.8}$$

Then, with the typical signal demodulation as shown in Fig. 2.4 [JAN04] [RAC08c], the carrier response from (2.5) can be described as

$$I_{qh} = LPF(\hat{i}_{qh} \cdot 2\sin\omega_h t) = \frac{U}{|Z|}\{\sin\varphi[r_{dif}\sin(2\Delta\theta) - r_{dq}\cos(2\Delta\theta)] + \omega_h\cos\varphi[L_{dif}\sin(2\Delta\theta)$$
$$-L_{dq}\cos(2\Delta\theta)]\} \tag{2.9}$$

where I_{qh} presents the position error signal, and then is sent to the observer for the position estimation, Fig. 2.4. Therefore, the signal to noise (S/N) ratio of I_{qh} is very important, which eventually determines the position tracking performances.

Practically, as stated in [DEG98], due to the discrete nature of the windings, nonlinear magnetics, and manufacturing deviations, etc., the secondary and parasitic inductive saliencies in a PM machine arise. These secondary saliencies can be also observed in the measured HF resistances [YAN12a] [YAN12b] [ALB15]. Actually, it will be shown that for the prototype IPM machine (machine parameters are given in Table 2.1), the secondary HF resistive saliencies could bring about undesirable position estimation errors. Hence, with the consideration of the parasitic saliencies, from (2.9), I_{qh} actually can be described as (the cross-coupling terms r_{dq} and L_{dq} are neglected for the simplified analyses)

$$I_{qh} \approx \frac{U}{|Z|}\{\sin\varphi\sin(2\Delta\theta)[r_{dif-0} + \sum_{k=1}r_{dif-k}\cos(k\theta_e + \varphi_{rk})] + \omega_h\cos\varphi\sin(2\Delta\theta)[L_{dif-0}$$
$$+\sum_{k=1}L_{dif-k}\cos(k\theta_e + \varphi_{Lk})]\} \tag{2.10}$$

where r_{dif-0} and r_{dif-k} present the amplitude of the dc and the kth harmonic components for the d-/q-axis resistive saliencies, L_{dif-0} and L_{dif-k} present the dc and k^{th} harmonic components of d-/q-axis inductive saliencies, θ_e is the electrical rotor position, φ_{rk} and φ_{Lk} are the phase angle for the kth harmonic components, respectively.
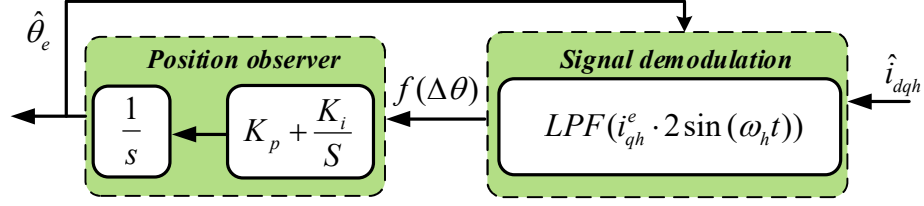
Fig. 2.4 Signal demodulation for position estimation for the pulsating injection method.

2.2.2 Model verification and position estimation performances at higher injection frequency

In order to verify the derivation of above model in (2.10), with the aid of the machine encoder, the position error $\Delta\theta$ is kept as $\pi/4$ to amplify all the saliency signals, i.e.,

$$I_{qh} = \frac{U}{|Z|}\{\sin\varphi[r_{dif-0} + \sum_{k=1} r_{dif-k}\cos(k\theta_e + \varphi_{rk})] + \omega_h\cos\varphi[L_{dif-0} + \sum_{k=1} L_{dif-k}\cos(k\theta_e + \varphi_{Lk})]\} \quad (2.11)$$

Accordingly, the spectra of I_{qh} of (2.11) can be measured and shown in Fig. 2.5(a)-(b) under different injection frequency and machine load conditions, respectively. From Fig. 2.5, rich harmonics arise due to the secondary inductive and resistive saliencies as expected. Due to the increase of phase angle φ (Fig. 2.2), the dc component of I_{qh} (dominated by '$\omega_h\cos\varphi L_{dif-0}$') reduces significantly with the increased injection frequency, which well agrees with (2.11), Fig. 2.5. The 6th harmonic components of I_{qh} are also observed to have the same variation trends with the dc component, and therefore should be produced from the secondary inductive saliencies, i.e., '$\omega_h\cos\varphi L_{dif-k}$', which also reduces with the increase of angle φ due to the increase of injection frequency.

Moreover, it is interesting to note that the 2nd and 3rd harmonic components of I_{qh}, Fig. 2.5(a)-(b), increase with the injection frequency under no-load and load conditions, respectively. These harmonics can be explained by the HF resistance effect, i.e., the secondary resistive saliencies in (2.11). Since both the phase angle φ and r_{dif-k} increase with the injection frequency, the harmonic amplitude '$\sin\varphi r_{dif-k}$' in (2.11) increases significantly with the injection frequency. It should be noted that these harmonics severely deteriorate the position estimation performances at higher injection frequencies, due to that the ratio of these secondary resistive saliencies ('$\sin\varphi r_{dif-k}$') to the primary inductive saliency components ('$\omega_h\cos\varphi L_{dif-0}$') significantly increases, Fig. 2.5.
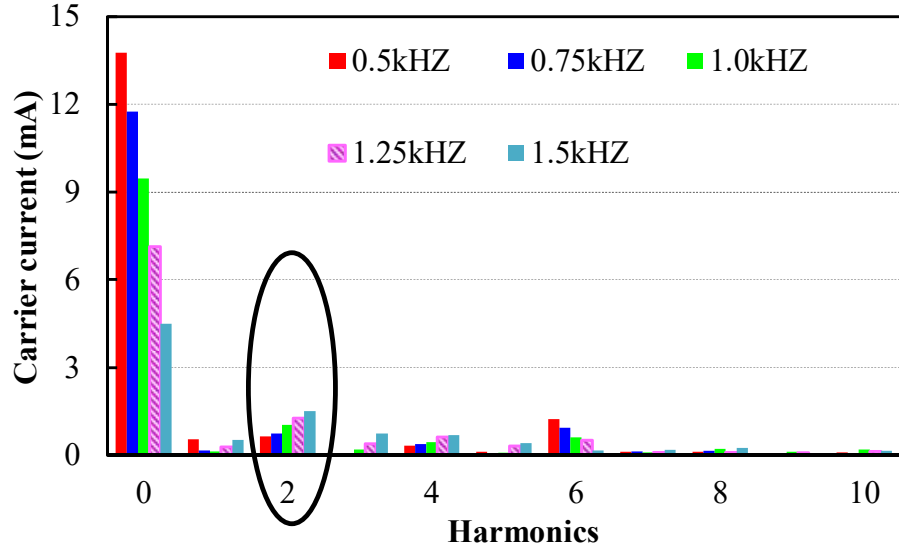
(a) No load condition
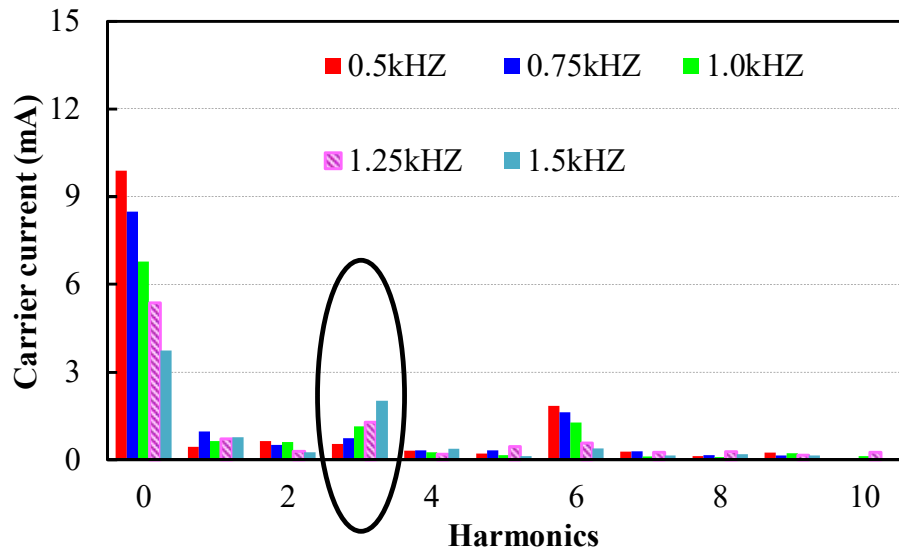
(b) Load condition-75% load

Fig. 2.5 Measured spectra of I_{qh} at different injection frequencies with different loads (U/f_h=0.03V/Hz, f_h is the injection frequency).

Those disturbed harmonics of the HF resistances in the d-/q-axis reference frame can be explained by the asymmetry distribution in the three phase HF resistances. By way of example, if the three phase resistances are asymmetric, the d-/q-axis HF resistances can be expressed as

$$r_d = \frac{r_b + r_c}{2} + \frac{\cos^2(\theta_e)}{3}(2r_a - r_b - r_c) - \frac{\sqrt{3}\sin(2\theta_e)}{6}(r_b - r_c)$$

$$r_q = \frac{r_b + r_c}{2} + \frac{\sin^2(\theta_e)}{3}(2r_a - r_b - r_c) + \frac{\sqrt{3}\sin(2\theta_e)}{6}(r_b - r_c) \qquad (2.12)$$

$$r_{dq} = \frac{\sin(2\theta_e)}{6}(-2r_a + r_b + r_c) - \frac{\sqrt{3}\cos(2\theta_e)}{6}(r_b - r_c)$$

where r_a, r_b, r_c are the three phase resistance, and θ_e is the electrical rotor position, respectively. Clearly, if $r_a \neq r_b \neq r_c$, the additional harmonic components (e.g., the 2nd harmonic) in the d-/q-axis HF resistances will be generated as given in (2.10).

Then, accordingly, the position estimation performances at higher injection frequency (1.5 kHz) are shown in Fig. 2.6, compared to the normal injection frequency 0.5 kHz in Fig. 2.7, under no-load and load conditions, respectively. As expected, under different load conditions, the position estimation performances at 1.5 kHz are both significantly degraded compared to those of 0.5 kHz injection. Therefore, from the above analyses, the large oscillating position errors at higher injection frequencies for the pulsating signal injection have been clearly explained in this chapter, which actually is due to the synthesis of the delay and HF resistive saliency effects (the oscillating errors can also be observed in [MOG13], etc.). Besides, Fig. 2.8 also shows the peak-to-peak position error with carrier injection frequency under different load conditions, which also clearly verifies the above analyses.
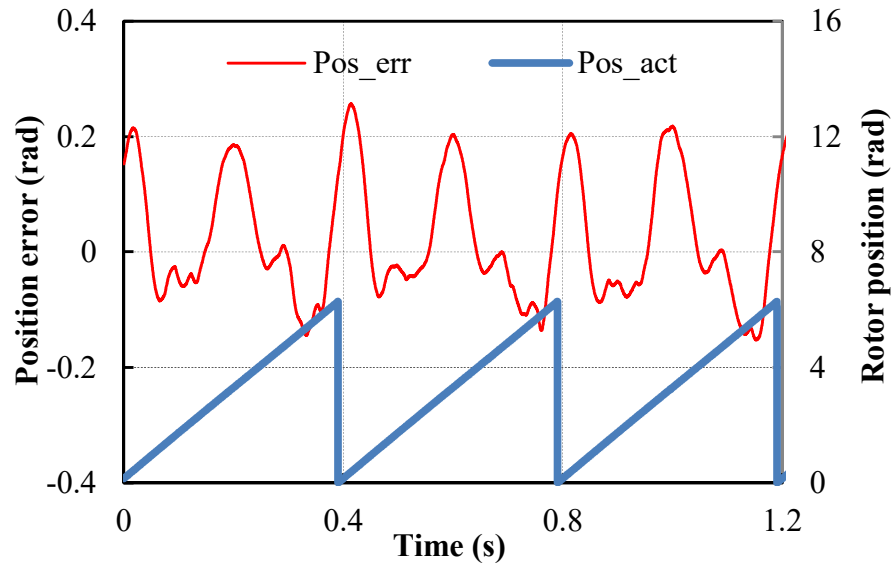
(a) No load
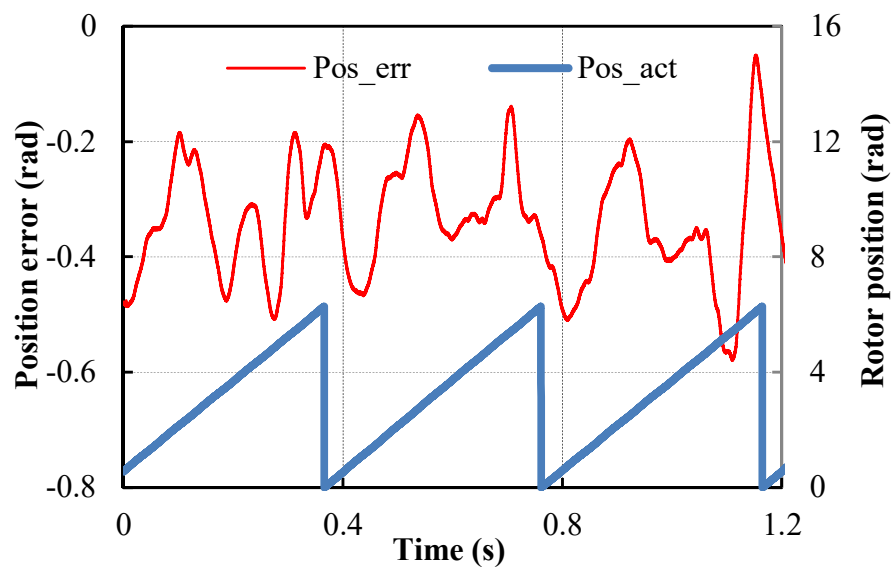
(b) Load condition-75% load

Fig. 2.6 Position estimation performances for the pulsating signal injection at 1.5 kHz, under sensorless open-loop condition.
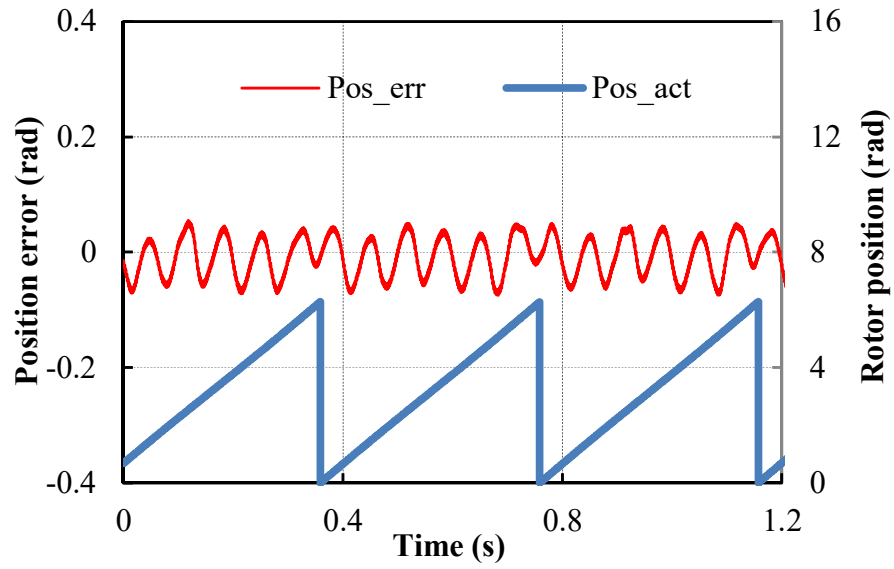
(a) No load
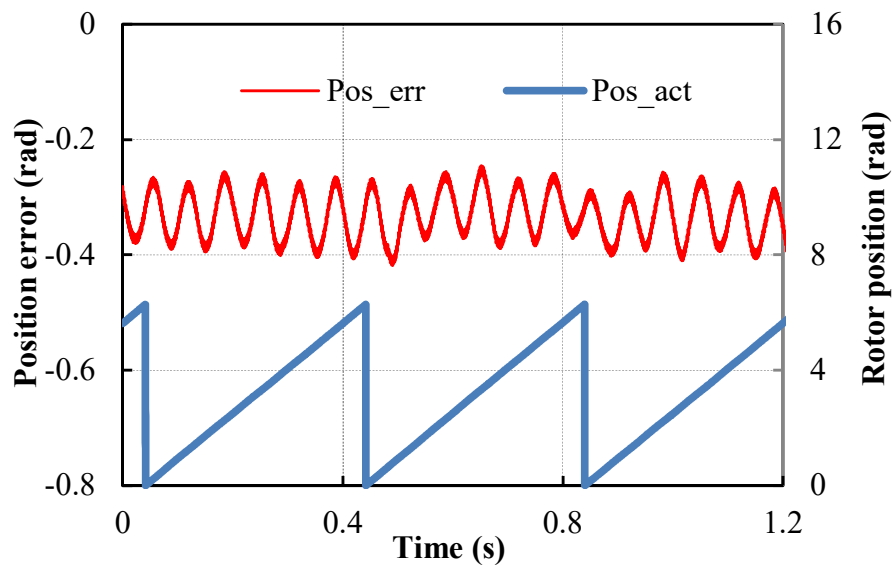
(b) Load condition-75% load

Fig. 2.7 Position estimation performances for the pulsating signal injection at 0.5 kHz, under sensorless open-loop condition.
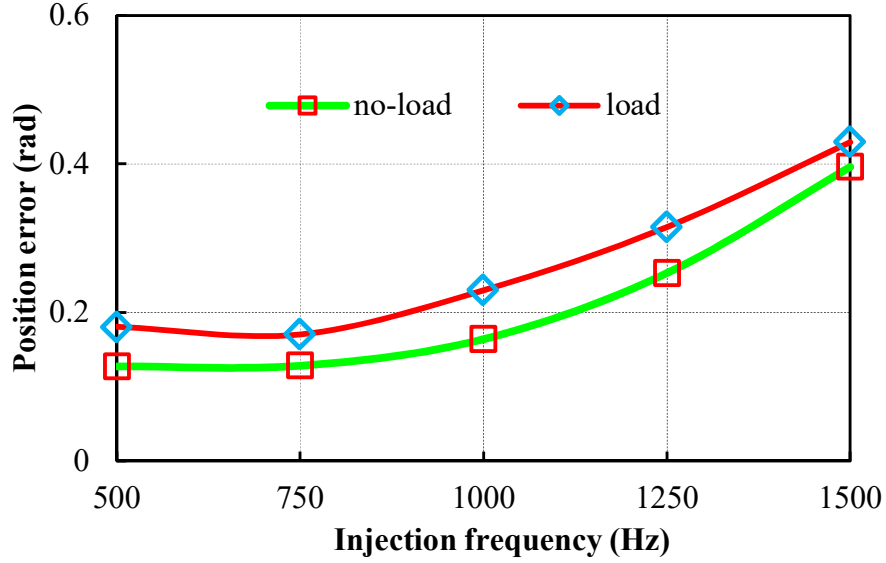
Fig. 2.8 Position errors (peak-to-peak) with carrier frequency for the pulsating signal injection under different loads.

2.3 Proposed Error Compensation Method at Higher Injection Frequency

From the above analyses, due to the delay and HF resistance effects, the position estimation performances at higher injection frequency for the pulsating signal injection method is severely deteriorated, which may cause instability for the control system.

Therefore, based on the above analyses, a new compensation strategy based on tracking the phase shift of the carrier signals using PI regulator is proposed. The principle of the proposed method is that by modifying the demodulation signal phase angle, the amplitude of inductive saliency part used for position estimation is significantly increased while the undesirable HF resistance part is suppressed, which will be clearly explained as follows. The proposed method does not require offline measurements, and moreover keeps the advantages of classical signal demodulation method. Therefore, it is very easy and simple to implement, and furthermore significantly improves the sensorless control performance.

Specifically, from (2.9)-(2.10), if the phase angle of the demodulation signal is changed as φ_1, the resultant carrier current signal can be expressed as

$$I_{qh} = LPF(\hat{i}_{qh} \cdot 2\sin(\omega_h t - \varphi_1)) = \frac{U}{|Z|}\{\sin(\varphi - \varphi_1)\sin(2\Delta\theta)[r_{dif-0} + \sum_{k=1} r_{dif-k}\cos(k\theta_e + \varphi_{rk})]$$
$$+\omega_h\cos(\varphi - \varphi_1)\sin(2\Delta\theta)[L_{dif-0} + \sum_{k=1} L_{dif-k}\cos(k\theta_e + \varphi_{Lk})]\} \qquad (2.13)$$

From (2.13), if the angle φ_1 can be adjusted to approximately equal the angle of φ, the resultant I_{qh} can be described as

$$I_{qh} \approx \frac{U}{|Z|}\{\omega_h\sin(2\Delta\theta)[L_{dif-0} + \sum_{k=1} L_{dif-k}\cos(k\theta_e + \varphi_{Lk})]\} \qquad (2.14)$$

Therefore, compared with (2.10), the HF resistance effects can be significantly suppressed in (2.14) and also the amplitude for the inductive saliency part will be greatly increased. Consequently, the better position estimation performance is expected. In this chapter, in order to track the phase shift of φ, the estimated d-axis carrier current is utilised, i.e.,

$$\hat{i}_{dh} = \frac{U}{|Z|}\{\cos(\omega_h t - \varphi)[r_{avg} + r_{dif}\cos(2\Delta\theta) + r_{dq}\sin(2\Delta\theta)] + \sin(\omega_h t - \varphi)\cdot\omega_h[L_{avg} +$$
$$L_{dif}\cos(2\Delta\theta) + L_{dq}\sin(2\Delta\theta)]\} \qquad (2.15)$$

Since the term of '$\omega_h L_{avg}$' is dominant at higher injection frequency, the resultant estimated d-axis carrier current response can be described as

$$I_{dh} = LPF(\hat{i}_{dh} \cdot 2\cos(\omega_h t - \varphi_1)) \approx \frac{U}{|Z|}\omega_h[L_{avg} + L_{dif}\cos(2\Delta\theta) + L_{dq}\sin(2\Delta\theta)]\sin(\varphi - \varphi_1) \qquad (2.16)$$

Then, by controlling the I_{dh} to be zero with PI regulator, the phase angle φ can then be tracked by the demodulation signal phase angle φ_1, and finally the estimated q-axis carrier responses can be obtained as (2.14). The block diagram of the proposed compensation strategy for the pulsating injection is depicted in Fig. 2.9. It should be noted that since the added PI regulator is not in the main loop for position estimation, the system bandwidth is unaffected. The proposed compensation method for the pulsating injection will be verified experimentally in section 2.4.
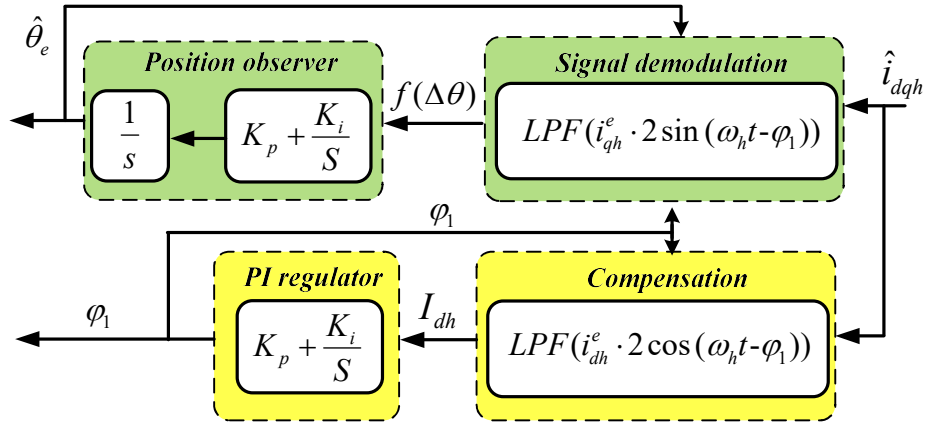
Fig. 2.9 Block diagram of the proposed compensation strategy for the pulsating signal injection method.

2.4 Experimental Validation

The experiments are implemented on a dSPACE DS1006 platform to validate the proposed compensation method for the signal processing delay and HF resistance effects. The prototype PM machine (the machine parameters are given in Table 2.1) is fed by SEMIX 71GD12E4s inverter, and the inverter switching frequency is set to 10 kHz, the same as the current sampling frequency. The machine phase currents are measured by the transducers LEM LA25-NP. The PM machine is also equipped with an incremental encoder (resolution of 5000 PPR) to provide the accurate rotor position for reference. The overall control scheme for carrier signal injection with signal processing delay compensation is shown in Fig. 2.10.
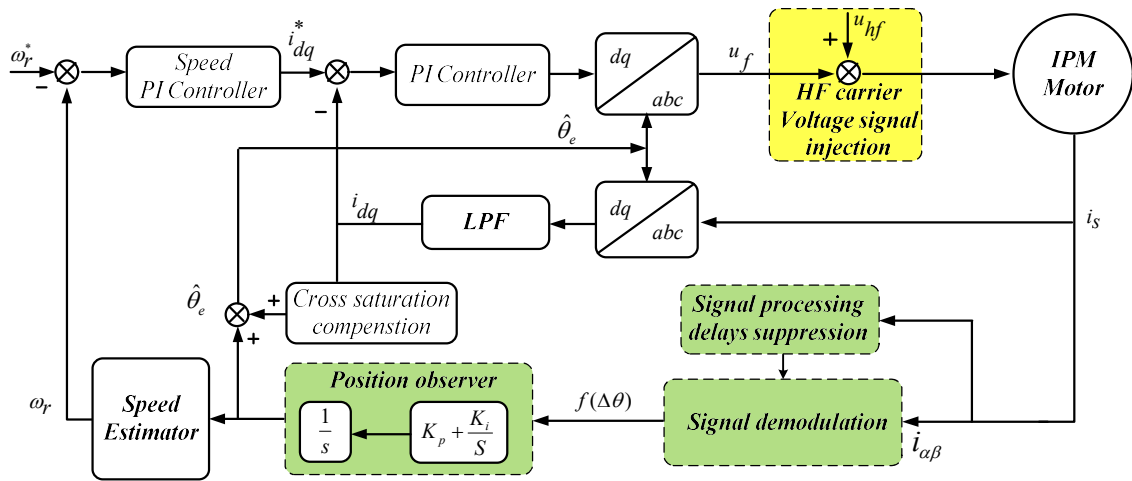
Fig. 2.10 Block diagram of overall control system for carrier signal injection considering signal processing delays.

Table 2.1 Parameters of IPM Machine Tested

Rated voltage	158	V
Rated current	4.0	A
Rated power	600	W
Rated torque	4.0	Nm
Pole number	6	
PM flux-linkage	0.236	Wb
Resistance	6	Ω
d-/q-axis Inductance (@0A)	44.2/65.5	mH

Fig. 2.12 (a)-(b) illustrate the steady-state position estimation performances without compensation, with the conventional and proposed compensation strategy for the pulsating signal injection, respectively. It is noted that the conventional method [SAT11] [HA03] is based on the demodulation of the carrier responses in the 45 deg. axis (i.e., the d_m- and q_m-axes in Fig. 2.11, and the d_m- and q_m-axes have 45 deg. phase shift to the estimated d-axis). According to [SAT11], the related carrier responses can be described as

$$\frac{d}{dt}\begin{bmatrix} i_d^m \\ i_q^m \end{bmatrix} = U \frac{(L_q - L_d)}{2\sqrt{2}L_d L_q} \cos(\omega_h t) \begin{bmatrix} L_q + L_d + (L_q - L_d)(\cos(2\Delta\theta) - \sin(2\Delta\theta)) \\ L_q + L_d + (L_q - L_d)(\cos(2\Delta\theta) + \sin(2\Delta\theta)) \end{bmatrix} \quad (2.17)$$

From (2.17), because both i_q^m and i_d^m are the carrier responses with considerable large amplitudes, they are less sensitive to the digital delay effects, and consequently the S/N ratio can be improved. Then, by controlling the amplitude of i_q^m to exactly equal that of i_d^m, the position error $\Delta\theta$ becomes zero, i.e., the estimated rotor position can be obtained.
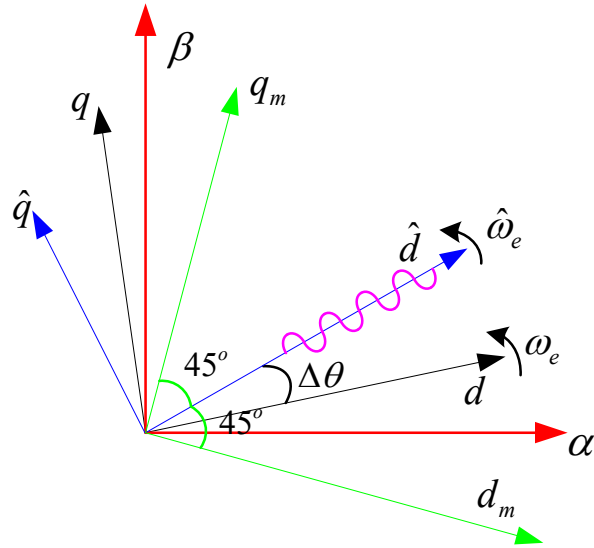
Fig. 2.11 Conventional compensation method with signal demodulation in the 45 deg. axis.

Accordingly, the injection signals are all set as 45V and 1.5 kHz. It can be seen that at different load conditions, both compensation strategies have significantly improved the position estimation performances. However, since the HF resistance effects are not considered in the conventional method [SAT11] [HA03], the position estimation performances for the conventional method are slightly compromised compared to the proposed method, especially under load conditions, Fig. 2.12(b). It should be noted that the dc position errors caused by the cross-coupling saturation effects have been compensated using the offline measurement strategy under different load conditions [LI09].
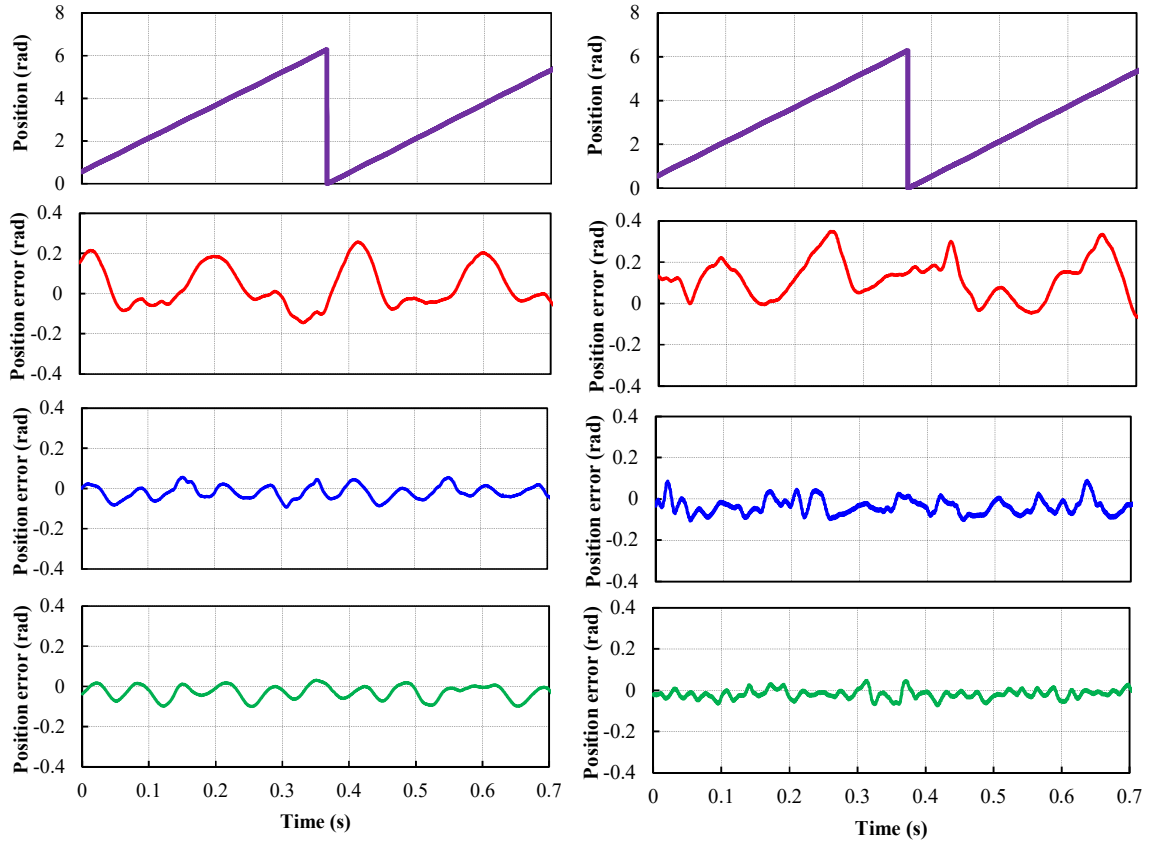
(a) Under no load condition (top-actual rotor position, second-position error before compensation, third-position error with conventional method, bottom-position error with proposed method)

(b) Under 75% load condition (top-actual rotor position, second-position error before compensation, third-position error with conventional method, bottom-position error with proposed method)

Fig. 2.12 Position error compensation for the pulsating signal injection method at higher injection frequency (45V/1.5kHz)-50rpm, under sensorless open-loop condition.

The dynamic performances under step speed and step load conditions are also examined to further confirm the effectiveness of the proposed compensation method for the pulsating signal injection, Fig. 2.13-Fig. 2.14. The injected carrier signal is the same as the steady conditions, i.e., 45V/1.5 kHz. The step speed reference is set as 0-50-100 r/min, Fig. 2.13, from which it can be seen that the overall position estimation error is very small. Besides, good position tracking performances are also observed for the step-load conditions, Fig. 2.14. It is noted that the peak invariant transformation is adopted for the dq currents in the control system, and hence the q-axis current in Fig. 2.14 presents the peak-value of the phase currents.

Therefore, both in the steady and dynamic states, it can be seen that the proposed compensation method presents excellent position estimation performances at higher injection frequency.
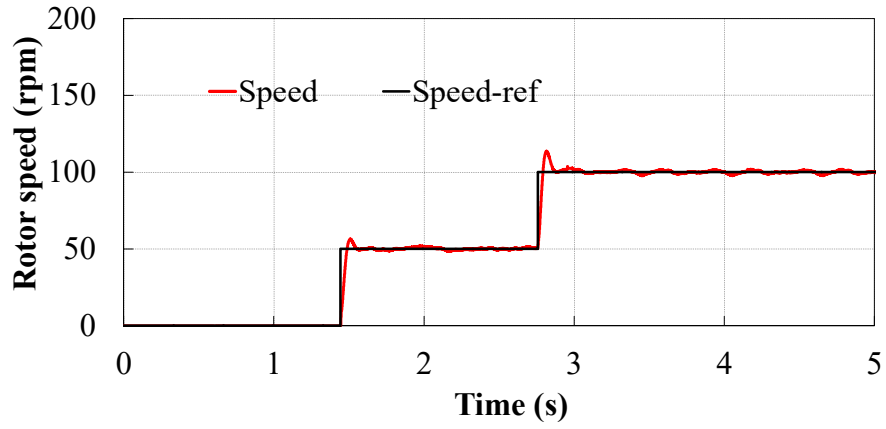
(a) Rotor speed
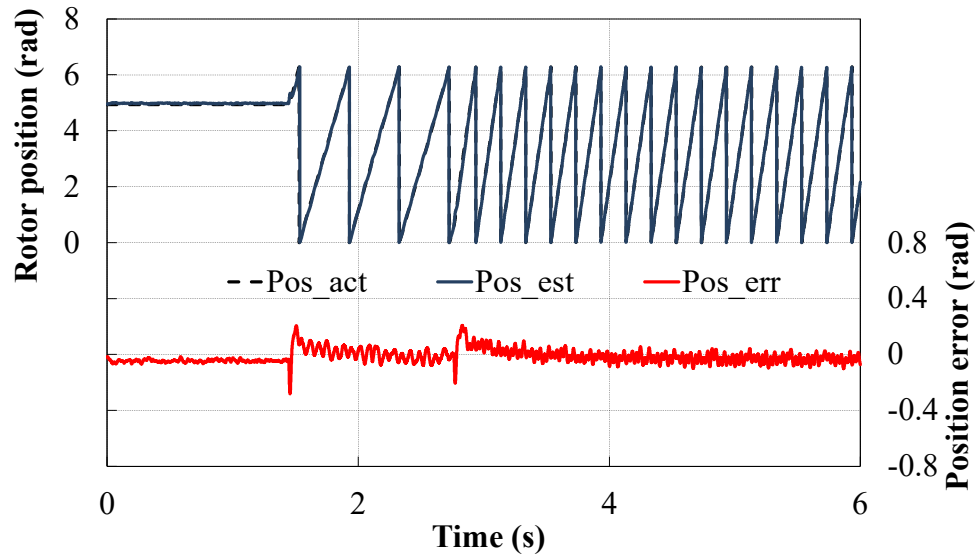
(b) Position estimation performance

Fig. 2.13 Dynamic performances under step speed condition in sensorless mode.
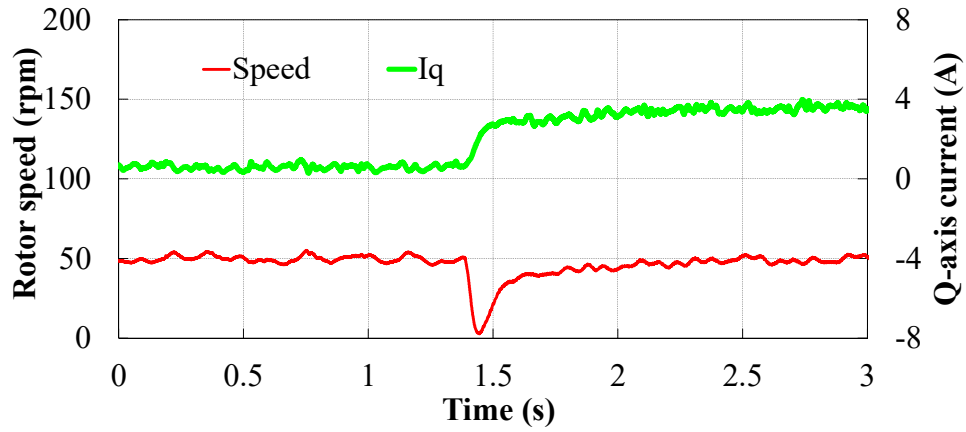
(a) Q-axis current and speed
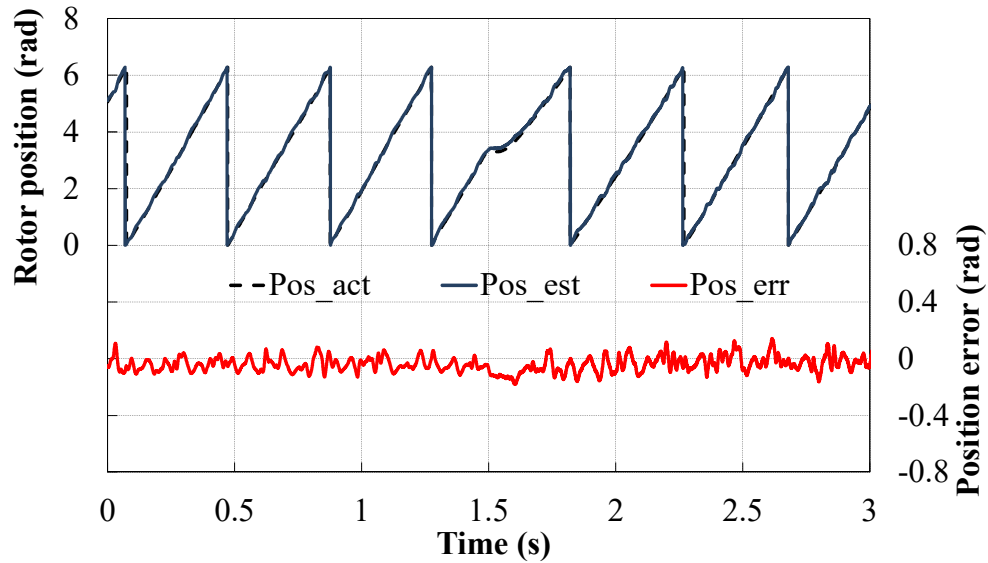
(b) Position estimation performance

Fig. 2.14 Dynamic performances under step load condition, in sensorless mode.

2.5 Further Discussion for Rotating Signal Injection

The rotating signal injection at higher injection frequency is further discussed in this chapter. Due to different position estimation mechanisms and also the signal demodulation strategies [RAC08c] [KIM04a], the rotating signal injection method is not sensitive to the HF resistance effects compared to the pulsating injection, while it is much affected by the signal processing delays, the details of which will be explained as follows.

Similarly, considering the delay and HF resistance effects, the carrier current for rotating signal injection as shown in Fig. 2.15 neglecting the cross-coupling effects can be derived as

$$i_\alpha + ji_\beta = -\frac{U}{|Z|}[(r_{avg} + j\omega_h L_{avg})e^{j(\omega_h t - \varphi)} + r_{dif} e^{j2\theta_e} e^{-j(\omega_h t - \varphi)} + j\omega_h L_{dif} e^{j2\theta_e} e^{-j(\omega_h t - \varphi)}]$$ (2.18)

Then, with the signal demodulation, the resultant carrier signal response can be expressed as

$$I_\alpha + jI_\beta = LPF[(i_\alpha + ji_\beta)e^{j\omega_h t}] = \frac{U}{|Z|}[r_{dif} e^{j(2\theta_e + \varphi)} + j\omega_h L_{dif} e^{j(2\theta_e + \varphi)}]$$ (2.19)

From (2.19), it can be seen that the phase angle φ appears as the phase shift for the resistive and inductive saliency signals in (2.19) for rotating signal injection, rather than the amplitude terms in (2.10) for pulsating signal injection. Therefore, the useful inductive saliency signal amplitude will not be further decreased and besides the HF resistance effects will not be further amplified by angle φ when higher injection frequency is employed. Consequently, the large oscillating error does not appear for rotating signal injection method at higher injection frequency, but only the average error increases due to the phase angle of the carrier responses being modified in (2.19). In order to verify the above analyses, both the average and oscillating errors for the rotating signal injection with the injection frequency are shown in Fig. 2.16. The peak-to-peak errors are quite small, only ~0.12 rad, and approximately unchanged with the increase of carrier frequency. However, the average position error increases significantly due to the increased phase shift of carrier signals as expected.

In order to compensate the average position errors for rotating signal injection, similarly, the PI regulator based strategy can be also utilised as analysed as follows. It should be noted that the conventional methods in [MOG13] [SAT11] [HA03] cannot be simply applied for rotating injection method. Specifically, at higher injection frequency for rotating signal injection in (1.13), the positive sequence carrier current has approximately the same phase shift with the negative sequence current due to the delays. Thus, the positive sequence carrier current can be then processed as

$$I_{pos} = LPF(i_{\alpha\beta}^h e^{j(-\omega_h t + \frac{\pi}{2} + \varphi_1)}) = I_{pos\_\alpha} + jI_{pos\_\beta} \approx \frac{U}{|Z|}\omega_h L_{avg}(\cos\Delta\varphi + j\sin\Delta\varphi)$$ (2.20)

where I_{pos_β} and φ_1 are the input and output of the added PI regulator, Fig. 2.17, $\Delta\varphi$ is the difference between the angle φ and φ_1 , respectively. Obviously, with the PI regulator, the I_{pos_β} can be zero, i.e., $\Delta\varphi=0$. Then, according to Fig. 2.17, the carrier current in the negative sequence frame can be described as

$$I_{\alpha\beta}^h = LPF(i_{\alpha\beta}^h e^{j(\omega_h t - \frac{\pi}{2} - \varphi_1)}) \approx \frac{U}{|Z|}\omega_h L_{dif} e^{j(2\theta_e + \Delta\varphi)} \tag{2.21}$$

Therefore, comparing to (2.19), it can be seen from (2.21) that the position errors due to the delay angle φ will be significantly suppressed for the rotating injection with the proposed compensation strategy. To simply verify the effectiveness for the proposed method, the position estimation performances before and after the compensation are shown in Fig. 2.18, under different load conditions. The carrier injection signal is the same as the pulsating injection, i.e., 45V/1.5 kHz. It can be clearly observed that the average error is significantly suppressed after the delay compensation. It is noted that under the load condition, Fig. 2.18(b), the cross-coupling saturation effects will also cause the average errors [LI09], which further result in unstable sensorless control performance. Therefore, the error before any compensation can be only observed separately, Fig. 2.18(b). Then, further with the cross-coupling effect compensation [LI09], the position estimation error is further reduced, as shown in Fig. 2.18(b).
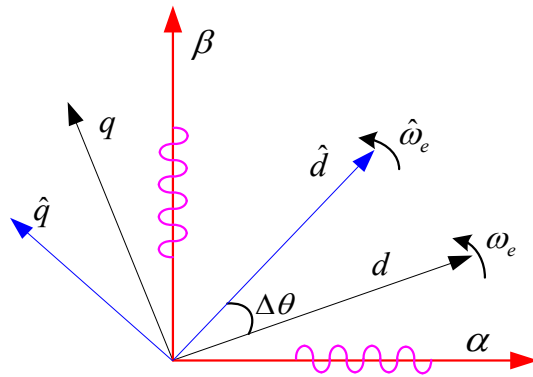
Fig. 2.15 Rotating signal injection method in the stationary reference frame.
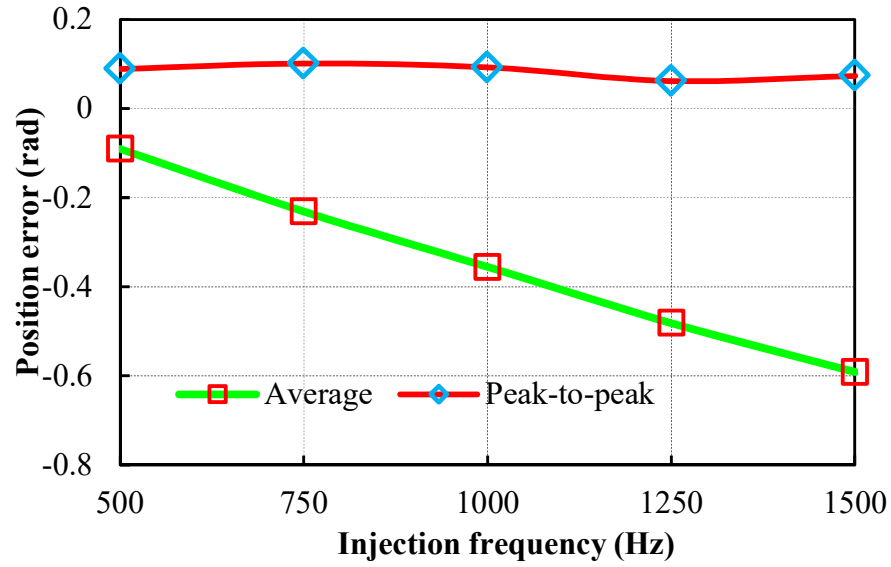
Fig. 2.16 Average and peak-to-peak position error for the rotating signal injection-no-load.
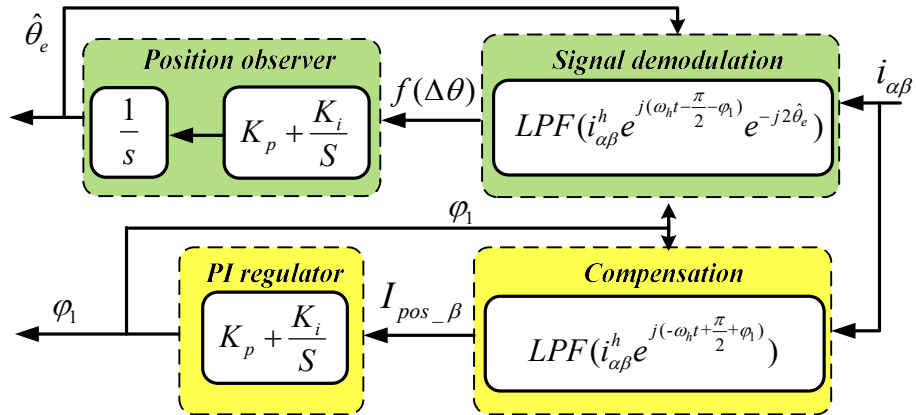
Fig. 2.17 Block diagram of the proposed compensation strategy for the rotating signal injection.
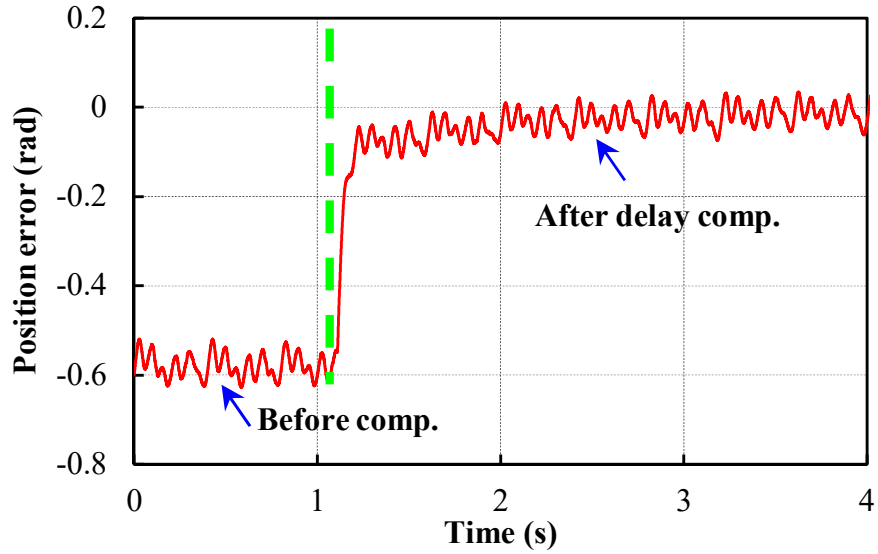
(a) Under no-load condition-under sensored open-loop observations
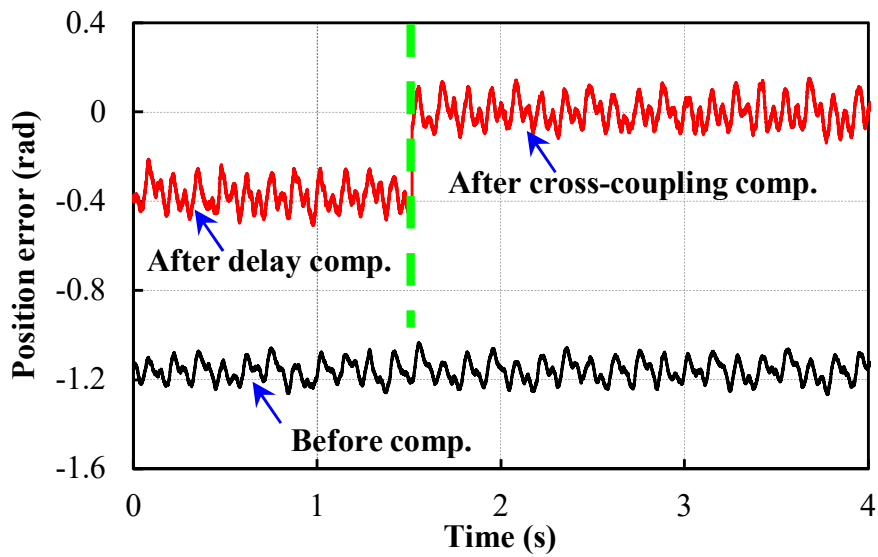
(b) Under 75% load condition-under sensored open-loop observations

Fig. 2.18 Position error compensation for rotating signal injection at 45V/1.5 kHz injection.

2.6 Conclusion

The synthesis of signal processing delay and HF resistance effects can give rise to the oscillating position errors for the pulsating signal injection, and these errors have been shown to be intolerable when higher injection frequency is selected for the enhancement of system

bandwidths. The PI regulator based compensation strategy has been proposed to suppress the position errors via tracking the phase shift due to the delays. The proposed compensation method is easy and simple to implement, and furthermore can significantly enhance the sensorless control performance. Similar theoretical analysis and compensation strategy have been also applied for the rotating signal injection method. All theoretical analyses and compensation effectiveness have been verified by experiments on a prototype IPM machine.

3 Carrier Signal Injection Based Sensorless Control for Permanent Magnet Synchronous Machines Considering Machine Parameter Asymmetries

3.1 Introduction

In the previous chapter, the carrier signal injection methods have shown great capability for rotor position estimation for the permanent magnet synchronous machines (PMSMs). However, currently, the investigations on carrier signal injection methods mostly assume that the machine parameters are symmetrical [JAN95] [JAN03] [GON11]. However, practically three phase unbalanced PM machines are frequently present, resulting in machine parameter asymmetries. Specifically, cabling, inverter or stator windings may cause resistance asymmetry [REI10], while inductance asymmetry may come from rough mechanical manufacturing, machine eccentricity, winding fault [DEG98], etc. Moreover, the influence of machine asymmetry on the position estimation accuracy is rarely investigated except in [REI10] [DEG98]. In [REI10], the phase resistance asymmetry has been considered, and it shows that 2nd harmonic error arises due to the resistance asymmetry. However, the detailed comparisons for different signal injection methods as well as the influence of inductance asymmetry are not discussed. In [DEG98], the authors have presented the analyses of stationary saliency, i.e., the inductance asymmetry, whilst the details, e.g., the analytical position error expressions, the comparisons for the two carrier injection methods, and moreover the online compensation strategies, are not given.

Therefore, in this chapter, the detailed modelling, comparison and compensation strategies for machine parameter asymmetry will be fully presented for the two typical carrier injection methods (i.e., the rotating injection [JAN95] and the pulsating injection [JAN03]). It will be shown that with either phase resistance or inductance asymmetry, the 2nd harmonic position errors arise regardless of carrier injection methods. It should be noted that the 2nd harmonic errors are more difficult to suppress by the position observer bandwidth than the 6th harmonic errors caused by inverter nonlinearity [GUE05] [GON11] or multiple saliency effects [DEG98], since they are closer to the fundamental frequency. In order to suppress the 2nd harmonic position errors, the carrier signal selection guidelines will be given for resistance asymmetry. Whilst for inductance asymmetry, new online compensation strategies with dual frequency injection will also be presented. Finally, the theoretical analyses and compensation

effectiveness for machine parameter asymmetry will be confirmed by experiments on a prototype IPM machine.

The major new results of this chapter have been published in [XU16a].

3.2 High Frequency Models with Machine Parameter Asymmetries

Since the phase back-EMF is neglected in the carrier signal injection model [JAN95] [JAN03], only the phase resistance and inductance asymmetries will be considered for the two carrier signal injection methods, respectively.

3.2.1 Influence of resistance asymmetry on carrier signal injection methods

In practice, the phase resistance asymmetry may result from cabling, inverter or stator windings [REI10]. Based on the derivations in (2.9) in chapter 2, with the position tracking observer as shown in Fig. 3.1 where the asymmetry part is modelled as the disturbance, the position estimation error ($\Delta\theta$) for the pulsating injection with resistance asymmetry is obtained as

$$\Delta\theta = \frac{1}{2}\arctan\frac{r_{dq}\tan\varphi + L_{dq}\omega_h}{r_{dif}\tan\varphi + L_{dif}\omega_h} \tag{3.1}$$
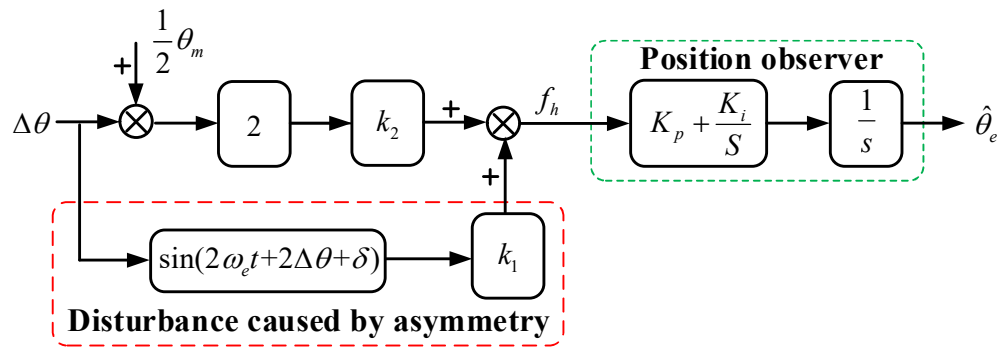

Fig. 3.1 Position tracking observer considering machine parameter asymmetry (k_1 and k_2 are the equivalent gains).

From (3.1), since r_{dq} and r_{dif} in (2.12) are the 2nd harmonic components due to phase resistance asymmetry, they do not generate average estimation errors but only 2nd harmonic oscillating errors, (3.1) then can be simplified as

$$\Delta\theta \approx \frac{1}{2}\arctan\frac{L_{dq}}{L_{dif}} + \frac{1}{2}\arctan\left(\frac{\hat{r}_{dif}\tan\varphi}{\omega_h \hat{L}_{dif}}\right)\sin(2\theta_e + \delta_r) \tag{3.2}$$

where $\hat{L}_{dif} = \sqrt{L_{dq}^2 + L_{dif}^2}$, $\hat{r}_{dif} = \sqrt{r_{dq}^2 + r_{dif}^2}$ ($\hat{r}_{dif}$ is constant), and δ_r presents the phase angle under different resistance asymmetry conditions.

Similarly, for the rotating signal injection, the carrier current responses from (2.18) can be further expressed as

$$i_\alpha + ji_\beta = -\frac{U}{|Z|}[(r_{avg} + j\omega_h L_{avg})e^{j(\omega_h t - \varphi)} + \hat{r}_{dif}e^{j(2\theta_r + \theta_{m1})}e^{-j(\omega_h t - \varphi)} + j\omega_h\hat{L}_{dif}e^{j(2\theta_r + \theta_m)}e^{-j(\omega_h t - \varphi)}] \tag{3.3}$$

where $\theta_{m1} = \tan^{-1}(-r_{dq}/r_{dif})$ and $\theta_m = \tan^{-1}(-L_{dq}/L_{dif})$, respectively. Then, with signal demodulation, the resultant carrier signal can be expressed as

$$I_\alpha + jI_\beta = LPF[(i_\alpha + ji_\beta)e^{j\omega_h t}] = \frac{U}{|Z|}[\hat{r}_{dif}e^{j(2\theta_r + \theta_{m1} + \varphi)} + j\omega_h\hat{L}_{dif}e^{j(2\theta_r + \theta_m + \varphi)}] \tag{3.4}$$

Accordingly, the position estimation error for rotating injection with resistance asymmetry can be derived as

$$\Delta\theta = -\frac{1}{2}\varphi + \frac{1}{2}\arctan\frac{\hat{r}_{dif}\sin(\theta_{m1} + \varphi) + \omega_h L_{dq}}{-\hat{r}_{dif}\cos(\theta_{m1} + \varphi) + \omega_h L_{dif}} \tag{3.5}$$

Similar to (3.1)-(3.2), (3.5) can be simplified as

$$\Delta\theta \approx -\frac{1}{2}\varphi + \frac{1}{2}\arctan\frac{L_{dq}}{L_{dif}} + \frac{1}{2}\arctan\frac{\hat{r}_{dif}}{\omega_h\hat{L}_{dif}}\sin(2\theta_e + \delta_r) \tag{3.6}$$

Therefore, from the above derivations for phase resistance asymmetry in (3.2) and (3.6), it can be seen that the 2nd harmonic position errors arise for both carrier injection methods. Furthermore, from (3.1)-(3.2) and (3.5)-(3.6), it is noted that the 2nd harmonic error amplitudes are different for the two carriers due to different position estimation mechanisms and signal demodulation processes [RAC08c] [KIM04a]. Specifically, with resistance asymmetry, the 2nd harmonic error amplitude for pulsating injection is modulated by the phase φ, while that for rotating injection is not related to φ. Detailed experimental comparisons will be given in section 3.4.

3.2.2 Influence of inductance asymmetry on carrier signal injection methods

Practically, the inductance asymmetry may originate from rough mechanical manufacturing, machine eccentricity, winding fault [DEG98], etc. Firstly, assuming that one phase self-inductance is unbalanced, the inductance matrix can be expressed as

$$L(a,b,c) = \begin{bmatrix} L_{AA} & M_{AB} & M_{AC} \\ M_{BA} & L_{BB} & M_{BC} \\ M_{CA} & M_{CB} & M_{CC} \end{bmatrix} + \begin{bmatrix} \Delta L & 0 & 0 \\ 0 & 0 & 0 \\ 0 & 0 & 0 \end{bmatrix} \tag{3.7}$$

where ΔL presents the asymmetry part for the self-inductance. With coordinate transformation, the inductances in the d-/q-axis can be expressed as

$$L(d,q) = \begin{bmatrix} L_d + \dfrac{2}{3}\Delta L \cos^2\theta_e & L_{dq} - \dfrac{1}{3}\Delta L \sin 2\theta_e \\ L_{dq} - \dfrac{1}{3}\Delta L \sin 2\theta_e & L_q + \dfrac{2}{3}\Delta L \sin^2\theta_e \end{bmatrix} \tag{3.8}$$

Thus, with the pulsating signal injection, from (3.7)-(3.8), the carrier current neglecting phase resistance can be obtained as

$$\hat{i}_{qh} \approx \frac{U\sin(\omega_h t - \varphi)}{\omega_h L_d L_q}[L_{dif}\sin 2\Delta\theta - L_{dq}\cos 2\Delta\theta - \frac{1}{3}\Delta L\cos 2\theta_e \sin 2\Delta\theta + \frac{1}{3}\Delta L\sin 2\theta_e \cos 2\Delta\theta] \tag{3.9}$$

Accordingly, the position error with one phase inductance asymmetry for the pulsating injection can be obtained as

$$\Delta\theta_{P\_L} = \frac{1}{2}\arctan\frac{L_{dq} - \dfrac{\Delta L}{3}\sin 2\theta_e}{L_{dif} - \dfrac{\Delta L}{3}\cos 2\theta_e} \tag{3.10}$$

i.e.,

$$\Delta\theta_{P\_L} \approx \frac{1}{2}\arctan\frac{L_{dq}}{L_{dif}} + \frac{1}{2}\arctan\frac{\Delta L}{3\hat{L}_{dif}}\sin(2\theta_e + \delta_L) \tag{3.11}$$

where δ_L presents the phase angle under various inductance asymmetry conditions. Similarly, the position error with three phase inductance asymmetry for the pulsating injection can be

also obtained as (3.12), where ΔM presents the asymmetry part for the mutual inductances, i=1-3 for phase A-C, respectively.

$$\Delta\theta_{p\_L} = \frac{1}{2}\arctan\frac{L_{dq} - \sum_{i=1,2,3}\{\frac{1}{3}\Delta L_i \sin 2(\theta_e - \frac{2}{3}\pi\cdot(i\text{-}1)) + \frac{2}{3}\Delta M_i \sin 2(\theta_e + \frac{2}{3}\pi\cdot i)\}}{L_{dif} - \sum_{i=1,2,3}\{\frac{1}{3}\Delta L_i \cos 2(\theta_e - \frac{2}{3}\pi\cdot(i\text{-}1)) + \frac{2}{3}\Delta M_i \cos 2(\theta_e + \frac{2}{3}\pi\cdot i)\}} \tag{3.12}$$

Then, for rotating signal injection, the carrier current with one phase inductance asymmetry can be obtained as

$$i_\alpha + ji_\beta = \frac{\omega_h U}{|Z|\angle\varphi}\{(L_{avg} + \frac{\Delta L}{3})e^{j(\omega_h t - \pi/2)} - \frac{\Delta L}{3}e^{-j(\omega_h t - \pi/2)} + \hat{L}_{dif}\, e^{j(2\theta_e + \theta_m)}e^{-j(\omega_h t - \pi/2)}\} \tag{3.13}$$

Similarly, according to (3.4)-(3.6), the position error for rotating injection can be derived as

$$\Delta\theta_{r\_L} \approx -\frac{1}{2}\varphi + \frac{1}{2}\arctan\frac{L_{dq}}{L_{dif}} + \frac{1}{2}\arctan\frac{\Delta L}{3\hat{L}_{dif}}\sin(2\theta_e + \delta_L) \tag{3.14}$$

for one phase inductance asymmetry and (3.15) for three phase inductance asymmetry, respectively.

$$\Delta\theta_{r\_L} = -\frac{1}{2}\varphi + \frac{1}{2}\arctan\frac{L_{dq} - \sum_{i=1,2,3}\{\frac{1}{3}\Delta L_i \sin 2(\theta_e - \frac{2}{3}\pi\cdot(i-1)) + \frac{2}{3}\Delta M_i \sin 2(\theta_e + \frac{2}{3}\pi\cdot i)\}}{L_{dif} - \sum_{i=1,2,3}\{\frac{1}{3}\Delta L_i \cos 2(\theta_e - \frac{2}{3}\pi\cdot(i-1)) + \frac{2}{3}\Delta M_i \cos 2(\theta_e + \frac{2}{3}\pi\cdot i)\}} \tag{3.15}$$

Thus, from the above derivations with inductance asymmetry in (3.11)-(3.12) and (3.14)-(3.15), it is noted that the 2nd harmonic position errors are exactly the same for the two carrier injection methods. Moreover, different from the resistance asymmetry in (3.2) and (3.6), the 2nd harmonic error for inductance asymmetry is neither related to carrier injection frequency nor the angle φ as can be seen from (3.10)-(3.12) and (3.14)-(3.15). Experimental results will also be provided to verify the above theoretical analyses in section 3.4.

3.3   Suppression of Oscillating Position Errors Due To Parameter Asymmetry

In order to suppress the influence of machine parameter asymmetry, the position error suppression strategies are introduced in this part. For the resistance asymmetry in (3.2) and (3.6), it is expected that just by selecting proper carrier injection frequency, the oscillating

error can be largely reduced. For inductance asymmetry, the compensation strategy using dual frequency injection is proposed in this chapter, which will be analysed in detail as follows.

3.3.1 Position error suppression for resistance asymmetry

Firstly, for resistance asymmetry, from (3.2) and (3.6), the reasonable injection frequency range for carrier signals can be determined to suppress the 2nd harmonic errors. Assuming the 2nd harmonic errors are constrained within ± 2 electric degrees, the injection frequency should satisfy

$$\frac{1}{2} \frac{\hat{r}_{dif} \tan \varphi}{\omega_h \hat{L}_{dif}} < \frac{2}{180} \pi \tag{3.16}$$

for the pulsating signal injection, and

$$\frac{1}{2} \frac{\hat{r}_{dif}}{\omega_h \hat{L}_{dif}} < \frac{2}{180} \pi \tag{3.17}$$

for rotating signal injection, respectively. Then, with (2.7), (3.16) can be expressed as

$$|\frac{\hat{r}_{dif}}{2\omega_h \hat{L}_{dif}} \tan(-\arctan \frac{2r_{avg}L_{avg}}{\omega_h(L_d L_q - L_{dq}{}^2)} + \varphi_d)| \le \frac{2}{180} \pi \tag{3.18}$$

It is not easy to solve (3.18). Thus, for simplified analysis, the lower and upper limit of injection frequency can be determined, respectively, i.e.,

1) Lower limit of injection frequency

Normally, if the injection frequency is relatively low, the digital delay ϕ_d is negligible, therefore from (3.18), it can be obtained that

$$\frac{\hat{r}_{dif}}{\hat{L}_{dif}} \frac{r_{avg}L_{avg}}{\omega_h{}^2(L_d L_q - L_{dq}{}^2)} < \frac{2}{180} \pi \tag{3.19}$$

Then, the injection frequency range is solved as

$$\omega_h > \sqrt{\frac{90}{\pi} \hat{r}_{dif} r_{avg} \frac{L_{avg}}{\hat{L}_{dif}(L_d L_q - L_{dq}{}^2)}} \tag{3.20}$$

2) Upper limit of injection frequency

At higher injection frequency, the digital delay φ_d is dominant while the resistance part of angle φ in (2.7) can be neglected. For simplicity, assuming that φ_d is mainly the phase shift caused by one-beat PWM updating delay, i.e., $\varphi_d = \omega_h/f_{PWM}$ (f_{PWM} is the PWM switching frequency), it can be deduced that

$$\frac{\tan(x)}{x} < \frac{\pi}{45} \frac{\hat{L}_{dif}}{\hat{r}_{dif}} f_{pwm}$$

(3.21)

where $x = \omega_h/f_{pwm}$. Since the function $\tan(x)/x$ is a monotonic increasing function when $0 < x < \pi/2$, the upper limit of carrier frequency can then be determined according to (3.21). Therefore, for the pulsating injection with resistance asymmetry, the carrier injection frequency cannot be selected either too large or very small, and there exists an optimal frequency to have the 2nd harmonic error to approach zero, i.e., from (2.7) and (3.18)

$$\varphi \approx -\arctan \frac{2r_{avg}L_{avg}}{\omega_h(L_d L_q - L_{dq}{}^2)} + \frac{\omega_h}{f_{PWM}} = 0$$

(3.22)

Thus, from (3.22), the optimal injection frequency can be obtained as

$$\omega_{h\_op} \approx \sqrt{\frac{2f_{PWM}r_{avg}L_{avg}}{(L_d L_q - L_{dq}{}^2)}}$$

(3.23)

From (3.23), it can be seen that the optimal injection frequency actually is determined by the machine parameters, which are then affected by machine load, temperature, etc. By way of example, based on the inductances in the dq-plane are given in Fig. 3.2, the optimal injection frequency at different load conditions is theoretically calculated and shown in Fig. 3.3. It is seen that both the d- and q-axis saturations result in the increase of the optimal injection frequency.
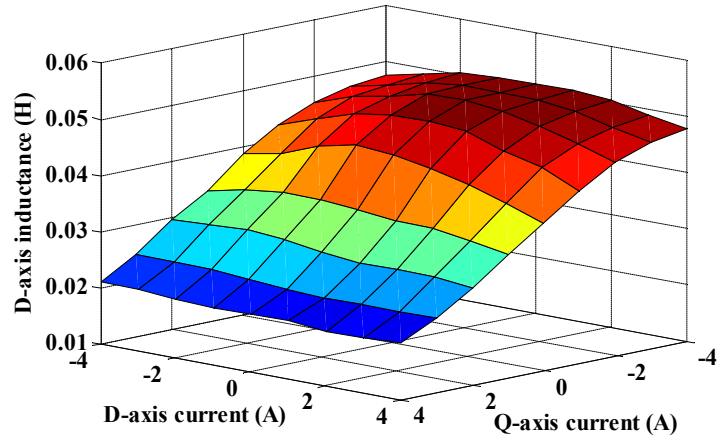
(a) D-axis inductance
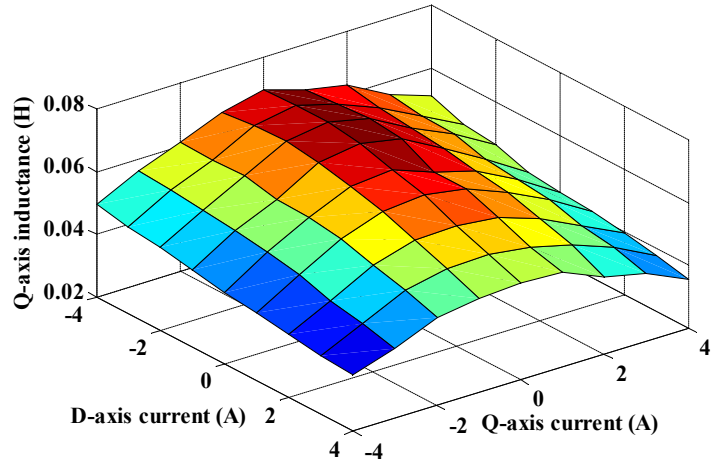
(b) Q-axis inductance
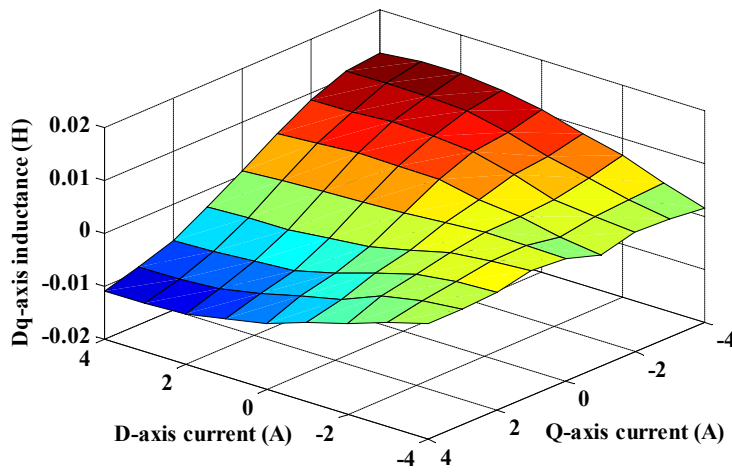
(c) D/q-axis mutual inductance

Fig. 3.2 Incremental d-/q-axis inductances in the dq-axis plane.
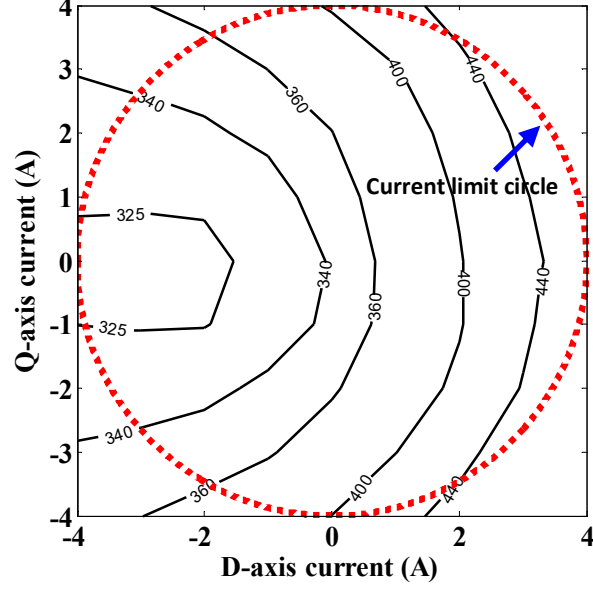
Fig. 3.3 Optimal injection frequency (Hz) in the dq-axis plane (f_{PWM}=10 kHz, r_{avg}=8Ω).

While for rotating signal injection, the reasonable carrier frequency range from (3.17) can be easily derived as

$$\omega_h > \frac{45}{\pi} \frac{\hat{r}_{dif}}{\hat{L}_{dif}} \tag{3.24}$$

It should be noted that the carrier frequency selection principles in (3.19)-(3.24) only consider the asymmetric effects. Practically, other factors such as estimation bandwidths, noises and losses, etc. should be taken into account comprehensively [BRI01].

3.3.2 Position error suppression for inductance asymmetry

On the other hand, for inductance asymmetry, online compensation strategies with dual frequency injection are employed in this chapter. By way of example, for rotating signal injection with one-phase inductance asymmetry, from (3.13), the negative sequence carrier current can be expressed as

$$i_{neg} = \frac{Ue^{-j(\omega_h t - \pi/2)}}{\omega_h L_d L_q} [-\frac{\Delta L}{3} + \hat{L}_{dif} e^{j(2\theta_e + \theta_m)}] \tag{3.25}$$

81

It is noted from (3.25) that the additional part caused by inductance asymmetry presents as the dc component, and the amplitude is only related to the ratio of U/ω_h. Therefore, if the dual frequency carrier signal is injected, i.e.,

$$\begin{bmatrix} u_\alpha \\ u_\beta \end{bmatrix} = U \begin{bmatrix} \cos\omega_h t \\ \sin\omega_h t \end{bmatrix} + U_1 \begin{bmatrix} \cos\omega_{h1} t \\ \sin\omega_{h1} t \end{bmatrix} \tag{3.26}$$

where $U/\omega_h = U_1/\omega_{h1}$, the resultant negative sequence carrier currents can be obtained as

$$i_{neg} \approx \frac{Ue^{-j(\omega_h t - \pi/2)}}{\omega_h L_d L_q}[-\frac{\Delta L}{3} + \hat{L}_{dif} e^{j(2\theta_e + \theta_m)}] + \frac{U_1 e^{-j(\omega_{h1} t - \pi/2)}}{\omega_{h1} L_d L_q}[-\frac{\Delta L}{3} + \hat{L}_{dif} e^{j(2\theta_e + \theta_m)}] \tag{3.27}$$

With the signal demodulation processing, the carrier signal can be further expressed as

$$I_{neg} = LPF1(i_{neg} e^{j(\omega_h t - \pi/2)}) = \frac{U}{\omega_h L_d L_q}(-\frac{\Delta L}{3} + \hat{L}_{dif} e^{j(2\theta_e + \theta_m)}) \tag{3.28}$$

$$I_{neg1} = LPF2(i_{neg} e^{j(\omega_{h1} t - \pi/2)}) = \frac{U_1}{\omega_{h1} L_d L_q}(-\frac{\Delta L}{3} + \hat{L}_{dif} e^{j(2\theta_e + \theta_m)}) \tag{3.29}$$

Since the injected second frequency (ω_{h1}) signal is only used for error compensation for the inductance asymmetry, the cut-off frequency of $LPF2$ can be selected much lower than that of $LPF1$, i.e., (3.29) can be expressed as

$$I_{neg1} = LPF2(i_{neg} e^{j(\omega_{h1} t - \pi/2)}) \approx -\frac{U_1}{\omega_{h1} L_d L_q}\frac{\Delta L}{3} \tag{3.30}$$

Thus, from (3.28)-(3.30), it can be derived that

$$I_{neg2} = I_{neg} - I_{neg1} \approx \frac{U}{\omega_h L_d L_q}\hat{L}_{dif} e^{j(2\theta_e + \theta_m)} \tag{3.31}$$

Compared to (3.25), the asymmetry component in (3.31) has been largely suppressed with the proposed compensation strategy. It should be noted that since the added *LPF2* is only used for the second frequency (ω_{h2}) carrier signals, the bandwidth of the main position estimation loop is unaffected. The block diagram for rotating signal injection with the inductance asymmetry compensation is shown in Fig. 3.4. In addition, when the dual frequency signals are injected, the influence of injection frequency on machine inductance should be considered due to the eddy current effects [BIA09]. Thanks to the laminated steel,

the inductance variation due to different injected frequencies is negligible [BIA09], and therefore the derivation of (3.26)-(3.31) is reasonable theoretically.

Similarly, for the pulsating signal injection, the dual frequency signals are injected as

$$\begin{bmatrix} \hat{u}_{dh} \\ \hat{u}_{qh} \end{bmatrix} = \begin{bmatrix} U\cos\omega_h t \\ 0 \end{bmatrix} + \begin{bmatrix} U_1\cos\omega_{h1} t \\ 0 \end{bmatrix} \tag{3.32}$$

Accordingly, the carrier current can be expressed as

$$\hat{i}_{dqh} = \hat{i}_{dh} + j\hat{i}_{qh} = (\frac{U\sin\omega_h t}{\omega_h L_d L_q} + \frac{U_1\sin\omega_{h1} t}{\omega_{h1} L_d L_q})[L_{avg} + \frac{1}{3}\Delta L + \hat{L}_{dif} e^{j(2\Delta\theta+\theta_m)} - \frac{1}{3}\Delta L e^{j(-2\theta_e+2\Delta\theta)}] \tag{3.33}$$

Then, the signal demodulation as shown in Fig. 3.5 can be expressed as

$$\hat{I}_{qh} = \mathrm{Im}\{[LPF1(\hat{i}_{dqh}\sin\omega_h t \cdot e^{j2\hat{\theta}_e}) - LPF2(\hat{i}_{dqh}\sin\omega_{h1} t \cdot e^{j2\hat{\theta}_e})]\cdot e^{j-2\hat{\theta}_e}\} = \frac{U\hat{L}_{dif}\sin(2\Delta\theta+\theta_m)}{2\omega_h L_d L_q} \tag{3.34}$$

where I_m presents the imaginary part of the estimated d/q-axis carrier current component. From the above derivations in (3.32)-(3.34), it can be seen that the asymmetry component for pulsating injection is also significantly suppressed with the dual frequency injection strategy compared to (3.9). The effectiveness for the proposed compensation strategies will be verified experimentally in section 3.4.
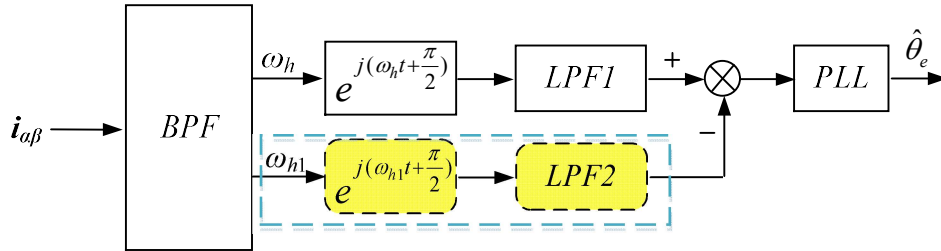
Fig. 3.4 Dual frequency injection based inductance asymmetry compensation for rotating signal injection.
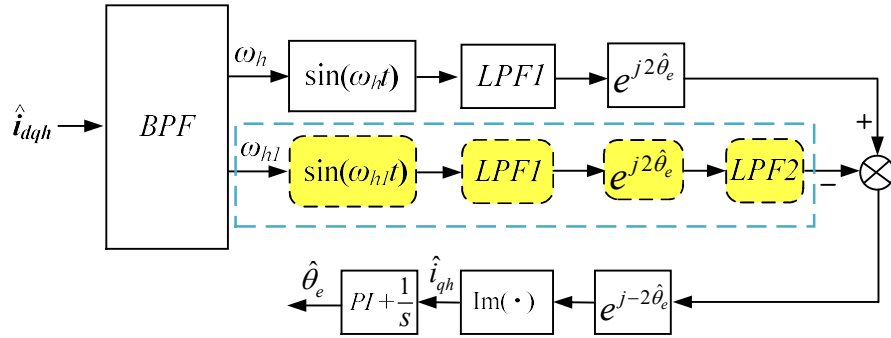
Fig. 3.5 Dual frequency injection based inductance asymmetry compensation for the pulsating signal injection.

3.4 Experimental Validation

The experiments are implemented on a dSPACE platform to validate the above theoretical analyses. The overall control scheme with carrier signal injection is shown in Fig. 3.6. The main parameters of tested IPM machine are shown in Table 2.1 in chapter 2. To simulate the asymmetry conditions discussed in this chapter, extra phase resistances and inductances are connected in series to the phases of the IPM machine.
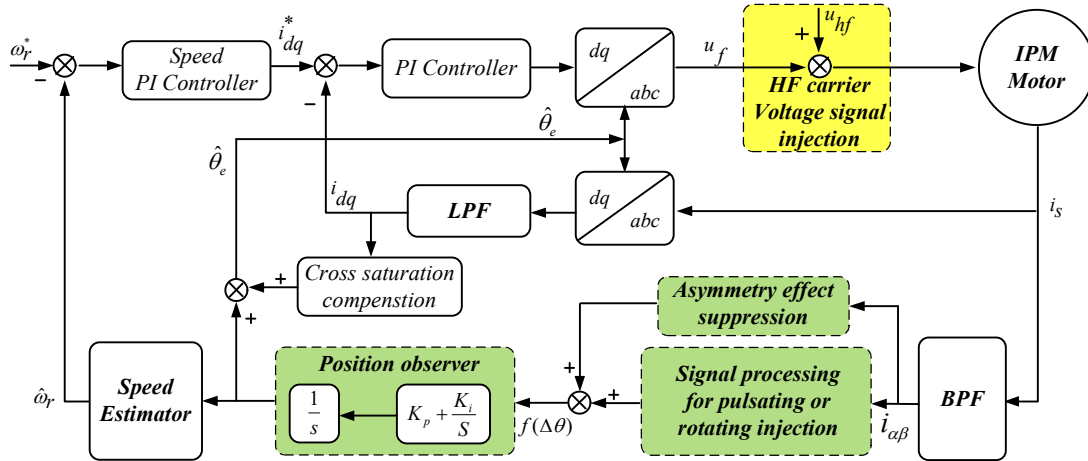
Fig. 3.6 Block diagram of overall control system with carrier signal injection with asymmetry.

3.4.1 Position estimation performances due to parameter asymmetry

Firstly, with one phase +66% resistance asymmetry, the position errors for the pulsating and rotating injection at 330 Hz injection frequency are shown in Fig. 3.7-Fig. 3.8, respectively. In both cases, the 2nd harmonic position error can be observed, which is

consistent with above theoretical derivations. Besides, it can be clearly seen that the rotating injection has much larger 2nd errors than pulsating injection, Fig. 3.7-Fig. 3.8. This is because the phase angle φ is very small at such carrier frequency resulting in decreased oscillating errors for the pulsating injection according to (3.2). Further comparisons for the two carriers at 330 Hz and 800 Hz injection frequency with different asymmetric resistances are shown in Fig. 3.9-Fig. 3.10. In Fig. 3.9, as expected, due to the modulation of phase angle φ, the oscillating errors for the pulsating injection are always smaller than those of rotating injection at 330 Hz. While at injection frequency 800 Hz, Fig. 3.10, since φ increases, the 2nd harmonic error is even larger than that of rotating injection under certain resistance asymmetry conditions. Furthermore, the 2nd harmonic position errors with + 100% one phase resistance asymmetry at different injection frequencies under different load conditions are also illustrated in Fig. 3.11, from which it can be seen that pulsating injection is more advantageous with the carrier frequency from 200 Hz to 800Hz due to the modulation of φ. Besides, it is noted that the 2nd harmonic errors slightly increase under load conditions. This can be explained by that the 2nd harmonic errors in (3.2) and (3.6) only depend on the machine saliency level, i.e., $\hat{L}_{dif} = \sqrt{L_{dq}^2 + L_{dif}^2}$, which only slightly changes because the reduction of L_{dif} with load is compensated by the increase of L_{dq} for the prototype IPM machine, Fig. 3.2.
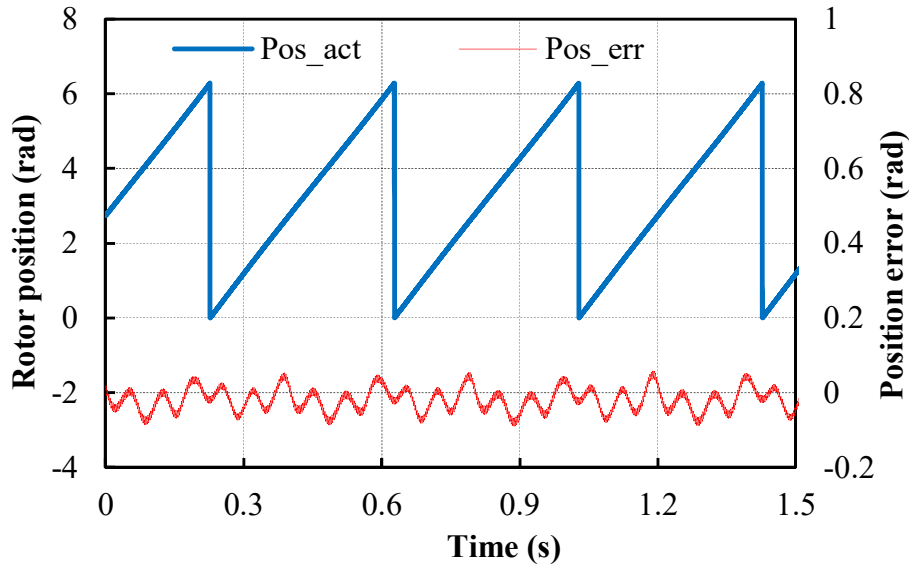
Fig. 3.7 Position errors with one phase +66% resistance asymmetry for pulsating signal injection (330Hz injection).
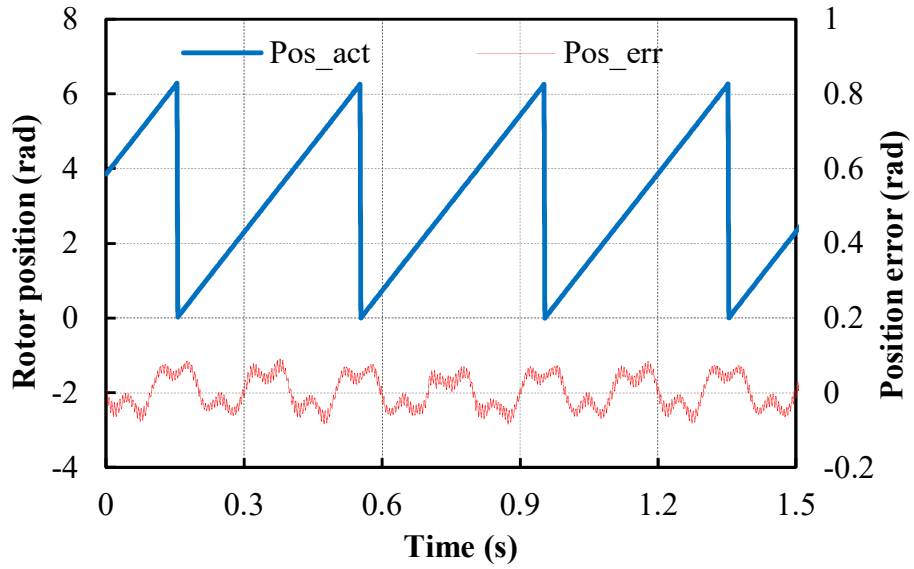
Fig. 3.8 Position errors with one phase +66% resistance asymmetry for rotating signal injection (330Hz injection).
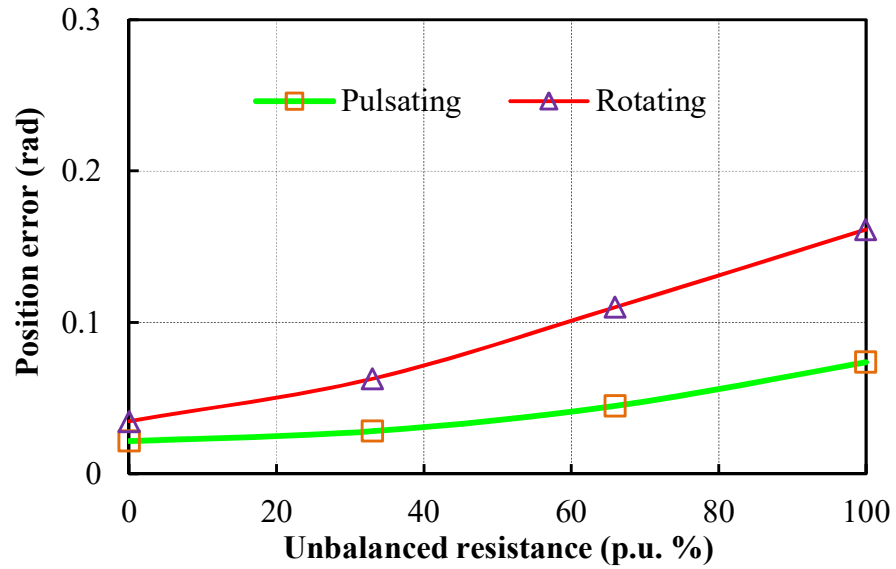
Fig. 3.9 The 2nd harmonic position errors with different resistance asymmetry for the two carriers with 330Hz injection.
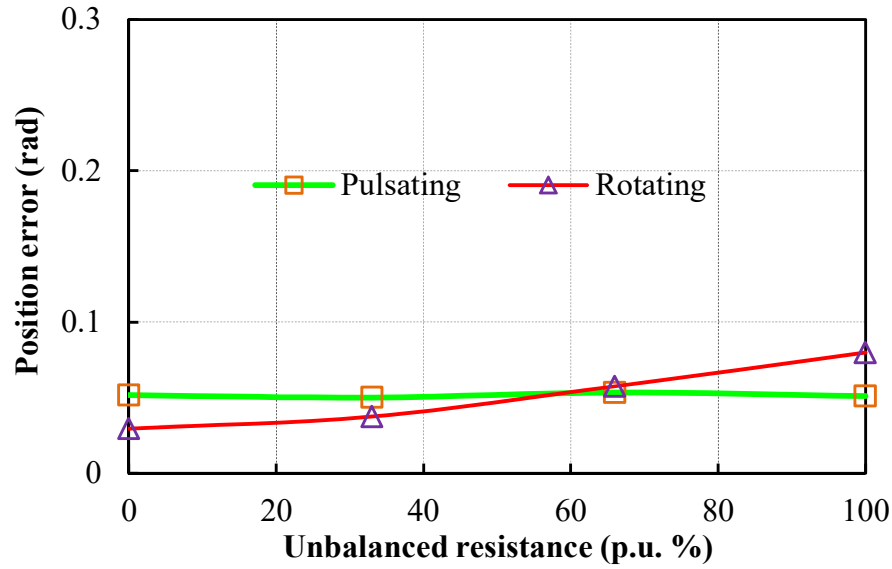
Fig. 3.10 The 2nd position errors with different resistance asymmetry for the two carriers with 800 Hz injection.
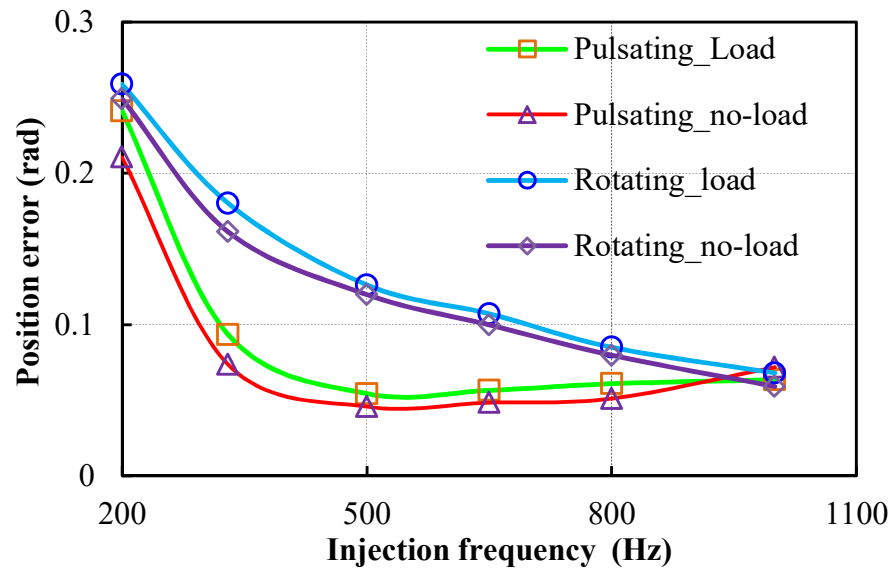
Fig. 3.11 The 2nd harmonic position errors with +100% phase resistance asymmetry at different injection frequencies with/without load.

Then, for inductance asymmetry with added 2 mH inductance (~4% phase inductance asymmetry), the position errors at 500 Hz injection for the two carriers are shown in Fig. 3.12-Fig. 3.13. It can be clearly seen that the two position errors are approximately the same also with 2nd harmonic oscillations. Besides, the 2nd harmonic position errors at different injection frequencies under different load conditions are also shown in Fig. 3.14, and slightly

increased errors are observed under loaded condition, which are all consistent with above analyses.
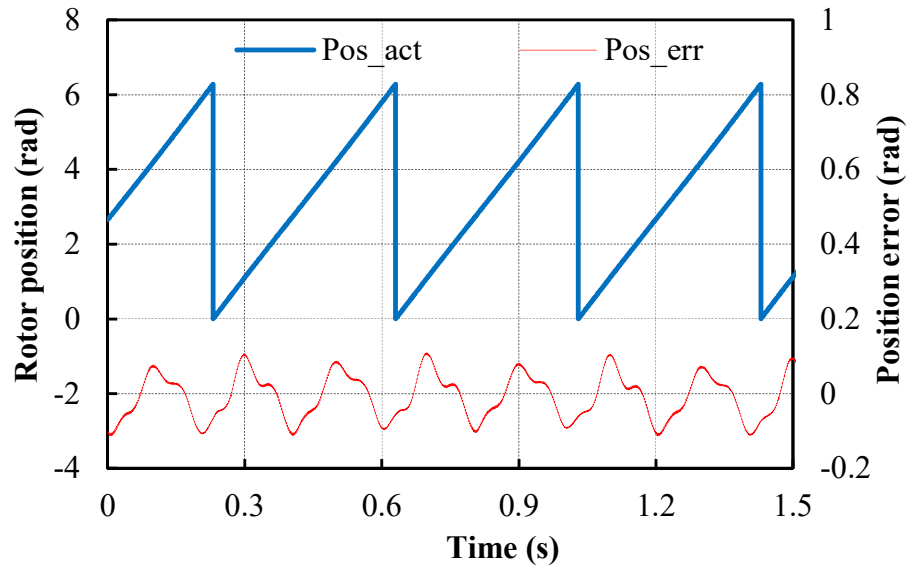
Fig. 3.12 Position errors with ~4% self-inductance asymmetry of one phase for rotating signal injection (500Hz injection).
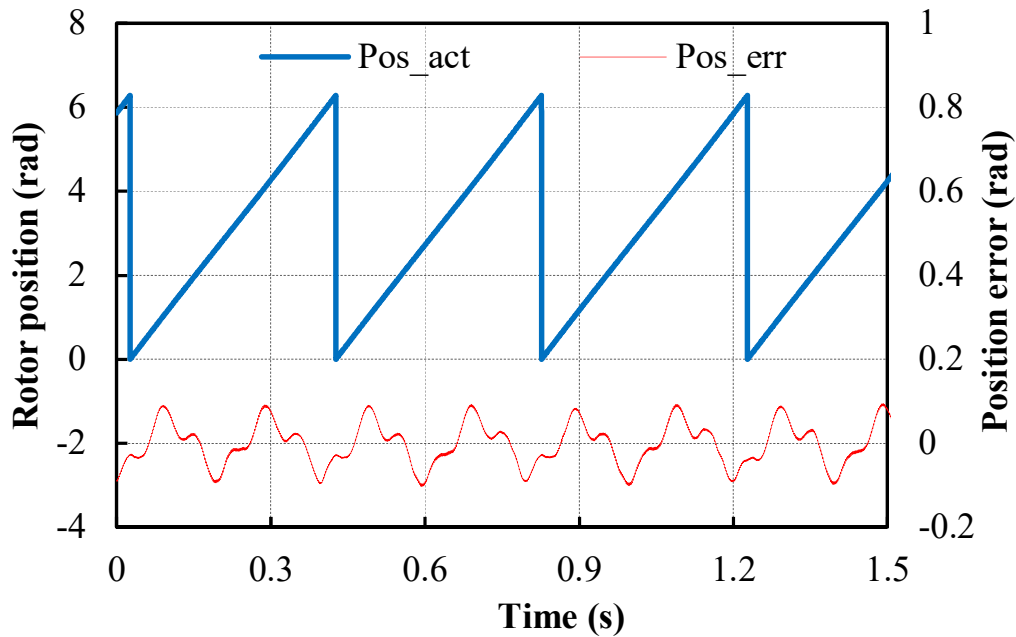
Fig. 3.13 Position errors with ~4% self-inductance asymmetry of one phase for pulsating signal injection (500Hz injection).
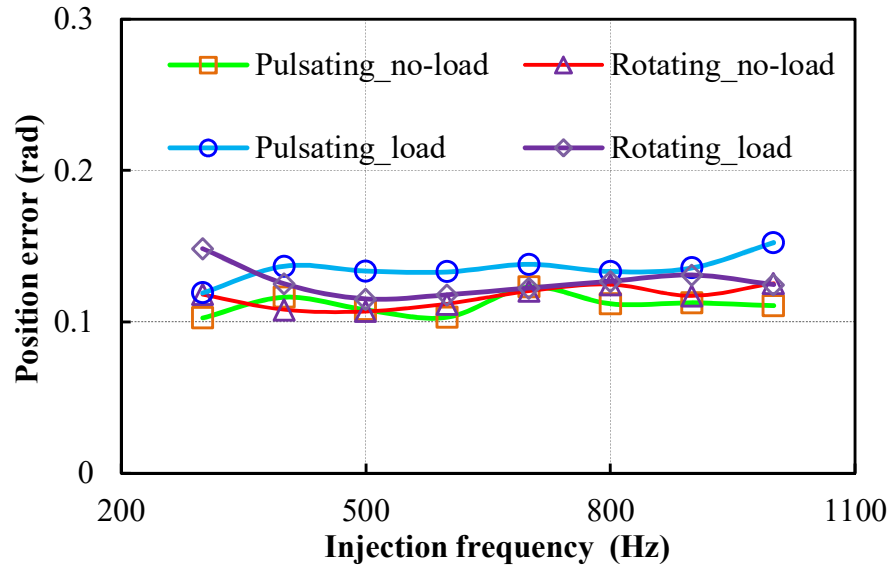
Fig. 3.14 The 2nd harmonic position errors with ~4% self-inductance asymmetry at different injection frequencies with/without load.

3.4.2 The 2nd harmonic oscillating error suppression verification

Further, the 2nd harmonic error suppression strategies for resistance asymmetry are also illustrated in Fig. 3.15. In Fig. 3.15, with one phase 100% resistance asymmetry, it can be seen that the reasonable carrier frequency range is from 450 Hz to 850 Hz for the pulsating injection, and the optimal frequency in (3.23) is around 650 Hz. The difference between the theoretical and the actual value of the optimal frequency may originate from the measurement error of the machine parameters (Fig. 3.2) used for the calculations in Fig. 3.3. While for rotating injection, over 750 Hz carrier frequency is desirable as shown in Fig. 3.15. Therefore, the resistance asymmetry effects can be significantly suppressed just by selecting proper injection frequency, which is consistent with above theoretical results.
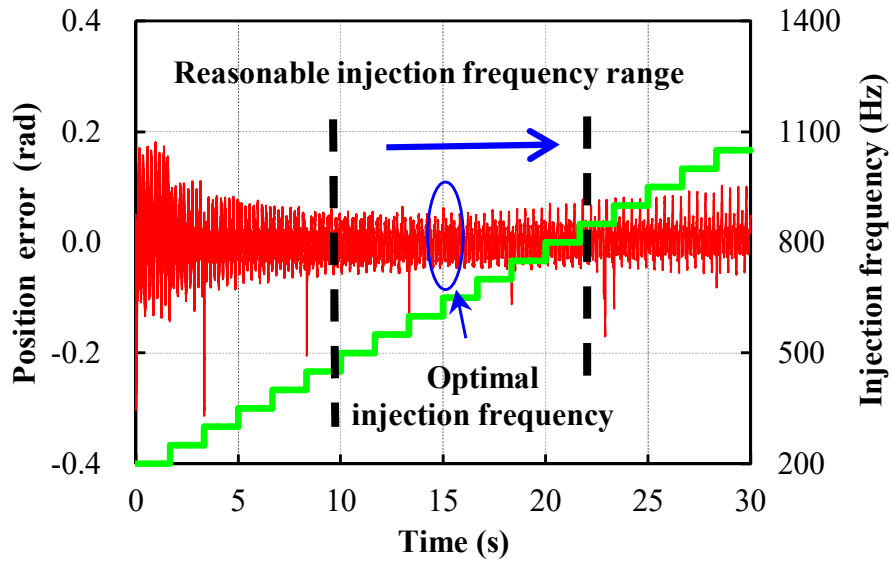
(a) Pulsating signal injection
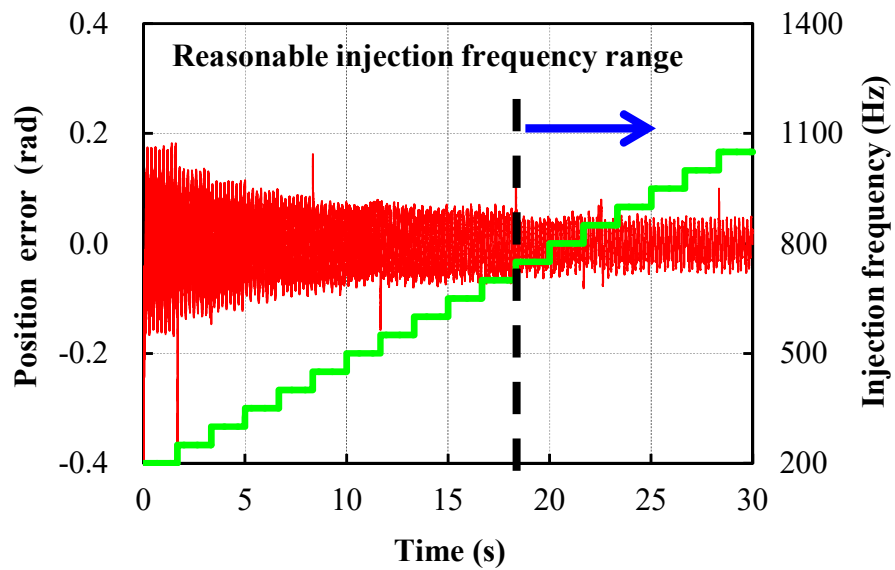
(b) Rotating signal injection

Fig. 3.15 Carrier signal selection with one phase +100% resistance asymmetry.

On the other hand, for inductance asymmetry, with the compensation methods based on dual frequency injection (12V/400 Hz and 18V/600 Hz carrier signals are selected), the oscillating harmonic errors are significantly reduced under various load conditions for the two carriers, respectively, Fig. 3.16-Fig. 3.17. The spectra of these position estimation errors before and after the compensation are also illustrated in Fig. 3.18, from which it is observed that the 2nd harmonic errors have been significantly suppressed. Therefore, it can be

90

concluded that with the proposed strategy, the oscillating position errors due to inductance asymmetry can be reduced effectively under different load conditions.
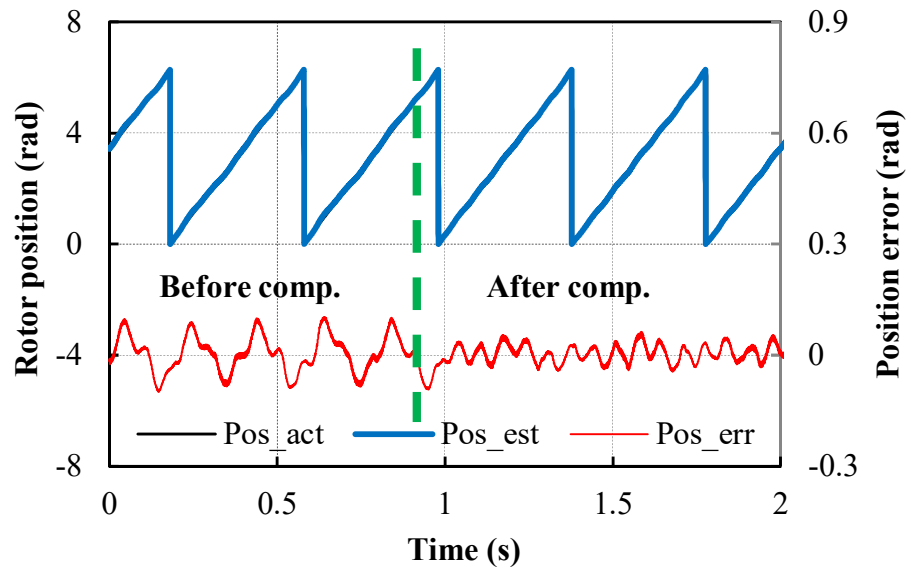
(a) No-load condition
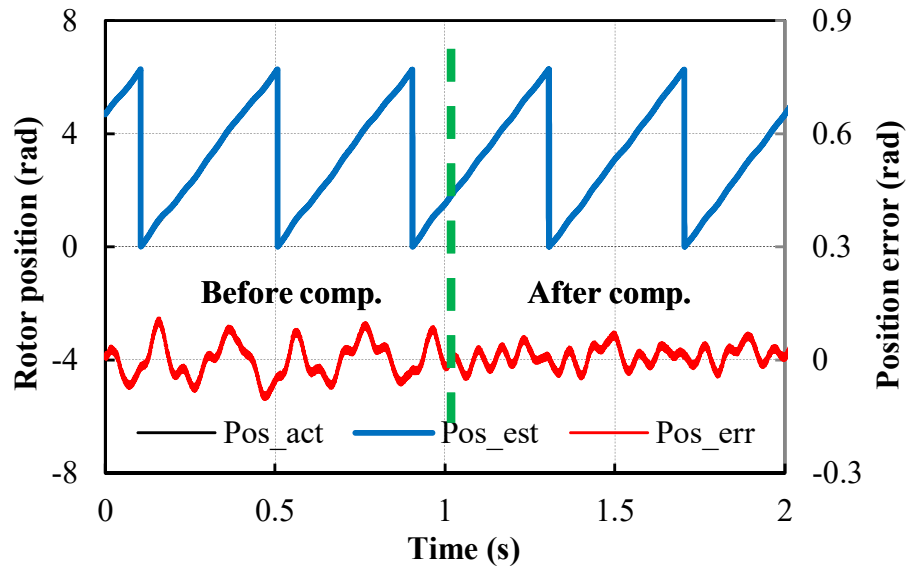
(b) Load condition (I_q=4A)

Fig. 3.16 The 2nd harmonic error suppression for inductance asymmetry with rotating signal injection.
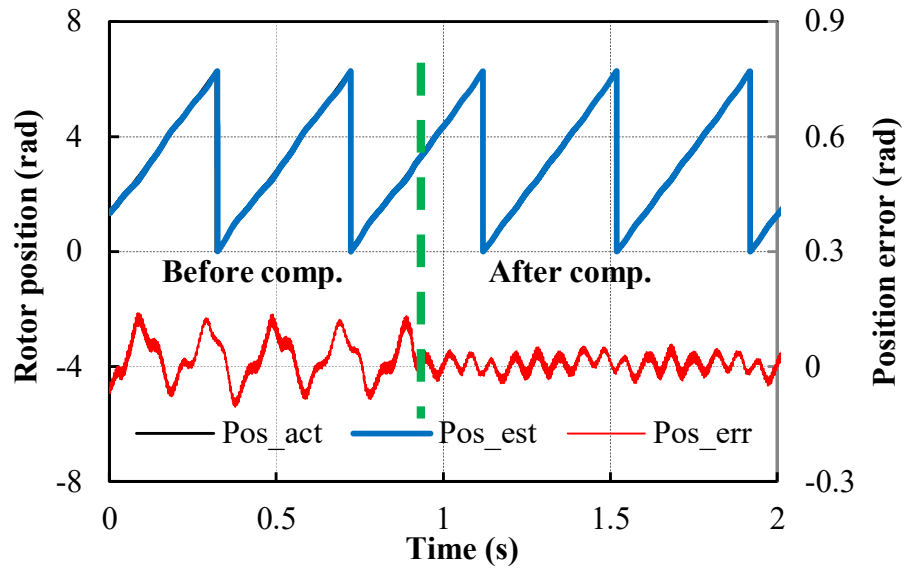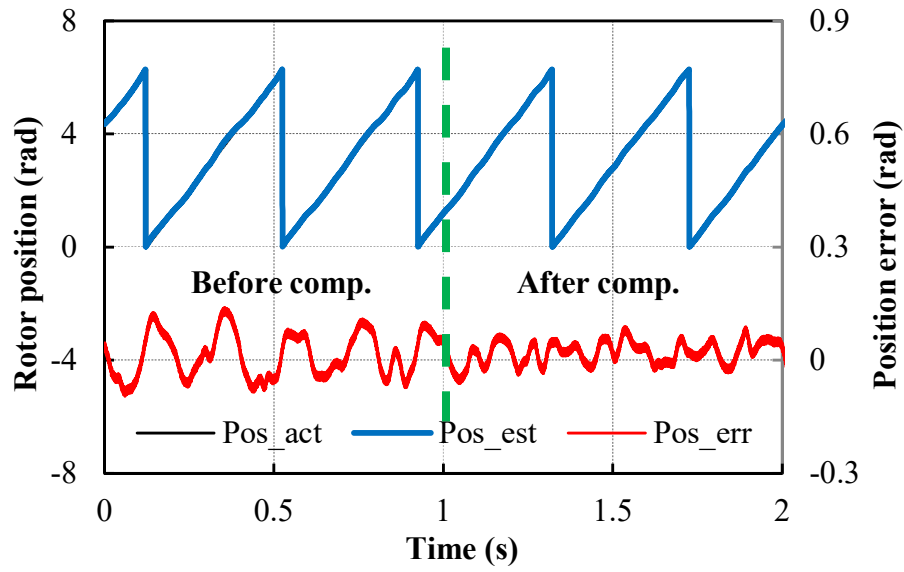
(a) No-load condition

(b) Load condition (Iq=4A)

Fig. 3.17 The 2nd harmonic error suppression for inductance asymmetry with the pulsating signal injection.
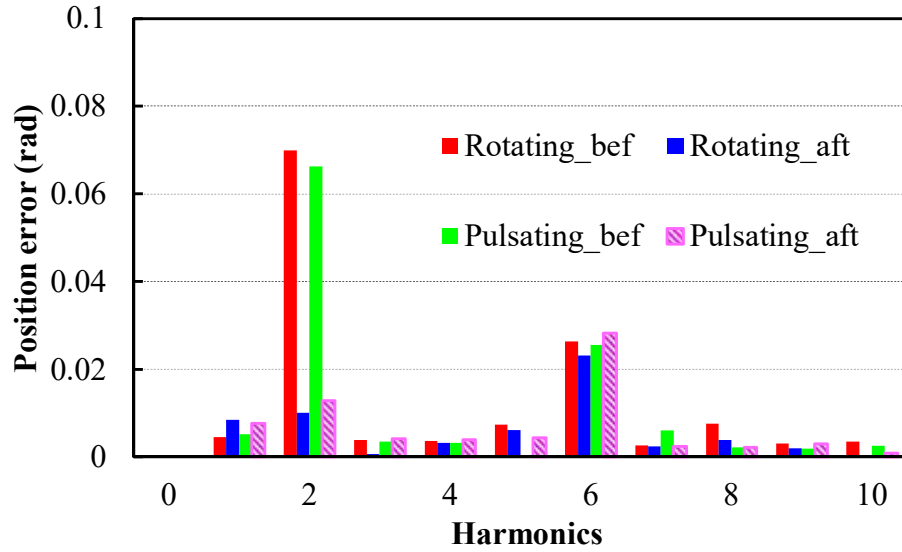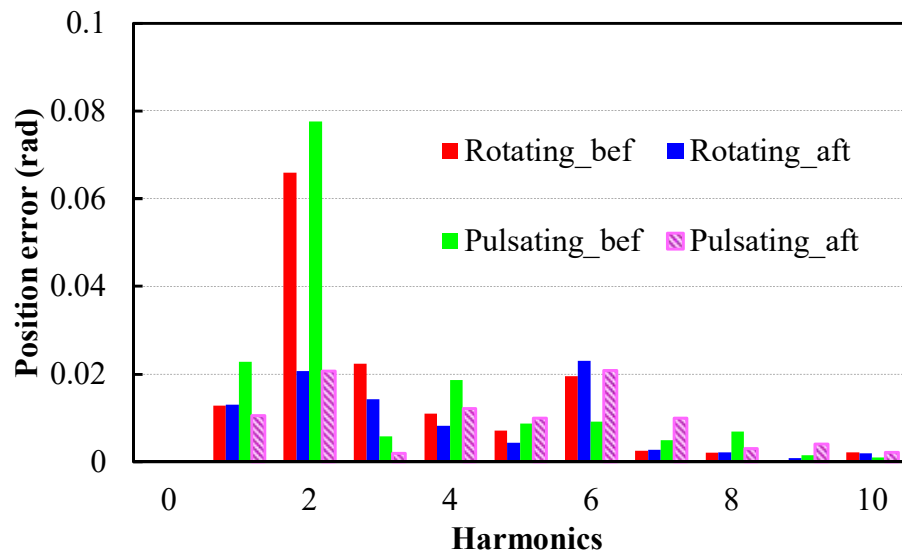
(a) No-load condition

(b) Load condition

Fig. 3.18 Spectra of position error before/after the compensation for inductance asymmetry.

3.5 Conclusions

This chapter has investigated the influence of asymmetric machine parameters on carrier signal injection based sensorless control for PMSMs. All the theoretical analyses have been

verified by experiments on a prototype IPM machine. Several conclusions can be obtained as follows.

1) The 2nd harmonic position estimation errors arise due to phase asymmetry irrespective of injection types.

2) The pulsating and rotating carrier injections present different amplitudes of the 2nd position errors for resistance asymmetry, and at normal injection frequency (~1/20 PWM switching frequency), pulsating injection is more advantageous than rotating injection.

3) By selecting proper injection frequency, position errors due to resistance asymmetry can be largely suppressed.

4) Position errors caused by inductance asymmetry are the same for the two injection methods, and moreover the error compensation strategies based on dual frequency injection have shown great effectiveness.

It is noted that if the signal processing delays discussed in chapter 2 is very significant, the delay compensation should be adopted at the first place. Then, the asymmetry compensation strategies discussed in this chapter can be performed as the next step.

4 Novel Sinusoidal-Wave Signal Injection Method Using Zero Sequence Voltage for Sensorless Control of Permanent Magnet Synchronous Machines

4.1 Introduction

In the previous chapters, for carrier voltage signal injection methods, the carrier current responses are normally utilised for the rotor position estimation. In this chapter, the zero sequence carrier voltage responses will be introduced for the position estimation.

For the rotating injection, apart from the negative sequence carrier current, the zero sequence carrier voltage is also found to contain the rotor position information [BRI04][GAR07]. In [GAR07], in terms of signal total harmonic distortion (THD), it is found that zero sequence carrier voltage is less sensitive to the injection distortions compared to the negative sequence carrier current. Moreover, it is observed that the system bandwidth can be significantly enhanced by the use of zero sequence voltage and consequently position estimation accuracy and stability are increased [GAR07].

However, since the conventional zero sequence voltage sensing method is based on rotating signal injection [BRI05] [CON06] [GAR07], the position information signal is phase-modulated by machine saliency. Thus, any signal processing delays (e.g., digital delay, sampling circuit delay, etc.) which affect the phase shift of zero sequence voltage can then give rise to the position estimation errors [RAC08c]. Whilst in [KIM04a] [RAC08c], it is pointed out that the pulsating injection in the estimated synchronous reference frame is of high accuracy because the phase lags and phase leads caused by signal processing delays are approximately cancelled. Alternatively, it can be explained that the pulsating injection is amplitude-modulated by machine saliency and the signal processing delays mainly affect the amplitude rather than the phase shift of saliency position, which results in high estimation accuracy and robustness. Therefore, if the zero sequence carrier voltage sensing based sensorless control utilises pulsating injection rather than rotating injection, the resultant position estimation performance may be further enhanced. However, the conventional pulsating injection method in the estimated synchronous reference frame with zero sequence voltage sensing deteriorates the position estimation performances as will be shown later in this chapter.

Thus, this chapter proposes a novel pulsating carrier signal injection strategy utilising zero sequence carrier voltage for the sensorless control of permanent magnet synchronous machines (PMSMs). Different from the commonly-used rotating injection in the stationary reference frame and pulsating injection in the estimated synchronous reference frame, the proposed method will be injected on the estimated reference frame anti-rotating at twice the rotor's estimated electrical speed. Then, the position tracking will be fulfilled by controlling the zero sequence carrier voltage to zero. Additionally, the cross-coupling magnetic saturation effects for zero sequence carrier voltage sensing method will be also investigated. Finally, experimental results confirm all the theoretical analyses on a prototype PM machine.

The major new results of this chapter have been published in [XU16b].

4.2   Conventional Carrier Signal Model with Zero Sequence Carrier Voltage Detection

Generally, the modelling of carrier signal injection method using zero sequence voltage is implemented on the natural reference frame [BRI04] [BRI05]. However, the model in [BRI04][BRI05] does not consider the mutual-inductances between phases, which will also be included as follows. On the other hand, in order to measure the zero sequence carrier voltage, the balanced resistor network and access to the machine neutral point are required [BRI05], as shown in Fig. 4.1.
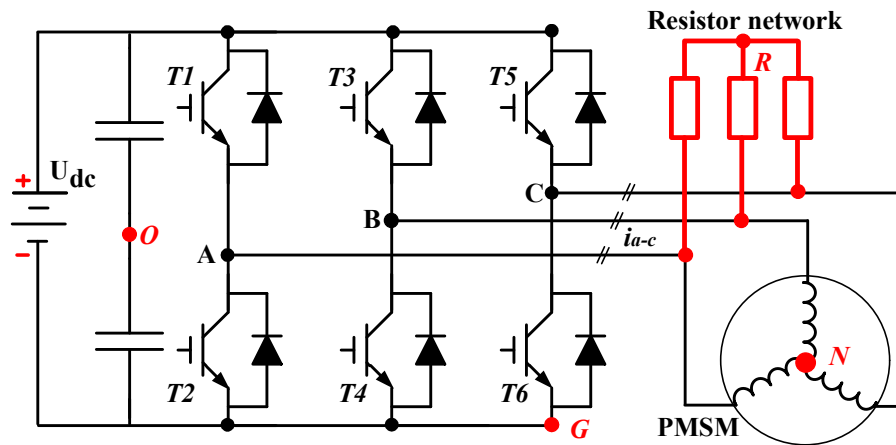
Fig. 4.1 Zero sequence carrier voltage measurement.

4.2.1   Zero sequence carrier voltage response for rotating signal injection

Firstly, the three phase voltage equations neglecting resistances and back-EMF can be

expressed as

$$\begin{bmatrix} U_{AN} \\ U_{BN} \\ U_{CN} \end{bmatrix} = \begin{bmatrix} L_{aa} & M_{ab} & M_{ac} \\ M_{ba} & L_{bb} & M_{bc} \\ M_{ca} & M_{cb} & L_{cc} \end{bmatrix} \begin{bmatrix} \dfrac{di_a}{dt} \\ \dfrac{di_b}{dt} \\ \dfrac{di_c}{dt} \end{bmatrix} \qquad (4.1)$$

where U_{AN}, U_{BN} and U_{CN}, i_a, i_b and i_c are voltages and currents of phase A-C, L_{aa}, L_{bb}, L_{cc}, $M_{ab}(M_{ba})$, $M_{ac}(M_{ca})$, $M_{bc}(M_{cb})$ are self- and mutual-inductances for phase A-C, respectively. The self- and mutual-inductances are generally described as

$$\begin{cases} L_{aa} = L_0 - L_2 \cos\left(2\theta_e\right) \\ L_{bb} = L_0 - L_2 \cos\left(2\theta_e + \dfrac{2}{3}\pi\right) \\ L_{cc} = L_0 - L_2 \cos(2\theta_e - \dfrac{2}{3}\pi) \end{cases} \qquad (4.2)$$

$$\begin{cases} M_{ab} = M_{ba} = M_0 - M_2 \cos\left(2\theta_e - \dfrac{2}{3}\pi\right) \\ M_{bc} = M_{cb} = M_0 - M_2 \cos\left(2\theta_e\right) \\ M_{ca} = M_{ac} = M_0 - M_2 \cos\left(2\theta_e + \dfrac{2}{3}\pi\right) \end{cases} \qquad (4.3)$$

where L_0, L_2 are the dc and 2nd harmonic amplitudes of self-inductances, M_0, M_2 are the dc and 2nd harmonics amplitudes of mutual-inductances, respectively. Then, for the conventional rotating signal injection with zero sequence voltage sensing [BRI05] [CON06], the three phase injection voltages from Fig. 2.15 can be expressed as

$$\begin{aligned} U_{AO} &= U \cos \omega_h t \\ U_{BO} &= U \cos(\omega_h t - \dfrac{2}{3}\pi) \\ U_{CO} &= U \cos(\omega_h t + \dfrac{2}{3}\pi) \end{aligned} \qquad (4.4)$$

where U and ω_h are the carrier voltage and frequency. Then, as shown in Fig. 4.1, the relations of the voltages for machine neutral point N, the resistor network central point R and capacitor mid-point O can be expressed as

$$U_{AO} = U_{AN} - U_{RN} + U_{RO}$$
$$U_{BO} = U_{BN} - U_{RN} + U_{RO} \tag{4.5}$$
$$U_{CO} = U_{CN} - U_{RN} + U_{RO}$$

where U_{RN} is the zero sequence voltage between the network central point R and machine neutral point N, and U_{RO} is the voltage between the network central point R and capacitor mid-point O, respectively.
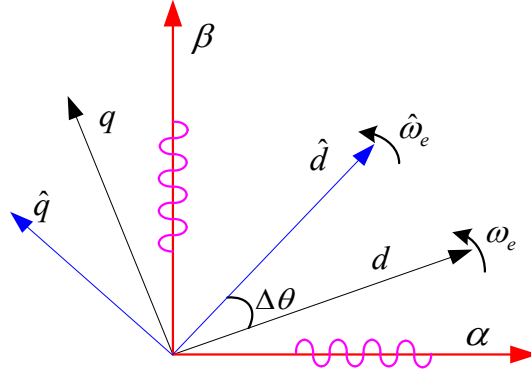
Fig. 4.2 Rotating signal injection method in the stationary reference frame.

It can be easily proved that U_{RO} equals zero for brushless AC operation around the injection frequency. To be more specific, according to Fig. 4.1, the relations of the voltages for the resistor network central point R, capacitor mid-point O and the point G of the dc bus can be expressed as

$$U_{AG} = U_{AR} + U_{RO} + U_{OG}$$
$$U_{BG} = U_{BR} + U_{RO} + U_{OG} \tag{4.6}$$
$$U_{CG} = U_{CR} + U_{RO} + U_{OG}$$

Then, from (4.6) and Fig. 4.1, the voltage of U_{RO} can be obtained as [SHE04]

$$U_{RO} = \frac{U_{AG} + U_{BG} + U_{CG}}{3} - \frac{U_{DC}}{2} \tag{4.7}$$

By only considering the components around carrier injection frequency, U_{AG}, U_{BG}, and U_{CG} can be expressed as

$$U_{AG} = \frac{U_{DC}}{2} + U \cos \omega_h t$$

$$U_{BG} = \frac{U_{DC}}{2} + U \cos(\omega_h t - \frac{2\pi}{3})$$

$$U_{CG} = \frac{U_{DC}}{2} + U \cos(\omega_h t + \frac{2\pi}{3})$$

(4.8)

Therefore, with (4.8), it can be easily derived from (4.7) that U_{RO} equals zero at carrier injection frequency. However, it should be noted that around PWM switching frequency, the PWM noises in U_{RO} will be generated by the inverter [SHE04] [BRI05]. However, obviously, the PWM frequency noises will not affect the theoretical derivations for the zero sequence voltage at carrier injection frequency.

Then, for three phase Y-connected windings, it is derived that

$$\frac{di_a}{dt} + \frac{di_b}{dt} + \frac{di_c}{dt} = 0$$

(4.9)

With (4.1)-(4.9), the zero sequence carrier voltage U_{RN} in Fig. 4.1 can be obtained as

$$U_{RN} = V_{o1} \cos(\omega_h t + 2\theta_e) - V_{o2} \cos(\omega_h t - 4\theta_e)$$

$$V_{o1} = U \frac{2(-M_0 + L_0)}{4L_0^2 - 8L_0 M_0 - L_2^2 - 4M_2^2 - 4L_2 M_2 + 4M_0^2}(-M_2 + L_2)$$

$$V_{o2} = U \frac{(-2M_2 + L_2)}{4L_0^2 - 8L_0 M_0 - L_2^2 - 4M_2^2 - 4L_2 M_2 + 4M_0^2}(-M_2 + L_2)$$

(4.10)

From (4.10), the zero sequence carrier voltage for the conventional rotating injection consists of two frequency components at $\omega_h t + 2\theta_e$ and $\omega_h t - 4\theta_e$, respectively, [BRI05][CON06]. Then, for the prototype PM machine with finite element (FE) simulation (Fig. 4.3), the incremental self- and mutual-inductances can be obtained as illustrated in Fig. 4.4. From Fig. 4.4, since typically $2(-M_0 + L_0)$ is much larger than $(-2M_2 + L_2)$, the first term of (4.10) is normally utilised for rotor position estimation [BRI05], i.e.,

$$U_{RN} = U \frac{2(-M_2 + L_2)(-M_0 + L_0)}{4L_0^2 - 8L_0 M_0 - L_2^2 - 4M_2^2 - 4L_2 M_2 + 4M_0^2} \cos(\omega_h t + 2\theta_e)$$

(4.11)

It is worth noting that the signal amplitude in (4.11) for position tracking is not related to the injection frequency. Thus, compared with negative sequence current where the signal amplitude is inversely proportional to the injection frequency, larger injection frequency can be employed for zero sequence voltage method leading to boosted system bandwidths, which

consequently increases the stability of system [GAR07].
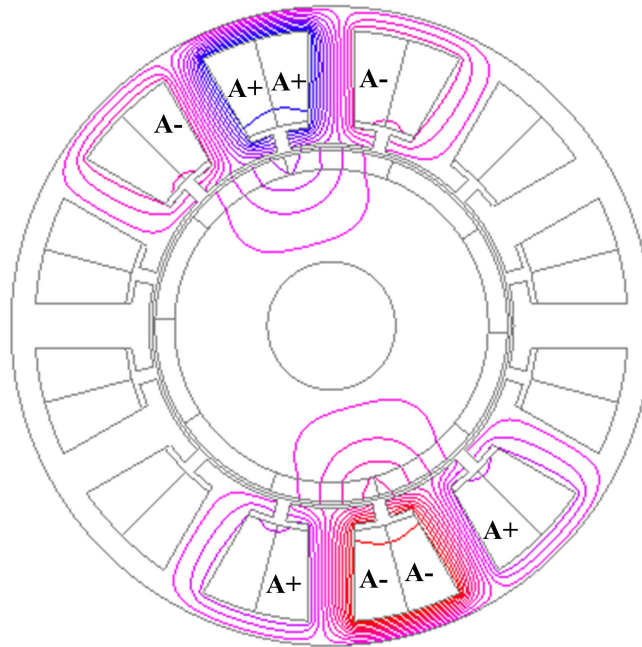
Fig. 4.3 Armature reaction flux distribution of one phase for the prototype PM machine.
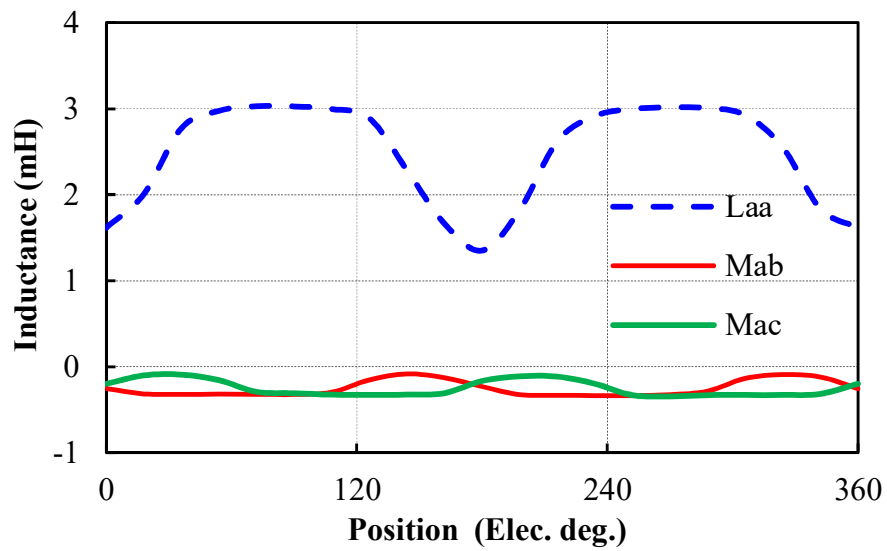
Fig. 4.4 Incremental self- and mutual-inductances of phase A by FE simulation.

4.2.2　Carrier signal demodulation

In order to obtain the position information from (4.11), the zero sequence carrier voltage is further processed as

$$U_{RN\_cos} = LPF(U_{RN} * (-\cos(\omega_h t))) = -\frac{1}{2}V_{o1}\cos(2\theta_e) \quad (4.12)$$

$$U_{RN\_sin} = LPF(U_{RN} * (-\sin(\omega_h t))) = \frac{1}{2}V_{o1}\sin(2\theta_e) \quad (4.13)$$

Then, based on (4.12)-(4.13), the estimated rotor position can be obtained with the position observer as shown in Fig. 4.5.
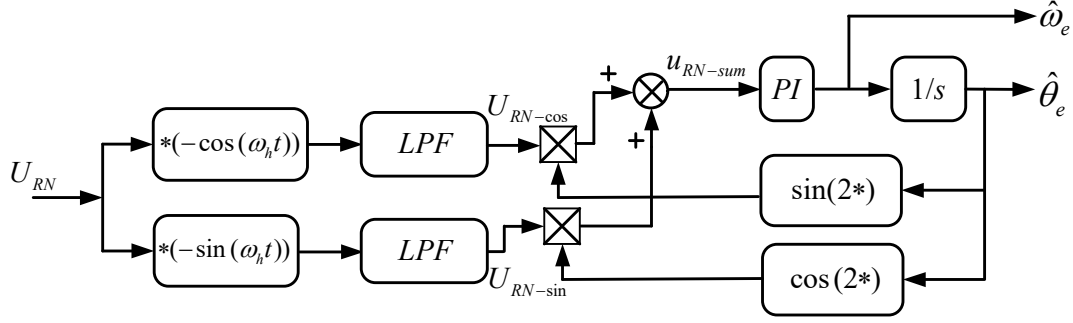
Fig. 4.5 Zero sequence carrier signal demodulation for rotating injection.

From above analyses, it can be seen that the conventional zero sequence voltage response is based on rotating signal injection and phase-modulated by the saliency position in (4.11) [BRI05]. However, as reported in [RAC08c] [CUP12], the rotating signal injection is sensitive to signal processing delays since the phase of saliency position can be shifted by the delays and consequently these delays can cause larger position estimation errors.

In contrast, it is found that the pulsating injection in the estimated synchronous reference frame is more accurate and robust to these delays since the resultant carrier current response is amplitude-modulated by saliency position with the intrinsic cancellation of the phase shifts caused by signal processing delays [RAC08c] [CUP12]. Besides, the signal demodulation is less computationally intensive compared to that of rotating injection [RAC08c] [KIM04a]. Thus, it is expected that the zero sequence voltage sensing method with pulsating injection should be more advantageous since both the merits can be integrated. However, the conventional pulsating injection in the estimated synchronous reference frame using zero sequence voltage degrades the position estimation performances, which is analysed as follows.

4.2.3   Zero sequence carrier voltage response for conventional pulsating injection

Specifically, if the conventional pulsating signal injection on the estimated synchronous reference frame is employed, the injected voltages of three phases from Fig. 2.3 can be expressed as

$$U_{AO} = U \cos \omega_h t \cos(\hat{\theta}_e)$$

$$U_{BO} = U \cos \omega_h t \cos(\hat{\theta}_e - \frac{2}{3}\pi) \qquad (4.14)$$

$$U_{CO} = U \cos \omega_h t \cos(\hat{\theta}_e + \frac{2}{3}\pi)$$
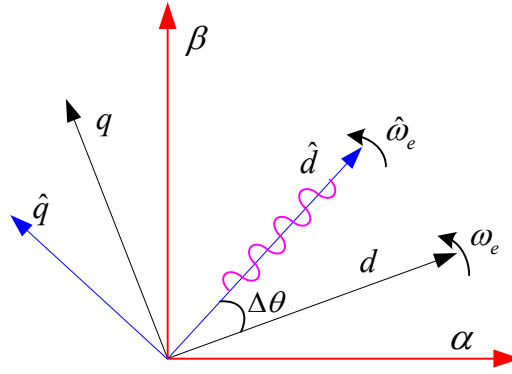
Fig. 4.6 Conventional pulsating signal injection method in the estimated synchronous reference frame.

Similarly, with (4.1)-(4.3), (4.5)-(4.9) and (4.14), the resultant zero sequence carrier voltage can be obtained as

$$U_{RN} = U \frac{2(-M_2 + L_2)(-M_0 + L_0)}{4L_0^2 - 8L_0M_0 - L_2^2 - 4M_2^2 - 4L_2M_2 + 4M_0^2} \cos \omega_h t \cos(2\theta_e + \hat{\theta}_e) \qquad (4.15)$$

Then, the signal demodulation can be expressed as

$$u_{RN-sum} = LPF(U_{RN} \cdot 4\sin(\omega_h t - 3\hat{\theta}_e)) =$$
$$\frac{2U(-M_2 + L_2)(-M_0 + L_0)}{4L_0^2 - 8L_0M_0 - L_2^2 - 4M_2^2 - 4L_2M_2 + 4M_0^2}(\sin(2\Delta\theta) + \sin(2\theta_e + 4\hat{\theta}_e)) \qquad (4.16)$$

where u_{RN-sum} is the final position information signal. From (4.16), it can be seen that additional 6th harmonics having larger amplitudes arise in steady condition, which is expected to affect the stability of sensorless control and significantly deteriorate the position estimation

performance.

Accordingly, with the zero sequence carrier voltage response for the conventional pulsating injection, the estimated rotor position and position estimation error are obtained as shown in Fig. 4.7. It can be clearly observed that large dc and oscillation errors arise, which states that the zero sequence voltage response for the conventional pulsating injection is not suitable for the rotor position tracking.
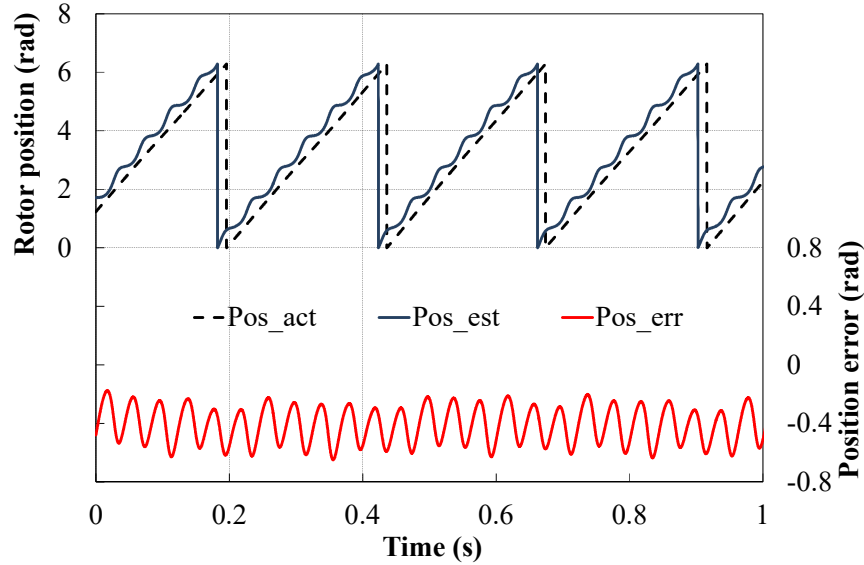
Fig. 4.7 Position estimation with conventional pulsating signal injection in the estimated synchronous reference frame (4V/800 Hz).

4.3   Proposed Novel Pulsating Injection Method Using Zero Sequence Carrier Voltage

From the above analyses, it can be seen that the conventional pulsating injection using zero sequence voltage has undesirable dc and large 6th harmonic errors. In order to utilise both the synergies of zero sequence voltage sensing and pulsating injection, a novel carrier injection method is proposed in this chapter.

4.3.1   Anti-rotating pulsating injection method with zero sequence carrier voltage

Actually, from (4.15), it is noted that the zero sequence voltage response is modulated by the component of $(2\theta_e + \hat{\theta}_e)$, where $2\theta_e$ appears beacuse the phase inductances vary twice during one electrical period of time, while $+\hat{\theta}_e$ is due to that the injection axis is in the estimated synchronous reference frame (Fig. 2.3). Therefore, it is expected that if the

injection axis is anti-rotating in the estimated reference frame, the resultant zero sequence response is possible to be amplitude-modulated by $\sin(2\Delta\theta)$, which will be exactly the same to the carrier current response of the conventional pulsating injection, resulting in high accuracy [RAC08c].

With the above analyses, one novel carrier signal injection method is proposed as shown in Fig. 4.8. It can be seen that the proposed injection is performed on the q_2-axis in the estimated reference frame, anti-rotating at twice the rotor's estimated electrical speed. The injected signal can be expressed as

$$\hat{U}_{2d} = 0$$
$$\hat{U}_{2q} = U\cos\omega_h t \tag{4.17}$$
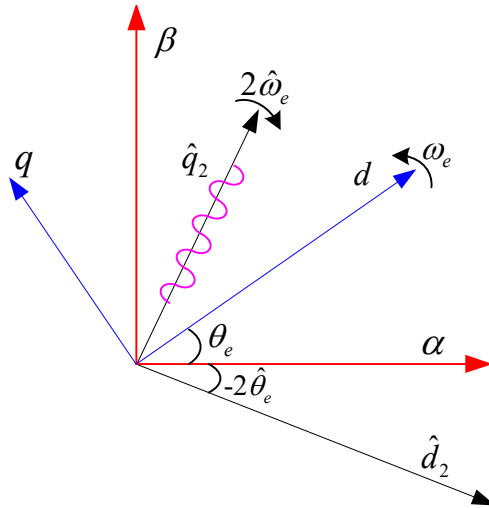
Fig. 4.8 Novel anti-rotating pulsating signal injection strategy.

Then, with coordinate transformation matrix, the injection voltage in the α-/β-axis frame is described as

$$\begin{bmatrix} U_\alpha \\ U_\beta \end{bmatrix} = \begin{bmatrix} \cos(-2\hat{\theta}_e) & -\sin(-2\hat{\theta}_e) \\ \sin(-2\hat{\theta}_e) & \cos(-2\hat{\theta}_e) \end{bmatrix} \begin{bmatrix} \hat{U}_{2d} \\ \hat{U}_{2q} \end{bmatrix} \tag{4.18}$$

Further, with (4.17)-(4.18), the actual injected three phase voltages can be expressed as

$$U_{AO} = U \cos \omega_h t \sin(2\hat{\theta}_e)$$

$$U_{BO} = U \cos \omega_h t \sin(2\hat{\theta}_e + \frac{2}{3}\pi) \qquad (4.19)$$

$$U_{CO} = U \cos \omega_h t \sin(2\hat{\theta}_e - \frac{2}{3}\pi)$$

Similarly, with (4.1)-(4.3), (4.5)-(4.9) and (4.19), the zero sequence carrier voltage for the proposed injection method can be derived as

$$U_{RN} = V_{o1} \cos \omega_h t \sin(2\Delta\theta) - V_{o2} \cos \omega_h t \sin(4\theta_e + 2\hat{\theta}_e)$$

$$V_{o1} = U \frac{2(-M_0 + L_0)}{4L_0^2 - 8L_0 M_0 - L_2^2 - 4M_2^2 - 4L_2 M_2 + 4M_0^2}(-M_2 + L_2) \qquad (4.20)$$

$$V_{o2} = U \frac{(-2M_2 + L_2)}{4L_0^2 - 8L_0 M_0 - L_2^2 - 4M_2^2 - 4L_2 M_2 + 4M_0^2}(-M_2 + L_2)$$

Then, similar to (4.10)-(4.11), the first term of (4.20) has much larger amplitude and will be utilised for the position estimation, i.e.,

$$U_{RN} = U \frac{2(-M_0 + L_0)(-M_2 + L_2)}{4L_0^2 - 8L_0 M_0 - L_2^2 - 4M_2^2 - 4L_2 M_2 + 4M_0^2} \cos \omega_h t \sin(2\Delta\theta) \qquad (4.21)$$

From (4.21), it is observed that the zero sequence voltage response for the proposed injection strategy is very simple. Furthermore, from (4.21), the zero sequence voltage is amplitude-modulated by machine saliency, and therefore, the phase shifts of saliency position due to signal processing delays can be approximately cancelled. Besides, compared to the conventional pulsating injection on the estimated synchronous reference frame in (4.16), the undesirable 6th harmonic amplitude is much smaller.

Thus, it is expected that the proposed method can perfectly combine both the synergies of pulsating injection and zero sequence voltage sensing, i.e., high accuracy and bandwidths, great dynamic response and robustness, etc. as will be verified experimentally in the following. It should be noted that the principle of proposed position tracking is to enable the zero sequence voltage to be zero in the steady conditions, i.e., $U_{RN}=0$ when $\Delta\theta=0$.

4.3.2 Carrier signal demodulation

To further obtain the estimated rotor position, the zero sequence voltage response in (4.21) for the proposed signal injection method can be processed as

$$u_{RN-sum} = LPF(U_{RN} * 2\cos\omega_h t) = \frac{2U(-M_0 + L_0)(-M_2 + L_2)}{4L_0^2 - 8L_0 M_0 - L_2^2 - 4M_2^2 - 4L_2 M_2 + 4M_0^2} \sin(2\Delta\theta) \quad (4.22)$$

Accordingly, the signal demodulation for the zero sequence carrier voltage of the proposed injection method is shown in Fig. 4.9. Due to the simpler signal response in (4.21)-(4.22), the signal demodulation for the proposed injection method is also much simpler than that of conventional rotating signal injection in Fig. 4.5.
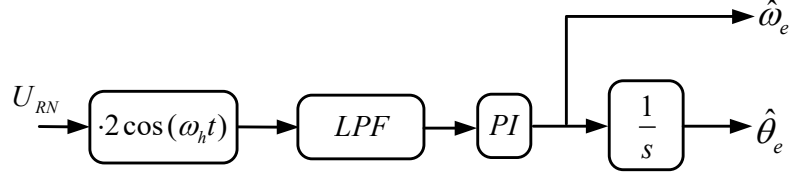
Fig. 4.9 Zero sequence carrier signal demodulation for the proposed injection method.

4.3.3 Cross-coupling magnetic saturation effects using zero sequence voltage

The cross-coupling magnetic saturation effects have been systematically investigated for the carrier current sensing based carrier signal injection methods [GUG06] [LI09] [REI08]. However, for the zero sequence voltage sensing based methods, the cross-coupling effects have not been investigated and will be discussed in detail as follows.

Firstly, by considering the saturation effects, the three phase inductances can be expressed as [YAN06]

$$\begin{cases} L_{aa} = L_0 - L_2 \cos(2\theta_e) - L_c \sin(2\theta_e) \\ L_{bb} = L_0 - L_2 \cos\left(2\theta_e + \frac{2}{3}\pi\right) - L_c \sin(2\theta_e + \frac{2}{3}\pi) \\ L_{cc} = L_0 - L_2 \cos(2\theta_e - \frac{2}{3}\pi) - L_c \sin(2\theta_e - \frac{2}{3}\pi) \end{cases} \quad (4.23)$$

$$\begin{cases} M_{ab} = M_{ba} = M_0 - M_2 \cos\left(2\theta_e - \frac{2}{3}\pi\right) - M_c \sin(2\theta_e - \frac{2}{3}\pi) \\ M_{bc} = M_{cb} = M_0 - M_2 \cos(2\theta_e) - M_c \sin(2\theta_e) \\ M_{ca} = M_{ac} = M_0 - M_2 \cos\left(2\theta_e + \frac{2}{3}\pi\right) - M_c \sin(2\theta_e + \frac{2}{3}\pi) \end{cases} \quad (4.24)$$

where L_c and M_c represent the 2nd harmonic amplitude of sine inductance terms in the self- and mutual-inductances, respectively. To introduce the phase shift angle caused by the cross-

coupling effects, by way of example, the self- and mutual-inductances of phase A can be rewritten as,

$$L_{aa} = L_0 - L_s \cos(2\theta_e + \theta_{s1})$$
$$M_{ab} = M_0 - M_s \cos(2\theta_e - \frac{2\pi}{3} + \theta_{s2})$$

(4.25)

where $L_s = \sqrt{L_2^2 + L_c^2}$, $M_s = \sqrt{L_2^2 + L_c^2}$, θ_{s1}=arctan($-L_c/L_2$), and θ_{s2}=arctan($-M_c/M_2$). The same amplitude and phase shifts can be also derived for phase B and C, respectively. Then, with either the conventional rotating or the proposed anti-rotating pulsating injection, the zero sequence carrier voltage can be obtained as

$$U_{RN} = \frac{U(L_0 - M_0)(L_s - M_s)\cos(\omega_h t + 2\theta_e + \theta_{s3})}{2L_0^2 + 2M_0^2 - 4L_0M_0 - 2L_sM_s - \frac{L_s^2}{2} - 2M_s^2}$$

(4.26)

for rotating signal injection, and

$$U_{RN} = \frac{U(L_0 - M_0)(L_s - M_s)\cos\omega_h t \sin(2\Delta\theta + \theta_{s3})}{2L_0^2 + 2M_0^2 - 4L_0M_0 - 2L_sM_s - \frac{L_s^2}{2} - 2M_s^2}$$

(4.27)

for the proposed signal injection, respectively, where θ_{s3} presents the phase shift of the zero sequence carrier voltage due to the cross-coupling effect and can be derived as

$$\theta_{s3} = -\arctan\frac{L_s\sin(\theta_{s1}) - M_s\sin(\theta_{s2})}{L_s\cos(\theta_{s1}) - M_s\cos(\theta_{s2})} = -\arctan\frac{L_c - M_c}{L_2 - M_2}$$

(4.28)

Therefore, from (4.26) and (4.27), the position estimation errors due to the cross-coupling magnetic effects are exactly the same for the two injection methods with zero sequence voltage sensing. Accordingly, the position estimation errors can be obtained from (4.28) as

$$\Delta\theta = -\frac{1}{2}\theta_{s3} = \frac{1}{2}\arctan\frac{L_c - M_c}{L_2 - M_2}$$

(4.29)

Then, in order to compensate the position errors due to cross-coupling effects, neural network structure [REI08] or offline measurements [LI09] [LIU14b], etc. are normally used for the compensation. In this chapter, similar to [LIU14b], the estimation error caused by cross-coupling effects is approximately proportional to the fundamental q-axis current, i.e.,

$\theta_m \approx k*i_q$ as shown in Fig. 4.10. Thus, the measured results can be then directly employed for online compensation.
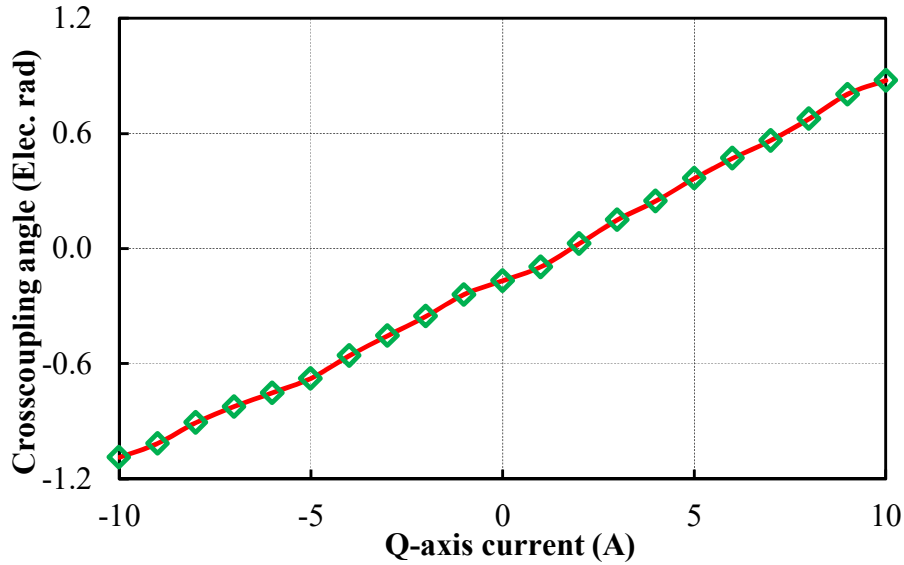
Fig. 4.10 Measured phase shift due to cross-coupling effect with q-axis current.

4.4 Experimental Validation

The experiments are implemented on a dSPACE DS1006 platform to validate the proposed pulsating signal injection method on the prototype PM machine (machine parameters are shown in Table 4.1), which is fed by SEMIX 71GD12E4s inverter. The overall control block diagram for the proposed injection method with zero sequence voltage sensing is shown in Fig. 4.11 where the $I_d=0$ control strategy is employed. The machine phase currents are measured by the transducers LEM LA25-NP. In order to measure the zero sequence carrier voltage, one balanced resistor network, one additional A/D sampling channel, the hardware circuit for signal conditioning, and also the access to the machine neutral point are required [GAR07]. Although this may increase the cost for the industrial application, on the other hand zero-sequence techniques provide some advantages over other methods [GAR07] [BRI04]. The inverter switching frequency is set to 10 kHz, and is the same as current/voltage sampling frequency. The PM machine is also equipped with an incremental encoder (resolution of 5000 PPR) to provide the accurate rotor position for reference. A 0.75-kW brushed DC motor is then used to provide the load torque (~5.5Nm).
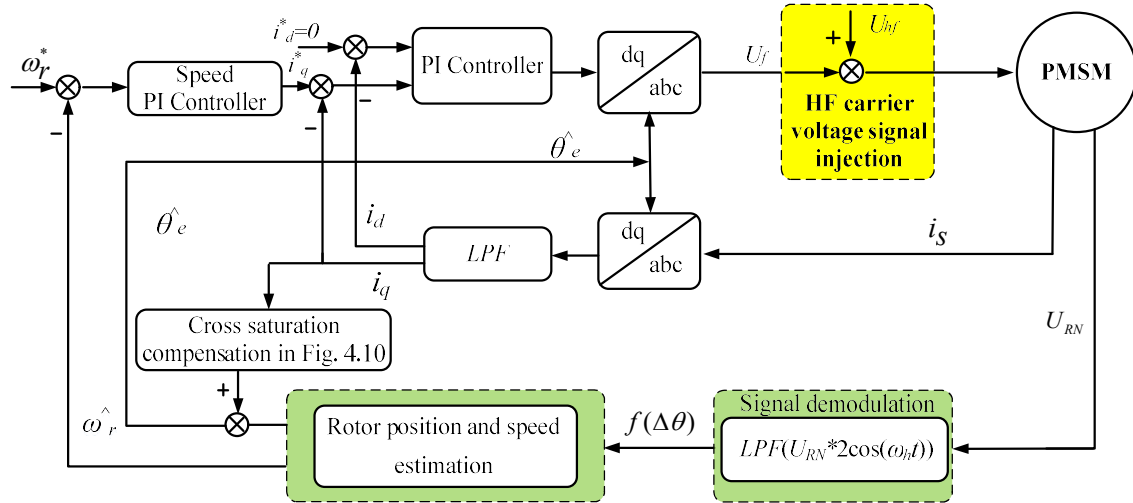
Fig. 4.11 Block diagram of overall control system with carrier signal injection using zero sequence voltage.

Table 4.1 Parameters of Prototype PM Machine Tested

Rated voltage	36	V
Rated current	10	A
Rated speed	400	rpm
Rated torque	5.5	Nm
Nominal phase resistance	0.32	Ω
Pole number	10	
PM flux-linkage	70.7	mWb

4.4.1 Zero sequence voltage model verification

In order to simply verify the analyses about the zero sequence voltages with conventional and proposed signal injection methods, Fig. 4.12 illustrates the measured zero sequence carrier voltage spectra. Specifically, for the proposed method, the position error is set to $\pi/4$ with the assistance of position sensor to maximise the zero sequence signal. Both the injected signal is set as 8V and 600Hz, and the fundamental frequency f_e is 2.5Hz. From Fig. 4.12, it is observed that the zero sequence voltage components for rotating injection are primarily at f_h+2f_e and f_h-4f_e (242nd and 236th), while conventional pulsating injection in the estimated synchronous reference frame mainly at $f_h\pm3f_e$ (237th and 243rd). By comparison, for the proposed pulsating injection method, the frequency components at f_h and $f_h\pm6f_e$ (240th and

234th/246th) arise as illustrated in Fig. 4.12. All the measured results are in consistent with the theoretical analyses in (4.10), (4.15) and (4.20), respectively.
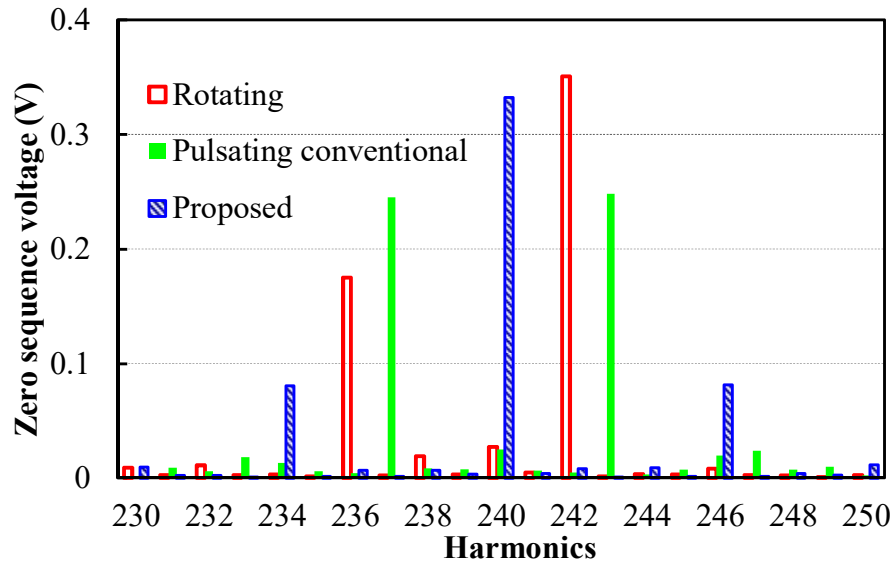
Fig. 4.12 Measured zero sequence carrier voltage with different injection methods.

Furthermore, to verify that the zero sequence voltage response with proposed injection method is amplitude-modulated by machine saliency, the method in [LIN14] is employed here, i.e., the estimated virtual position is rotating at 2 Hz while the machine rotor is locked at θ_e=0 rad. The measured zero sequence voltage response is illustrated in Fig. 4.13, which clearly shows that the amplitude of carrier voltage is modulated by the position difference $\Delta\theta$ between actual and virtual rotor positions.
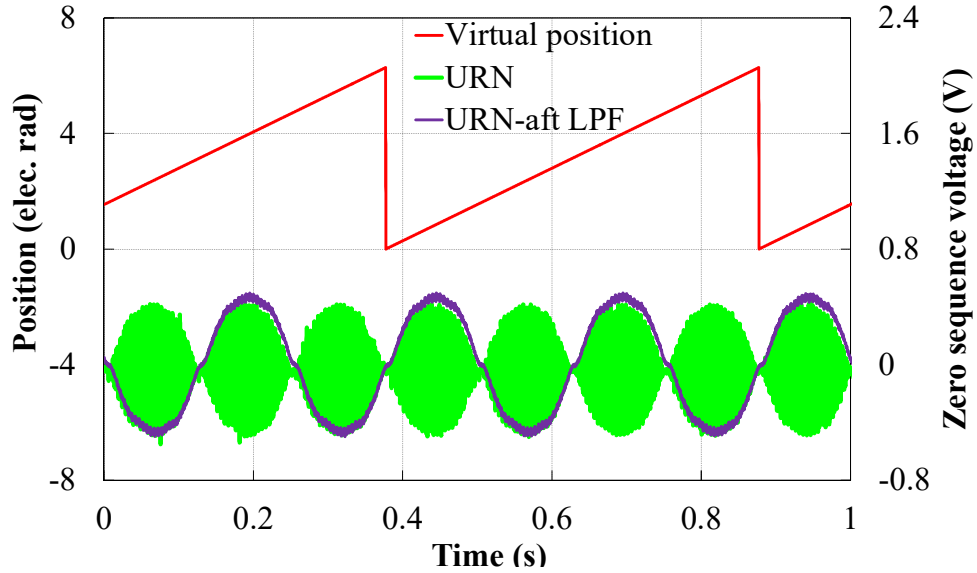
Fig. 4.13 Measured zero sequence carrier voltage with proposed injection method.

4.4.2 Steady- and dynamic-state position estimation performances

The steady-state sensorless control performance with proposed injection method is illustrated in Fig. 4.14 with q-axis current = 10 A. The injection signal is set as 4V and 800Hz with the rotor reference speed = 40 rpm. It can be seen that under load conditions, due to cross-coupling effects, there exist significant position estimation errors. Then, by the compensation methods as given in Fig. 4.10, better steady estimation performance can be ensured. Besides, it is noted from Fig. 4.14 that the noticeable 6th harmonic position error exists and may mainly arise from the second term of (4.10) and (4.20), and therefore the decoupling of the undesirable effect is important as discussed in [BRI04] [BRI05] [GAR07].

The initial rotor position detection with the proposed injection method is also verified and shown in Fig. 4.15, where the fundamental current references is set as 0 A. It can be seen that the actual rotor position can be quickly tracked but with the ambiguity of π, i.e., both the estimated rotor positions are ~0.9 rad regardless of whether the rotor stops in the north- or south-pole (0.86 rad or 4 rad (0.86+π)). This is exactly the same as the conventional carrier injection methods because the machine saliency undergoes two cycles during one electrical period [HAQ03] [JEO05] [GON13]. Accordingly, the methods in [HAQ03] [JEO05] [GON13] can be employed for the magnetic polarity identification, which however is not addressed in detail in this chapter. It is noted that the magnetic polarity detection performance can be also improved with the use of the zero sequence carrier voltage, which will be

presented in chapter 6.

The dynamic performance with proposed injection method is shown in Fig. 4.16 where the rotor speed reference is given as 0-50-100 rpm. The injected carrier signals are as the same as those in the steady state conditions. The quick dynamic response can be observed and the overall position errors are small with cross-coupling effects compensation.
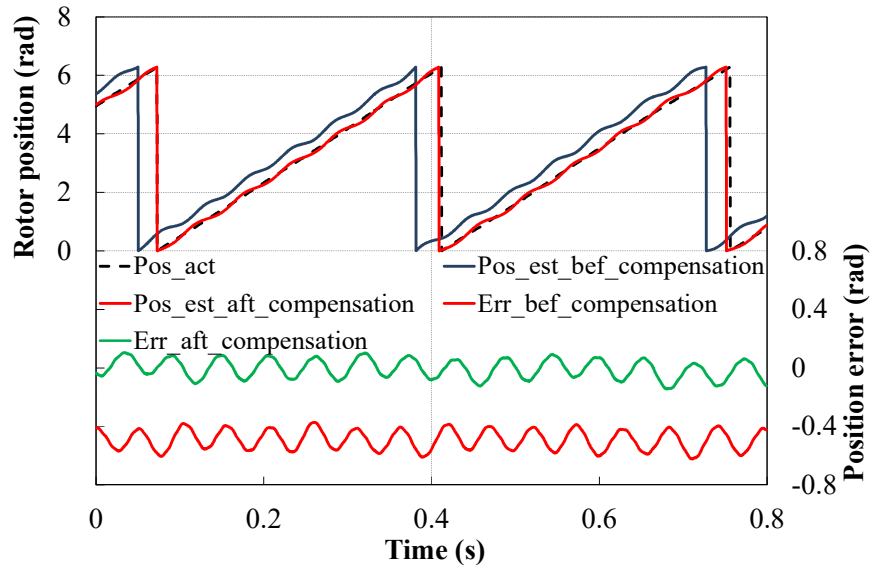
Fig. 4.14 Position estimation with and without compensation of cross-coupling effects in the steady state (rated load).
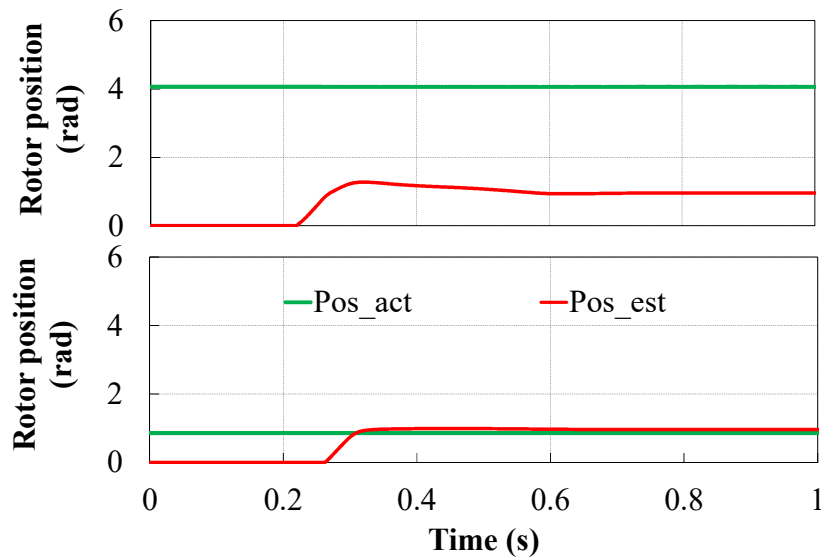
Fig. 4.15 Initial rotor position estimation with proposed carrier injection method with zero sequence voltage sensing (top-4 rad, bottom-0.86 rad)
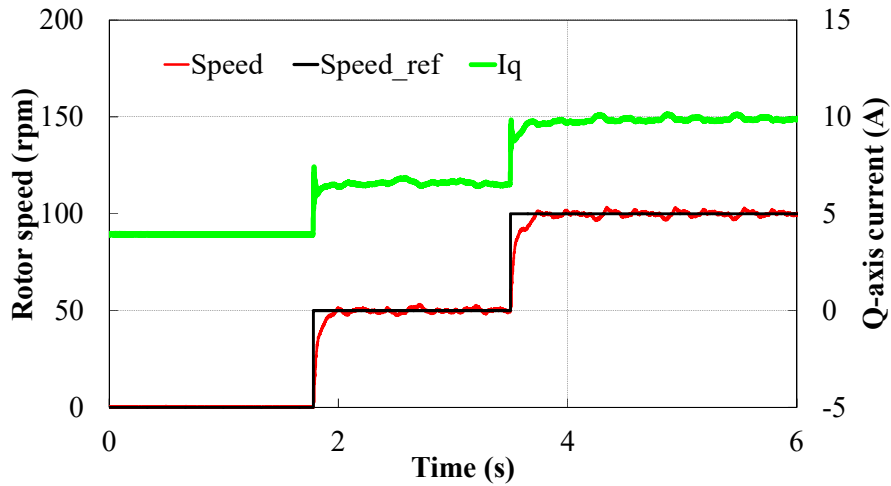
(a) Rotor speed and q-axis current
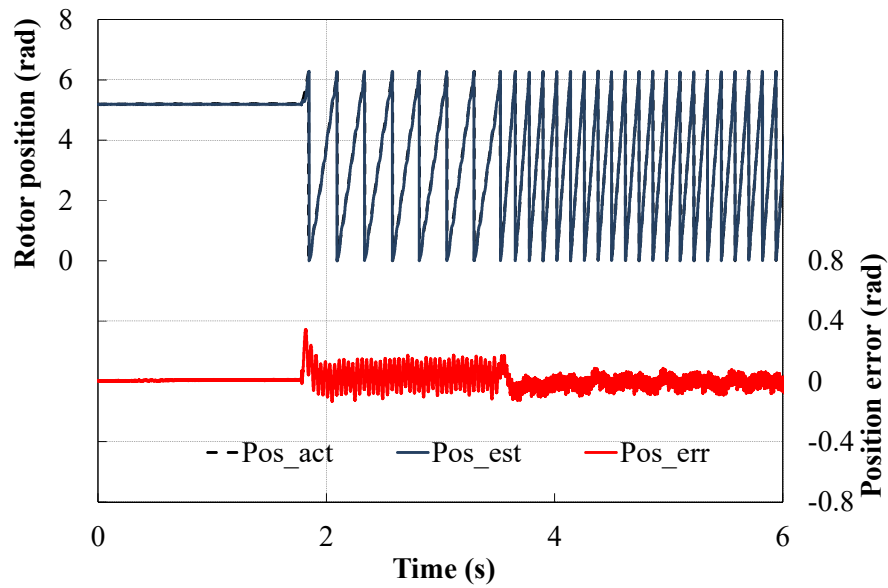
(b) Rotor position estimation

Fig. 4.16 Dynamic position estimation performances under step-speed condition.

The step load test is also implemented on the prototype machine with proposed injection method as shown in Fig. 4.17. Good position tracking performances are observed when q-axis current is rapidly increased from 0.3 A to 10 A. Therefore, it can be concluded that the proposed injection method presents good dynamic performances at various speed and load conditions.
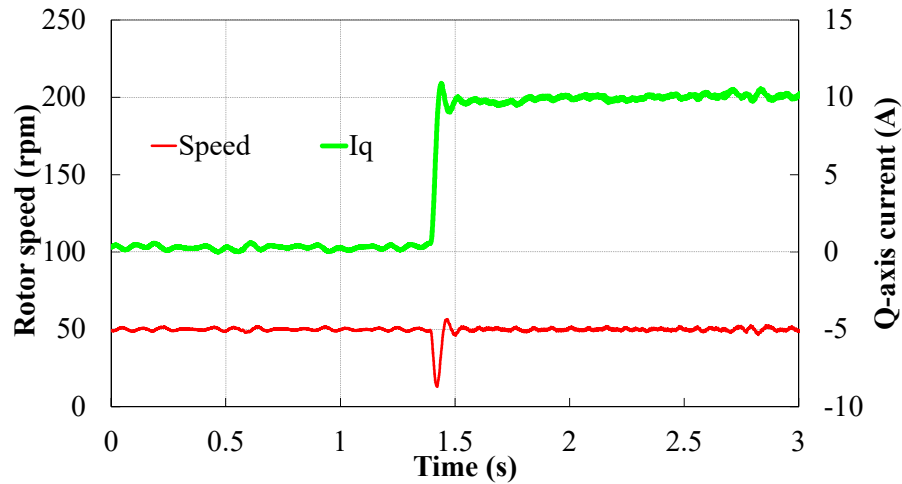
(a) Rotor speed and q-axis current
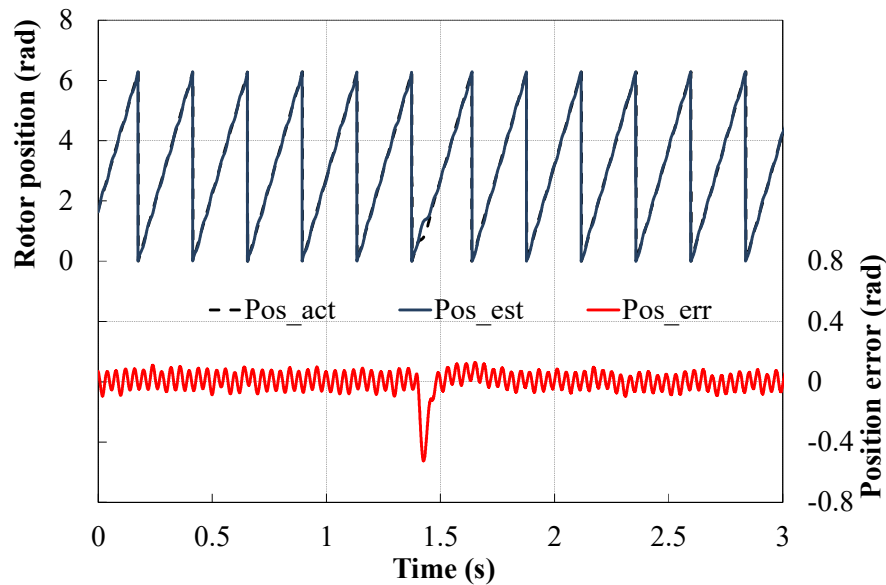
(b) Rotor position estimation

Fig. 4.17 Dynamic position estimation performances under step-load condition.

4.4.3 Robustness and accuracy compared to conventional signal injection methods

To further verify the robustness and accuracy of the proposed signal injection method, the conventional injection methods (i.e., rotating and conventional pulsating injections) with zero sequence voltage sensing are also performed and compared to the proposed method. Specifically, the sensitivity to the injection frequency and the cut-off frequency of low pass filter (LPF) for signal demodulation are compared for the three injection methods,

respectively. The comparative conditions for the three injection methods are listed in Table 4.2.

Fig. 4.18 illustrates the position errors for three carriers with carrier injection frequencies ranging from 300 to 1000 Hz while the cut-off frequency of LPF is kept the same as 60 Hz. It can be seen that position errors for rotating and conventional pulsating injection have shown strong sensitivity with the injection frequency. This is due to the signal processing delays (PWM updating delay) introduces additional phase shifts in the carrier responses as discussed above. While for the proposed signal injection method, it demonstrates great robustness due to the amplitude-modulation by saliency as analysed above.

Similarly, as shown in Fig. 4.19, at the same injection frequency 800 Hz, the position estimation errors of rotating injection are observed to vary with the cut-off frequency of LPF. This is due to that the rotor angular frequency causes the phase shifts of saliency position when being processed through LPF. In contrast, the conventional and proposed pulsating injection methods are not sensitive to cut-off frequency of LPF. However, it is clearly observed that the proposed injection method is of higher accuracy. Thus, compared to conventional injection methods, the proposed injection method utilising zero sequence voltage is more advantageous as expected.
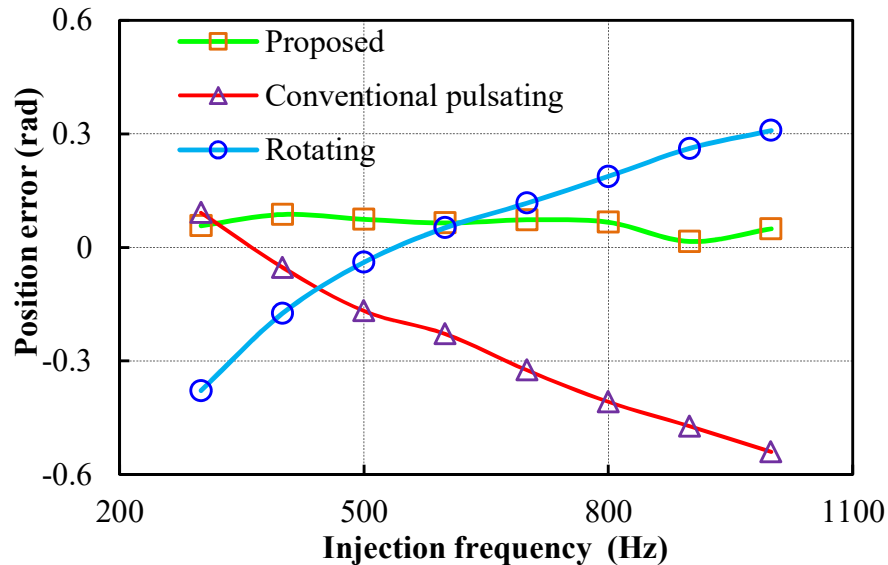
Fig. 4.18 Position errors with sensitivity to injection frequency.
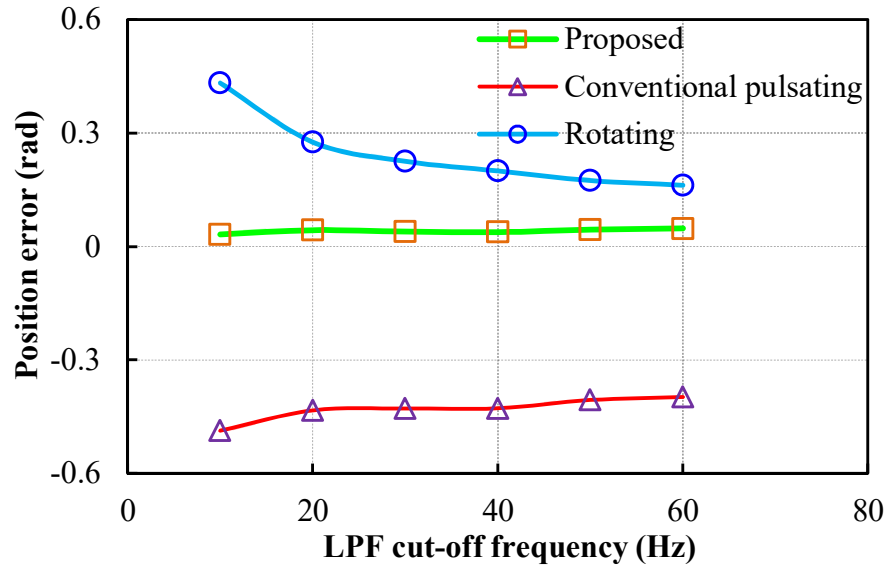
Fig. 4.19 Position errors with sensitivity to cut-off frequency of LPF.

Table 4.2 Comparison Condition for the Three Injection Methods

	Method	Carrier signal	LPF	Position Observer	
				K_p	K_i
Fig. 4.18	Rotating	4V (0.3-1kHz)	60Hz	400	1000
	Conventional pulsating		60Hz	400	1000
	Proposed		60Hz	400	1000
Fig. 4.19	Rotating	4V/800 Hz	10-60 Hz	400	1000
	Conventional pulsating			400	1000
	Proposed			400	1000

4.5   Conclusions

In this chapter, a novel pulsating signal injection strategy utilising zero sequence carrier voltage is proposed for sensorless control of PMSMs. The carrier signal is injected on the estimated reference frame, anti-rotating at twice the rotor's estimated electrical angular speed. It is found that compared to conventional zero sequence voltage sensing based injection methods, the proposed strategy is simpler for signal processing and less sensitive to the signal processing delays.

Thus, it can be concluded that the proposed method is of high bandwidth and stability due to the use of zero sequence carrier voltage and of high accuracy and fast dynamic response due to pulsating injection. Furthermore, the cross-coupling effects due to magnetic saturation for zero sequence voltage based sensorless control are investigated and compensated. All theoretical analyses have been verified by experimental results on a prototype PM machine in both steady and dynamic conditions.

5 Novel Square-Wave Signal Injection Method Using Zero Sequence Voltage for Sensorless Control of Permanent Magnet Synchronous Machines

5.1 Introduction

In the previous chapter 4, a novel sinusoidal-wave signal injection strategy is proposed utilising the zero sequence carrier voltage for sensorless control of PMSMs. Actually, for carrier signal injection methods, in terms of injected signal waveforms, they can be grouped into sinusoidal-wave [JAN95] [JAN03] and square-wave signal injection [YOO11] [HAM10] [YU13], respectively. Generally, the sinusoidal-wave signal injection strategy is easy and simple for implementation [JAN03]. However, due to the limited PWM switching frequency, the injection frequency cannot be too high, which makes the separation between fundamental and carrier signals very difficult, eventually resulting in limited system bandwidths [YOO11] [LIU14]. In contrast, the square-wave injection strategy can adopt higher injection frequency. This is due to that when the square-wave signal is discretised, only two points are required, while obviously much more points are needed in order to form the sinusoidal-wave signal. Accordingly the system bandwidths can be significantly enhanced because the low pass filters (LPFs) used for signal demodulation are completely eliminated [YOO11].

However, the conventional square-wave injection methods also have two main disadvantages, one of which is that the carrier injection voltage needs to be much higher with the increase of injection frequency to maintain the reasonable signal-to-noise (S/N) ratio [LEI08] [SUN11], while the carrier voltage is restricted to the dc-bus voltage available for control [BRI01] [SUN11]. This may severely challenge the application of the square-wave injection strategy to some specific applications, e.g., the low bus voltage electro-mobiles, etc. In order to reduce the injection voltage for square-wave injection strategy, in [KWO15], additional capacitor is added to the inverter output to suppress the inverter nonlinearity effects, which however may increase the switching losses [KWO15]. Besides, in [KIM16], the injected voltage magnitude is regulated to suppress the induced HF current ripples, and accordingly under the constraint of the same RMS value of the current ripple, the average injection voltage is reduced. However, compared to the conventional square-wave strategy with fixed injection amplitude [YOO11], additional current ripple regulator is required to adjust the injection magnitude [KIM16], which results in increased implementation

complexity.

The other disadvantage for the existing square-wave injection methods is that generally the resultant carrier responses used for rotor position estimation require the differentiation processing (i.e., $\Delta i/\Delta t$) [YOO11] [LEI08] [LIU14c], which however increases the signal demodulation complexity compared to the conventional sinusoidal signal injection methods [JAN03] [RAC08c]. Besides, it is also noted that the differentiation of the carrier current signals is sensitive to current measurement noises, and consequently may result in low S/N ratio [XIE16].

On the other hand, for carrier signal injection methods, the zero sequence carrier voltage also contains rotor position information [BRI05], as described in chapter 4. Since the zero sequence voltage amplitude is not related to the injection frequency, higher injection voltage is not required with the increase of injection frequency. Furthermore, the zero sequence carrier voltage is less sensitive to injection distortions from the inverter nonlinear behaviours, current regulators, and etc., leading to enhanced position estimation performances [GAR07]. Therefore, it is expected that if the square-wave injection method uses the zero sequence carrier voltage sensing rather than the carrier current, the resultant position estimation performances may be further improved. However, for the conventional square injection methods in the stationary or estimated synchronous reference frame, the resultant zero sequence carrier voltage responses deteriorate the position estimation performances as will be shown theoretically and experimentally in this chapter.

Therefore, a novel square-wave carrier signal injection strategy using zero sequence carrier voltage for sensorless control of PMSMs is proposed in this chapter. Different from the conventional square-wave injection methods employed in the stationary and estimated synchronous reference frame, the proposed method will be injected on the estimated reference frame anti-rotating at twice estimated rotor electrical angular speed (i.e., the sinusoidal-wave injection strategy in the previous chapter is further applied to the square-wave injection in this chapter). It will be shown that compared to the conventional square-wave methods, the proposed strategy using zero sequence voltage has two main advantages, one of which is that the carrier response amplitude is not related to the injection frequency, i.e., higher injection voltage is not required. The other is that the carrier response does not need signal differentiation processing, which significantly simplifies the signal demodulation process and moreover increases the position estimation robustness. Finally, experimental

results confirm all the theoretical analyses on a prototype PM machine.

The major new results of this chapter have been published in [XU16c].

5.2 Conventional Square-Wave Injection Methods

5.2.1 Carrier current responses

The conventional square-wave injection methods for sensorless control of PM machines [YOO11] [LIU14c] are employed in the stationary and estimated synchronous reference frames, Fig. 5.1-Fig. 5.2, both based on carrier current sampling. In Fig. 5.1-Fig. 5.2, it is noted that that the actual d-axis in the synchronous reference frame aligns exactly with the magnetic north-pole.

According to [YOO11] [LIU14c], the carrier current responses can be described as

$$\begin{bmatrix} \Delta i_{\alpha h} \\ \Delta i_{\beta h} \end{bmatrix} = U\Delta T \begin{bmatrix} \dfrac{\cos(\theta_e)\cos(\Delta\theta)}{L_{dh}} + \dfrac{\sin(\theta_e)\sin(\Delta\theta)}{L_{qh}} \\ \dfrac{\sin(\theta_e)\cos(\Delta\theta)}{L_{dh}} - \dfrac{\cos(\theta_e)\sin(\Delta\theta)}{L_{qh}} \end{bmatrix} \tag{5.1}$$

for the square-wave injection in the estimated synchronous reference frame, and

$$\begin{bmatrix} \Delta i_{\alpha h} \\ \Delta i_{\beta h} \end{bmatrix} = U\Delta T \begin{bmatrix} \dfrac{L_{dh}+L_{qh}}{2L_{dh}L_{qh}} + \dfrac{-L_{dh}+L_{qh}}{2L_{dh}L_{qh}}\cos(2\theta_e) \\ \dfrac{-L_{dh}+L_{qh}}{2L_{dh}L_{qh}}\sin(2\theta_e) \end{bmatrix} \tag{5.2}$$

for the square-wave injection in the stationary reference frame, respectively, where U is the carrier voltage, $i_{\alpha h}$ and $i_{\beta h}$ are the carrier currents in the stationary reference frame, L_{dh} and L_{qh} are the incremental d- and q-axis self-inductances, ΔT is the sampling interval, respectively. From (5.1)-(5.2), it can be seen that both carrier current responses require differentiation processing, i.e., $\Delta i_{\alpha h}$ and $\Delta i_{\beta h}$, which is sensitive to the current measurement noises [XIE16]. Moreover, since ΔT is very small at higher injection frequency, the signal amplitudes in (5.1)-(5.2) are very small, easily affected by nonlinear parasitic effects [KWO15] [KIM16]. Accordingly, the injection voltage should be increased to maintain the reasonable S/N ratio for A/D sampling, which may conflict with the available voltage for the control [BRI01] [LIU14c].

In contrast, the zero sequence voltage for carrier injection methods is found to have less injection distortions, larger S/N ratio, and moreover the signal amplitude is not related to the injection frequency, leading to increased available voltage for control and enhanced system bandwidths and stability [BRI05] [GAR07]. Therefore, if the above square-wave injection strategies use zero sequence carrier voltage sensing rather than the carrier current sampling, the position estimation performances may be further enhanced. However, unfortunately, both the zero sequence carrier voltage responses for the two injection methods degrade the rotor position estimation performances, which will be analysed in detail as follows.
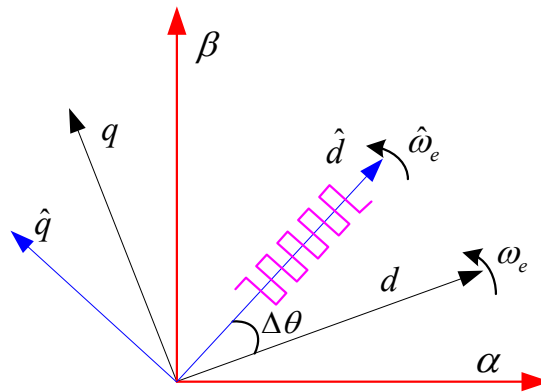
Fig. 5.1 Pulsating square-wave signal injection in the estimated synchronous reference frame.
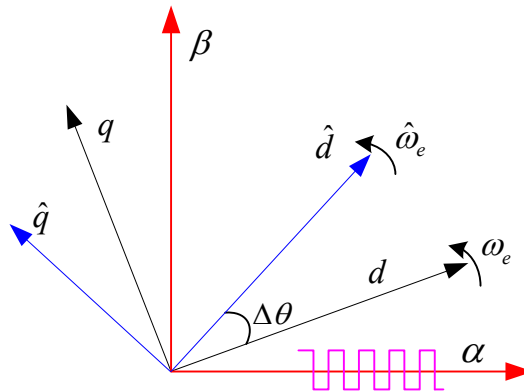
Fig. 5.2 Pulsating square-wave signal injection in the stationary reference frame.

5.2.2 Zero sequence voltage responses

Firslty, for the square-wave pulsating injection (Fig. 5.3) in the estimated synchronous reference frame, the injected signals are expressed as [YOO11]

$$
\begin{bmatrix} \hat{U}_d \\ \hat{U}_q \end{bmatrix} = \begin{cases} \begin{bmatrix} U \\ 0 \end{bmatrix} & \textit{half duty} \\ \begin{bmatrix} -U \\ 0 \end{bmatrix} & \textit{otherwise} \end{cases}
\tag{5.3}
$$

where U is the carrier voltage. Considering the Fourier series of a square-wave signal, (5.3) can be further expressed as

$$
\hat{U}_d = \frac{4}{\pi} U \sum_{k=1} \frac{1}{2k-1} \cos k\omega_h t
$$
$$
\hat{U}_q = 0
\tag{5.4}
$$

Then, with the coordinate transformation, from Fig. 5.1, the three phase injection voltages can be described as

$$
U_{AO} = \frac{4}{\pi} U \cos(\hat{\theta}_e) \sum_{k=1} \frac{1}{2k-1} \cos k\omega_h t
$$
$$
U_{BO} = \frac{4}{\pi} U \cos(\hat{\theta}_e - \frac{2}{3}\pi) \sum_{k=1} \frac{1}{2k-1} \cos k\omega_h t
$$
$$
U_{CO} = \frac{4}{\pi} U \cos(\hat{\theta}_e + \frac{2}{3}\pi) \sum_{k=1} \frac{1}{2k-1} \cos k\omega_h t
\tag{5.5}
$$

Then, based on (4.1)-(4.3), (4.5)-(4.7), (4.9), and (5.3)-(5.5) the zero sequence carrier voltage U_{RN} as shown in Fig. 4.3Fig. 4.1 can be obtained as

$$
U_{RN} = \frac{2}{\pi} \frac{U(L_0 - M_0)(L_2 - M_2)\cos(2\theta_e + \hat{\theta}_e)}{(L_0 - M_0)^2 - (\frac{L_2}{2} + M_2)^2} \sum_{k=1} \frac{1}{2k-1} \cos k\omega_h t
\tag{5.6}
$$

It is very interesting to see from (5.6) that the zero sequence carrier response for square-wave injection is still modulated by the square-wave signal, while the carrier current is modulated by the triangular wave signal [YOO11] [YOO14] [KIM16] [LIU14c]. Consequently, the signal differentiation calculation required in the current-sensing based square-wave injection methods is not needed for the zero sequence voltage sensing based methods, leading to much simpler demodulation process and robustness.
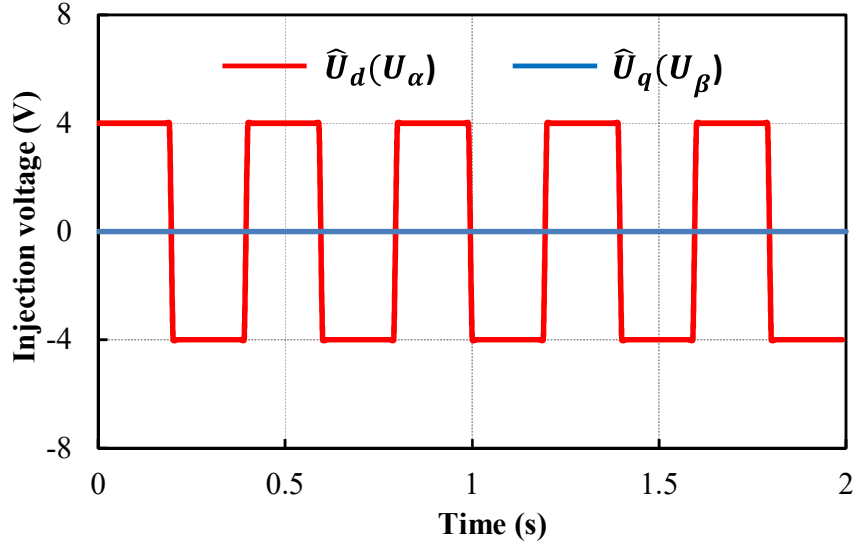
Fig. 5.3 Injected square-wave carrier voltage at 4 V/2.5 kHz.

Moreover, compared to (5.1)-(5.2) where the signal amplitude is inversely proportional to the injection frequency [YOO11] [LIU14c], the zero sequence carrier voltage amplitude in (5.6) is not related to the injection frequency. Therefore, with the increase of injection frequency, higher injection voltage is not required, and consequently the voltage margin issues for the square wave injection methods can be easily met for the zero sequence voltage sensing strategy.

However, as aforementioned, the zero sequence voltage in (5.6) for the conventional pulsating square-wave signal injection method deteriorates the position estimation performance. To be more specific, from (5.6), the corresponding signal demodulation is expressed as

$$U_{RN\_d} = U_{RN} \cdot \frac{\hat{U}_d}{U} \cdot (-\sin(3\hat{\theta}_e)) = \frac{1}{\pi} \frac{U(L_0 - M_0)(L_2 - M_2)}{(L_0 - M_0)^2 - (\frac{L_2}{2} + M_2)^2} (\sin(2\Delta\theta) - \sin(2\theta_e + 4\hat{\theta}_e)) \qquad (5.7)$$

From (5.7), it can be seen that the additional 6th harmonic (i.e. $\sin(2\theta_e + 4\hat{\theta}_e)$) having the same amplitude with the term of '$\sin(2\Delta\theta)$' exists, which can severely affect the position estimation performance as shown in Fig. 5.4. Large oscillation errors can be observed, and it is very difficult to suppress these errors from the disturbance of the 6th harmonics in (5.7).

On the other hand, for the conventional square-wave injection strategy employed in the stationary reference frame [LIU14] in Fig. 5.2, the injected signals can be expressed as

$$U_\alpha = \frac{4}{\pi} U \sum_{k=1} \frac{1}{2k-1} \cos k\omega_h t \tag{5.8}$$

$$U_\beta = 0$$

Accordingly, the three phase carrier voltage can be easily obtained as

$$U_{AO} = \frac{4}{\pi} U \sum_{k=1} \frac{1}{2k-1} \cos k\omega_h t$$

$$U_{BO} = -\frac{2}{\pi} U \sum_{k=1} \frac{1}{2k-1} \cos k\omega_h t \tag{5.9}$$

$$U_{CO} = -\frac{2}{\pi} U \sum_{k=1} \frac{1}{2k-1} \cos k\omega_h t$$

Similarly, with (4.1)-(4.3), (4.5)-(4.7), (4.9) and (5.9), the resultant zero sequence voltage can be calculated as

$$U_{RN} \approx \frac{2}{\pi} \frac{U(L_0-M_0)(L_2-M_2)\cos(2\theta_e)}{(L_0-M_0)^2 - (\frac{L_2}{2}+M_2)^2} \sum_{k=1} \frac{1}{2k-1} \cos k\omega_h t \tag{5.10}$$

Then, similar to (5.10), the corresponding signal demodulation is expressed as

$$U_{RN\_d} = U_{RN} \cdot \frac{U_\alpha}{U} \cdot (-\sin(2\hat{\theta}_e)) = \frac{1}{\pi} \frac{U(L_0-M_0)(L_2-M_2)}{(L_0-M_0)^2 - (\frac{L_2}{2}+M_2)^2} (\sin(2\Delta\theta) - \sin(2\theta_e+2\hat{\theta}_e)) \tag{5.11}$$

From (5.11), it can be seen that the undesirable 4th harmonic having the same amplitude with 'sin(2Δθ)' arises in the zero sequence carrier response, which also gives rise to larger oscillating errors as shown in Fig. 5.5.

From the above analyses, although the zero sequence carrier responses are simpler for signal demodulation and can easily ensure the voltage margin issues, the resultant estimated position errors for the square-wave injections in the estimated synchronous and stationary reference frame are intolerable. Therefore, in this chapter, to utilise the synergies of both zero sequence voltage sensing and square-wave injection, a novel pulsating injection method with zero sequence voltage sensing will be proposed as follows.
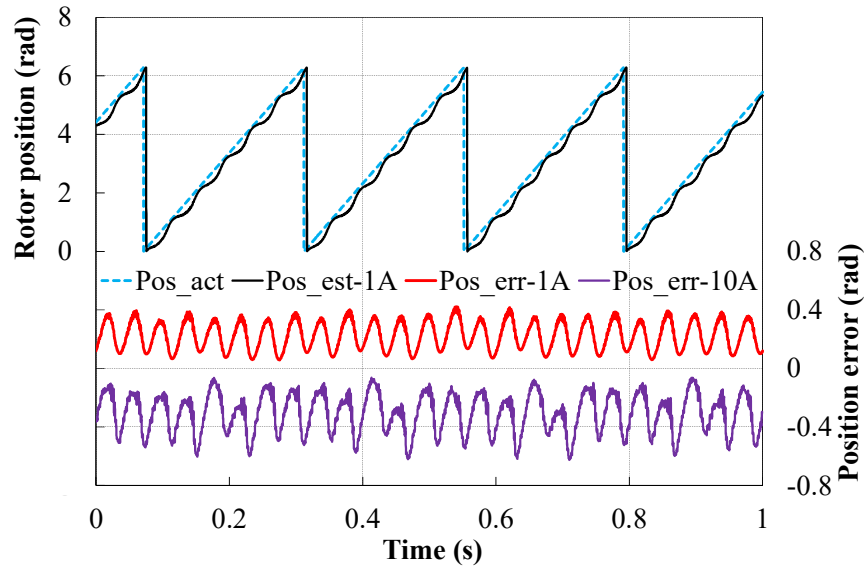
Fig. 5.4 Position estimation with 4 V/2.5 kHz square-wave injection for conventional pulsating injection in the estimated synchronous reference frame.
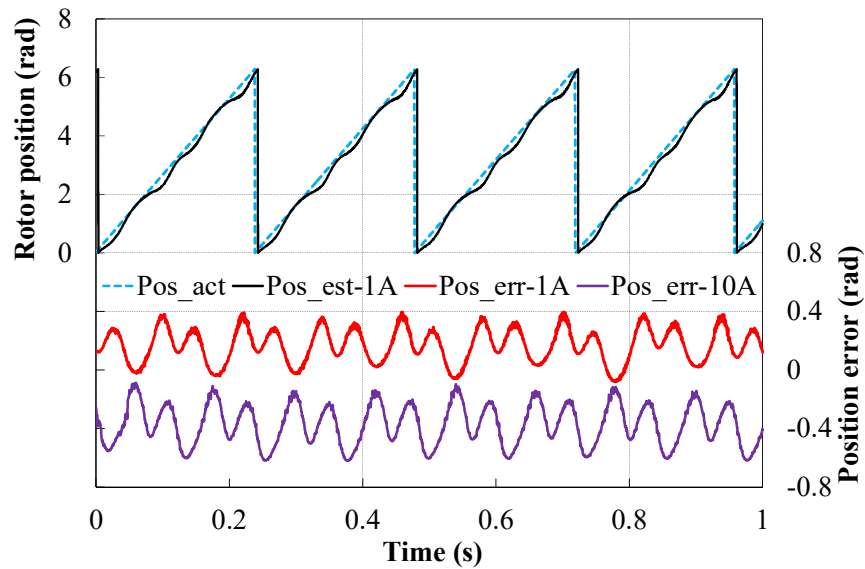
Fig. 5.5 Position estimation with 4 V/2.5 kHz square-wave injection for conventional pulsating injection in the stationary reference frame.

5.3 Proposed Novel Square-Wave Injection Method

5.3.1 Improved zero sequence carrier voltage response

As aforementioned, the conventional square-wave injection methods with zero sequence voltage sensing deteriorate the rotor position estimation performances due to the undesirable

harmonic disturbances. In order to improve the issue, in this chapter, a novel square-wave injection method with zero sequence voltage sensing is proposed as shown in Fig. 5.6. It can be seen that the injection strategy actually is exactly the same as that proposed in chapter 4, but with the different signal injection waveforms.

Specifically, from Fig. 5.6, the proposed square-wave injection is at the q_2-axis in the estimated reference frame, anti-rotating at twice the rotor's estimated electrical speed. Accordingly, the injected signal can be expressed as

$$
\begin{aligned}
\hat{U}_{2d} &= 0 \\
\hat{U}_{2q} &= \frac{4}{\pi} U \sum_{k=1} \frac{1}{2k-1} \cos k\omega_h t
\end{aligned}
\tag{5.12}
$$

Then, by coordinate transformation, the actual injected phase voltages can be expressed as

$$
\begin{aligned}
U_{AO} &= \frac{4}{\pi} U \sum_{k=1} \frac{1}{2k-1} \cos k\omega_h t \sin(2\hat{\theta}_e) \\
U_{BO} &= \frac{4}{\pi} U \sum_{k=1} \frac{1}{2k-1} \cos k\omega_h t \sin(2\hat{\theta}_e + \frac{2}{3}\pi) \\
U_{CO} &= \frac{4}{\pi} U \sum_{k=1} \frac{1}{2k-1} \cos k\omega_h t \sin(2\hat{\theta}_e - \frac{2}{3}\pi)
\end{aligned}
\tag{5.13}
$$

Similarly, with (4.1)-(4.3), (4.5)-(4.7), (4.9) and (5.13), the zero sequence carrier voltage for the proposed injection strategy can be derived as

$$
\begin{aligned}
U_{RN} &= \frac{4}{\pi} [V_{o1} \sin(2\Delta\theta) - V_{o2} \sin(4\hat{\theta}_e + 2\hat{\theta}_e)] \sum_{k=1} \frac{1}{2k-1} \cos k\omega_h t \\
V_{o1} &= \frac{U}{2} \frac{(L_0 - M_0)}{(L_0 - M_0)^2 - (\frac{L_2}{2} + M_2)^2} (L_2 - M_2) \\
V_{o2} &= \frac{U}{4} \frac{(L_2 - 2M_2)}{(L_0 - M_0)^2 - (\frac{L_2}{2} + M_2)^2} (L_2 - M_2)
\end{aligned}
\tag{5.14}
$$
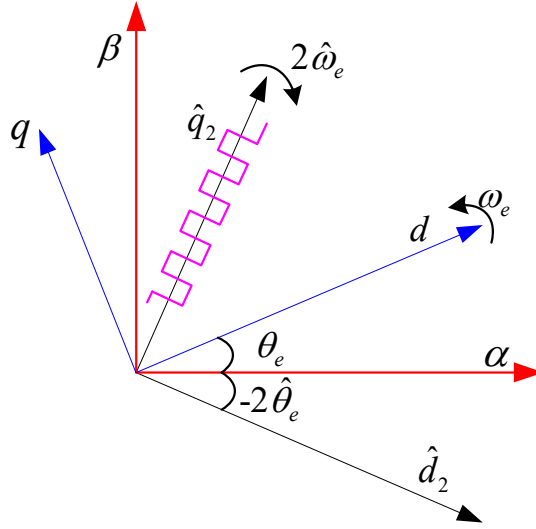
Fig. 5.6 Proposed novel square-wave signal injection.

Then, because typically (L_0-M_0) is much larger than (L_2-2M_2), the first term of (5.14) has much larger amplitude [BRI05] and therefore will be utilised for the position estimation, i.e.,

$$U_{RN} = \frac{2}{\pi} \frac{U(L_0-M_0)(L_2-M_2)\sin(2\Delta\theta)}{(L_0-M_0)^2-(\frac{L_2}{2}+M_2)^2} \sum_{k=1} \frac{1}{2k-1} \cos k\omega_h t \qquad (5.15)$$

Then, by further signal demodulation, (5.15) becomes

$$U_{RN\_d} = U_{RN} \cdot \frac{\hat{U}_{2q}}{U} = \frac{2}{\pi} \frac{U(L_0-M_0)(L_2-M_2)}{(L_0-M_0)^2-(\frac{L_2}{2}+M_2)^2} \sin(2\Delta\theta) \qquad (5.16)$$

From (5.16), it can be seen that the zero sequence carrier signal responses for the proposed method is amplitude-modulated by machine saliency, leading to higher estimation accuracy [RAC08c]. Besides, compared to the conventional square-wave injections on the estimated synchronous and stationary reference frame in (5.7) and (5.11), the undesirable disturbance components (e.g., the 4th harmonic for the stationary pulsating injection in (5.11)) do not exist for the proposed injection method. Thus, it is expected that the position estimation accuracy will be greatly enhanced.

Furthermore, from (5.15)-(5.16), it can be seen that the zero sequence carrier voltage for the proposed method also keeps the advantages of the conventional square-wave injection methods. Firstly, the signal response is also modulated by the square waveform, and

accordingly the signal differentiation for rotor position estimation is not required. Consequently, the signal demodulation process is also much simpler, Fig. 5.7, where the conventional current sensing method in [YOO11] is also illustrated for the clear comparison. Secondly, the zero sequence voltage for the proposed method is also not related to the injection frequency, i.e., higher injection voltage is not required with the increased injection frequency, resulting in reduced noises, increased available voltage for control, etc.
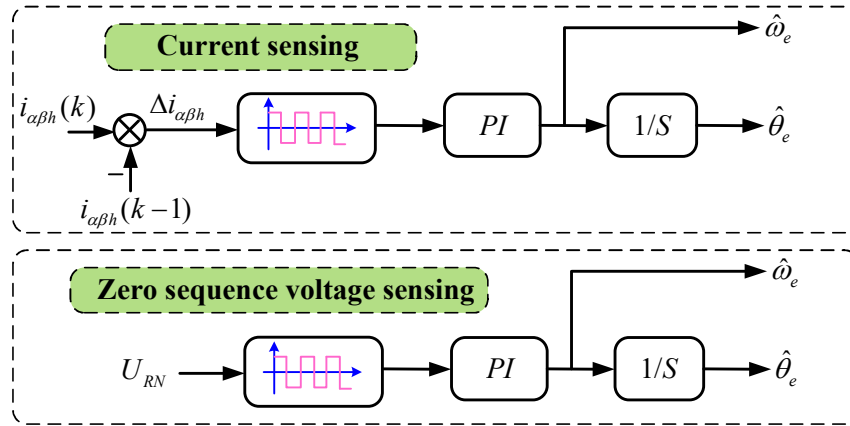
Fig. 5.7 Carrier signal demodulation for conventional and proposed square wave injection methods.

Thus, it is expected that the proposed method can perfectly combine both the synergies of square-wave pulsating injection and zero sequence voltage sensing, i.e., high accuracy and bandwidths, increased voltage margin, great dynamic response and robustness, etc. as will be verified experimentally.

5.3.2 Cross-coupling magnetic saturation effects

Furthermore, the cross-coupling magnetic saturation effects [GUG06] [LI09] [REI08] for the proposed square-wave injection strategy using zero sequence voltage are also investigated in this part. By considering the saturation effects, phase inductances can be expressed as [YAN06]

$$\begin{cases} L_{aa} = L_0 - L_2 \cos\left(2\theta_e\right) - L_c \sin(2\theta_e) \\ L_{bb} = L_0 - L_2 \cos\left(2\theta_e + \frac{2}{3}\pi\right) - L_c \sin(2\theta_e + \frac{2}{3}\pi) \\ L_{cc} = L_0 - L_2 \cos(2\theta_e - \frac{2}{3}\pi) - L_c \sin(2\theta_e - \frac{2}{3}\pi) \end{cases} \tag{5.17}$$

$$\begin{cases} M_{ab} = M_{ba} = M_0 - M_2 \cos\left(2\theta_e - \frac{2}{3}\pi\right) - M_c \sin(2\theta_e - \frac{2}{3}\pi) \\ M_{bc} = M_{cb} = M_0 - M_2 \cos\left(2\theta_e\right) - M_c \sin(2\theta_e) \\ M_{ca} = M_{ac} = M_0 - M_2 \cos\left(2\theta_e + \frac{2}{3}\pi\right) - M_c \sin(2\theta_e + \frac{2}{3}\pi) \end{cases} \tag{5.18}$$

where L_c and M_c presents the 2nd harmonic amplitude of sine inductance terms in the self- and mutual-inductances, respectively. Accordingly, for the proposed square-wave injection method, the zero sequence carrier voltage can be obtained as

$$U_{RN} = \frac{2}{\pi} \frac{U(L_0 - M_0)(L_s - M_s)\sin(2\Delta\theta + \theta_{s3})}{(L_0 - M_0)^2 - (\frac{L_s}{2} + M_s)^2} \sum_{k=1} \frac{1}{2k-1} \cos k\omega_h t \tag{5.19}$$

where θ_{s3} presents the phase shift of the zero sequence carrier voltage due to the cross-coupling effect and can be obtained as

$$\theta_{s3} = -\arctan\frac{L_c - M_c}{L_2 - M_2} \tag{5.20}$$

Therefore, the position error due to the cross-coupling effects is obtained as

$$\Delta\theta = \frac{1}{2}\arctan\frac{L_c - M_c}{L_2 - M_2} \tag{5.21}$$

Thus, from (4.29) in chapter 4 and (5.21), it is seen that actually the cross-coupling magnetic effects cause exactly the same position estimation errors regardless of signal injection waveforms. Accordingly, the offline measured cross-coupling correction angle in Fig. 4.10 can also be utilised for the online compensation for the proposed square-wave injection method.

5.4 Experimental Validation

The experiments are implemented on a dSPACE DS1006 platform to validate the proposed square-wave signal injection method on the prototype PM machine (the machine parameters are shown in Table 4.1 in chapter 4). The overall control diagram for the proposed square-wave injection method with zero sequence voltage sensing is shown in Fig. 5.8.
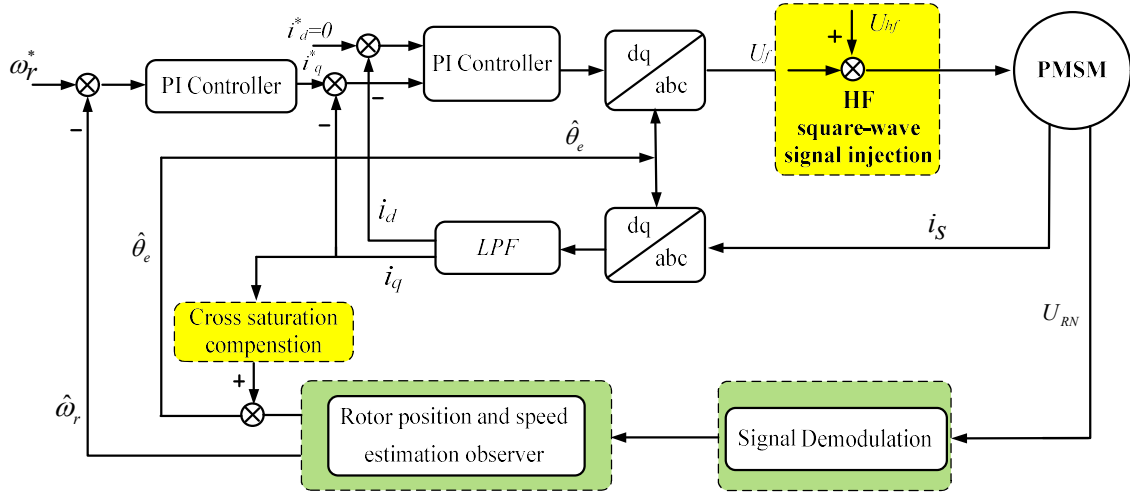
Fig. 5.8 Block diagram of overall control system with square-wave signal injection using zero sequence voltage.

5.4.1 Zero sequence voltage model verification

In order to simply verify all above analyses about the zero sequence voltages with conventional and proposed square-wave injection methods, Fig. 5.9 illustrates the measured zero sequence carrier voltage spectra (the injected square-wave signal is set as 4 V/1 kHz, and the fundamental frequency f_e is 2.5 Hz, and only the main harmonics are illustrated). It is noted that in order to maximise the zero sequence signal in (5.14) for the proposed injection strategy, the position error is set to $\pi/4$ with the assistance of position sensor. From Fig. 5.9, it is observed that the zero sequence voltage components with stationary injection [LIU14c] are mainly at f_h+2f_e and f_h-2f_e (402nd and 398th), while the conventional pulsating injection [YOO11] are primarily at $f_h\pm3fe$ (397th and 403rd), respectively. By comparison, for the proposed square-wave injection method, the frequency components f_h and $f_h\pm6f_e$ (400th and 394th/406th) exist as shown in Fig. 5.9. Hence, all the measured results agree well with the theoretical derivations in (5.6), (5.10) and (5.14), respectively. Besides, from the measured spectra in Fig. 5.9, obviously the proposed method is also much easier for signal processing

and has higher S/N ratio compared to other two methods.
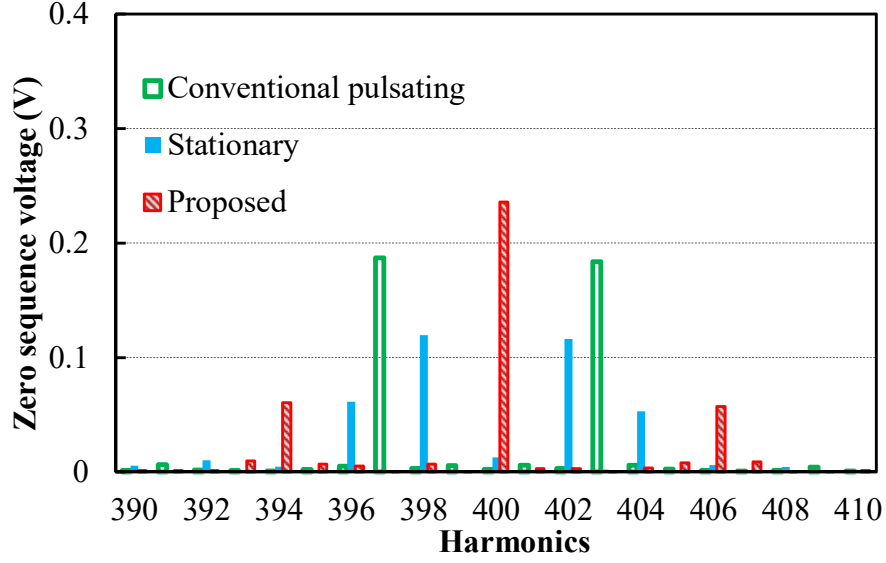
Fig. 5.9 Measured zero sequence carrier voltage with different square-wave injection methods.

Then, the spectra for the proposed square-wave injection method under different loads are also shown in Fig. 5.10. Considering the cross-coupling magnetic saturation effects, the position error in (5.19) is set as 0 and $\pi/4$ rad, respectively, with the assistance of position sensor, i.e.,

$$U_{RN} = \frac{2}{\pi} \frac{U(L_0 - M_0)(L_s - M_s)\cos(\theta_{s3})}{(L_0 - M_0)^2 - (\frac{L_s}{2} + M_s)^2} \sum_{k=1} \frac{1}{2k-1} \cos k\omega_h t \tag{5.22}$$

for $\Delta\theta = \pi/4$ rad, and

$$U_{RN} = \frac{2}{\pi} \frac{U(L_0 - M_0)(L_s - M_s)\sin(\theta_{s3})}{(L_0 - M_0)^2 - (\frac{L_s}{2} + M_s)^2} \sum_{k=1} \frac{1}{2k-1} \cos k\omega_h t \tag{5.23}$$

for $\Delta\theta = 0$ rad, respectively. Under no-load condition, since the cross-coupling angle θ_{s3} is quite small as shown in Fig. 4.10, the measured zero sequence voltage amplitude (400th) is maximised in (5.22), Fig. 5.10(a), while the amplitude in (5.23) is negligible, Fig. 5.10(b). In contrast, with the increase of load, particularly under rated load condition (I_q=10 A), due to the significantly increased cross-coupling angle θ_{s3}, the amplitude in (5.23) is even larger than that in (5.22), Fig. 5.10(a)-(b). This states that $\theta_{s3} > \pi/4$ according to (5.22)-(5.23) and

also agrees with the measured results in Fig. 4.10. Besides, it is also noted that under load conditions, the disturbance harmonics (e.g. 394th and 406th) in the zero sequence voltage only slightly increase, Fig. 5.10.
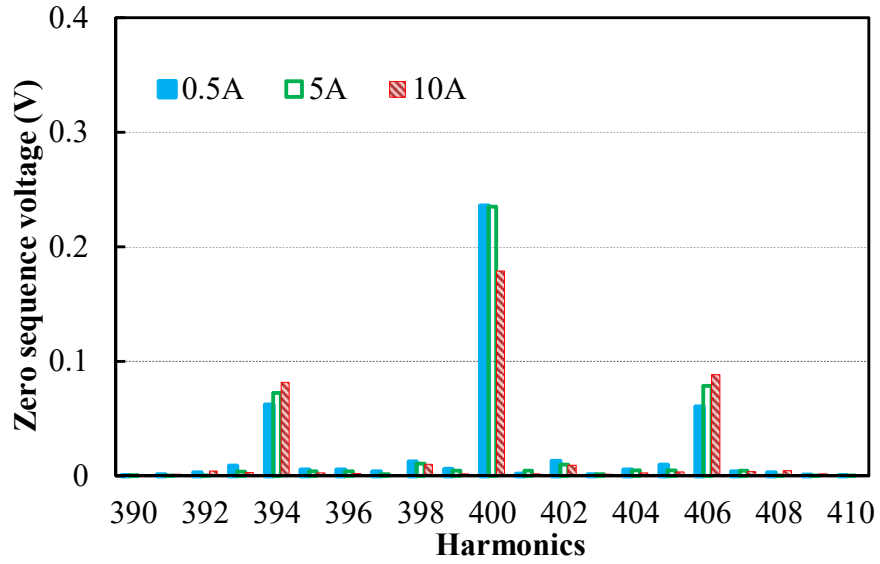
(a) $\Delta\theta=\pi/4$ rad
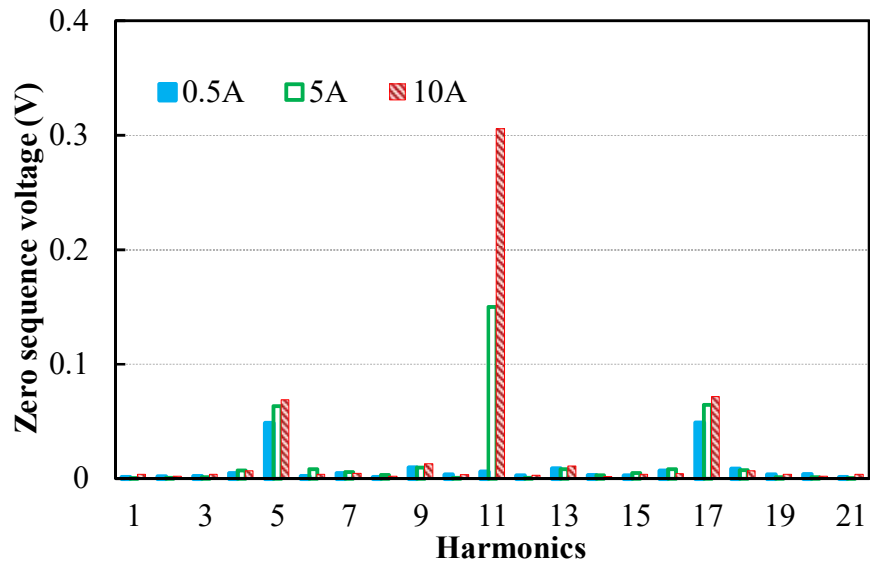
(b) $\Delta\theta=0$ rad

Fig. 5.10 Measured zero sequence carrier voltages for the proposed method under different load current conditions.

5.4.2 Steady- and dynamic-state position estimation performance

The steady-state position estimation performance with the proposed square-wave injection method is illustrated in Fig. 5.11. The q-axis current is set as 5 A, and the injection signal is set as 4 V/2.5 kHz. It can be observed that under load conditions, due to the cross-coupling effects, there exist dc position estimation errors. Then, with the compensation information from Fig. 4.10, the estimation accuracy is greatly improved as shown in Fig. 5.11.

The initial rotor position estimation with the proposed square-wave injection method is also performed and illustrated in Fig. 5.12. The injection signal is also set as 4 V/2.5 kHz, and the fundamental excitation is set as 0 A. It can be seen that when the rotor stops at 0.86 rad, the estimated rotor position can quickly reach ~0.9 rad showing fast tracking capability. However, it is also noted that when the rotor stops at 4 rad (i.e., (0.86 +π) rad), the estimated position is still ~0.9 rad. This is because the inherent machine saliency varies twice during one electrical period [GON13]. It should be noted that the magnetic polarity identification strategy will be specifically investigated in chapter 6.
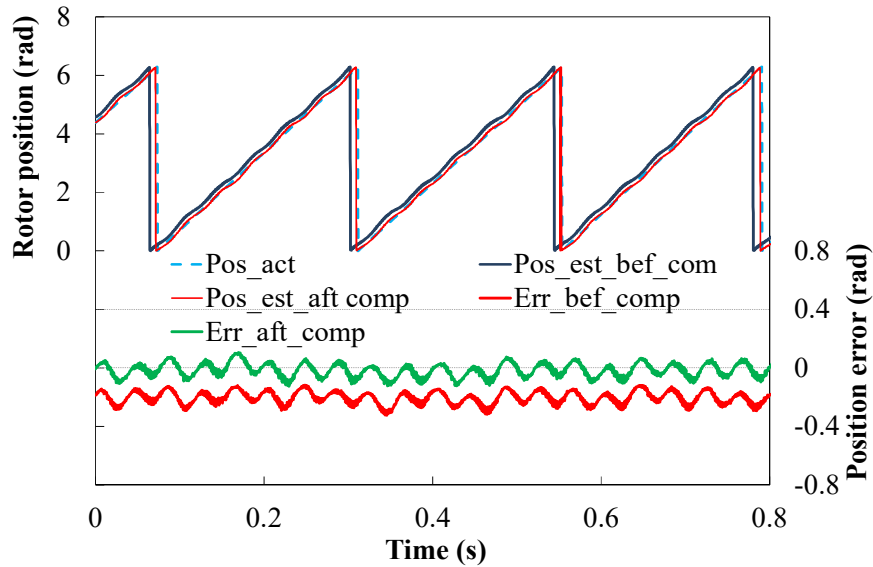
Fig. 5.11 Position estimation with and without compensation of cross-coupling effects in the steady state.
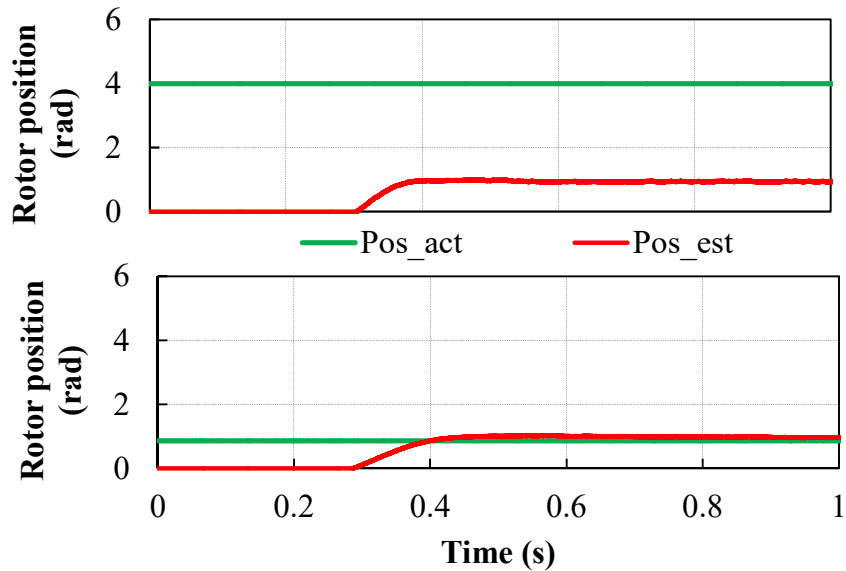
Fig. 5.12 Initial rotor position estimation with proposed carrier injection method with zero sequence voltage sensing (top-4 rad, bottom-0.86 rad).

The dynamic position estimation performance with proposed square-wave injection method is also shown in Fig. 5.13 in which the speed reference is given as 0-50-100 rpm. The injected carrier signals are the same with that in the steady-state conditions. The quick dynamic response can be observed and the overall position errors are small with cross-coupling effects compensation.

5.4.3 Comparison to conventional square-wave injection method with carrier current sensing [YOO11]

In this section, the conventional square-wave injection method with current sensing [YOO11] is also implemented to compare the position estimation performances with the proposed square-wave injection method, Fig. 5.14. Three injection conditions have been considered, i.e., 2.5 kHz/4 V and 2.5 kHz/8 V injection for the conventional square-wave injection method [YOO11], and 2.5 kHz/4 V injection for the proposed method. In order to clearly illustrate the position tracking capability, the estimated position is observed in the sensored mode to avoid losing synchronisation [KWO15]. As can be seen from Fig. 5.14, if the conventional method [YOO11] is performed with only 4 V injection voltage, the position estimation is apparently degraded as shown in Fig. 5.14(a), losing the position tracking capability during the transient process. Experimentally it is found that with around twice injection voltage, i.e., 8 V, the stable position estimation capability can then be ensured as

can be seen from Fig. 5.14(b) for the conventional injection method. In contrast, for the proposed injection method, with only 4 V injection voltage, the same stable position estimation performances (as the 8 V injection for the conventional method, Fig. 5.14(b)) can be obtained as illustrated in Fig. 5.14(c). Further, in the sensorless mode, with 2.5 kHz/8 V injection for the conventional method and 2.5 kHz/4 V injection for the proposed method, the step load tests for the two methods are also performed, as shown in Fig. 5.15-Fig. 5.16. It can be seen that both the two injection methods have shown good dynamic performances. Therefore, the available voltage margins for control, noise issues, etc. are significantly improved for the proposed square-wave injection method.
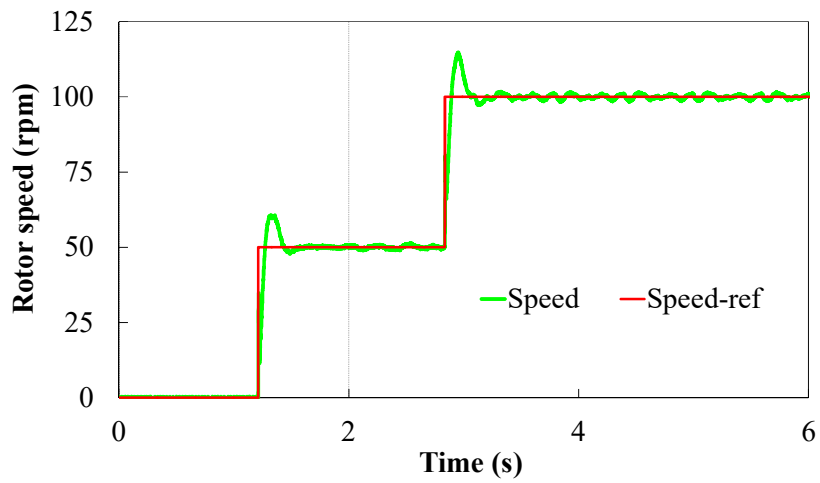
(a) Rotor speed
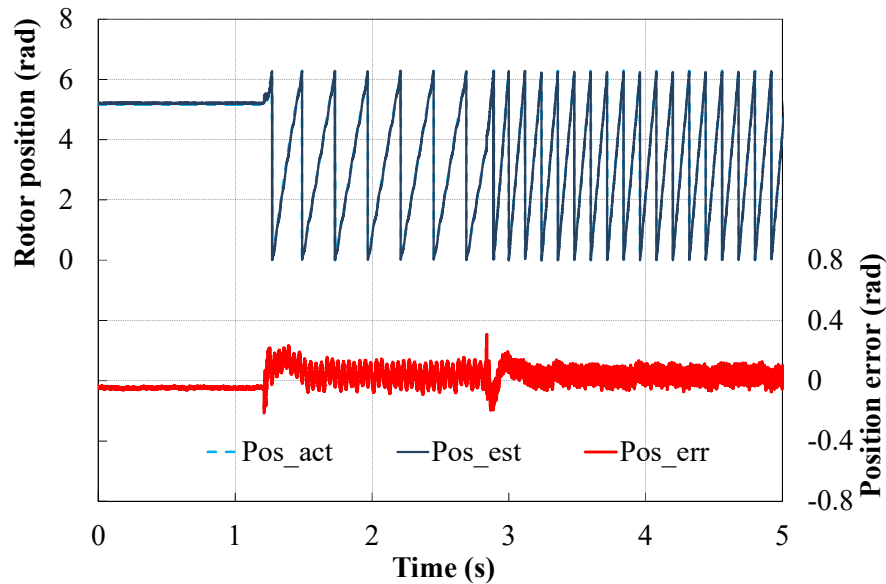
(b) Rotor position estimation

Fig. 5.13 Dynamic rotor position performance under step-speed condition.
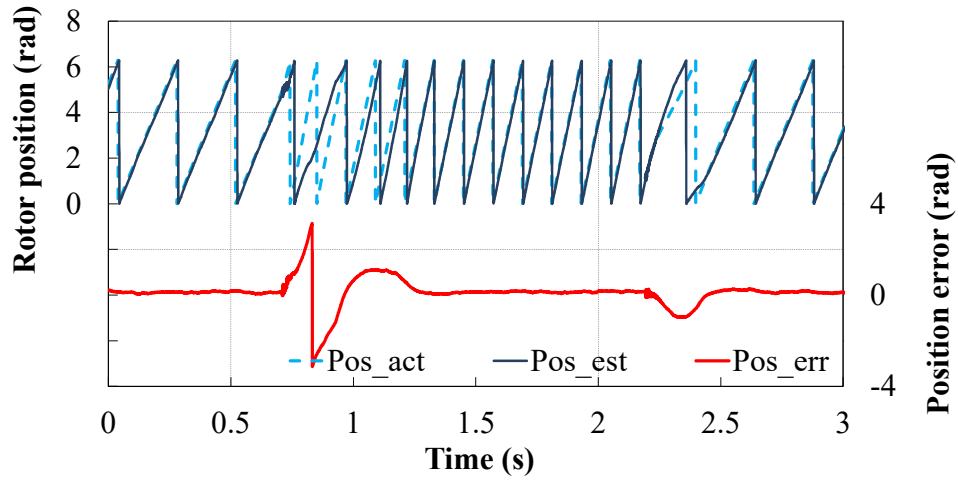
(a) 2.5 kHz/4 V injection-conventional pulsating injection method
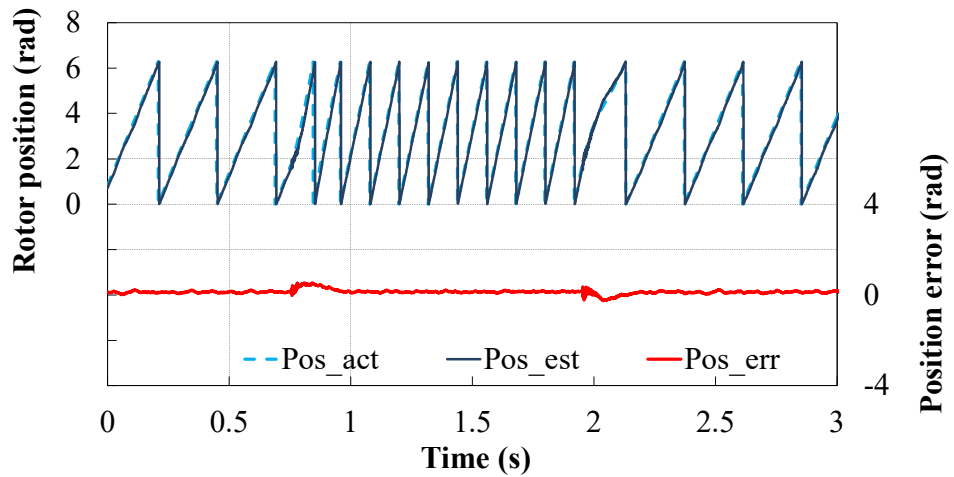
(b) 2.5 kHz/8 V injection-conventional pulsating injection method
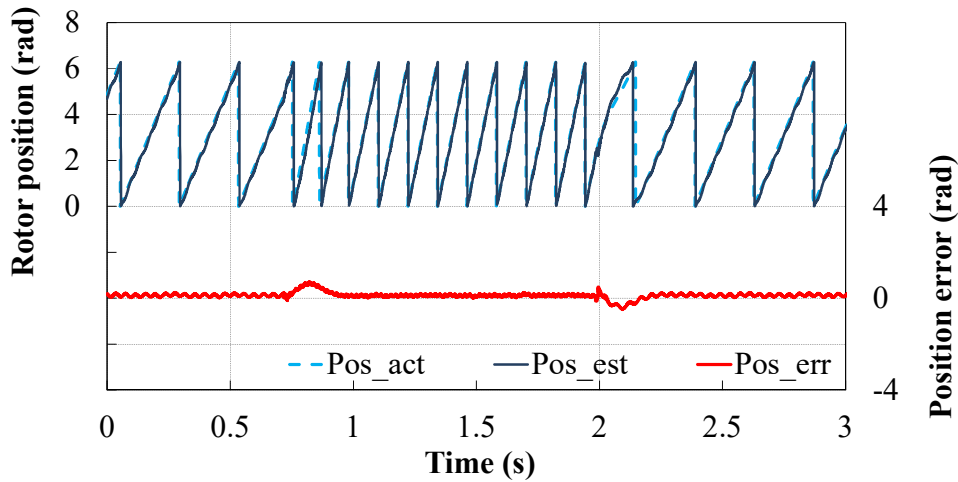
(c) 2.5 kHz/4 V injection-proposed injection method

Fig. 5.14 Observed estimated rotor position for the conventional and proposed pulsating injection methods.
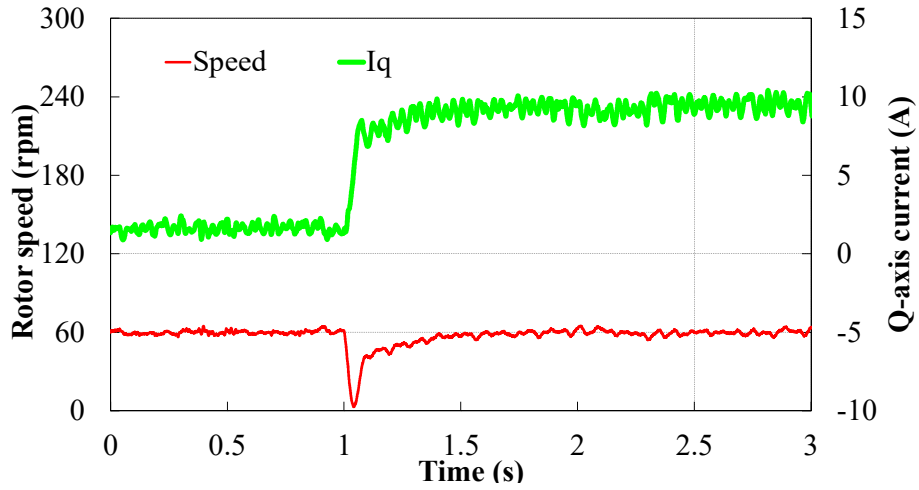
(a) Rotor speed and q-axis current
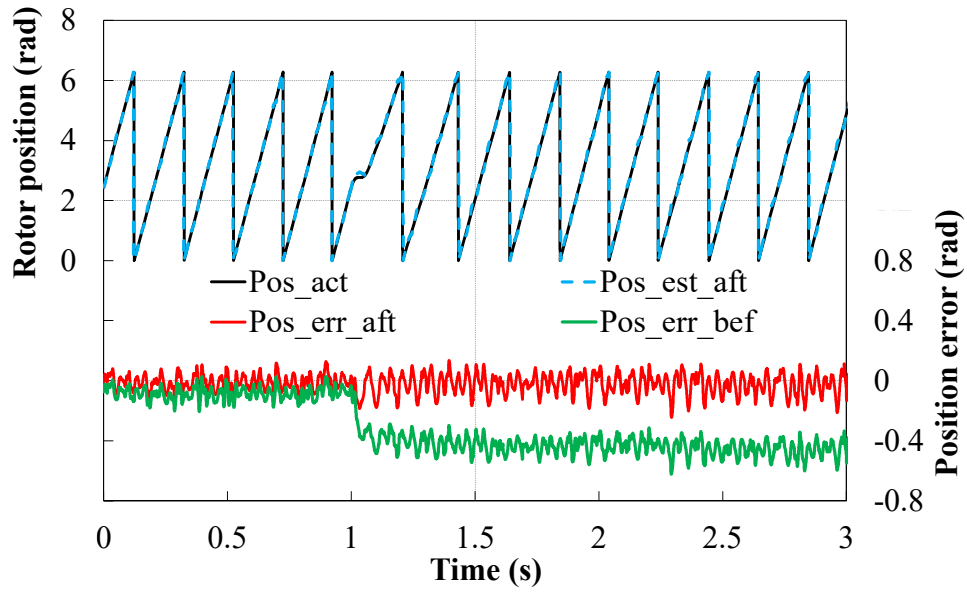
(b) Position estimation performance

Fig. 5.15 Step load tests for the conventional method with 2.5 kHz/8 V injection (Pos_err_aft-position error after cross-coupling compensation, Pos_err_bef- position error before the compensation).
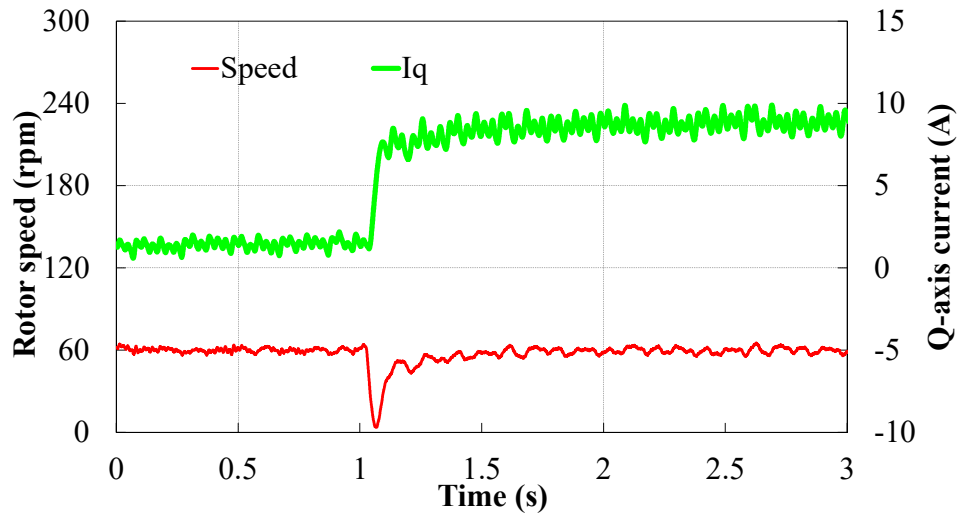
(a) Rotor speed and q-axis current
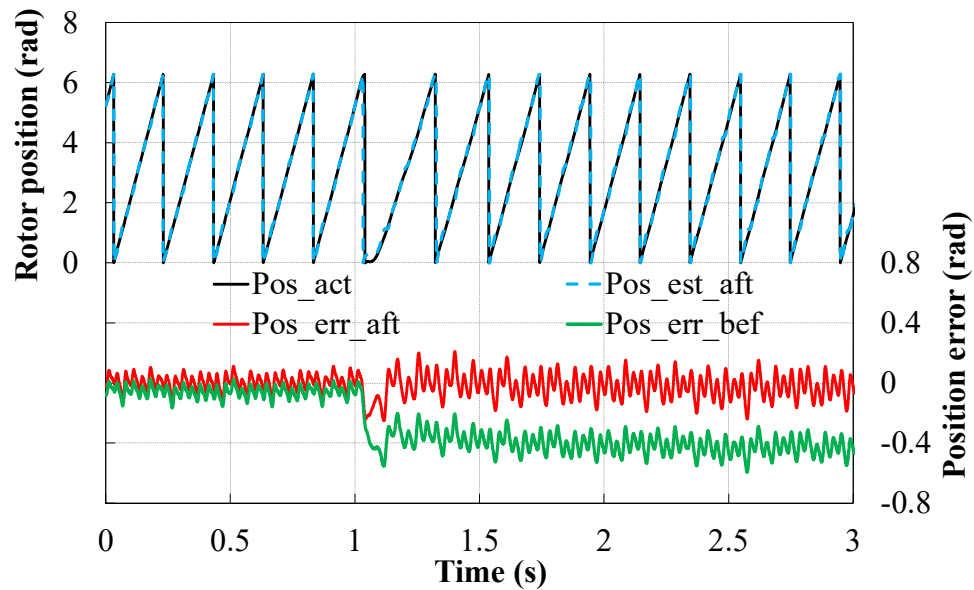
(b) Position estimation performance

Fig. 5.16 Step load tests for the proposed method with 2.5 kHz/4 V injection (Pos_err_aft-position error after cross-coupling compensation, Pos_err_bef- position error before the compensation).

5.5 Conclusion

In this chapter, a novel square-wave signal injection strategy utilising zero sequence carrier voltage is proposed for sensorless control of PMSMs. The square-wave signal is injected on

the estimated reference frame, anti-rotating at twice the rotor's estimated electrical speed. It is found that the resultant carrier response for the proposed method is simpler for signal demodulation, and has higher accuracy compared to the conventional square-wave methods with zero sequence voltage sensing. Therefore, it can be concluded that the proposed strategy can perfectly combine both the synergies of square-wave pulsating injection and zero sequence voltage sensing, i.e., high accuracy and bandwidths, increased available voltage for control, great dynamic response and robustness, etc. All theoretical analyses have been verified by experimental results on a prototype PM machine in both steady and dynamic conditions.

6 Improved Initial Rotor Position Estimation Using Zero Sequence Carrier Voltage for Permanent Magnet Synchronous Machines

6.1 Introduction

In the previous chapters, the carrier signal injection methods with either carrier current or zero sequence carrier voltage sensing have been introduced for the rotor position estimation of PMSMs. Although these methods have shown good effectiveness for position tracking, they suffer from the ambiguity of magnetic polarity [JEO05] [RAC08b] [GON13]. This is because these carrier injection methods are all based on the inductive saliency detection, while the inductive saliency undergoes two cycles during one electrical period [GON13].

Therefore, many papers have investigated on the magnetic polarity detection, which can be mainly divided into transient short pulses [NOG98] [HAQ03] [HOL08], secondary current harmonics [KIM04b] [JEO05] [HAR05] and amplitude variation due to saturation changing [GON13]. Among the three types of methods, in terms of S/N ratio, short pulses and amplitude variation based methods are superior to the secondary harmonic method [GON13]. However, the secondary current harmonic based method has faster convergence since it does not need to change the magnetic saturation with additional signals as the further step [JEO05] [HAR05] [RAC08b] [GON13].

Currently, these existing polarity identification methods are mainly implemented with carrier current sampling, and the zero sequence carrier voltage based detection methods have not been reported. Hence, this chapter seeks to investigate whether the zero sequence carrier voltage can be effectively used for polarity detection for the first time and can be even more advantageous than current sensing based detection methods. Furthermore, it should be noted that if the magnetic polarity can be identified using zero sequence voltage sensing, the integration with the sensorless algorithms based on zero sequence voltage sensing (e.g., the rotating signal injection in [GAR07] and anti-rotating pulsating signal injection in chapter 4) can be achieved.

Therefore, in this chapter, the initial position estimation and the magnetic polarity identification using zero sequence carrier voltage will be investigated for the rotating signal injection and anti-rotating pulsating signal injection, respectively. Two types of magnetic polarity detection methods, i.e., the amplitude variation of zero sequence carrier voltage due

to magnetic saturation changing and the secondary harmonics of zero sequence carrier voltage, will be presented. Modelling, implementation and effectiveness investigation for these polarity identification methods will be discussed and analysed in detail for the two carrier injection methods. It should be noted that the zero sequence voltage responses are not suitable for the magnetic polarity identification for the conventional pulsating injection method [JAN03] in the estimated synchronous reference frame, which will also be further discussed in the chapter. Finally, experimental results will confirm the theoretical analyses on a prototype PM machine.

The major new results of this chapter have been published in [XU17b].

6.2   Carrier Signal Model with Zero Sequence Voltage Detection

Firstly, the zero sequence voltage responses for the carrier signal injection methods are analysed, and it is then to be examined whether they can be effectively utilised for the magnetic polarity identification.

According to the derivations in chapter 4, the zero sequence carrier voltage can be expressed as [BRI05]

$$U_{RN} = \frac{U}{2} \frac{(-M_0 + L_0)}{(L_0 - M_0)^2 - (\frac{L_2}{2} + M_2)^2}(L_2 - M_2)\cos(\omega_h t + 2\theta_e)$$
(6.1)

for rotating signal injection in Fig. 4.2, and

$$U_{RN} = \frac{U}{2} \frac{(-M_0 + L_0)}{(L_0 - M_0)^2 - (\frac{L_2}{2} + M_2)^2}(L_2 - M_2)\cos(\omega_h t)\sin(2\Delta\theta)$$
(6.2)

for the proposed anti-rotating pulsating signal injection in Fig. 4.8, respectively.

Since the mutual inductances for the prototype machine are much smaller than the self-inductances as shown in Fig. 4.4, and also do not affect the rotor position estimation, they are neglected for the simplified analyses. Accordingly, (6.1)-(6.2) can be further described as

$$U_{RN} = \frac{2UL_0L_2}{4L_0^2 - L_2^2}\cos(\omega_h t + 2\theta_e)$$
(6.3)

$$U_{RN} = \frac{2UL_0L_2}{4L_0{}^2 - L_2{}^2} \cos \omega_h t \sin(2\Delta\theta) \qquad (6.4)$$

As analysed in the previous chapters, the advantages of zero sequence carrier voltage sensing based methods are that system bandwidths, estimation accuracy and stability can be greatly enhanced [GAR07]. Though great effectiveness using zero sequence carrier voltage has been shown for rotor position estimation [GAR07] [BRI05] [CON06], the ambiguity of magnetic polarity still exists. It can be seen from (6.3) and (6.4) that the position estimation error can converge at either 0 or π. To clear the ambiguity, transient short pulses [NOG98] [HAQ03] [HOL08], secondary harmonics [KIM04b] [JEO05] and amplitude variation due to saturation changing [GON13] based methods have been developed. Basically, short pulses and amplitude variation based methods are superior in terms of S/N ratio whilst the secondary harmonic based method has faster response [JEO05] [HAR05]. However, currently, most of these detection methods are based on carrier current sampling, and zero sequence voltage based method has not been reported. Thus, this chapter seeks to investigate whether zero sequence carrier voltage can be effective on polarity detection and whether even more advantageous than current sensing based detection methods. The detailed analyses for polarity detection using zero sequence voltage are given as follows.

6.3 Magnetic Polarity Detection with Zero Sequence Voltage

In this section, two types of magnetic polarity detection methods, i.e., the zero sequence voltage amplitude variation due to saturation changing and secondary harmonics of zero sequence carrier voltage, are examined for rotating and anti-rotating pulsating injection methods, respectively. The principles of these methods are analysed in detail as follows.

6.3.1 Amplitude variation based magnetic polarity detection method

The principle of amplitude variation method is based on the d-/ q-axis inductance variation with d-axis magnetic saturation [GON13]. Accordingly, by neglecting the mutual inductances in **Error! Reference source not found.**, the d-/q-axis inductances (i.e., L_d and L_q) by coordinate transformation are obtained as

$$L_d = L_0 - \frac{L_2}{2}$$
$$L_q = L_0 + \frac{L_2}{2} \tag{6.5}$$

Thus, based on (6.5), the zero sequence carrier voltages in (6.3)-(6.4) can then be expressed as

$$U_{RN} = \frac{U}{4}(\frac{L_q}{L_d} - \frac{L_d}{L_q})\cos(\omega_h t + 2\theta_e) \tag{6.6}$$

for rotating signal injection, and

$$U_{RN} = \frac{U}{4}(\frac{L_q}{L_d} - \frac{L_d}{L_q})\cos\omega_h t \sin(2\Delta\theta) \tag{6.7}$$

for anti-rotating pulsating injection, respectively.

For the prototype machine, the incremental d- and q-axis inductances calculated by the finite element (FE) simulation are illustrated in Fig. 6.1, from which it can be seen that L_d is significantly changed with d-axis current (i.e., d-axis magnetic saturation) while L_q is approximately unchanged. Then, based on the simulated inductances in Fig. 6.1, the value of $(L_q/L_d - L_d/L_q)$ related to the zero sequence voltage amplitude in (6.6)-(6.7) can be further calculated and is shown in Fig. 6.2. Since the zero sequence voltage amplitude which is proportional to $(L_q/L_d - L_d/L_q)$ changes significantly with the magnetic saturation from Fig. 6.2, the magnetic polarity can be then identified with the d-axis fundamental excitation variations.

Specifically, the amplitude of zero sequence carrier voltage can be extracted as

$$|U_{RN}| = LPF(U_{RN} \cdot 2\cos(\omega_h t + 2\hat{\theta}_e)) = \frac{U}{4}(\frac{L_q}{L_d} - \frac{L_d}{L_q})\cos(2\Delta\theta) \tag{6.8}$$

for rotating signal injection, and

$$|U_{RN}| = LPF(U_{RN} \cdot 2\cos\omega_h t) = \frac{U}{4}(\frac{L_q}{L_d} - \frac{L_d}{L_q})\sin(2\Delta\theta) \tag{6.9}$$

for anti-rotating pulsating signal injection, respectively. From (6.8), for rotating signal injection, the estimated rotor position is required as the feedback for the signal demodulation.

Whilst for the anti-rotating pulsating signal injection in (6.9), the position error $\Delta\theta$ should be modified not equalling to $0/\pi$ to better indicate the amplitude variation. For simplicity, for the anti-rotating pulsating injection, adding $\pi/4$ to the estimated rotor position is very effective since the amplitude of (6.9) is then maximised. The whole process for magnet polarity detection consisting of 3 steps is described in detail as follows.
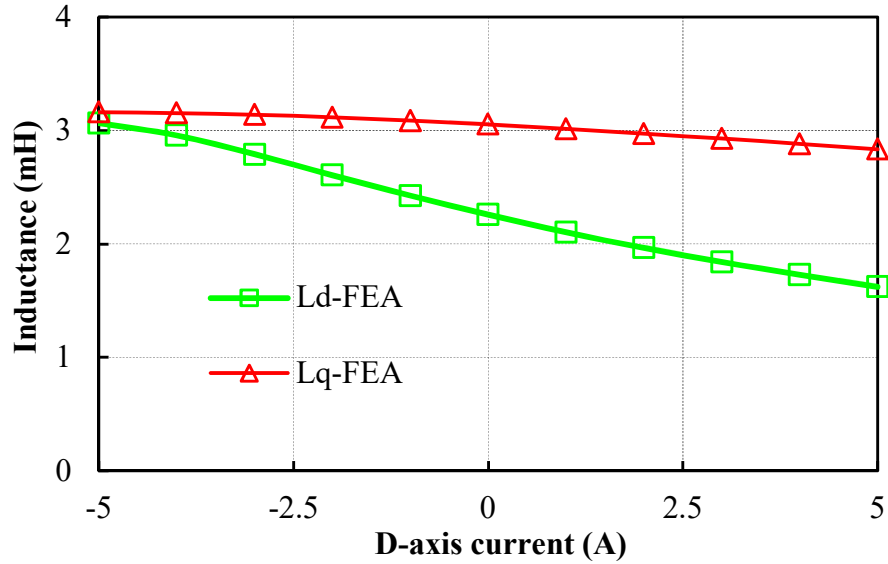
Fig. 6.1 Incremental inductances with d-axis current based on FE analyses.
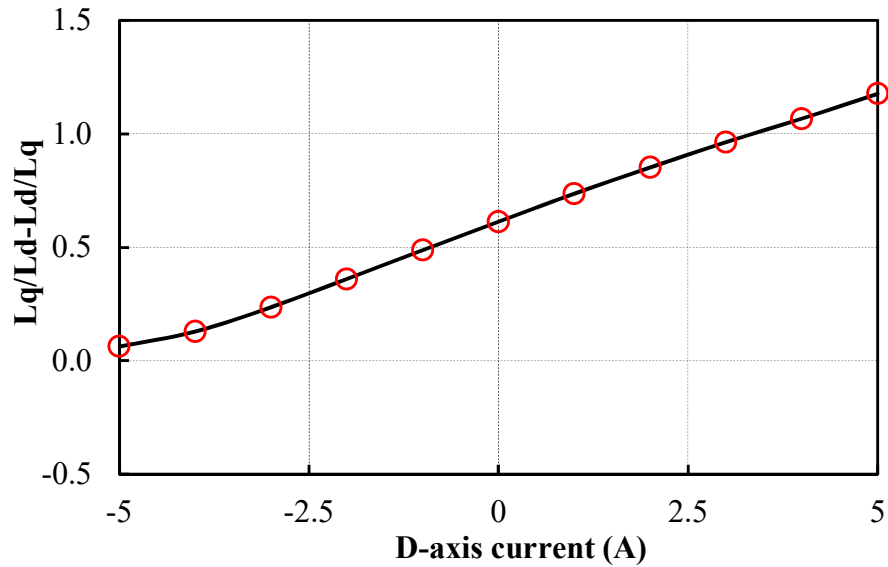
Fig. 6.2 Calculated (L_q/L_d-L_d/L_q) with d-axis current.

Step 1: For either rotating or anti-rotating pulsating injection method, the initial estimated rotor position $\hat{\theta}_e$ can be obtained using zero sequence carrier voltage before the machine is

started. With the ambiguity of π, the estimated position is either on the positive or negative d-axis.

Step 2: With the signal processing in (6.8) or (6.9), the resultant zero sequence voltage amplitude is then recorded as U_1 for the rotating or anti-rotating pulsating injection.

Step 3: Referring to the estimated rotor position $\hat{\theta}_e$, the negative d-axis voltage U_d changing the d-axis magnetic saturation is applied and then the zero sequence voltage amplitude is recorded as U_2.

Finally, by comparing the values of U_1 and U_2, the real d-axis can be identified. Specifically, as shown in Fig. 6.3, if $U_1>U_2$, it states that the estimated position is in the positive d-axis, otherwise, additional phase shift angle π should be added. More experimental results will be presented in section 6.4.
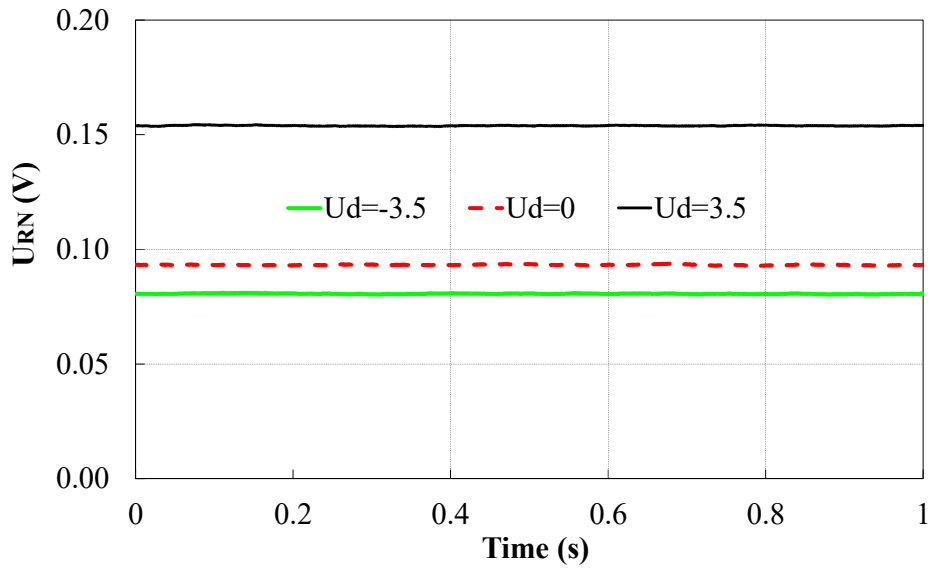
Fig. 6.3 Measured zero sequence voltage amplitudes with different d-axis voltages.

Furthermore, the amplitude variation methods using the carrier current as illustrated in [GON13] and the zero sequence voltage as illustrated above are also compared in this section. According to [GON13], the carrier current used for the magnetic polarity identification is described as

$$|i_{dh}|=\frac{U}{\omega_h}\frac{1}{L_d} \tag{6.10}$$
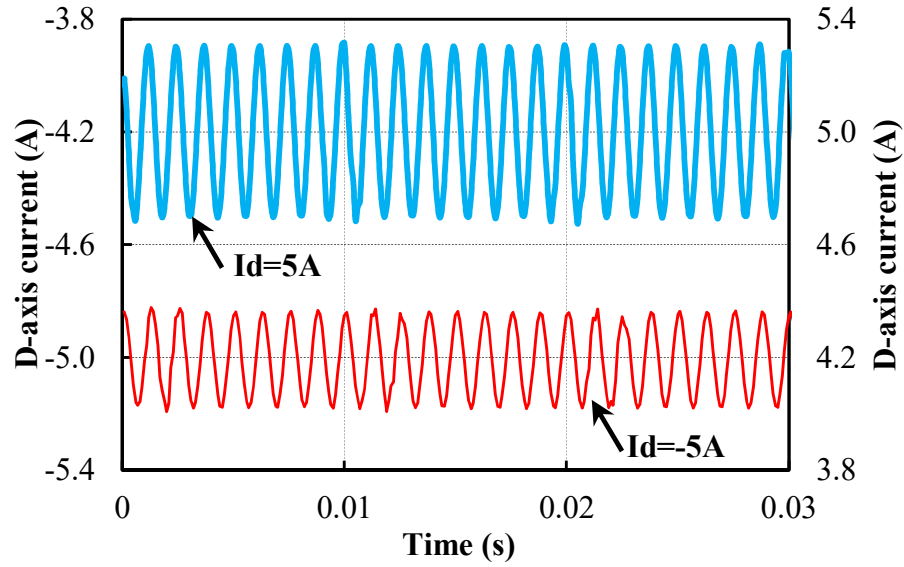
(a) D-axis current waveforms at -5A and 5A.
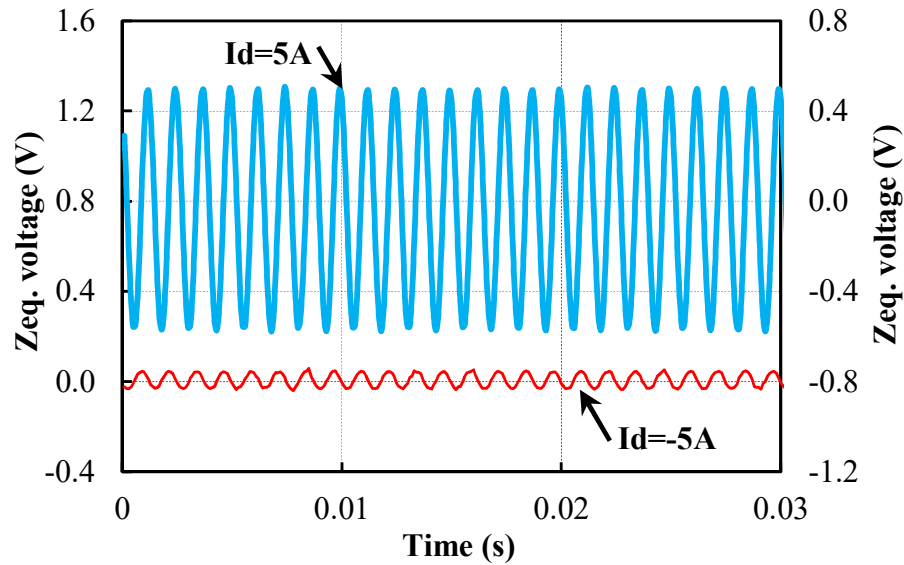
(b) Zero sequence voltage waveforms at -5A and 5A.

Fig. 6.4 Measured carrier response amplitude variations with d-axis currents.

Comparing (6.10) with (6.8)-(6.9), it can be seen that under certain injection voltage and frequency, the carrier current amplitude only depends on the d-axis inductance, which only changes ~1.9 times (from ~3.07 mH to ~1.62 mH, FEA results, Fig. 6.1) from -5A to 5A, Fig. 6.1. By comparison, the zero sequence carrier voltage amplitude changes as much as ~18.8 times (from ~1.18 to ~0.06) as shown Fig. 6.2. The measured carrier signal response variations also agree well with the theoretical analyses, as shown in Fig. 6.4(a)-(b), from

which it can be clearly seen that the zero sequence voltage has much more significant variations than the carrier current. Therefore, the amplitude variation based polarity detection method using zero sequence voltage is more advantageous since the detection sensitivity for the magnetic polarity has been significantly enhanced.

6.3.2　Secondary harmonic based polarity detection method

The amplitude variation based polarity detection method requires the magnetic saturation to be changed as the further step, which means that the response for polarity detection is not as fast as secondary harmonic based methods [HAR05] [GON13]. However, the S/N ratio is the major problem for secondary harmonic method with current sampling [JEO05] [GON13]. Thus, in this section, alternatively, the secondary harmonic of zero sequence carrier voltage will be investigated to examine whether it can be utilised or even be better than the conventional method in [JEO05] [HAR05].

Firstly, the modelling of secondary harmonics is described for the rotating and anti-rotating pulsating injection, respectively. For rotating signal injection, it has been derived that two dominant HF inductance (permeance) harmonics exist, i.e., f_h+f_e/f_h-f_e (f_h and f_e are the carrier frequency and fundamental frequency), which is due to the saturation modulation between main flux field and HF fields [CON06]. It is noted that the detailed modelling and more in-depth investigations for the saturation modulation effects will be given in chapter 7.

Accordingly, the equivalent three phase inductances can be described as

$$
\begin{aligned}
L_{aa} &= L_0 - L_2 \cos(2\theta_e) + L_{f_h-f_e} \sin(\theta_h - \theta_e) + L_{f_h+f_e} \sin(\theta_h + \theta_e) \\
L_{bb} &= L_0 - L_2 \cos(2\theta_e + 2\pi/3) + L_{f_h-f_e} \sin(\theta_h - \theta_e) + L_{f_h+f_e} \sin(\theta_h + \theta_e + 2\pi/3) \\
L_{cc} &= L_0 - L_2 \cos(2\theta_e - 2\pi/3) + L_{f_h-f_e} \sin(\theta_h - \theta_e) + L_{f_h+f_e} \sin(\theta_h + \theta_e - 2\pi/3)
\end{aligned}
\tag{6.11}
$$

where $\theta_h = \omega_h t$, L_{fh-fe} and L_{fh+fe} are the $(f_h/f_e-1)^{\text{th}}$, $(f_h/f_e+1)^{\text{th}}$ harmonic inductance amplitudes, respectively. Then, from (4.1), (4.4)-(4.9) in chapter 4, and (6.11), the secondary harmonic of the zero sequence carrier voltage for rotating injection can be obtained as

$$
U_{2nd} = U \frac{-(2L_0 L_{f_h+f_e} + L_2 L_{f_h-f_e})\sin(2\omega_h t + \theta_e)}{4L_0^2 - L_2^2}
\tag{6.12}
$$

For better illustration, according to [JEO05], the secondary harmonics of carrier current for rotating signal injection are also given as

$$i_{2nd} = k_1 e^{j(2\omega_h t - \theta_e)} + k_2 e^{j(-2\omega_h t + 3\theta_e)} \tag{6.13}$$

where k_1 and k_2 are the amplitudes of secondary carrier current harmonics. From (6.12)-(6.13), it can be seen that for rotating signal injection, the secondary zero sequence carrier voltage harmonic is located at $(2f_h+f_e)$, while the secondary carrier current harmonics are at $(2f_h-f_e)$ and $(2f_h-3f_e)$ [JEO05]. It is noted that since only one f_e exists in the secondary harmonics, i.e., $(2f_h+f_e)$ for the zero sequence voltage and $(2f_h-f_e)$ for the carrier current, the real magnetic polarity information has been recorded, which actually is the basic reason that these secondary harmonics can be utilised for the polarity detection.

To verify the carrier response expressions in (6.12)-(6.13), Fig. 6.5(a)-(b) illustrate the spectra of measured secondary harmonics with 8V/300 Hz injection (the fundamental frequency is set as 2.5 Hz). It can be seen that the 241st $(2f_h+f_e)$ harmonic arises for zero sequence carrier voltage whilst the 239th $(2f_h-f_e)$ and 237th $(2f_h-3f_e)$ harmonics exist for the carrier current, which are all consistent with the analyses in (6.12)-(6.13). Moreover, it is observed that the secondary zero sequence carrier voltage harmonics in Fig. 6.5(a) have considerably larger signal amplitude and less distortions compared to the carrier current harmonics in Fig. 6.5(b), i.e., larger S/N ratio can be obtained for the zero sequence voltage. Therefore, the secondary harmonic based detection method using zero sequence carrier voltage is superior since both the fast response and the increased S/N ratio can be obtained. Besides, since only one dominant frequency component $(2f_h+f_e)$ exists for the zero sequence voltage, the signal demodulation for the polarity identification is also simpler compared to that of the carrier current having two dominant harmonics $(2f_h-f_e$ and $2f_h-3f_e)$.

Accordingly, from (6.12), the further signal demodulation is described as

$$|U_{2nd}| = LPF[U_{RN} \cdot (-2\sin(2\omega_h t + \hat{\theta}_e))] = k\cos(\Delta\theta)(k > 0) \tag{6.14}$$

Thus, only by judging whether the value in (6.14) is positive or negative, the ambiguity of magnetic polarity can be cleared, which will be verified experimentally in the following.

On the other hand, for the anti-rotating pulsating signal injection method, it can be interpreted as two rotating signal injections, i.e., one is rotating anti-clockwise at the frequency of $f_h + 2\hat{f}_e$, while the other is anti-rotating at $f_h - 2\hat{f}_e$, respectively. Therefore, similarly, due to the saturation modulation effects [CON06], four HF inductance/permeance harmonic components will arise, i.e., $f_h + 2\hat{f}_e + f_e/f_h + 2\hat{f}_e - f_e$ for the rotating injection at

frequency of $f_h + 2\hat{f}_e$, and $f_h - 2\hat{f}_e + f_e$ / $f_h - 2\hat{f}_e - f_e$ at frequency of $f_h - 2\hat{f}_e$, respectively.
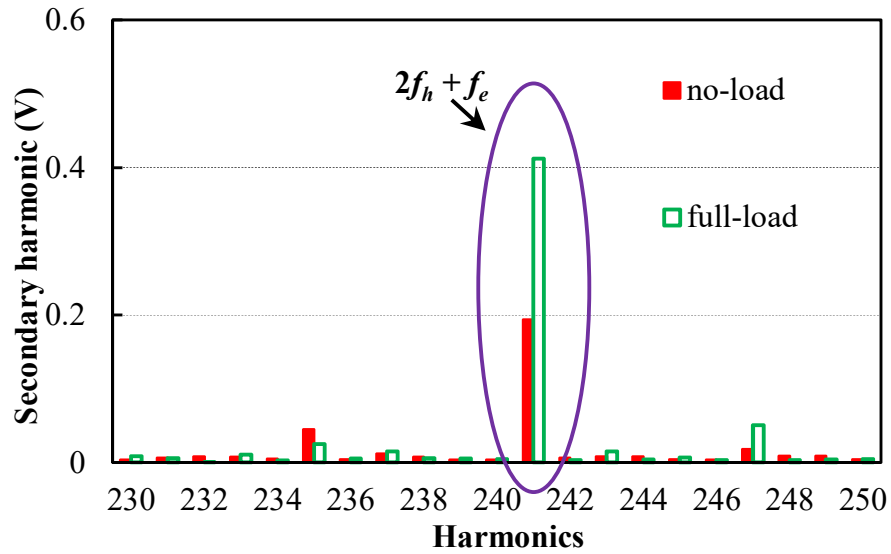
(a) Zero sequence carrier voltage
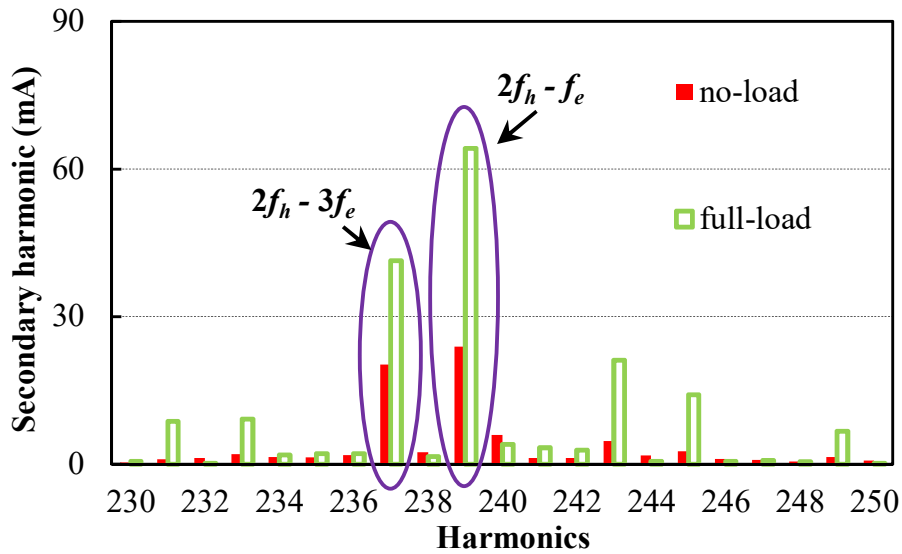
(b) Carrier current

Fig. 6.5 Spectra of measured secondary harmonic responses for rotating signal injection (8V and 300 Hz).

Then, based on the HF inductance/permeance information, similar to (6.14), the secondary harmonics of zero sequence carrier voltage for the anti-rotating pulsating signal injection method can be expressed as

$$U_{RN} = k_3 \sin(2\omega_h t - \theta_e + 4\hat{\theta}_e) + k_4 \sin(2\omega_h t + \theta_e - 4\hat{\theta}_e) \tag{6.15}$$

where k_3 and k_4 are the related secondary harmonic amplitudes. The spectrum of the measured secondary zero sequence carrier voltage harmonics for anti-rotating pulsating injection is shown in Fig. 6.6 (8V/300Hz injection, 2.5Hz fundamental frequency, no-load), which is in consistent with the analyses in (6.15). However, comparing with Fig. 6.5(a) for the conventional rotating signal injection method, it can be seen that for the anti-rotating pulsating injection, there exist two frequency components in (6.15) and Fig. 6.6, which can cause instability for magnetic polarity detection since the two components have similar amplitudes. To be more specific, the zero sequence responses in (6.15) for the anti-rotating pulsating injection method can be further demodulated as

$$|U_{2nd}| = LPF(U_{RN} \cdot 2\sin(2\omega_h t + 3\hat{\theta}_e)) = k_3 \cos(\Delta\theta_e) + k_4 \cos(\theta_e - 7\hat{\theta}_e) \tag{6.16}$$
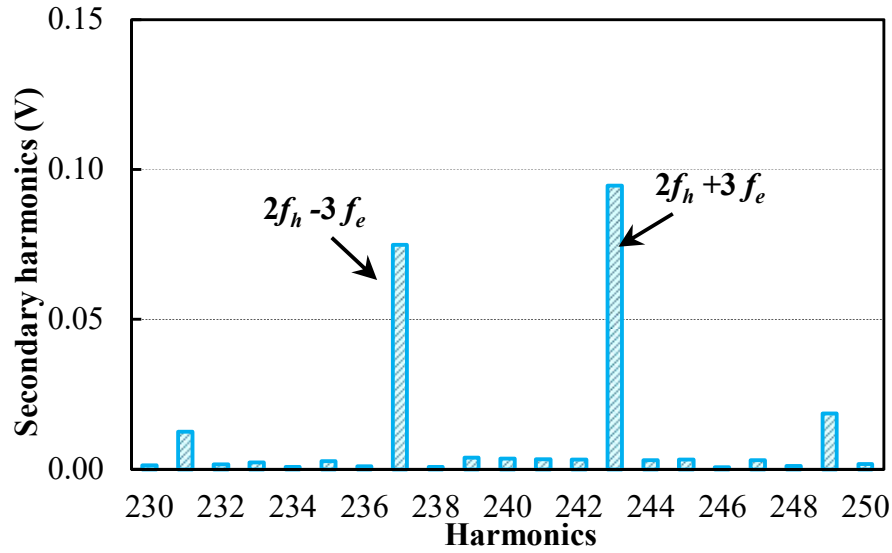
Fig. 6.6 Spectrum of measured secondary zero sequence carrier voltage harmonics for anti-rotating pulsating signal injection (8V and 300 Hz).

From (6.16), it can be seen that when the machine stops at different rotor positions, the resultant values of (6.16) could be different. Because $k_3 \approx k_4$ as can be seen from Fig. 6.6, the value of (6.16) may change the sign, and consequently the polarity identification capability is lost. Therefore, the secondary harmonic method with the zero sequence carrier voltage cannot be applied to the anti-rotating pulsating signal injection method.

6.4   Experimental Validation

The experiments of initial position estimation and magnetic polarity identification are implemented on a dSPACE platform for the prototype PM machine. The machine parameters of the PM machine are given in Table 4.1 in chapter 4. The overall block diagram of the initial rotor position estimation and magnetic polarity identification is shown in Fig. 6.7.
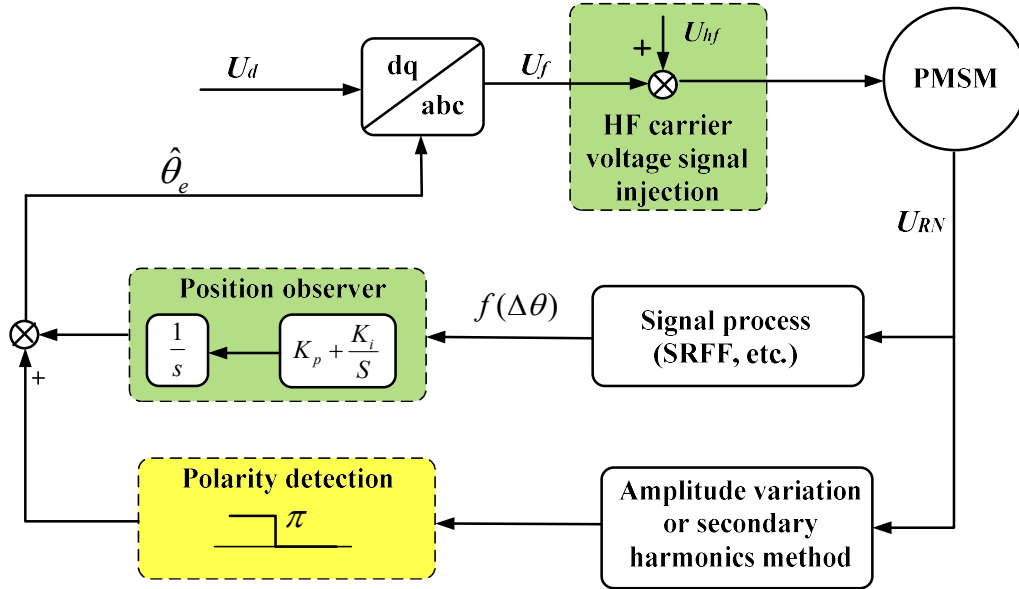
Fig. 6.7 Overall control system for initial position estimation and magnetic polarity identification.

6.4.1   Amplitude variation based polarity detection method

As shown in Fig. 6.8 with rotating signal injection, the initial rotor position can be quickly tracked but with ambiguity of π. Then, by the several steps introduced above, i.e., comparing the zero sequence voltage amplitudes with and without applying the d-axis voltage, the ambiguity can be removed. Specifically, as can be seen from Fig. 6.8(a), since $U_1 > U_2$, the estimated rotor position is correct, while in Fig. 6.8(b), adding phase shift of π to the initial estimated position is required for $U_1 < U_2$.

Besides, for anti-rotating pulsating signal injection, the similar results can also be obtained as shown in Fig. 6.9. The only difference during the polarity detection process compared to rotating injection is that $\Delta\theta$ should be modified according to the above analyses, Fig. 6.9(a)-(b). Therefore, from Fig. 6.8-Fig. 6.9, the amplitude variation based method using zero sequence carrier voltage can be effectively applied for the magnetic polarity identification for both types of injection methods.
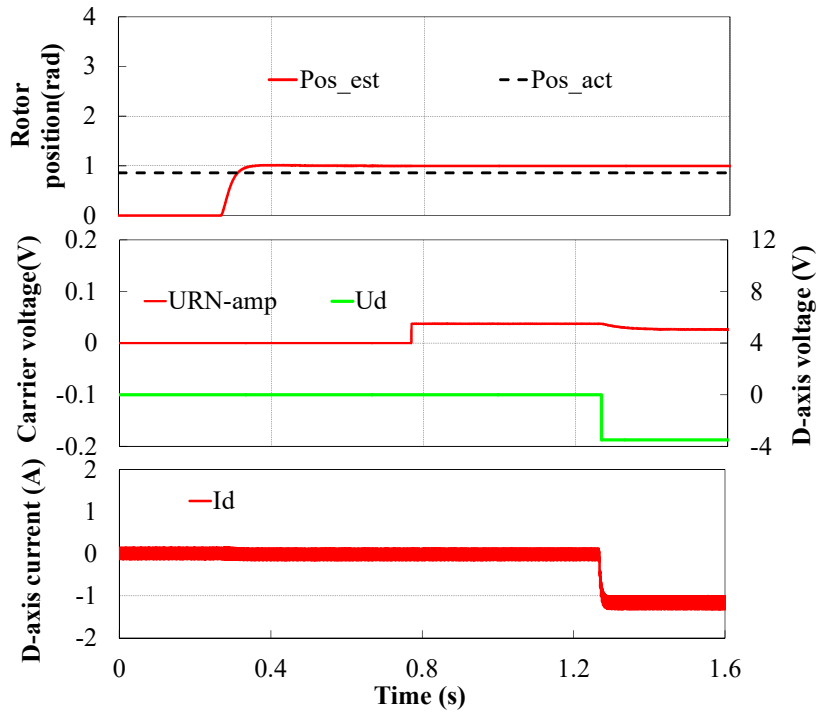
(a) Magnetic polarity detection without ambiguity of π
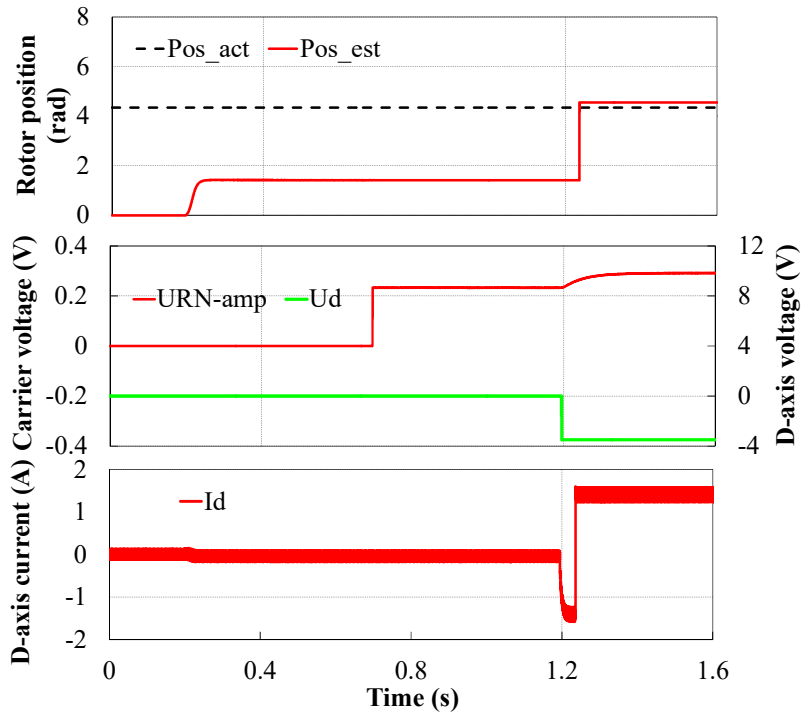
(b) Magnetic polarity detection with ambiguity of π

Fig. 6.8 Magnetic polarity detection based on amplitude variation for rotating signal injection (800Hz and 4V).
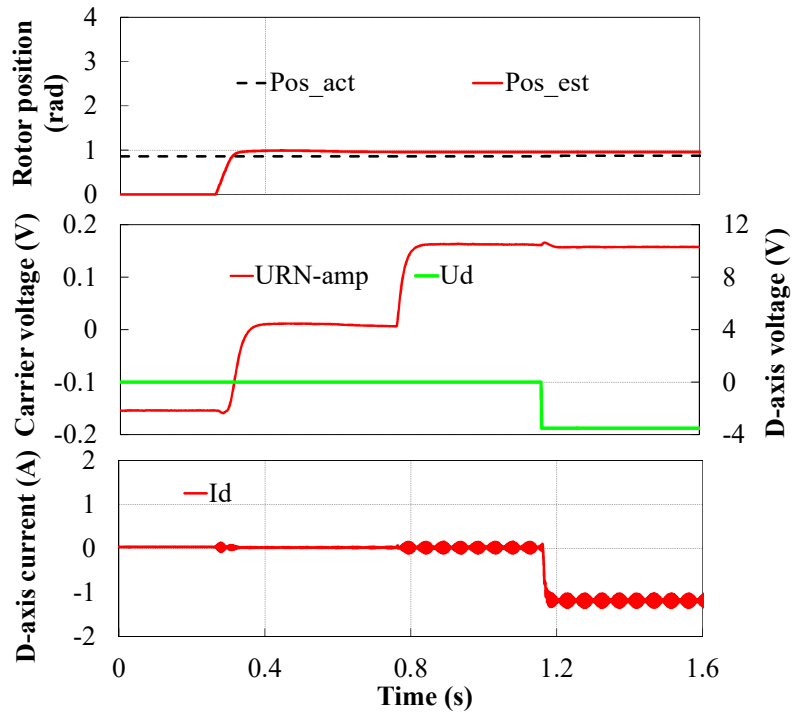
(a) Magnetic polarity detection without ambiguity of π
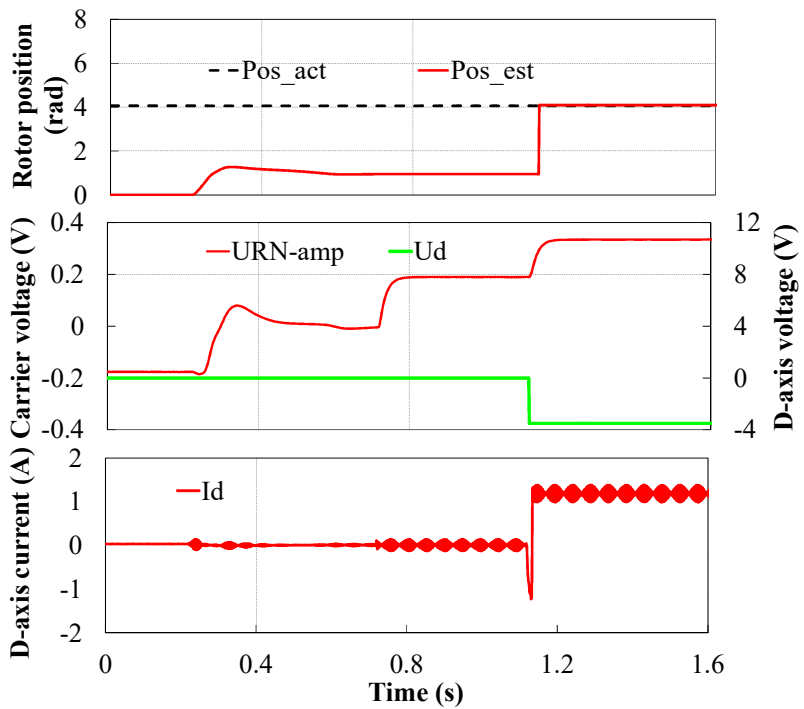
(b) Magnetic polarity detection with ambiguity of π

Fig. 6.9 Magnetic polarity detection based on amplitude variation for anti-rotating pulsating signal injection (800Hz and 4V).

6.4.2 Secondary harmonic based polarity detection method

As discussed above, the secondary zero sequence carrier voltage harmonics are not suitable for the magnetic polarity detection for the anti-rotating pulsating injection method, and therefore will not be illustrated in this chapter. Thus, only the rotating signal injection method using secondary zero sequence voltage harmonics is presented in this section, Fig. 6.10. The rotating carrier signals are selected as 8V and 300Hz to enhance the saturation modulation of main flux field and HF fields. As can be observed from Fig. 6.10, fast convergence is observed taking only 30 ms. Then, if the value of the amplitude of (6.14) is positive as shown in Fig. 6.10(a), the estimated rotor position is in the actual d-axis. Contrarily, as shown in Fig. 6.10(b), the estimated initial position should be added with the angle of π since the value of (6.14) is negative. Besides, since the secondary harmonic based methods have faster response, they can be also used in the machine running conditions to monitor the actual magnetic polarity. By way of example, in the no-load generating mode, the secondary harmonic amplitude for the zero sequence voltage can quickly respond to the sudden change of estimated position as shown in Fig. 6.11(a). By comparison, the secondary harmonic of the carrier current based method is also illustrated in Fig. 6.11(b). Obviously from Fig. 6.11(b), if the scale factor for A/D sampling is set as 1:1, the amplitude for the secondary current harmonic is much lower than that for the zero sequence voltage (Fig. 6.11(a)), while enlarging the scale factor (5:1) could then result in undesirable distortions (Fig. 6.11(b)). Therefore, the theoretical analyses for the magnetic polarity identification using secondary harmonics are clearly verified, and moreover the secondary harmonic of zero sequence voltage based method is more advantageous as discussed and verified above.
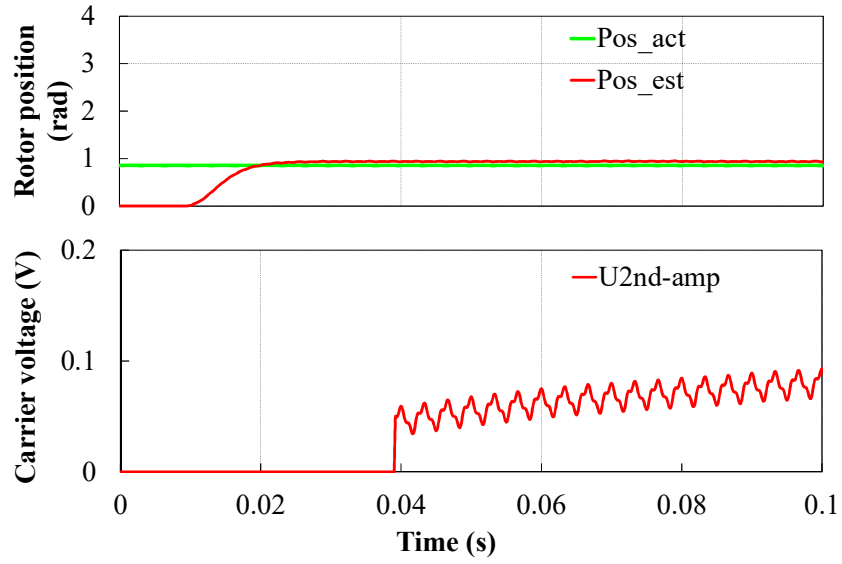
(a) Magnetic polarity detection without ambiguity of π
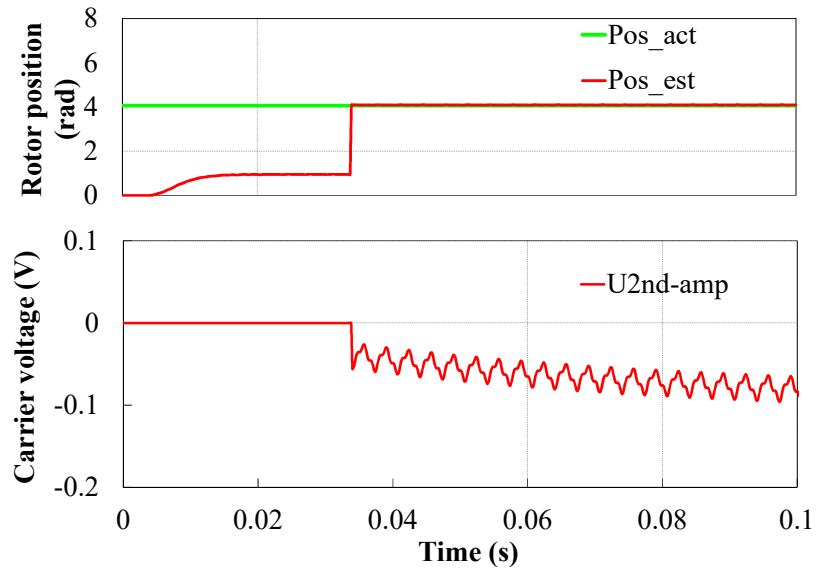
(b) Magnetic polarity detection with ambiguity of π

Fig. 6.10 Magnetic polarity identification based on secondary zero sequence voltage harmonics for rotating signal injection.
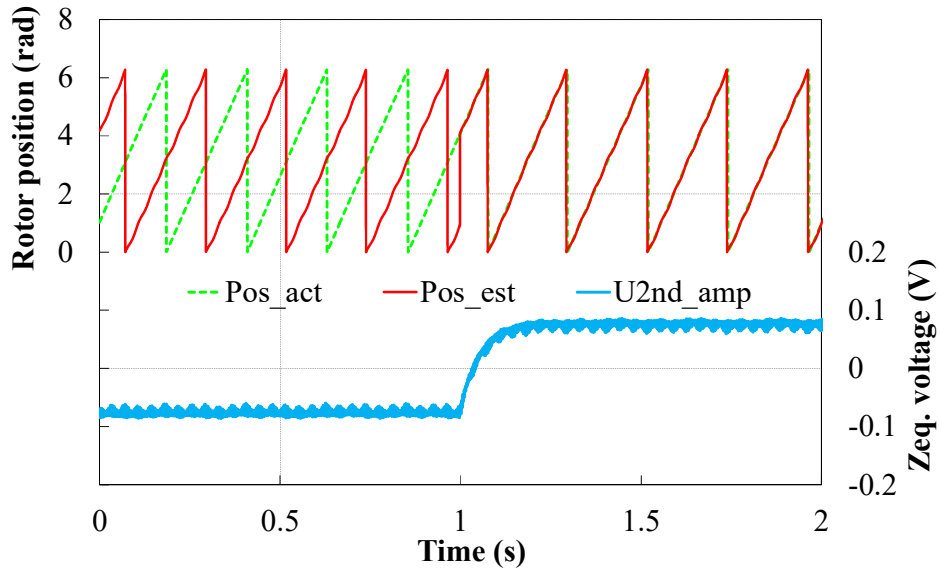
(a) Secondary harmonic of zero sequence voltage based (8 V/300 Hz)
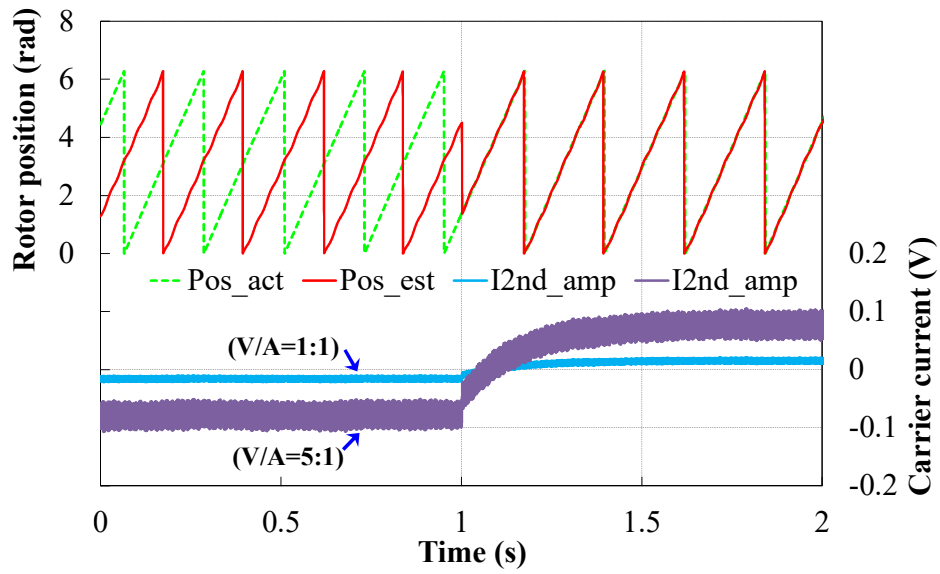
(b) Secondary harmonic of carrier current based (8 V/300 Hz)

Fig. 6.11 Secondary harmonic amplitude variation due to magnetic polarity ambiguity under no-load generating mode.

6.5 Further Discussions for the Pulsating Injection in the Estimated Synchronous Reference Frame

All the above analyses on the magnetic polarity identification using zero sequence voltage only focus on the two injection methods, i.e., rotating and anti-rotating pulsating injection. On the other hand, it is noted that the conventional pulsating injection method in the estimated synchronous reference frame is also widely employed for rotor position estimation [JAN03]. Therefore, whether the zero sequence voltage can be utilised for the polarity detection for the synchronous pulsating injection method [JAN03] will be further discussed in this section.

Accordingly, from (4.15) in chapter 4 with the pulsating injection in the estimated synchronous d-axis, the resultant zero sequence voltage can be obtained as

$$U_{RN} = \frac{2UL_0L_2}{4L_0^2 - L_2^2} \cos\omega_h t \cos(2\theta_e + \hat{\theta}_e) \tag{6.17}$$

With the further signal demodulation, the zero sequence voltage amplitude can be extracted as

$$|U_{RN}| = LPF(U_{RN} \cdot 4\cos(\omega_h t - 3\hat{\theta}_e)) = \frac{2UL_0L_2}{4L_0^2 - L_2^2}(\cos(2\Delta\theta) + \cos(2\theta_e + 4\hat{\theta}_e)) \tag{6.18}$$

From (6.18), the $|U_{RN}|$ may change the sign when the rotor stops at some positions, and consequently the polarity identification capability is lost, which is similar to (6.15)-(6.16). Therefore, the amplitude variation method using zero sequence voltage cannot be applied to the synchronous pulsating signal injection method. Similarly, since the synchronous pulsating injection can be also interpreted as two rotating signal injection [RAC08c], the secondary harmonics of zero sequence voltage also lose the capability for the magnetic polarity identification. The measured zero sequence voltage spectra for the synchronous pulsating injection are also shown in Fig. 6.12-Fig. 6.13 at the carrier frequency and twice carrier frequency range, respectively. Both two dominant harmonics in the zero sequence voltage exist as expected, and therefore similar to (6.16), they are both not suitable for the magnetic polarity detection for the synchronous pulsating injection method.
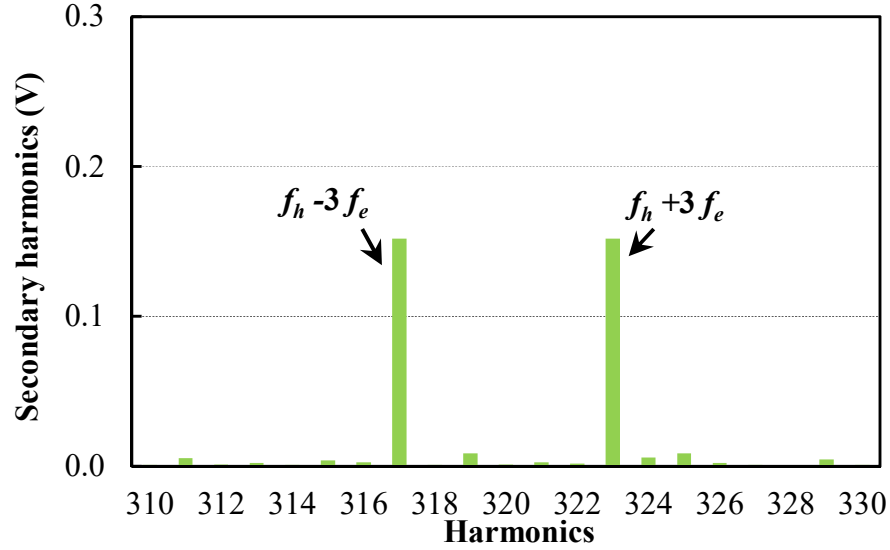
Fig. 6.12 Spectrum of measured zero sequence response for the synchronous pulsating signal injection at carrier frequency (4V/800Hz, f_e=2.5Hz).
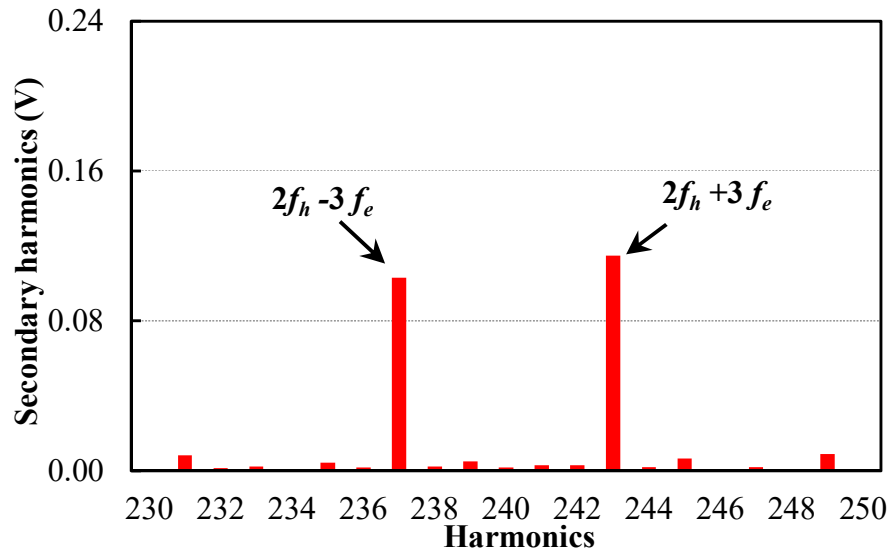
Fig. 6.13 Spectrum of measured secondary zero sequence response for the synchronous pulsating signal injection (8V/300Hz, f_e =2.5Hz).

6.6   Conclusions

This chapter has investigated the initial rotor position estimation and magnetic polarity identification by utilising zero sequence carrier voltage for PMSMs. Two types of magnetic polarity detection methods, i.e., the amplitude variation due to saturation changing and

secondary zero sequence carrier voltage harmonics, have been examined for rotating and anti-rotating pulsating injection, respectively. It is shown that the amplitude variation based method using zero sequence voltage has higher detection sensitivity for the magnetic polarity compared to the conventional method using the carrier current. For rotating signal injection, the secondary zero sequence voltage harmonic based polarity detection method has the advantages of simple signal demodulation, fast response, and moreover has larger S/N ratio compared with conventional secondary carrier current harmonics. However, the secondary zero sequence carrier voltage harmonics cannot be applied for anti-rotating pulsating signal injection since two dominant secondary harmonics exist and severely affect the polarity identification at different rotor positions. Further discussions also have shown that the zero sequence voltage responses cannot be applied to the conventional pulsating injection method performed in the estimated synchronous reference frame. Finally, the effectiveness of initial position and magnetic polarity identification using zero sequence carrier voltage has been verified by experimental results on a prototype PM machine.

7 Carrier Signal Injection Based Sensorless Control of Permanent Magnet Synchronous Machines without the Need of Magnetic Polarity Identification

7.1 Introduction

As stated in the previous chapter, the carrier signal injection methods suffer from the ambiguity of magnetic polarity, and accordingly different types of magnetic polarity detection methods have been developed to clear the ambiguity. Among these methods, the secondary harmonic based methods have faster convergence since they do not need to change the magnetic saturation with additional signals as the further step [JEO05].

However, as explained in [RAC08c] [JEO05], the amplitude of secondary harmonic carrier current is relatively small, and therefore is only considered for polarity identification, while it is not utilised for rotor position estimation. In contrast, as shown in chapter 6, for the rotating signal injection, the secondary harmonics of zero sequence carrier voltage have large signal amplitude and less distortions, and therefore whether this type of secondary harmonics can directly be used for position estimation will be examined in this chapter. It should be noted that if the secondary harmonic based position estimation method works, the time-consuming process of polarity identification can be completely eliminated, which can significantly improve the estimation response, and moreover the robustness and stability of position estimation will be greatly enhanced.

The modelling of the secondary harmonics is described in [JEO05] [HAR05] using the Taylor series which is based on the nonlinear magnetic saturation relationship between the current and the flux linkage in the d-axis rotor reference frame. In this chapter, a more insightful explanation will be given for the secondary harmonics as the interaction between HF field and HF reluctance (permeance) harmonics (i.e. the HF saliency). More importantly, the HF saliency contains the magnetic polarity information, which actually is the basic reason why these secondary harmonics can be utilised for polarity identification, [JEO05]. It should be noted that the presence of the HF saliency is due to the saturation modulation of main flux field and HF field [CON06] [CON09]. In [CON09], a new air-gap function model considering the saturation modulation effects has been utilised to derive the carrier responses. However, in [CON09], the HF inductance harmonic information is not analysed in detail, and

moreover the use of secondary harmonics for position estimation without any polarity ambiguity has not been discussed.

Therefore, in this chapter, the carrier signal injection method exploiting HF saliency will be investigated for the sensorless control of PMSMs without the need of magnetic polarity identification. The mechanism of HF saliency will be clearly described, and then the carrier signal responses (secondary harmonics) due to the interaction between HF field and HF saliency will also be derived. Finally, experimental results confirm the theoretical analysis on a prototype PM machine.

The major new results of this chapter have been published in [XU16d].

7.2 Modelling of HF Saliency

The inherent 2nd harmonic inductive and resistive saliencies have been widely employed for position estimation of PM machines with carrier signal injection methods [JAN95] [JAN03] [YAN11]. However, the ambiguity of magnetic polarity arises, which on one hand requires time-consuming polarity identification, and moreover may bring in instability during normal sensorless control. These issues can be significantly improved by utilising the HF saliency effect.

Specifically, the interaction between the injected HF field and main flux field results in the modulation of saturation level [CON06], and consequently the HF magnetic reluctance harmonic (i.e., HF saliency) arises. Actually, the HF saliency information is reflected in the machine phase inductances, which can then be obtained by the finite element (FE) simulation using frozen permeability (FP) method [CHU13] as follows.

7.2.1 Calculation of HF saliency using frozen permeability (FP) method

In the FE analyses, for the prototype PM machine, Fig. 7.1 (its parameters are given in Table 7.1), the fundamental frequency (f_e) is set as 2.5 Hz (30 rpm), and the carrier current is set as 1A (10% of the rated current) and 300 Hz frequency, i.e.,

$$
\begin{aligned}
i_{ah} &= I_h \sin(2\pi f_h t) \\
i_{bh} &= I_h \sin(2\pi f_h t - 2\pi/3) \\
i_{ch} &= I_h \sin(2\pi f_h t + 2\pi/3)
\end{aligned}
\tag{7.1}
$$

where i_{ah}, i_{bh} and i_{ch} are three phase carrier currents, I_h is the current amplitude, f_h is the carrier frequency, respectively. Then, according to [CHU13], after the save and frozen of the permeability (each element and every step) with non-linear FE simulation having both PM and armature fields, the three phase inductances can be obtained with single excitation under linear FE conditions, Fig. 7.2.
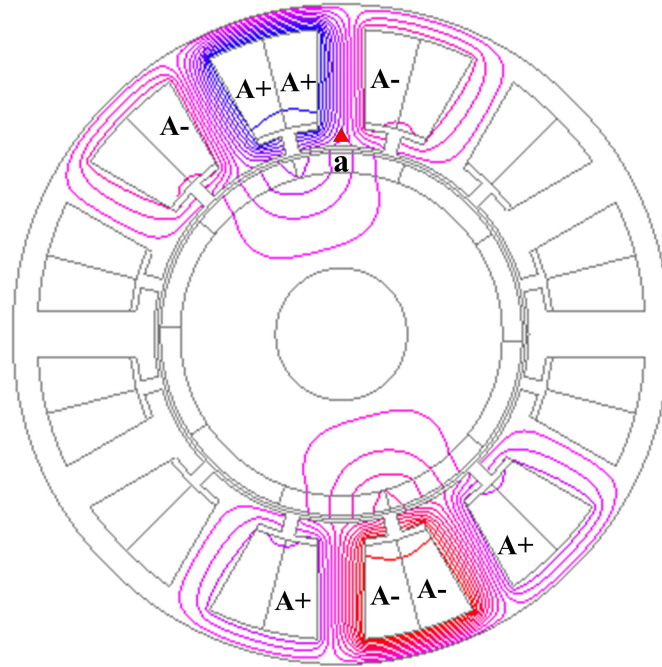
Fig. 7.1 Flux distribution of armature reaction for phase A only.

From Fig. 7.2, it can be seen that apart from the fluctuated 2nd harmonic component (i.e., the inherent saliency), the three phase inductances also contain rich harmonics due to the carrier injection. Besides, from Fig. 7.2, it can be seen that the phase mutual-inductance is much smaller than the self-inductance due to the magnetic path of armature reaction [BIA06]. Because the mutual inductances will not affect the rotor position estimation as modelled in chapter 4, they are neglected for the simplified analyses in this chapter. Subsequently, the magnitude and phase spectra for the three phase inductances are shown in Fig. 7.3(a)-(d) at fundamental and in the carrier frequency range, respectively.
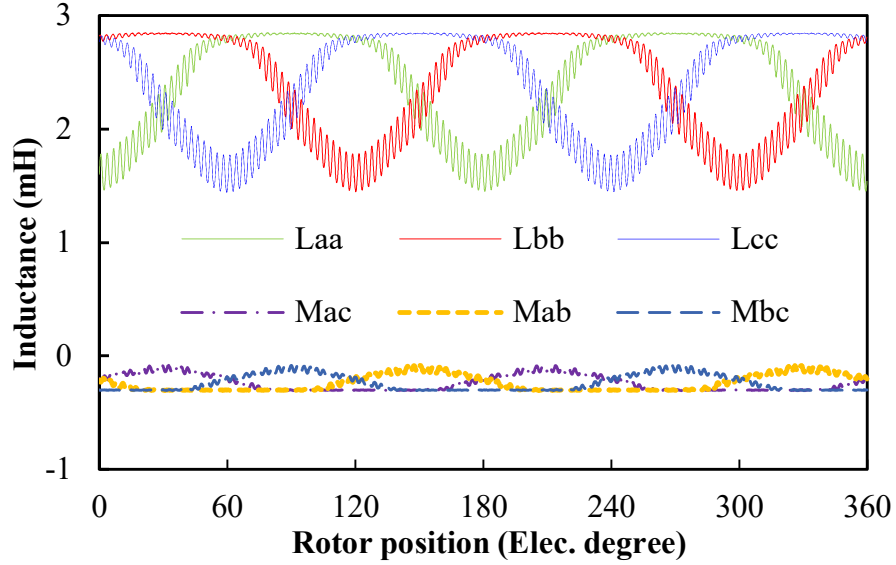
Fig. 7.2 Three phase inductances with 300 Hz HF injection using FP method.

From Fig. 7.3(a)-(b), it can be seen that mainly dc, 2nd ($2f_e$), 119th (f_h/f_e-1) and 121st ((f_h/f_e+1)) inductance harmonics exist. The presence of 2nd harmonics, i.e., the inherent machine saliency, is due to the magnetic saturation caused by d- or q-axis saturation [JAN03] [YAN11]. The 119th and 121th harmonics can be attributed to the magnetic saturation modulation between HF field and main flux field [CON06], i.e., the HF saliency. Besides, in order to further confirm the saturation modulation effects, a higher injection frequency at 800 Hz is also performed, and the three phase inductances including the spectra are also obtained and shown in Fig. 7.4-Fig. 7.5, respectively. It can be seen that the 319th (f_h/f_e-1) and 321st ((f_h/f_e+1)) harmonics also arise, respectively. These modulation effects will be more clearly explained in the following.
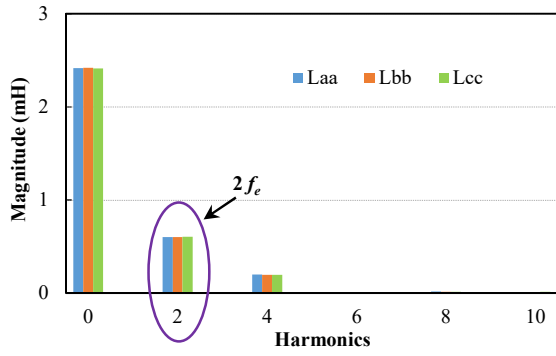
(a) Magnitude spectra around fundamental frequency
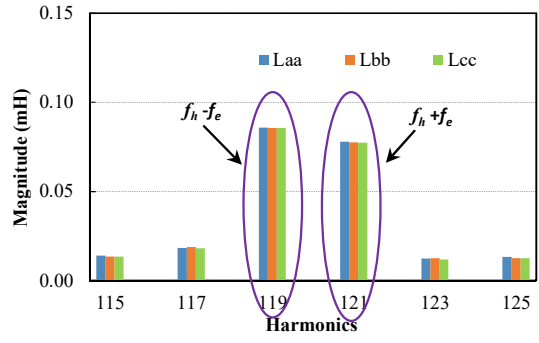
(b) Magnitude spectra around carrier injection frequency
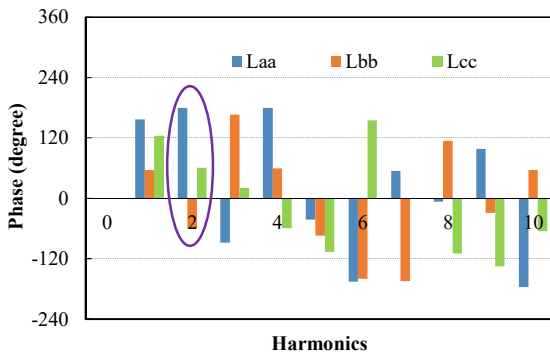
(c) Phase spectra around fundamental frequency
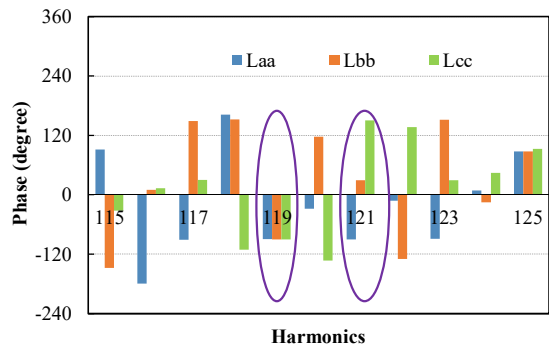
(d) Phase spectra around carrier frequency

Fig. 7.3 Spectra of three phase inductances with 300 Hz HF injection.
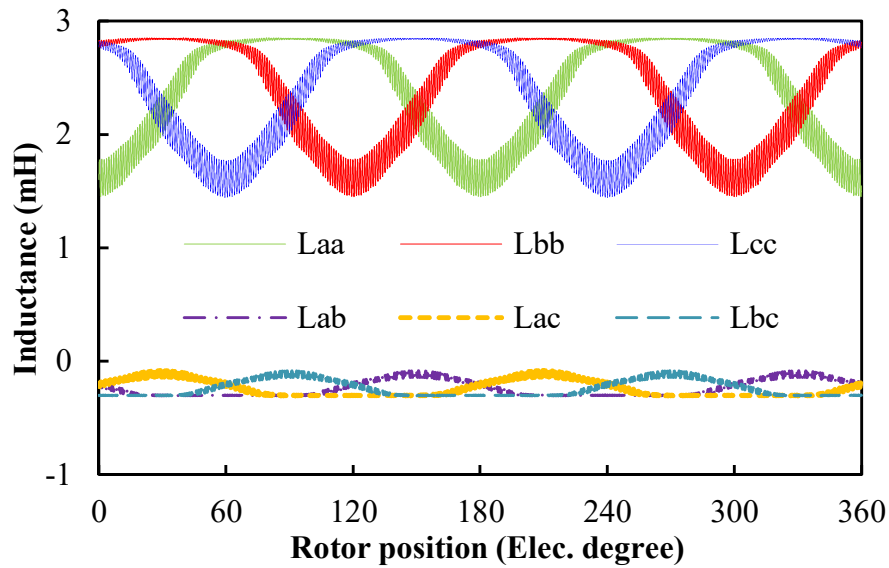
Fig. 7.4 Three phase inductances with 800 Hz HF injection using FP method.
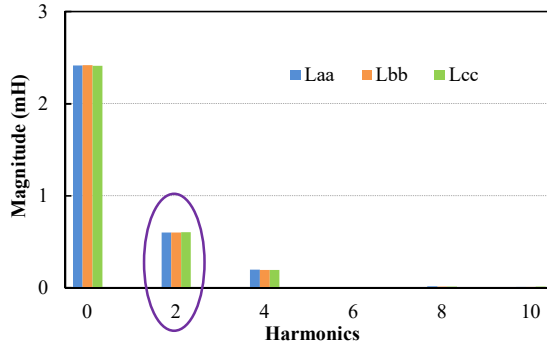
(a) Magnitude spectra around fundamental
frequency
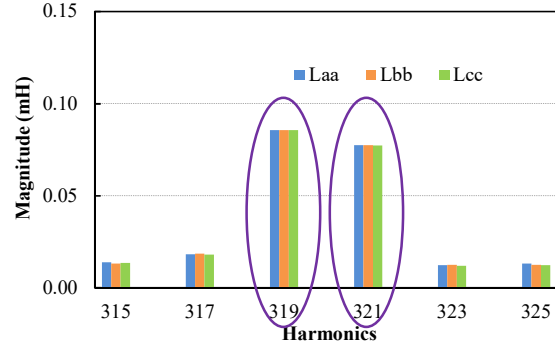
(b) Magnitude spectra around carrier
injection frequency
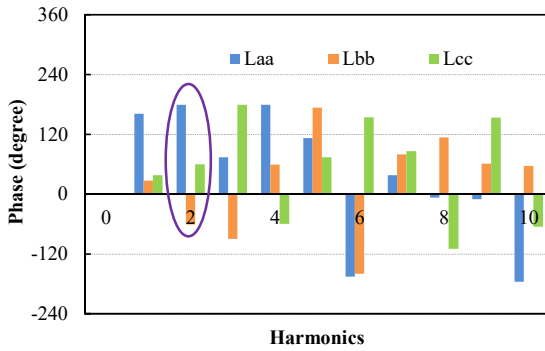
(c) Phase spectra around fundamental
frequency
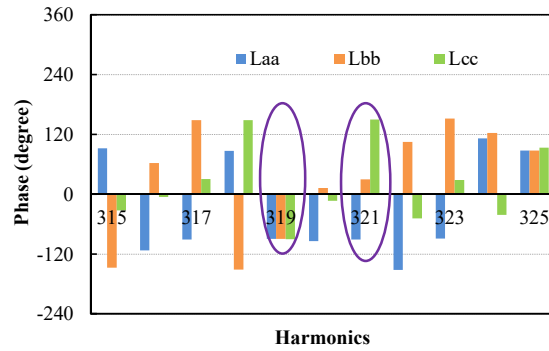
(d) Phase spectra around carrier frequency

Fig. 7.5 Spectra of three phase inductances with 800 Hz HF injection.

7.2.2 Saturation modulation effects

With the above calculated HF inductances, the equivalent phase magnetic reluctances can be obtained according to

$$L_{aa} = \frac{\psi}{I_A} = \frac{N^2 I_A}{I_A R_a} = \frac{N^2}{R_a} \tag{7.2}$$

where I_A and Ψ is the current and flux-linkage of phase A, L_{aa} and R_a is the self-inductance and equivalent magnetic reluctance for phase A, N is the number of turns for one phase, respectively. Therefore, from (7.2), it can be deduced that the inductance harmonics are all from the magnetic reluctance harmonics, while the magnetic reluctance harmonics are determined by the relative permeability harmonics in the stator or rotor irons in the magnetizing flux paths [CON00] [CON06]. By selecting certain point in the stator, e.g., point 'a' in Fig. 7.1, the relative permeability of point 'a' can be obtained according to the

definition ($\mu_r=|B|/(\mu_0|H|)$), Fig. 7.6(a)-(c). From Fig. 7.6(c), it can be seen that the relative permeability also has rich harmonics.

This can be explained by the B-H curve in Fig. 7.7, in which the working point is fluctuating with the HF injection due to the change of saturation level, i.e., the saturation modulation phenomenon. Accordingly, the spectrum for the relative permeability around carrier frequency is given in Fig. 7.6(d). As can be observed from Fig. 7.6(d), the spectrum of the relative permeability is approximately the same with the three phase inductances, i.e., mainly at the 119th (f_h/f_e-1) and 121st ((f_h/f_e+1)) harmonics, Fig. 7.3(b). The actual HF inductance (reluctance) harmonics are actually from the sum of the average relative permeability harmonics in all the magnetizing flux paths [CON06].

(a) Amplitude of flux density (|B|)

(b) Amplitude of flux intensity (|H|)

(c) Relative permeability

(d) Spectrum of relative permeability at carrier frequency
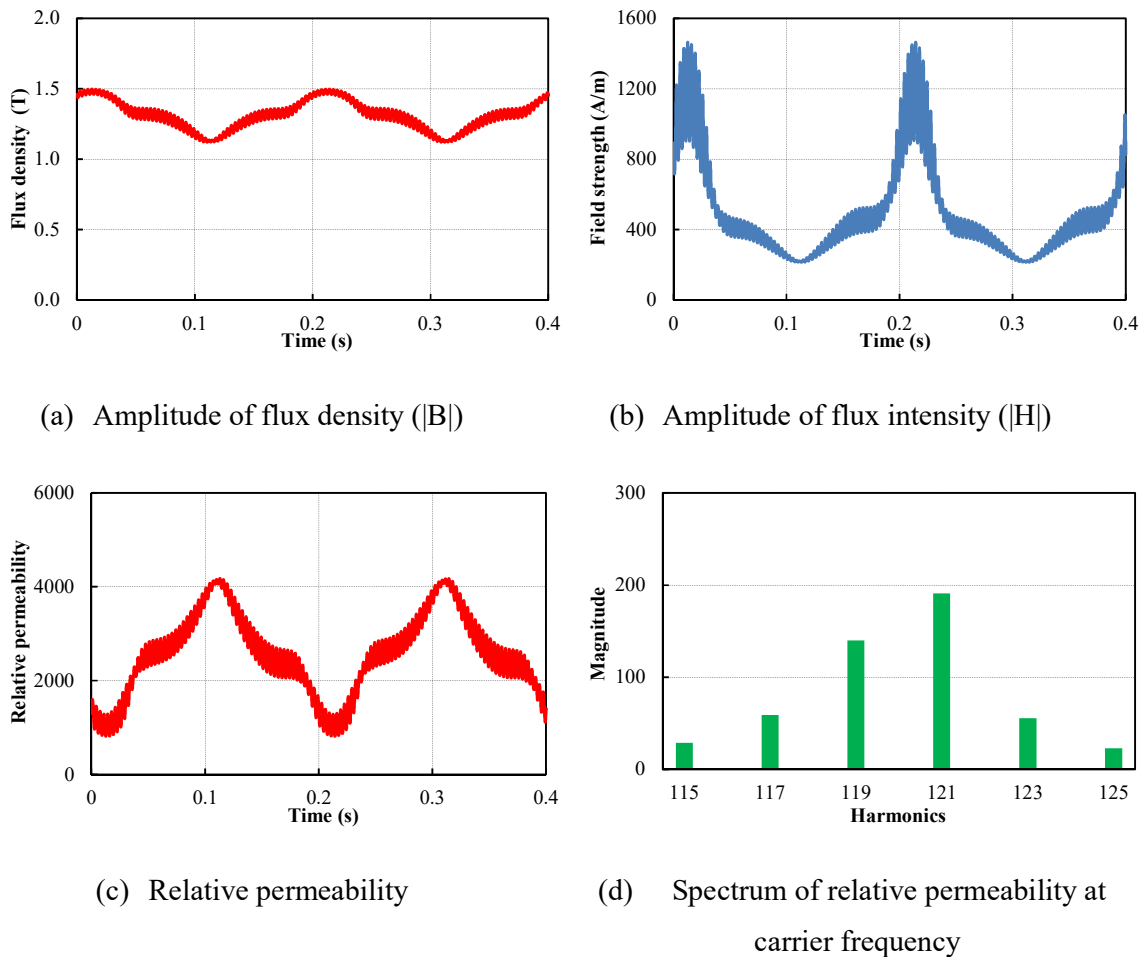
Fig. 7.6 Relative permeability calculation of point 'a' at 300 Hz injection frequency.

From the above analyses, it can be derived that the HF relative permeability harmonics determine the HF inductance harmonics. While according to the definition $\mu_r=|B|/(\mu_0|H|)$, the

HF relative permeability harmonics actually arise from the absolute value of flux density (flux intensity) since $|H|$ ($|B|$) has the dc components (Fig. 7.6(a)-(b)), which will be proved as follows.

Assume that the $|B|$ for point 'a' can be approximately expressed as

$$|B| \approx \left| \sum_{k=1}^{2n-1} B_{LF\_k} \cos(k\omega_e t + \delta_{1\_k}) + B_{HF} \cos(\omega_h t + \delta_2) \right| \tag{7.3}$$

where B_{LF_k} represents the amplitude of the kth flux density around the fundamental frequency, e.g., the PM and fundamental current excitation, B_{HF} represents the amplitude of flux density at the injection frequency, and δ_{1_k} and δ_2 are the phase shifts in the flux density. Therefore, from (7.3), the $|B|$ can be further expressed as (by only considering the fundamental and carrier injection frequency components)

$$|B| \approx \sqrt{B_{LF}^2 \cos^2(\omega_e t + \delta_1) + 2B_{HF}B_{LF}\cos(\omega_e t + \delta_1)\cos(\omega_h t + \delta_2) + B_{HF}^2 \cos^2(\omega_h t + \delta_2)} \tag{7.4}$$

Mathematically, it can be proved from (7.4) that the $|B|$ has the harmonic components at the frequency of $(f_h/f_e - 1)$ and $(f_h/f_e + 1)$. To be more specific, since $|B|(>0)$ has a dominant dc component, as shown in Fig. 7.6(a), it can be expressed as

$$|B| = B_0 + B_x + B_y + ... \tag{7.5}$$

where B_0 is the dc component, B_x and B_y present the components at the frequency of x and y (x and y are assumed around the injection frequency ω_h, and $y > x$), respectively. Then, with (7.4)-(7.5), it can be obtained that

$$\begin{aligned}(B_0 + B_x + B_y + ...)^2 &= B_{LF}^2 \cos^2(\omega_e t + \delta_1) + B_{HF}B_{LF}\cos[(\omega_h - \omega_e)t + \delta_2 - \delta_1] \\ &+ B_{HF}B_{LF}\cos[(\omega_h + \omega_e)t + \delta_2 + \delta_1] + B_{HF}^2 \cos^2(\omega_h t + \delta_2)\end{aligned} \tag{7.6}$$

The left side of (7.6) can be further written as

$$(B_0 + B_x + B_y + ...)^2 = \underbrace{B_0^2}_{dc} + \underbrace{2B_0 B_x + 2B_0 B_y}_{\approx \omega_h} + \underbrace{B_x^2 + B_y^2}_{\approx 2\omega_h}... \tag{7.7}$$

The right side of (7.6) can be further written as

$$B_{LF}^2 \cos^2(\omega_e t + \delta_1) + B_{HF}B_{LF}\cos[(\omega_h - \omega_e)t + \delta_2 - \delta_1] + B_{HF}B_{LF}\cos[(\omega_h + \omega_e)t + \delta_2 + \delta_1]$$
$$+B_{HF}^2 \cos^2(\omega_h t + \delta_2)$$
$$= \underbrace{\frac{B_{LF}^2}{2} + \frac{B_{HF}^2}{2}}_{dc} + \underbrace{B_{HF}B_{LF}\cos[(\omega_h - \omega_e)t + \delta_2 - \delta_1] + B_{HF}B_{LF}\cos[(\omega_h + \omega_e)t + \delta_2 + \delta_1]}_{\approx \omega_h} + ... \tag{7.8}$$

Since the components in (7.7)-(7.8) are decoupled in the frequency domain, it can be derived that

$$B_0 = \sqrt{\frac{B_{LF}^2}{2} + \frac{B_{HF}^2}{2}}$$

$$B_x = \frac{B_{HF}B_{LF}}{2\sqrt{\frac{B_{LF}^2}{2} + \frac{B_{HF}^2}{2}}}\cos[(\omega_h - \omega_e)t + \delta_2 - \delta_1] \tag{7.9}$$

$$B_y = \frac{B_{HF}B_{LF}}{2\sqrt{\frac{B_{LF}^2}{2} + \frac{B_{HF}^2}{2}}}\cos[(\omega_h + \omega_e)t + \delta_2 + \delta_1]$$

Clearly, from (7.9), B_x and B_y are the components at the frequency of (f_h/f_e-1) and (f_h/f_e+1), respectively, and the amplitude of these two harmonics is related to the interaction of the low frequency and high frequency flux density components.

Therefore, from the above derivations, it can be summarized that the saturation modulation effect actually is the interaction between the low and high frequency fields (B_{HF} and B_{LF}) due to the nonlinear B-H curve characteristics of the irons, which then results in the HF relative permeability harmonics, and consequently the HF reluctance and inductances harmonics, Fig. 7.3(b). Then, due to the interaction between HF field and these HF inductance (reluctance) harmonics, rotor position dependent carrier signal responses, i.e., the secondary harmonics arise. Moreover, since these two main HF inductance harmonics in Fig. 7.3(d) only contain one f_e (θ_e), i.e., the magnetic polarity information has been recorded in these inductance harmonics, the resultant secondary harmonics can be potentially utilised for the actual rotor position tracking without any ambiguity of machine polarity. Besides, from the above derivations, it should be pointed out that the reason why only one f_e appears in the inductance harmonics (i.e., the polarity information recorded) is due to that the main flux field participating in saturation modulation rotates at the synchronous rotor angular frequency, i.e., f_e.
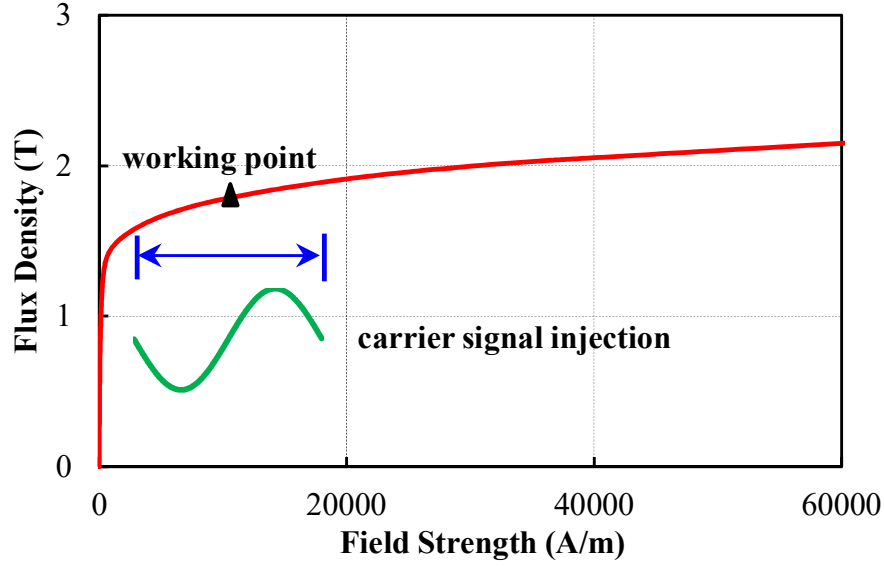
Fig. 7.7 The variation of relative permeability due to HF injection.

7.3 Secondary Harmonic Responses

In this part, based on the above analysis of the HF inductance (reluctance) harmonics, the secondary harmonic responses will be fully derived as follows.

Firstly, from Fig. 7.3, the self-inductance of phase A (L_{aa}) considering HF harmonics can be expressed as

$$L_{aa} \approx L_0 - L_2 \cos(2\omega_e t) + L_{f_h - f_e} \sin(\omega_h t - \omega_e t) + L_{f_h + f_e} \sin(\omega_h t + \omega_e t) \tag{7.10}$$

where L_0, L_2, $L_{fh\text{-}fe}$ and L_{fh+fe} are dc, 2nd, $(f_h/f_e\text{-}1)^{\text{th}}$, $(f_h/f_e+1)^{\text{th}}$ harmonic inductance components, respectively. Similarly, the inductances of phase B and C can be expressed as

$$L_{bb} \approx L_0 - L_2 \cos(2\omega_e t + \frac{2\pi}{3}) + L_{f_h - f_e} \sin(\omega_h t - \omega_e t) + L_{f_h + f_e} \sin(\omega_h t + \omega_e t + \frac{2\pi}{3}) \tag{7.11}$$

$$L_{cc} \approx L_0 - L_2 \cos(2\omega_e t - \frac{2\pi}{3}) + L_{f_h - f_e} \sin(\omega_h t - \omega_e t) + L_{f_h + f_e} \sin(\omega_h t + \omega_e t - \frac{2\pi}{3}) \tag{7.12}$$

It is worth noting from (7.10)-(7.12) that the $(f_h/f_e+1)^{\text{th}}$ inductance harmonics for three phases are with the difference of -120 degrees, i.e., the negative sequence components, while the $(f_h/f_e\text{-}1)^{\text{th}}$ harmonics are in the same phase, i.e., the zero sequence inductance components. The reason why the generated HF inductance harmonics are one negative and the other zero

sequence components can be explained by that the HF and main (fundamental) flux fields are both rotating in the positive sequence frame. Consequently, the saturation modulation between them results in one negative and the other zero sequence components according to (7.4). To be more specific, the HF three phase inductance harmonics can be approximately described as

$$
\begin{aligned}
L_{aa} &\propto \mu_{r\_a} \propto B_{LF}B_{HF}\cos(\omega_e t + \delta_1)\cos(\omega_h t + \delta_2) \\
&= \frac{1}{2}B_{LF}B_{HF}[\cos(\omega_e t + \omega_h t + \delta_2 + \delta_1) + \cos(\omega_h t - \omega_e t + \delta_2 - \delta_1)]
\end{aligned}
\tag{7.13}
$$

$$
\begin{aligned}
L_{bb} &\propto \mu_{r\_b} \propto B_{LF}B_{HF}\cos(\omega_e t + \delta_1 - \frac{2\pi}{3})\cos(\omega_h t + \delta_2 - \frac{2\pi}{3}) \\
&= \frac{1}{2}B_{LF}B_{HF}[\cos(\omega_e t + \omega_h t + \delta_2 + \delta_1 - \frac{4\pi}{3}) + \cos(\omega_h t - \omega_e t + \delta_2 - \delta_1)]
\end{aligned}
\tag{7.14}
$$

$$
\begin{aligned}
L_{cc} &\propto \mu_{r\_c} \propto B_{LF}B_{HF}\cos(\omega_e t + \delta_1 + \frac{2\pi}{3})\cos(\omega_h t + \delta_2 + \frac{2\pi}{3}) \\
&= \frac{1}{2}B_{LF}B_{HF}[\cos(\omega_e t + \omega_h t + \delta_2 + \delta_1 + \frac{4\pi}{3}) + \cos(\omega_h t - \omega_e t + \delta_2 - \delta_1)]
\end{aligned}
\tag{7.15}
$$

From (7.13)-(7.15), it can be seen that the first term of $B_{HF}{\cdot}B_{LF}$ for each phase is in the angle difference of -120 deg. (i.e., negative sequence components), while the second term is in phase (i.e., zero sequence components). Therefore, the resultant three phase HF inductance sequences are described in the expressions of (7.10)-(7.12) as analysed above. Accordingly, the vector relations for the three phase inductance harmonics are depicted in Fig. 7.8, in which the rotation sequence of these harmonics can be clearly observed.

Furthermore, from (7.10)-(7.12), due to that the magnetic polarity information has been recorded into the two HF inductance harmonics $((f_h/f_e-1)^{th}$ and $(f_h/f_e+1)^{th})$, the resultant position estimation performances utilising the interaction between HF field and the HF inductance (reluctance) harmonics can be significantly enhanced. This is due to that the time-consuming magnetic polarity identification processes can be completely eliminated. It should be noted that the secondary harmonics from the interaction between HF field and the HF inductance harmonics appear in both the carrier currents and zero sequence carrier voltages as analysed as follows.

(a) 2nd harmonic negative sequence inductance

(b) (f_h/f_e-1)th harmonic zero sequence inductance

(c) (f_h/f_e+1)th harmonic negative sequence inductance
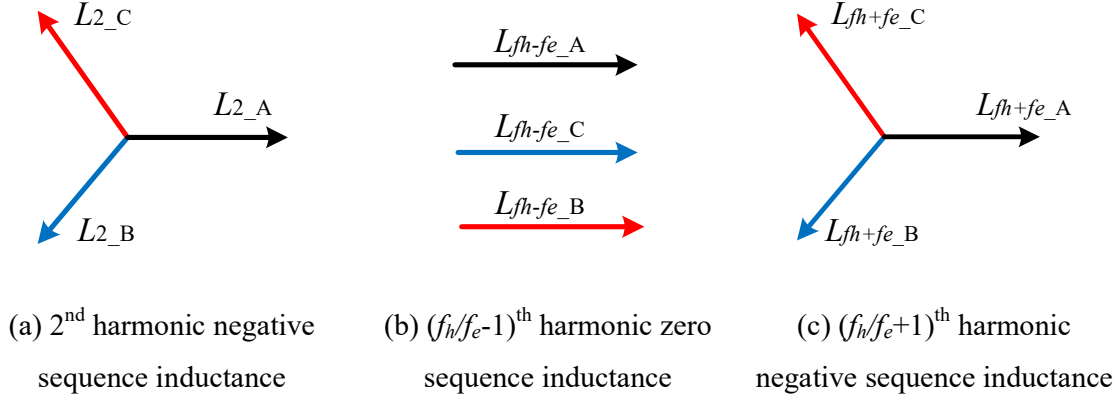
Fig. 7.8 Rotation sequence of inductance harmonics.

7.3.1 Carrier current expressions

From (7.10)-(7.12), by coordinate transformation, the d-axis and q-axis inductances can be derived as

$$L_d = L_0 - L_2/2 + L_{f_h-f_e}\sin(\omega_h t - \theta_e)/2 + L_{f_h+f_e}\sin(\omega_h t - \theta_e)/2$$
$$L_q = L_0 + L_2/2 + L_{f_h-f_e}\sin(\omega_h t - \theta_e)/2 - L_{f_h+f_e}\sin(\omega_h t - \theta_e)/2 \qquad (7.16)$$
$$L_{dq} = L_{f_h+f_e}\cos(\omega_h t - \theta_e)/2$$

Then, the rotating voltage signal injection in the stationary reference frame is derived as [JAN95]

$$U_\alpha + jU_\beta = U(\cos\omega_h t + j\sin\omega_h t) \qquad (7.17)$$

Thus, accordingly, the carrier currents in the stationary reference frame can be expressed as

$$i_{\alpha\beta}^h \approx \frac{U}{\omega_h(L_0^2 - L_2^2/4)}[2L_0 e^{j(\omega_h t - \frac{\pi}{2})} + L_2 e^{j(-\omega_h t + 2\theta_e + \frac{\pi}{2})} + \frac{L_{f_h-f_e}}{2}e^{j(2\omega_h t - \theta_e)} - \frac{L_{f_h+f_e}}{2}e^{j(-2\omega_h t + 3\theta_e)}] \qquad (7.18)$$

where $i_{\alpha\beta}^h$ represents the carrier currents in the αβ stationary reference frame. From (7.18), apart from the well-known positive and negative sequence carrier current components at f_h and $-f_h+2f_e$ [JAN95], additional secondary positive sequence harmonics at $2f_h-f_e$ and negative sequence carrier current at $-2f_h+3f_e$ arise due to the HF inductance harmonics (i.e., HF saliency). Since the positive sequence carrier current $2f_h-f_e$ contains the actual rotor position information, it can be used for magnetic polarity identification, which has been discussed in [JEO05] [RAC08c]. Therefore, from the above analyses in this chapter, the principle of the

carrier current secondary harmonics has been physically explained, i.e., the interaction of injected HF field and modulated HF saliency. However, as analysed in [JEO05] [GON13], the amplitudes of carrier current secondary harmonics are relatively small. Therefore, if they are directly used for position estimation, the resultant estimation performances are degraded, which will be shown experimentally in section 7.5.

7.3.2 Zero sequence carrier voltage expressions

On the other hand, as analysed in [BRI05] [CON06], zero sequence carrier voltage also contains rotor position information, and can be measured with one balanced resistor network and the access to the machine neutral point as shown in Fig. 4.1 in chapter 4. Accordingly, based on (4.1), (4.4)-(4.9), and the inductance information in (7.16), the zero sequence carrier voltage U_{RN} in Fig. 4.1 can be obtained as

$$U_{RN} \approx U \frac{[L_0 L_2 \cos(\omega_h t + 2\theta_e) - L_2^2 \cos(\omega_h t - 4\theta_e) - (L_0 L_{f_h + f_e} + \frac{L_2 L_{f_h - f_e}}{2}) \sin(2\omega_h t + \theta_e)]}{(2L_0^2 - L_2^2/2)} \tag{7.19}$$

From (7.19), it can be seen that the zero sequence carrier voltage mainly contains three components, i.e., $f_h + 2f_e$ and $f_h - 4f_e$ [BRI05] [CON06], and $2f_h + f_e$, respectively. Particularly, the presence of third term $2f_h + f_e$ is due to the HF saliency effects, due to the interaction between HF field and the modulated HF saliency as analysed above.

To verify the above derivations, rotating signals (U=8V and f_h=300 Hz) have been injected on the prototype PM machine, and the measured secondary harmonics of zero sequence carrier voltages and carrier currents under different loads are shown in Fig. 7.9-Fig. 7.10, respectively. The fundamental frequency f_e of machine is 2.5 Hz. Thus, the secondary current harmonics are mainly located at 237th ($2f_h/f_e$-1) and 239th (-$2f_h/f_e$+3), while zero sequence carrier voltage is mainly at 241th ($2f_h/f_e$+1), which are all in accordance with theoretical analyses in (7.18) and (7.19). Furthermore, from Fig. 7.9-Fig. 7.10, it is expected that the position estimation using secondary harmonics of zero sequence voltage will be more advantageous since the zero sequence carrier voltage has relatively large signal amplitude and less distortions (especially under load conditions), i.e., larger S/N ratio, compared to that of carrier current. Further experimental comparative results will be presented in 7.5.
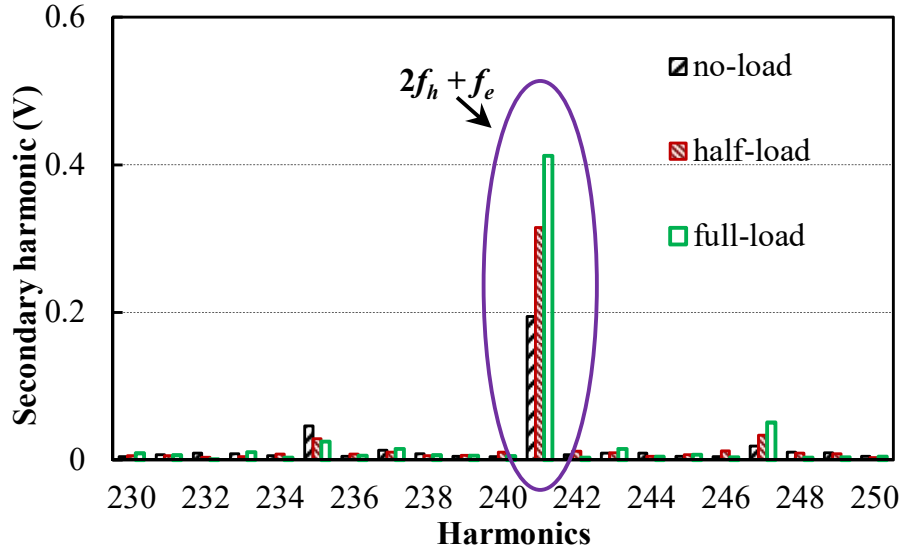
Fig. 7.9 Spectra of measured zero sequence carrier voltage secondary harmonics for rotating signal injection under different loads.
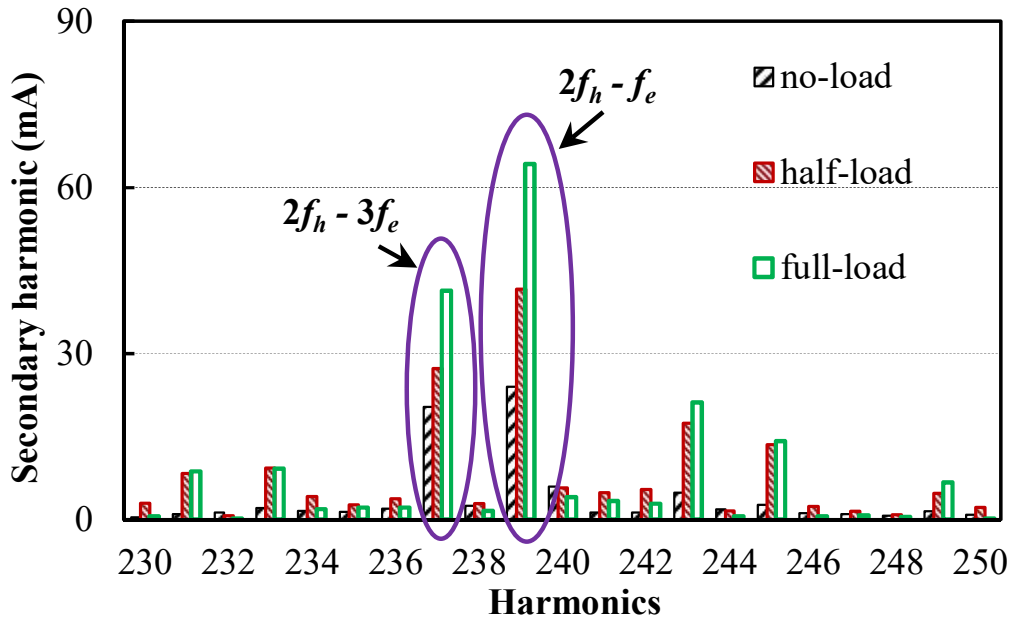
Fig. 7.10 Spectra of measured carrier current secondary harmonics for rotating signal injection under different loads.

7.4 Implementation for HF Saliency Based Sensorless Control

The signal processes for the HF saliency based position estimation method are introduced in this part. According to (7.18), the extraction of $(2f_h/f_e\text{-}1)^{\text{th}}$ harmonics can be expressed as

$$I_{\alpha\beta}^h = LPF(i_{\alpha\beta}^h e^{j(-2\omega_h t)}) = \frac{UL_{f_h-f_e}}{4\omega_h(L_0^2 - L_2^2/4)} e^{-j\theta_e} \tag{7.20}$$

Then, with (7.20), the final rotor position can be estimated with position tracking observer as shown in Fig. 7.11. For comparison, the conventional negative sequence carrier current based position estimation method [JAN95] is also depicted in Fig. 7.11. The differences between the two methods can be clearly observed in terms of signal demodulation.

Similarly, for the zero sequence carrier voltage in (7.19), the signal processing for the secondary harmonics can be expressed as

$$\begin{cases} U_{RN\alpha} = LPF(U_{RN} * \cos 2\omega_h t) = -\dfrac{U(2L_0 L_{f_h+f_e} + L_2 L_{f_h-f_e})}{8L_0^2 - 2L_2^2} \sin(\theta_e) \\[4mm] U_{RN\beta} = LPF(U_{RN} * \sin 2\omega_h t) = -\dfrac{U(2L_0 L_{f_h+f_e} + L_2 L_{f_h-f_e})}{8L_0^2 - 2L_2^2} \cos(\theta_e) \end{cases} \tag{7.21}$$

Accordingly, the block diagram for the signal demodulation of zero sequence carrier voltage in (7.21) is shown in Fig. 7.12 together with the conventional zero sequence method [BRI05]. It is expected that by utilising the modulated HF saliency rather than the inherent machine saliency, the output of position tracking observer $\hat{\theta}_e$ does not have the ambiguity of π as analysed above.
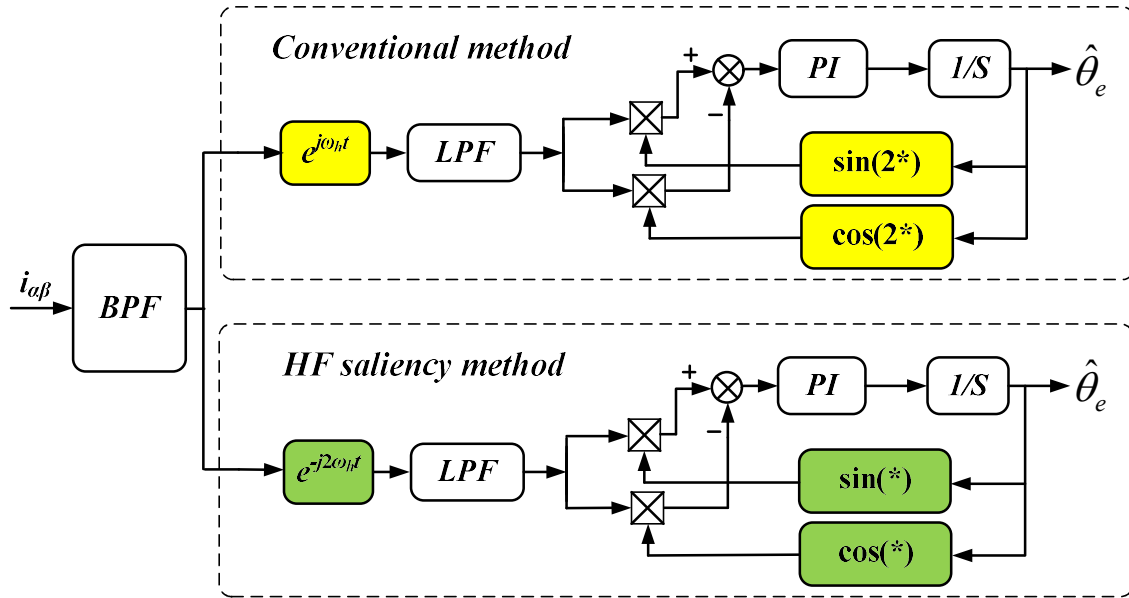
Fig. 7.11 Block diagram of position estimation using carrier current responses.
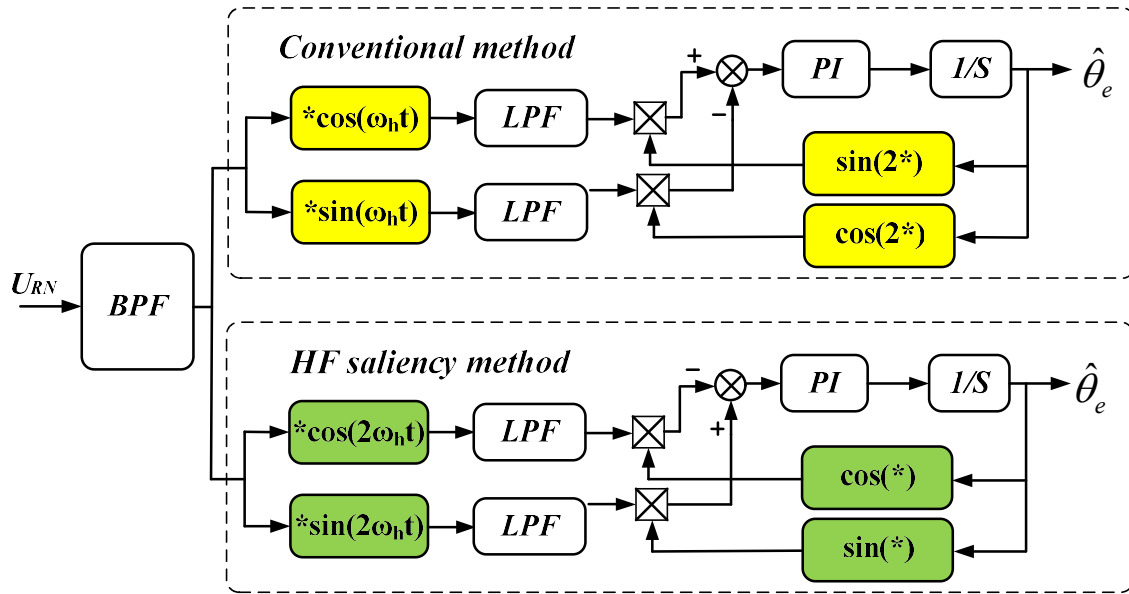
Fig. 7.12 Block diagram of position estimation using zero sequence voltage responses.

7.5 Experimental Validation

The experiments are implemented on a dSPACE DS1006 platform to validate the HF saliency based position estimation methods on the prototype PM machine. The machine parameters of the prototype PM machine are given in Table 7.1

Table 7.1 Parameters of Prototype PM Machine Tested

Rated voltage	36	V
Rated current	10	A
Rated speed	400	rpm
Rated torque	5.5	Nm
Nominal phase resistance	0.32	Ω
Average phase inductance (FE)	2.4	mH
2nd harmonic phase inductance (FE)	0.6	mH
$(f_h/f_e \pm 1)^{th}$ HF phase inductance (FE)	0.08/0.09	mH
Pole number	10	
PM flux-linkage	70.7	mWb

7.5.1 Steady-state and dynamic position estimation performances

The steady-state sensorless control performances utilising HF saliency are illustrated in Fig. 7.13-Fig. 7.14 with carrier current and zero sequence carrier voltage sensing, respectively. The injection signal is set as 8 V and 300Hz with the rotor reference speed given as 50 rpm. As can be seen from Fig. 7.13, the carrier current secondary harmonic (frequency at $2f_h$-f_e in (7.18)) based position estimation presents larger estimation error, and also undesirable distortions, which indicates that it is not suitable for the direct position estimation due to the smaller S/N ratio as discussed above [RAC08c]. In contrast, in Fig. 7.14, the secondary harmonic of zero sequence carrier voltage (frequency at $2f_h$+f_e in (7.19)) based method shows stable and robust estimation performance, which can be attributed to the larger signal amplitude and less distortions for the zero sequence carrier voltage in Fig. 7.9. Therefore, for the remaining experiments, only the zero sequence carrier voltage based method exploiting the HF saliency is performed for the further verification.
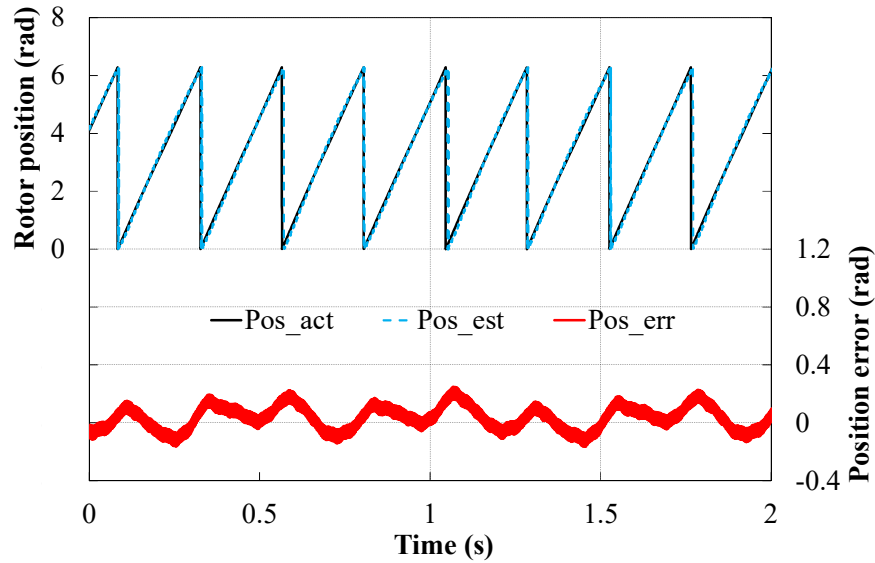
Fig. 7.13 Steady-state position estimation performances using secondary harmonics of carrier current.
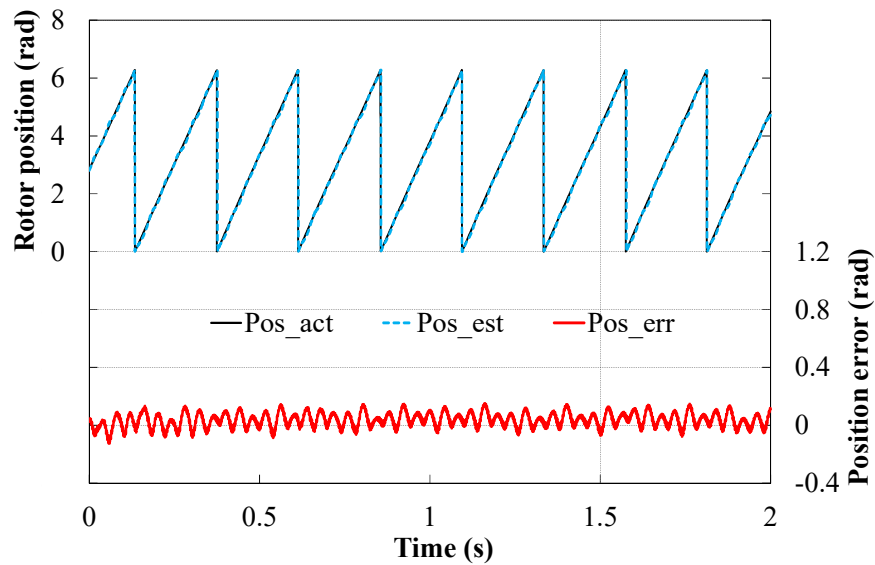
Fig. 7.14 Steady-state position estimation performances using secondary harmonics of zero sequence carrier voltage.

The dynamic performance is shown in Fig. 7.15 where rotor speed reference is changed from 0-30-50 rpm. The injected carrier signals are the same as that in the steady state conditions. The quick dynamic response can be obtained. The step load test is also performed on the prototype PM machine as shown in Fig. 7.16. Good position tracking performances are also demonstrated when q-axis current is quickly increased from 0.3 A to 7 A. Therefore, it

can be concluded that the HF saliency based position estimation method presents good dynamic performances at different speed and load conditions.
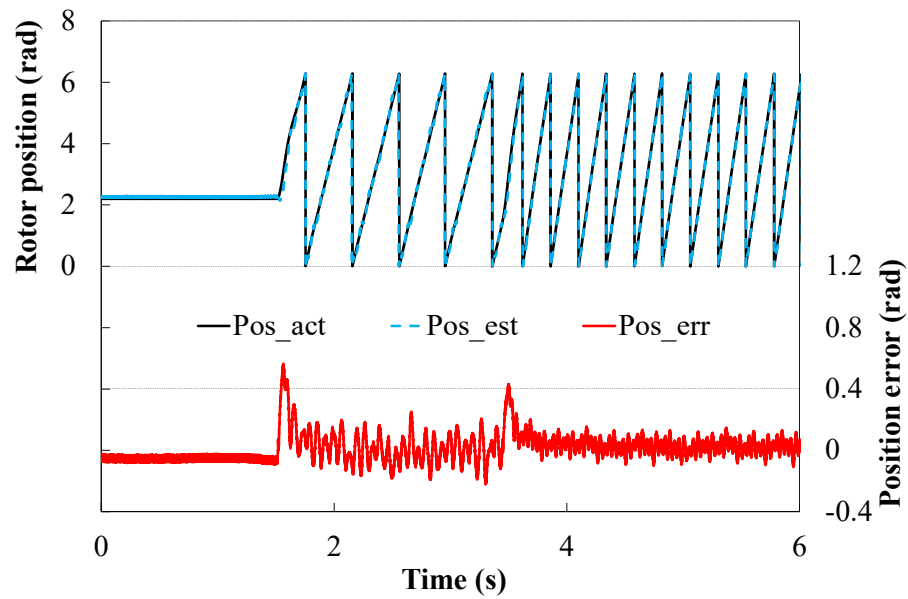
(a) Position estimation performance
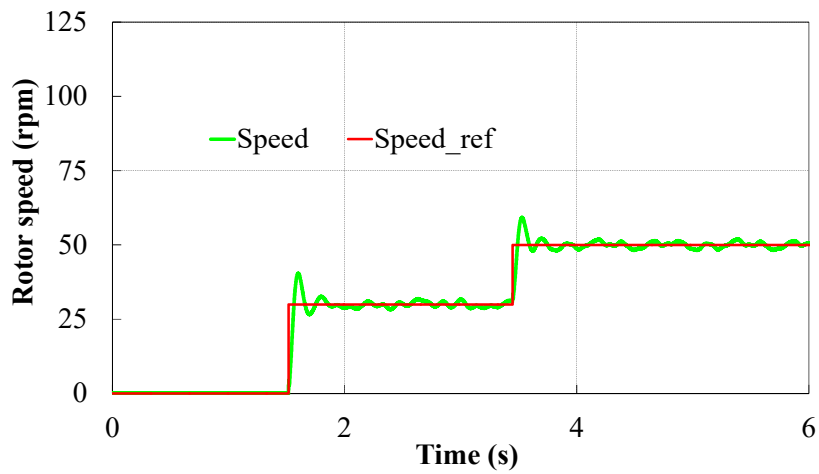
(b) Speed reference and actual rotor speed

Fig. 7.15 Dynamic performance under step speed reference.
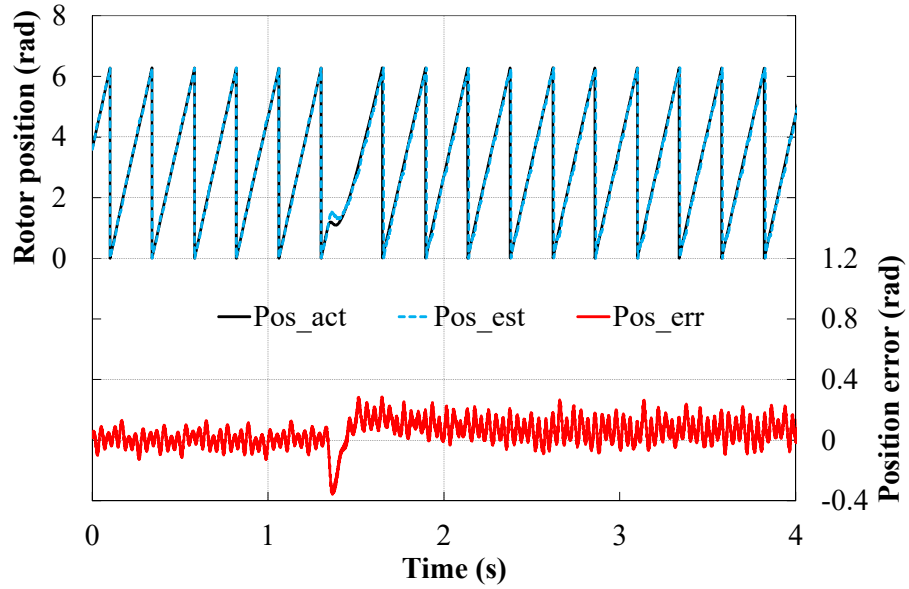
(a) Position estimation performance
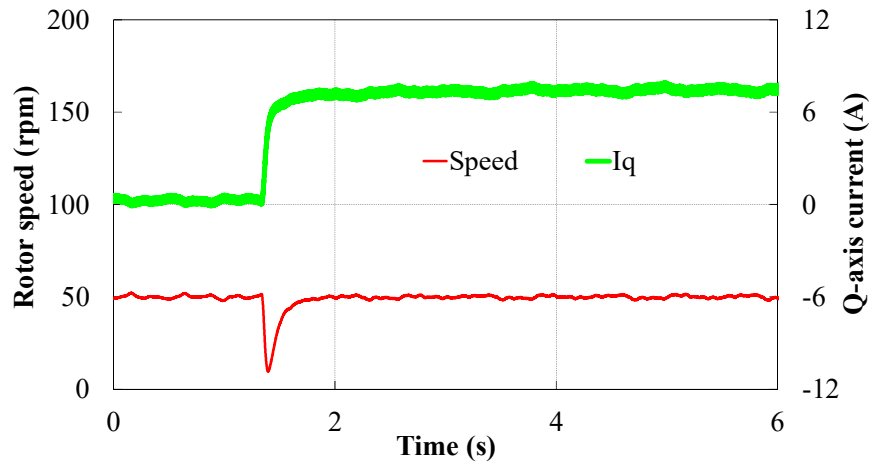
(b) Actual rotor speed and q-axis current

Fig. 7.16 Dynamic performance under step load.

7.5.2 Initial rotor position estimation and disturbance test

The initial rotor position estimation is implemented as shown in Fig. 7.17 utilising the modulated HF saliency, with the fundamental excitation set as 0 A. It can be seen that the actual position can be accurately tracked regardless of whether the rotor stops in the south- or north-pole (i.e., 0.86 rad or 4 (0.86+π) rads in Fig. 7.17). By contrast, at the same rotor positions, the conventional position tracking method using inherent saliency performed as

179

shown in Fig. 7.18, and the ambiguity of π is expected at 4 rads. Thus, the HF saliency based method is of great significance, not only for the elimination of time-consuming polarity identification, but because greatly enhances the estimation stability during normal operation, which is then verified by the disturbance tests in Fig. 7.19-Fig. 7.20. In Fig. 7.19-Fig. 7.20, the disturbance of π is added to the output of position tracking observer in Fig. 7.12 (i.e., the feedback of the observer adds π). It can be seen that for the conventional method, Fig. 7.19, the observed position estimation error changes rapidly with the error of angle π/-π. For the HF saliency based method in Fig. 7.20, it still converges to the actual rotor position showing great robustness and stability as expected.
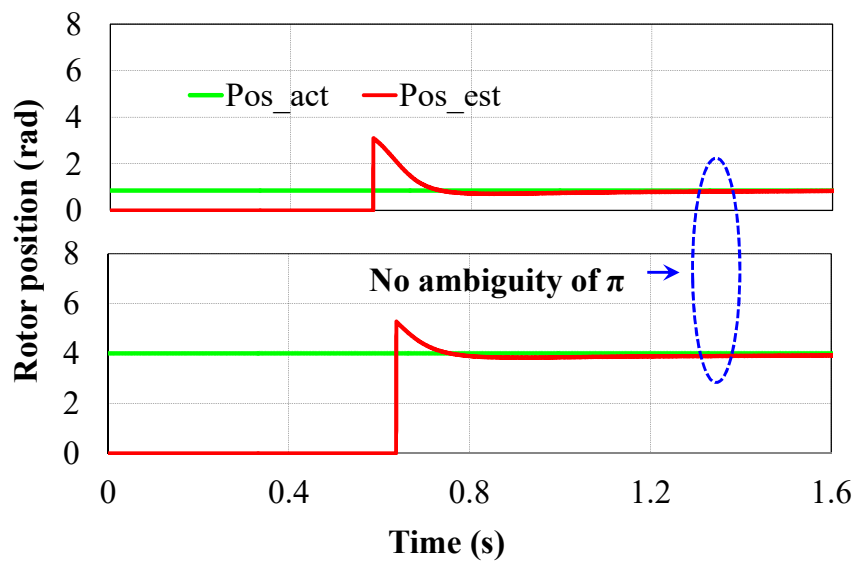
Fig. 7.17 Position estimation at 0.86 rad and 4 rad using HF saliency.
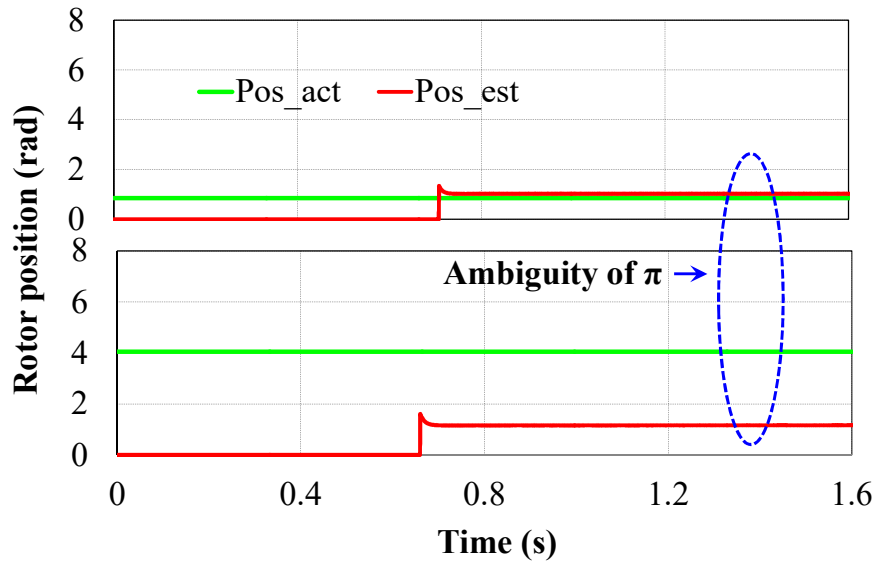
Fig. 7.18 Position estimation at 0.86 rad and 4 rad using inherent saliency.
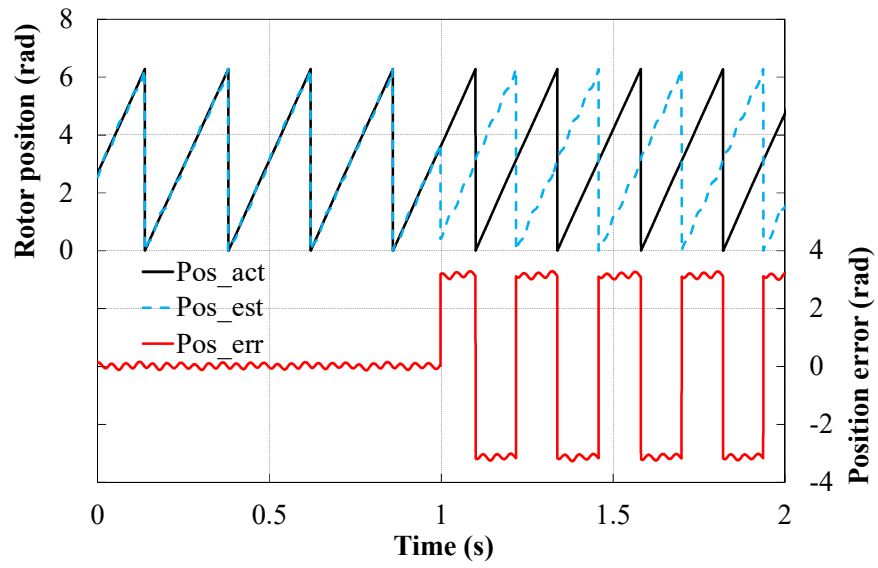
Fig. 7.19 Position estimation using inherent saliency with disturbance of π.
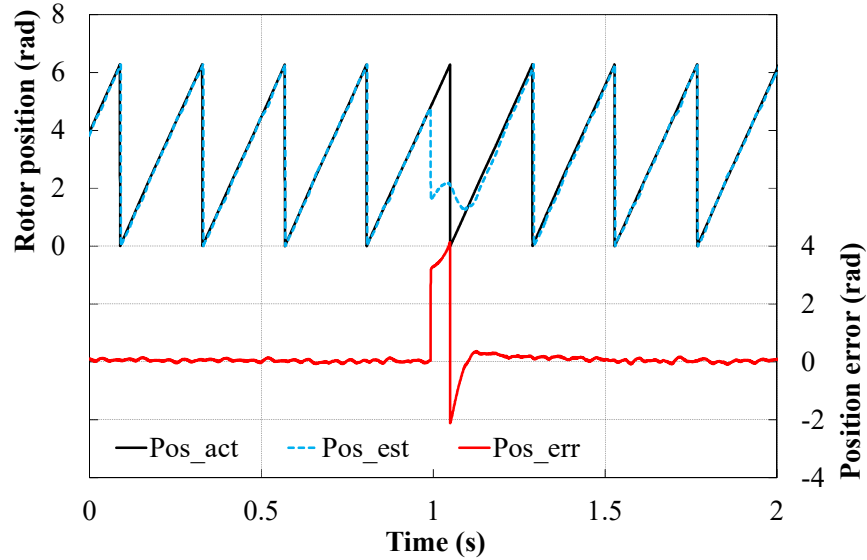
Fig. 7.20 Position estimation using HF saliency with disturbance of π.

7.6 Conclusions

This chapter has proposed the position estimation method using the modulated HF saliency for PMSMs without the need of magnetic polarity identification. Experimental analyses have been employed on the prototype PM machine to verify the theoretical analyses. Several main conclusions can be obtained as follows.

1) The presence of HF saliency is due to the saturation modulation between HF field and main flux field due to the nonlinear B-H curve characteristics.

2) The interaction between HF field and HF saliency generates rotor position dependant carrier signals containing actual rotor position information, which can be directly used for position estimation without ambiguity of machine polarity.

3) The HF saliency based zero sequence carrier voltage demonstrates better position estimation performances than those of carrier current due to larger signal amplitudes and less distortions.

4) The HF saliency based method not only removes time-consuming magnetic polarity identification process, but it also significantly improves the robustness and stability for rotor position estimation.

8 Comparison of Carrier Signal Injection Methods for Sensorless Control of Permanent Magnet Synchronous Machines

8.1 Introduction

As introduced in the previous chapters, the carrier signal injection methods exploiting the inherent machine saliency can be generally divided into the rotating injection in the stationary reference frame [JAN95] [DEG98] and the pulsating injection in the estimated synchronous reference frame (synchronous pulsating injection) [JAN03] [ZHU11]. Many efforts have been taken to compare the different carrier signal injection methods, and accordingly these comparisons can be classified into two groups. The first group is to compare different carrier responses for one specific injection method [BRI05] [GAR07]. In [BRI05], for rotating injection method, two carrier responses, i.e., the negative sequence carrier current and zero sequence carrier voltage have been compared. It is found that the zero sequence carrier voltage based strategy is more advantageous in terms of the THD, the sensitivity to the carrier injection distortion, the system bandwidth and estimation stability [GAR07]. However, in [GAR07], the physical explanations and detailed derivations, e.g., the inverter nonlinearity effects, are not given specifically and will be further derived analytically and explained insightfully in this chapter (e.g. why the zero sequence voltage is more advantageous). Besides, only the rotating injection method is discussed in [GAR07], and therefore the discussions will also be extended in this chapter to the other different injection methods considering alternative carrier responses.

The second group is to compare different injection methods but with only one specific type of carrier response sensing, e.g., the carrier current response [KIM04a] [RAC08a] [RAC08c]. In [KIM04a] [RAC08a], by comparing the rotating and the synchronous pulsating signal injection (both with carrier current sampling), it is found that the pulsating injection has higher estimation accuracy while rotating injection is more robust. In [RAC08c], further analytical work and experimental results under various conditions are also performed to compare the two injection methods considering the nonlinear parasitic effects, e.g., inverter nonlinearity, multiple saliencies, etc.

Obviously, the existing comparison efforts primarily focused on the two injection methods, i.e., the rotating injection and synchronous pulsating injection [GAR07] [KIM04a] [RAC08c]. There are actually limited discussions for the systematic comparisons between the three

injection methods (i.e., the two existing injection methods plus the anti-rotating pulsating injection method as illustrated in chapter 4) with the consideration of alternative sensing responses.

Therefore, this chapter presents the full comparisons for the different carrier signal injection methods for the sensorless control of PMSMs, considering alternative carrier responses. Specifically, the influence of signal processing delays, the cross-coupling magnetic saturation effects, inverter nonlinearity effects, multiple saliency effects, and the iron and PM losses due to carrier injection, will be presented. With the analyses of these effects, it provides more physical understandings about how the carrier injection method works and how it is affected by the nonlinear behaviours of the PM machine or inverter, etc. The theoretical comparative studies will be confirmed by the finite element (FE) simulation or experimental results on a prototype PM machine.

8.2   Carrier Signal Injection Model

Firstly, according to the previous chapters, the general model for the different carrier signal injection methods, i.e., the rotating injection [JAN95], synchronous pulsating [JAN03] and the anti-rotating pulsating injection will be briefly introduced in this section.

8.2.1   Rotating signal injection with carrier current sensing

According to [JAN95], for rotating signal injection, Fig. 2.15, the carrier current response can be expressed as

$$i_{\alpha\beta}^h = \frac{U}{2\omega_h L_d L_q}[(L_d + L_q)e^{j(\omega_h t - \frac{\pi}{2})} + (-L_d + L_q)e^{j(-\omega_h t + 2\theta_e + \frac{\pi}{2})}] \qquad (8.1)$$

where $i_{\alpha\beta}^h$ presents the carrier current in the αβ stationary reference frame, L_d and L_q are the incremental d- and q-axis inductances, θ_e is the electrical rotor position, respectively.

8.2.2   Rotating signal injection with zero sequence voltage sensing

Besides, for rotating signal injection, the zero sequence voltage (U_{RN}, Fig. 4.1) also contains rotor position information [BRI05], and can be described as

$$U_{RN} = \frac{2L_0 L_2 U}{4L_0^2 - L_2^2} \cos(\omega_h t + 2\theta_e) - \frac{L_2^2 U}{4L_0^2 - L_2^2} \cos(\omega_h t - 4\theta_e) \qquad (8.2)$$

where L_0, L_2 are the amplitudes of dc and 2nd harmonics of phase self-inductances, respectively. It is noted that in (8.2), the phase mutual-inductances have been neglected for the simplified analyses since the mutual inductances for the prototype PM machine are relatively small (Fig. 4.4). However, the mutual-coupling among phases will not affect the position estimation mechanisms as shown in chapter 4.

Then, from above, since typically $2L_0$ is much bigger than L_2, the 2nd term of (8.2) can be neglected [BRI05], and the first term is utilised for rotor position estimation, i.e.,

$$U_{RN} = \frac{2L_0 L_2 U}{4L_0^2 - L_2^2} \cos(\omega_h t + 2\theta_e) \qquad (8.3)$$

8.2.3 Synchronous pulsating signal injection with carrier current sensing

Generally, the pulsating signal injection as shown in Fig. 2.3 is performed in the estimated synchronous d-axis, and accordingly the estimated q-axis carrier current can be used for position estimation and described as [JAN03]

$$\hat{i}_{qh} = \frac{U}{\omega_h} \frac{(-L_d + L_q)}{2L_d L_q} \sin(2\Delta\theta) \sin\omega_h t \qquad (8.4)$$

From (8.4), it can be seen that the carrier current for the synchronous pulsating injection is amplitude-modulated by machine saliency, leading to high accuracy and robustness [RAC08c].

8.2.4 Anti-rotating pulsating signal injection with zero sequence voltage sensing

As illustrated in chapter 4, this type of pulsating signal injection is employed in the estimated reference frame, anti-rotating at twice the rotor's electrical angular speed, Fig. 4.8. The resultant zero sequence carrier voltage can be described as

$$U_{RN} = \frac{2UL_0 L_2 \cos\omega_h t}{4L_0^2 - L_2^2} \sin(2\Delta\theta) \qquad (8.5)$$

Therefore, from (8.5), it can be seen that with the anti-rotating injection method, the zero sequence voltage is also amplitude-modulated by machine saliency, showing high accuracy and robustness as discussed in chapter 4.

8.3 Comparison of Different Carrier Signal Injection Methods

Then, with the above modelling about the different injection methods with alternative sensing signals, the detailed comparisons in terms of signal processing delays, cross coupling magnetic saturation effects, inverter nonlinearity, multiple saliencies, iron and PM losses, etc., will be analysed as follows.

8.3.1 Influence of signal processing delay effects

As reported in chapter 2 and [CUP12] [MOG13], the digital delays, analog circuit delays, A/D sampling delays, etc., can cause the phase shifts of carrier responses. Considering these signal processing delays, the carrier currents in (8.1) and (8.4) can be expressed as

$$i_{\alpha\beta}^h = \frac{U}{2\omega_h L_d L_q}[(L_d+L_q)e^{j(\omega_h t+\frac{\pi}{2}-\varphi)}+(-L_d+L_q)e^{j(-\omega_h t+2\theta_e+\frac{\pi}{2}-\varphi)}]$$

(8.6)

for rotating signal injection, and

$$\hat{i}_{qh} = \frac{U}{\omega_h}\frac{(-L_d+L_q)}{2L_d L_q}\sin(2\Delta\theta)\sin(\omega_h t-\varphi)$$

(8.7)

for the synchronous pulsating injection, respectively, where angle φ represents the phase shifts due to the signal processing delays. Then, with the signal demodulation, the position information signals in (8.6)-(8.7) can be expressed as

$$\begin{cases} i_{\alpha 1}=RE(LPF(i_{\alpha\beta}^h e^{j(\omega_h t-\frac{\pi}{2})})=\dfrac{U(-L_d+L_q)}{2\omega_h L_d L_q}\cos(2\theta_e-\varphi) \\[4mm] i_{\beta 1}=IM(LPF(i_{\alpha\beta}^h e^{j(\omega_h t-\frac{\pi}{2})})=\dfrac{U(-L_d+L_q)}{2\omega_h L_d L_q}\sin(2\theta_e-\varphi) \end{cases}$$

(8.8)

$$\hat{I}_{qh}=LPF(\hat{i}_{qh}*2\sin\omega_h t)=\frac{(-L_d+L_q)U}{2\omega_h L_d L_q}\cos\varphi\sin(2\Delta\theta)$$

(8.9)

Therefore, it can be seen from (8.8)-(8.9), with carrier current sensing, the signal processing delays can cause the position errors for the rotating signal injection, while not introducing position errors for synchronous pulsating injection since only the amplitudes of (8.9) are affected.

Similarly, with the consideration of signal processing delays, the zero sequence carrier voltages in (8.3) and (8.5) can be expressed as

$$\begin{cases} U_{RN\text{-}\alpha} = LPF(U_{RN} * 2\cos\omega_h t) = \dfrac{L_0 L_2 U}{2L_0^2 - \dfrac{1}{2}L_2^2}\cos(2\theta_e - \varphi) \\[4mm] U_{RN\text{-}\beta} = LPF(U_{RN} * 2\sin\omega_h t) = \dfrac{L_0 L_2 U}{2L_0^2 - \dfrac{1}{2}L_2^2}\sin(2\theta_e - \varphi) \end{cases} \tag{8.10}$$

$$U_{RN1} = LPF(U_{RN} * 2\cos\omega_h t) = \dfrac{L_0 L_2 U}{2L_0^2 - \dfrac{1}{2}L_2^2}\cos\varphi\sin(2\Delta\theta) \tag{8.11}$$

From (8.10)-(8.11), with zero sequence carrier voltage sensing, the delays can also cause the position errors for rotating signal injection. For the anti-rotating pulsating injection, the position estimation errors are unaffected, which is similar to the synchronous pulsating injection with carrier current sensing in (8.9).

In order to verify the above analysis about signal processing delays, average position estimation errors at different carrier frequencies (i.e., different signal processing delays) are measured and shown in Fig. 8.1. It can be seen that synchronous pulsating injection with carrier current sensing and anti-rotating pulsating injection with zero sequence carrier voltage sensing show great robustness to the variation of carrier frequency, while others types are sensitive to the carrier frequency variation. All these measured results are consistent with the above theoretical analyses. Therefore, it can be concluded that the synchronous pulsating signal injection with carrier current sensing and the anti-rotating pulsating injection with zero sequence voltage sensing are insensitive to the signal processing delays, while other types of methods show more sensitivity.
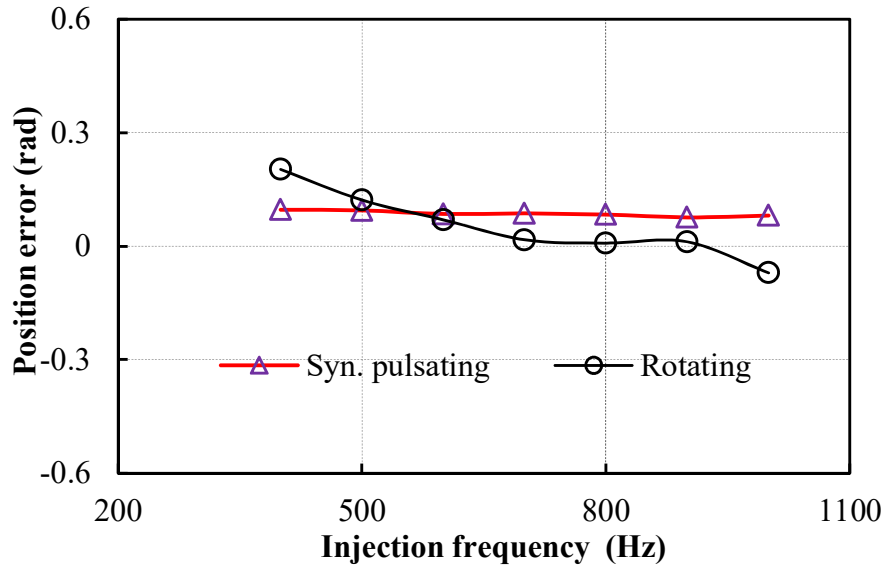
(a) Carrier current sensing based methods
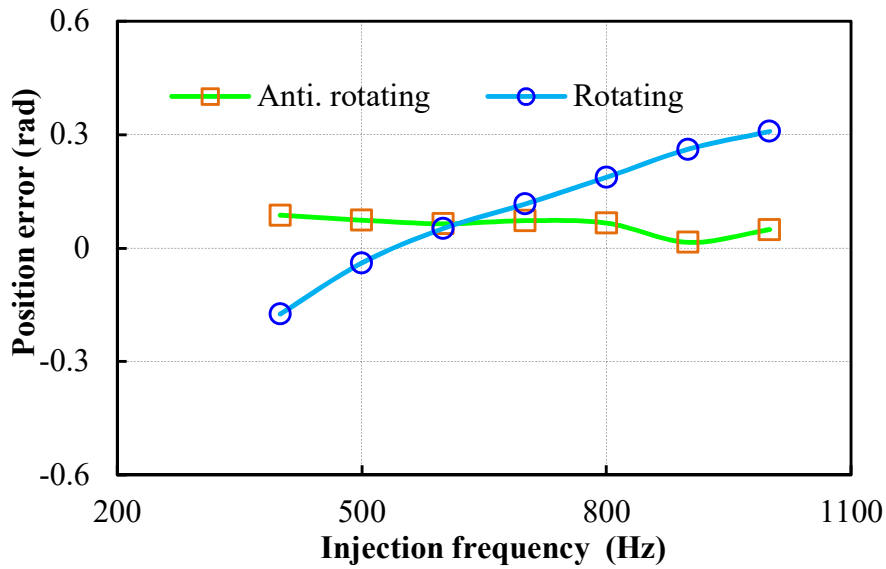
(b) Zero sequence voltage sensing based methods

Fig. 8.1 Average position errors with sensitivity to injection frequency considering delay effects.

8.3.2 Influence of cross coupling magnetic saturation effects

In this part, the magnetic saturation effects will be examined for the different injection methods. Although a lot of efforts have been taken to analyse the magnetic saturation effects

[GUG06] [LI09] [BIA07], the detailed comparisons for the different carrier responses of the carrier injection methods are not found, and will be investigated as follows.

From (8.1)-(8.5), under certain injection voltage and frequency, it can be seen that all the carrier responses for the three injections are only related to the machine inductance information. Accordingly, the inductance for one phase can be obtained by the frozen permeability (FP) method [CHU13] in the finite element (FE) simulation, under different load conditions, Fig. 8.2. The inductance calculated by the FP method is shown in Fig. 8.3.
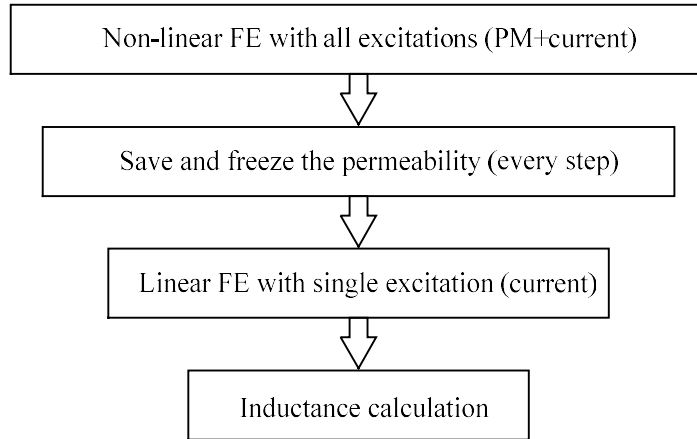
Fig. 8.2 Procedure of frozen permeability method for PM machine.

It can be seen from Fig. 8.3 that the maximum inductance point at load condition has been shifted due to the saturation effects. This can be explained by the relative permeability distribution at various load conditions as shown in Fig. 8.4. From Fig. 8.4, at the same d-axis position of the PM machine, the permeability distribution has been significantly shifted from no-load to load conditions, and obviously the on-load armature flux paths will be also changed, resulting in the inductance variations as shown in Fig. 8.3.

Accordingly, the magnitude and phase spectra of the inductances under various load conditions are also illustrated in Fig. 8.5(a)-(b). Because the average magnetic saturation increases under load conditions, the average (dc) inductance reduces as expected, Fig. 8.5(a), while the 2nd harmonic component, i.e., the main saliency, even increases, which can be attributed to the cross-coupling saturation effect. To be more specific, the inductances in dq-plane are calculated with the phase inductance data in Fig. 8.3 and then shown in Table 8.1. It can be seen that although the difference of d-/q-axis inductances (L_q-L_d) reduces from no-load

to full-load condition, the d-/q-axis mutual-inductance (L_{dq}) significantly increases from 0.02 mH to 0.34 mH, leading to even increased total inductive saliency, Fig. 8.5(a).

Table 8.1 Incremental Inductance at Different Loads

Inductance (mH)	L_d	L_q	L_q-L_d	L_{dq}
No-load	1.78	2.57	0.79	0.02
Full-load	1.69	2.18	0.49	0.34
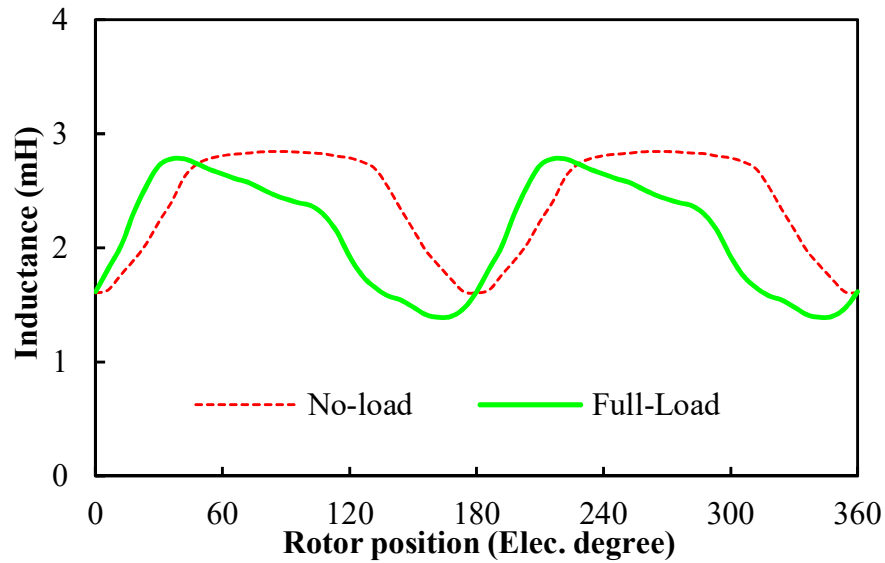
Fig. 8.3 Self-inductance for phase A obtained by FP method.

(a) No-load   (b) Full-load
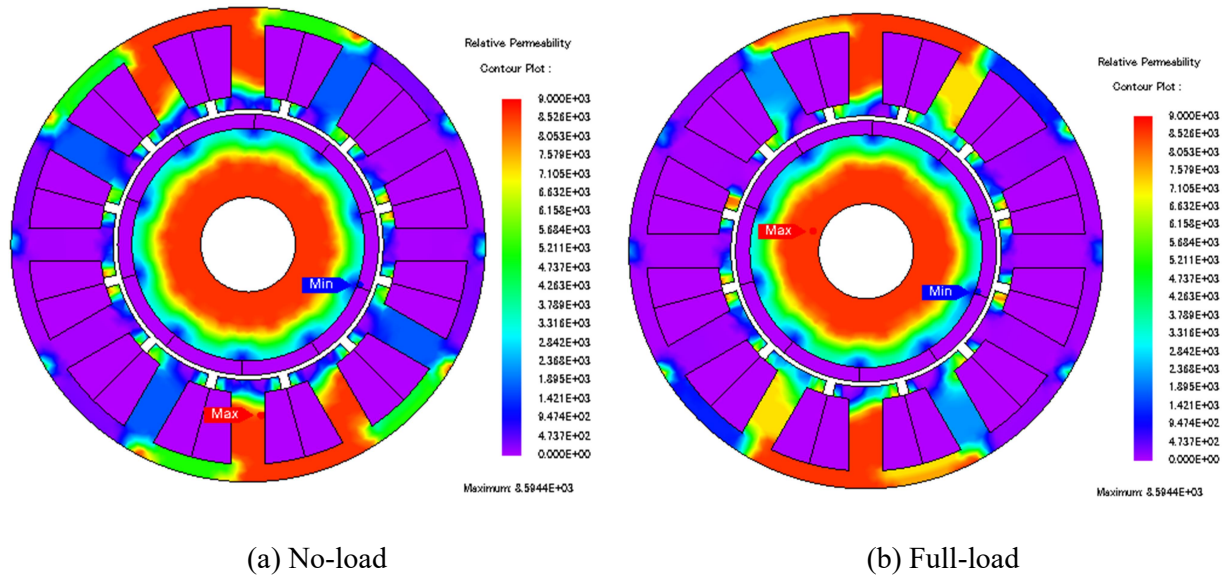
Fig. 8.4 Relative permeability distribution for the PM machine at θ_e=0 rad.
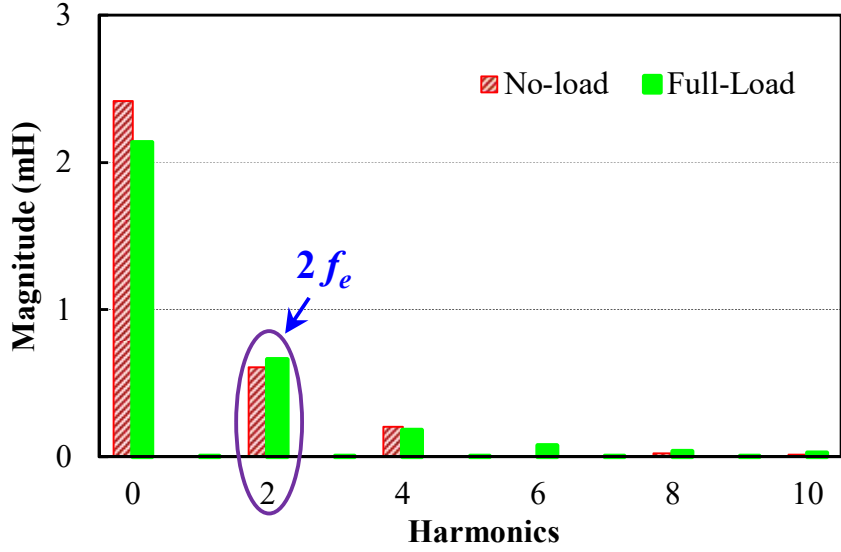
(a) Magnitude spectra
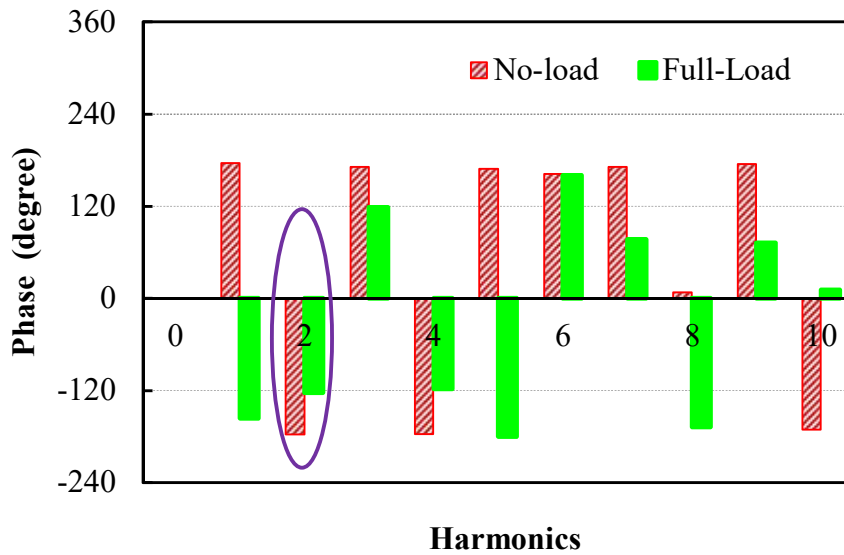
(b) Phase angle spectra

Fig. 8.5 Self-inductance spectra for phase A.

On the other hand, inevitably, the angle of the main saliency (2nd harmonic inductance) is shifted also due to the cross-coupling effects, Fig. 8.5(b), ~54.6 degs (2nd harmonic phase shift, Fig. 8.5(b)). This shifted angle can then lead to the phase shift of the carrier responses causing position estimation errors ($\Delta\theta$). Although the carrier current and zero sequence voltage responses in (8.1)-(8.5) are modelled in different reference frames, the position errors due to the cross-coupling effects are the same for the different injection methods. Specifically,

from Table 8.1, $\Delta\theta$ for carrier current based methods can be calculated as $\tan^{-1}(2L_{dq}/(L_q-L_d))\approx27$ degs [ZHU11], which equals to that for the zero sequence methods, i.e., the half of the phase shift of the 2nd harmonic inductance (~27.3 degs). This will be theoretically proved as follows.

Specifically, according to (4.23) [YAN06], with coordinate transformation, the d-/ q-axis inductances can be derived as

$$L_d = L_0 - \frac{L_2}{2}$$
$$L_q = L_0 + \frac{L_2}{2} \tag{8.12}$$
$$L_{dq} = \frac{L_c}{2}$$

Thus, considering cross-coupling magnetic effects, accordingly the carrier currents for the rotating and synchronous pulsating injection can be further obtained as

$$i_{\alpha\beta}^h = \frac{U}{2\omega_h L_d L_q}[(L_d + L_q)e^{j(\omega_h t - \frac{\pi}{2})} + (-L_d + L_q)e^{j(-\omega_h t + 2\theta_e + \frac{\pi}{2} + \theta_m)}] \tag{8.13}$$

$$\hat{i}_{qh} = \frac{U}{\omega_h}\frac{(-L_d + L_q)}{2L_d L_q}\sin(2\Delta\theta + \theta_m)\sin\omega_h t$$

where θ_m represents the cross coupling angle and can be expressed as [ZHU11] [LI09]

$$\theta_m = \arctan\frac{2L_{dq}}{L_d - L_q} \tag{8.14}$$

Similarly, the zero sequence carrier voltages for rotating and anti-rotating pulsating injection can be expressed as

$$U_{RN} = \frac{L_0 L_2 U}{2L_0{}^2 - \frac{1}{2}L_2{}^2}\cos(\omega_h t + 2\theta_e + \theta_{s3}) \tag{8.15}$$

$$U_{RN} = \frac{L_0 L_2 U}{2L_0{}^2 - \frac{1}{2}L_2{}^2}\cos\omega_h t\sin(2\Delta\theta + \theta_{s3}) \tag{8.16}$$

where θ_{s3} represents the cross coupling effects for zero sequence carrier voltages and can be expressed as

$$\theta_{s3} = -\arctan\frac{L_c}{L_2} \tag{8.17}$$

From (8.12), (8.14) and (8.17), it can be obtained that θ_m exactly equals θ_{s3}. Therefore, the cross-coupling saturation effects cause the same position estimation errors irrespective of signal injection and sensing types, as proved above. Accordingly, the cross-coupling angle can be measured by the offline tests, and then used for the online compensation as described in chapters 4-5.

Then, accordingly, the carrier responses under various load conditions are measured and shown in Fig. 8.6-Fig. 8.8 for the above carrier injection methods, respectively. The injection frequency and voltage for the three methods are all set as 600Hz/6V, and the fundamental frequency is set as 5 Hz. Firstly, for rotating signal injection, as illustrated in Fig. 8.6(a)-(b), it is observed that the main harmonics used for position estimation, i.e., the 122nd for the zero sequence voltage, and -118th for the negative sequence carrier current are increased under load conditions. Obviously, according to (8.1)-(8.3), this is because the average inductance reduces while the 2nd saliency inductance increases, as shown in Fig. 8.5(a). It is also noted that the disturbance harmonics, e.g., 110th and 116th for the zero sequence voltage, -130th and -112th for the negative sequence carrier current are also increased due to the load, which can also be attributed to the 6th, 8th, and 10th harmonic inductances in Fig. 8.5(a).

Further, for the pulsating injections in the estimated reference frame, it is quite difficult to measure the signal spectra since the main harmonic components in (8.4) and (8.5) become zero ($\Delta\theta \approx 0$) in the steady-state. In order to measure the carrier responses for the pulsating injections, with the assistance of encoder, $\Delta\theta$ is kept as $\pi/4$, i.e., the injected axis in Fig. 2.3-Fig. 4.8 has $\pi/4$ angular deviation to the actual rotor position. Accordingly, the measured spectra for the two injections are shown in Fig. 8.7-Fig. 8.8, from which it can be seen that the variations of the main harmonics are similar to those of rotating signal injection, Fig. 8.6. Therefore, from above analyses, it can be concluded that the magnetic saturation actually has similar influences on different injection methods with alternative sensing signals. Obviously, this is because they all rely on the same inductance saliency information to track the rotor position.
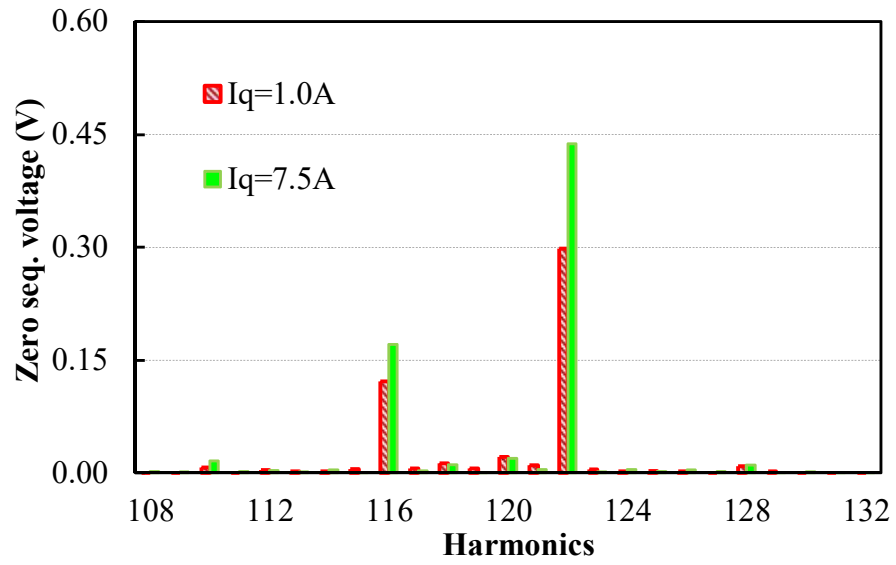
(a) Zero sequence voltage
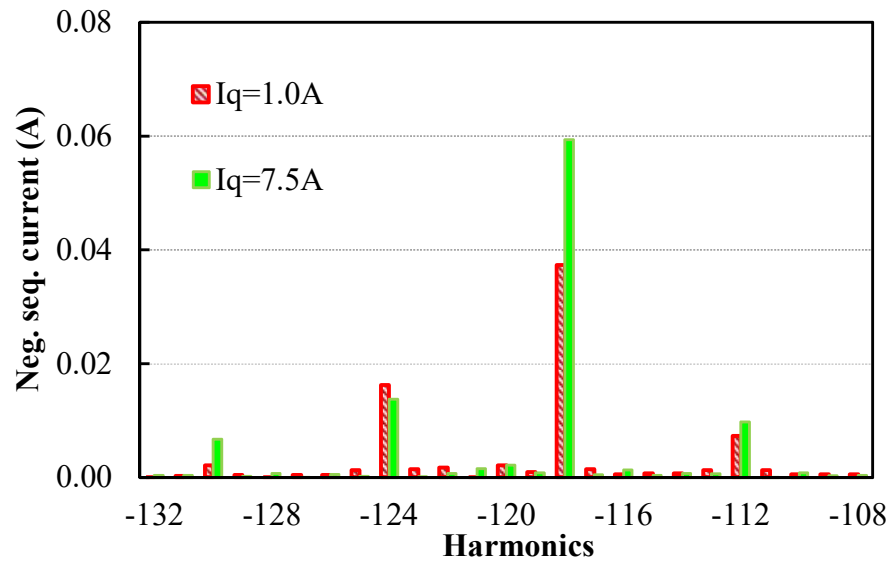
(b) Negative sequence carrier current

Fig. 8.6 Measured carrier responses for the rotating signal injection.
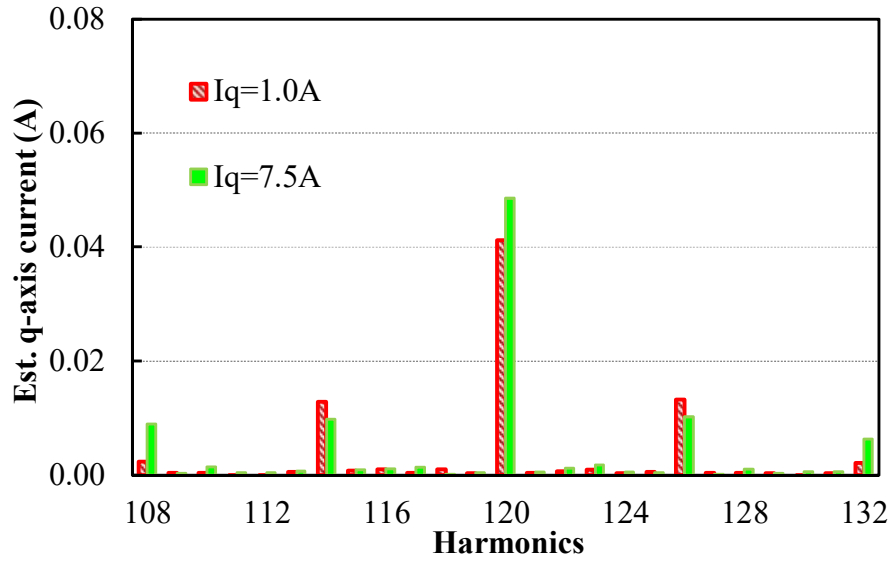
Fig. 8.7 Measured carrier current responses for the synchronous pulsating injection.
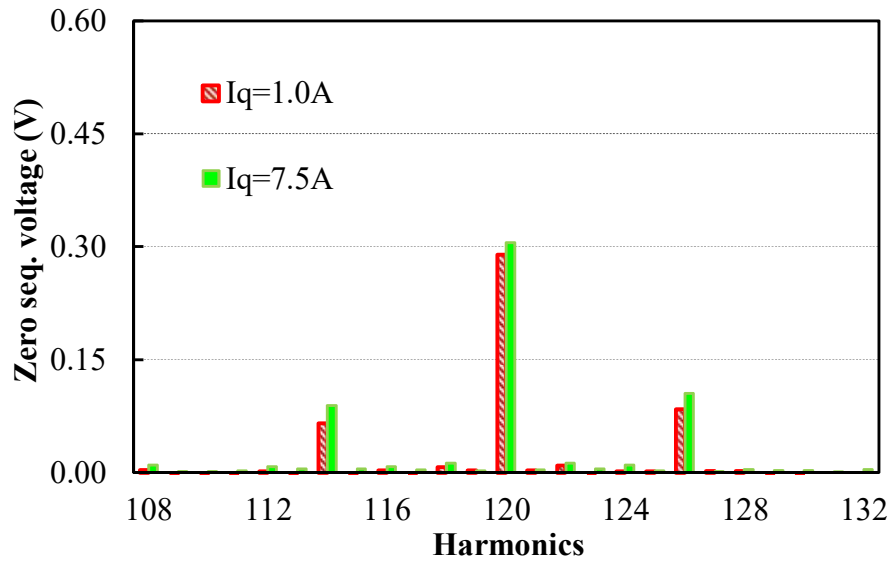
Fig. 8.8 Measured zero sequence responses for anti-rotating signal injection.

8.3.3 Influence of inverter nonlinearity effects

The position estimation of carrier signal injection methods is significantly affected by the inverter nonlinearity effects as reported in many literature, [GUE05] [GON11] [GAR07] [WAN14d], etc. In [GAR07], it is shown that for rotating signal injection, the zero sequence voltage response is less sensitive to the inverter distortions compared to the carrier current sensing, which however lacks of the more physical explanations. Besides, in [GAR07], only the rotating signal injection is discussed, and therefore in this section, the full comparisons

among the three injection methods considering inverter nonlinearity effects will be investigated. It will be found and shown analytically that the machine saliency ratio and semiconductor characteristics actually determine the inverter nonlinearity effects on different injection methods with alternative signal responses.

Specifically, according to [GON11], the voltage distortion around the carrier frequency due to the inverter nonlinearity effects is described as

$$\Delta \vec{u}_h = \frac{2}{3}[R_{ah}i_{ah} + R_{bh}i_{bh}e^{j2\pi/3} + R_{ch}i_{ch}e^{-j2\pi/3}]$$

(8.18)

where R_{ah}, R_{bh}, R_{ch} represent the equivalent HF resistances of inverter, which only exist when the phase currents are nearly crossing zero, i.e., in the zero current clamping (ZCC) zone [GON11] [CHO08]. Assuming instantly the phase A current around zero ($\theta_e \approx 0$), the distortion voltage in (8.18) can be simplified as

$$\Delta \vec{u}_h = \frac{2}{3}R_{ah}i_{ah}$$

(8.19)

For the HF injection method with zero sequence voltage sensing, this distortion voltage in (8.19) will give rise to the potential drifting of the voltage U_{RO}, which is normally believed to be zero without considering the inverter nonlinear behaviours (around the carrier injection frequency). Specifically, according to Fig. 4.1, the voltage equations can be expressed as

$$U_{AO} = U_{AR} + U_{RO}$$
$$U_{BO} = U_{BR} + U_{RO}$$
$$U_{CO} = U_{CR} + U_{RO}$$

(8.20)

Since at $\theta_e \approx 0$, the distortion voltage of $U_{AO}=2R_{ah}i_{ah}/3$, and $U_{BO}=U_{CO}=0$, while the injection voltages in U_{AO}, U_{BO} and U_{CO} are three phase balanced, the voltage in U_{RO} can be obtained as

$$U_{RO} = \frac{U_{AO}}{3} = \frac{2}{9}R_{ah}i_{ah}$$

(8.21)

Then, with the Y-connected windings and three phase voltage equations as given in (8.22) [GAR07], the zero sequence voltage for rotating signal injection considering the nonlinear behaviours of inverter can be obtained as (8.23) ($L_0=L_d/2+L_q/2$, $L_2=L_q-L_d$)

$$U_{AN} = U_{AO} - U_{RO} + U_{RN} = (L_0 - L_2\cos(2\theta_e))\frac{di_a}{dt}$$

$$U_{BN} = U_{BO} - U_{RO} + U_{RN} = (L_0 - L_2\cos(2\theta_e + \frac{2}{3}\pi))\frac{di_b}{dt}$$

(8.22)

$$U_{CN} = U_{CO} - U_{RO} + U_{RN} = (L_0 - L_2\cos(2\theta_e - \frac{2}{3}\pi))\frac{di_c}{dt}$$

$$U_{RN} = \frac{2UL_0 L_2\cos(\omega_h t + 2\theta_e)}{4L_0^2 - L_2^2} + R_{ah}i_{ah}\frac{4L_0 L_2}{12L_0^2 - 3L_2^2}$$

(8.23)

Then, from (8.23), the ratio γ of the distortion component (2nd term of (8.23)) to the main harmonic (1st term of (8.23)) used for position estimation can be defined and described as

$$\gamma_{zeq} = \frac{2R_{ah}}{3\omega_h L_d}$$

(8.24)

Similarly, with (2.1) and (8.18), the negative sequence carrier current for rotating injection considering the inverter nonlinearity effects can also be derived as follows. With (8.18), the distorted voltage for rotating injection can be further described as [GON11]

$$\Delta\vec{u}_h = \frac{1}{3}R_{ah}\frac{U}{\omega_h L_d}[e^{j(\omega_h t - \pi/2)} + e^{j(-\omega_h t + \pi/2)}]$$

(8.25)

Accordingly, the negative sequence carrier current considering the inverter nonlinearity effects can be expressed as

$$i_{neg}^h = \frac{U(-L_d + L_q)}{2\omega_h L_d L_q}e^{j(-\omega_h t + 2\theta_e + \frac{\pi}{2})} + \frac{UR_{ah}}{6\omega_h^2 L_d^2 L_q}(L_d + L_q)e^{j(-\omega_h t + \pi)}$$

$$+ \frac{UR_{ah}}{6\omega_h^2 L_d^2 L_q}(-L_d + L_q)e^{j(-\omega_h t + \pi)}$$

(8.26)

From (8.26), it is noted that in the negative sequence carrier current responses, there actually exist two distortion components due to the inverter nonlinearity effects, and obviously the middle term of (8.26) has the larger amplitude. The cause of this larger amplitude component is due to the interaction of the negative sequence carrier voltage in (8.25) (2nd term) and the average inductance ((L_d+L_q)/2, i.e., the zero sequence inductance). In contrast, from the above derivations, this large distortion component does exist in the zero sequence voltage in (8.23). Apparently, this is because the interaction of either the positive or the negative distorted voltage in (8.25) with the average inductance (i.e., the zero sequence

inductance) will not contribute to the zero sequence responses. Therefore, the physical reason why the zero sequence voltage has less sensitivity to the inverter distortions has been clearly explained as discussed above. The mechanism of inverter nonlinearity effects on different carrier signal responses for rotating signal injection is also depicted in Fig. 8.9. From Fig. 8.9, it can be further observed that the distortions of the negative sequence carrier current are mainly related to the average inductance, while those of the zero sequence carrier voltage are only affected by the saliency inductance. In other words, the inverter distorted voltages must interact with the saliency inductance (small) to produce the distortions (also small) in the zero sequence voltage response, while they can interact with the average inductance (large) to produce carrier current distortions (large). Hence, the distortions for the zero sequence voltage responses are much smaller, because the average inductance is much larger than the saliency inductance.
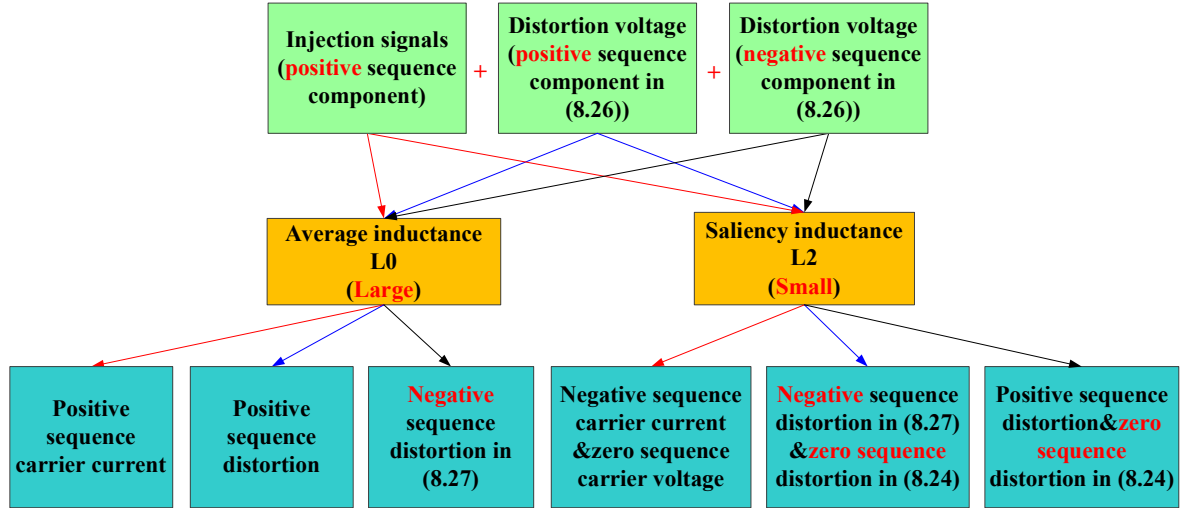
Fig. 8.9 Block diagram for inverter distortion mechanism for rotating signal injection method.

Furthermore, from (8.26), the distortion ratio γ of the negative sequence carrier current for rotating signal injection can be expressed as

$$\gamma_{neg} = R_{ah} \frac{2L_q}{3\omega_h L_d(-L_d + L_q)} \tag{8.27}$$

With (8.24) and (8.27), the distortion ratio comparisons between the zero sequence voltage and negative sequence carrier current can be described as

$$\delta_{zeq/neg} = |1 - \frac{L_d}{L_q}| \tag{8.28}$$

Therefore, from (8.28), the machine saliency ratio significantly influences the inverter nonlinearity effects on the two carrier responses for rotating signal injection, and the zero sequence voltage response will be much better than the carrier current especially when the machine saliency ratio is relatively small.

Similarly, for the anti-rotating pulsating injection, from (8.5) and (8.19)-(8.22), the distortion ratio for the zero sequence voltage response can be also obtained as

$$\gamma_{zeq} = \frac{2R_{ah}}{3\omega_h L_d} |\sin 2\theta_e| \tag{8.29}$$

Thus, from (8.29), compared to (8.24) for rotating signal injection, the distortion ratio γ_{zeq} is even smaller for the anti-rotating injection method since $|\sin(2\theta_e)|$ in (8.29) is quite small when phase A current nearly crosses zero ($\theta_e \approx 0$). It is noted that when the rotor position θ_e increases to certain angle, the phase A current will be out of the ZCC zone [GON11] [WAN14d], not affecting the carrier injection any more. Therefore, for the two injection methods both with zero sequence voltage sensing, the differences actually are relied on the inherent characteristics of the semiconductor devices (i.e., the parasitic capacitor effects determining the ZCC zone).

For the synchronous pulsating injection, the estimated d-/q-axis voltage distortions can be also obtained [WAN14]. To be more specific, the d-/q-axis voltage errors due to the inverter nonlinearities can be described as ($\theta_e \approx 0$, in the ZCC zone) [WAN14]

$$\Delta u_{dh} = \frac{2}{3} R_{ah} i_{ah} \cos \theta_e$$
$$\Delta u_{qh} = \frac{2}{3} R_{ah} i_{ah} \sin \theta_e \tag{8.30}$$

Accordingly, the q-axis carrier current in (8.4) can be further described as

$$\hat{i}_{qh} = \frac{(-L_d + L_q)}{2\omega_h L_d L_q} \sin(2\Delta\theta)(U \sin \omega_h t + \Delta u_{dh}) + \frac{(L_d + L_q) + (-L_d + L_q)\cos(2\Delta\theta)}{2\omega_h L_d L_q} \Delta u_{qh} \tag{8.31}$$

Therefore, the distortion ratio γ for synchronous pulsating injection can be approximately described as

$$\gamma_{\hat{q}} = R_{ah} \frac{(L_d + L_q)\sin 2\theta_e + 2(-L_d + L_q)\cos^2 \theta_e}{3\omega_h L_d (-L_d + L_q)} \tag{8.32}$$

From (8.32), similar to (8.26), the interaction of Δu_{qh} and the large average inductance could mainly cause the position error. However, since Δu_{qh} is attenuated by the term of 'sin(2θₑ)' when $\theta_e \approx 0$, the distortions in the carrier currents are expected to be smaller compared to the rotating injection in (8.27) for the prototype PM machine ($L_d/L_q \approx 7/9$). Accordingly, the distortion ratio comparisons between the synchronous pulsating injection in (8.32) and rotating injection in (8.27) can be described as

$$\delta_{\hat{q}/neg} = |\frac{1}{2}(1 + \frac{L_d}{L_q})\sin 2\theta_e + (1 - \frac{L_d}{L_q})\cos^2 \theta_e| \tag{8.33}$$

From (8.33), it can be seen that the difference between the rotating injection and the synchronous pulsating injection (both with carrier current sensing) also significantly depends on the saliency ratio and the ZCC zone (i.e., the inherent characteristics of the semiconductors). The detailed summary for the distortions of inverter nonlinearity effects on the three injection methods are given in Table 8.2.

Table 8.2 Summary of the Distortion Ratios for the Different Injection Methods

Method	*A	*B	*C	*D
Distortion ratio	$R_{ah} \frac{2L_q}{3\omega_h L_d (-L_d + L_q)}$	$\frac{2R_{ah}}{3\omega_h L_d}$	$R_{ah} \frac{(L_d + L_q)\sin 2\theta_e}{3\omega_h L_d (-L_d + L_q)} +$ $R_{ah} \frac{2(-L_d + L_q)\cos^2 \theta_e}{3\omega_h L_d (-L_d + L_q)}$	$\frac{2R_{ah}}{3\omega_h L_d} |\sin 2\theta_e|$
Distortion ratio (p.u.)	1	$|1 - \frac{L_d}{L_q}|$	$|\frac{1}{2}(1 + \frac{L_d}{L_q})\sin 2\theta_e + (1 - \frac{L_d}{L_q})\cos^2 \theta_e|$	$|(1 - \frac{L_d}{L_q})\sin 2\theta_e|$

*A-Rotating injection with carrier current sensing, *B-Rotating injection with zero sequence voltage sensing, *C-Synchronous pulsating injection with carrier current sensing, *D-Anti-rotating pulsating injection with zero sequence voltage sensing.

Therefore, from all the analytical derivations and discussions, it can be concluded that the inverter nonlinearity effects on different carrier injection strategies with alternative sensing signals mainly depend on the saliency ratios (i.e., different machine designs and topologies could be different) and also the inherent characteristics of semiconductor devices (i.e.,

different parasitic capacitors resulting in different ZCC zones). These two major effects could then cause different behaviours for the different injection methods with alternative sensing signals. However, generally, from the analytical results in Table 8.2, the zero sequence sensing based methods are more insensitive to the inverter nonlinearity effects than the current based methods (generally much less than 1 p.u.,Table 8.2).

Then, in order to examine and verify the analyses on carrier distortions for the above carrier injection methods, different dead time settings are performed under different load conditions, respectively, Fig. 8.10-Fig. 8.12. The injection frequency and voltage for the three methods are also set as 600Hz/6V, and the fundamental frequency is set as 5 Hz. Firstly, for rotating injection with negative sequence carrier current sensing as shown in Fig. 8.10(a)-(b), the distortion harmonics at -124th, -118th, and -112th are observed to be most sensitive with the increase of dead time, under different load conditions. In contrast, the zero sequence voltage sensing method for rotating injection in Fig. 8.10(c)-(d) has shown to be much less sensitive to the nonlinearity effects. According to the above analytical derivations, this is because for the prototype machine ($L_d/L_q \approx 7/9$), the resultant distortion ratio δ in (8.28) in the two carrier responses is only ~2/9. Thus, the distortion of the zero sequence voltage due to inverter nonlinearity effects is only around 22% of that of the negative sequence carrier current. Therefore, for rotating signal injection, the distortion differences in the two responses due to the inverter nonlinearity effects in Fig. 8.10(a)-(d) have been clearly verified above.
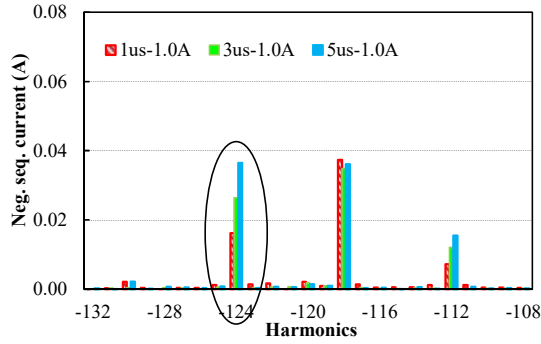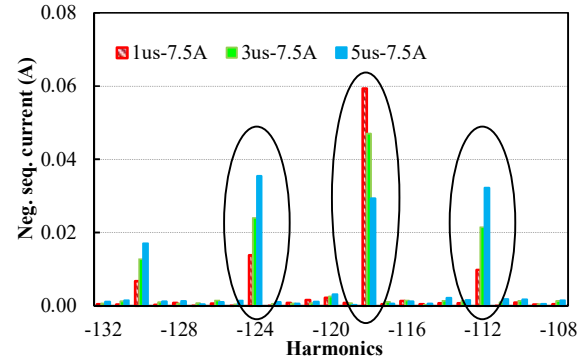
(a) Carrier current, I_q=1.0 A (b) Carrier current, I_q=7.5 A
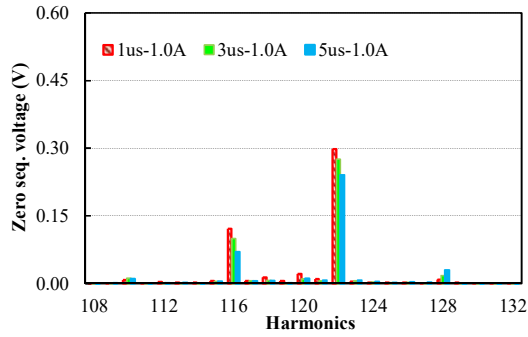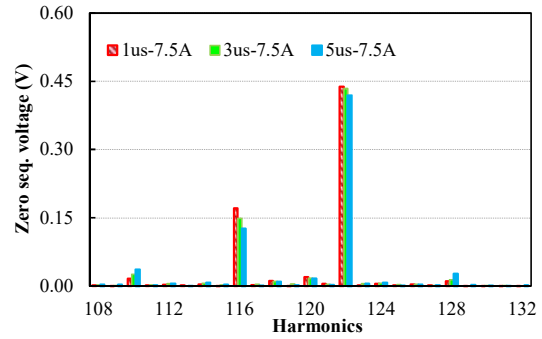
(c) Zero sequence voltage, I_q=1.0 A (d) Zero sequence voltage, I_q=7.5 A

Fig. 8.10 Measured carrier responses with dead-time for rotating injection.

Then, for the other two carrier injections, the main components in (8.4) and (8.5) approximately become zero ($\Delta\theta\approx0$, with the assistance of sensor) in the steady state (e.g., U_{RN} in (8.5) equals zero when $\Delta\theta\approx0$, as can be seen from the 120th harmonic in Fig. 8.12(a)) as aforementioned. Besides, since the injection axis cannot be shifted for fair comparisons of inverter nonlinearity effects [CHO08], it is very difficult to assess the inverter nonlinearity effects from the measured main harmonics, Fig. 8.11-Fig. 8.12. However, simply from the harmonic components at the 114th and 126th, Fig. 8.11-Fig. 8.12, it can be seen that the carrier current and zero sequence voltage responses for the two pulsating injection strategies are also less sensitive to the nonlinearity effects under different load conditions. According to (8.29) and (8.33), this can be also explained by the relatively low saliency ratio of the prototype PM machine, Table 8.1.
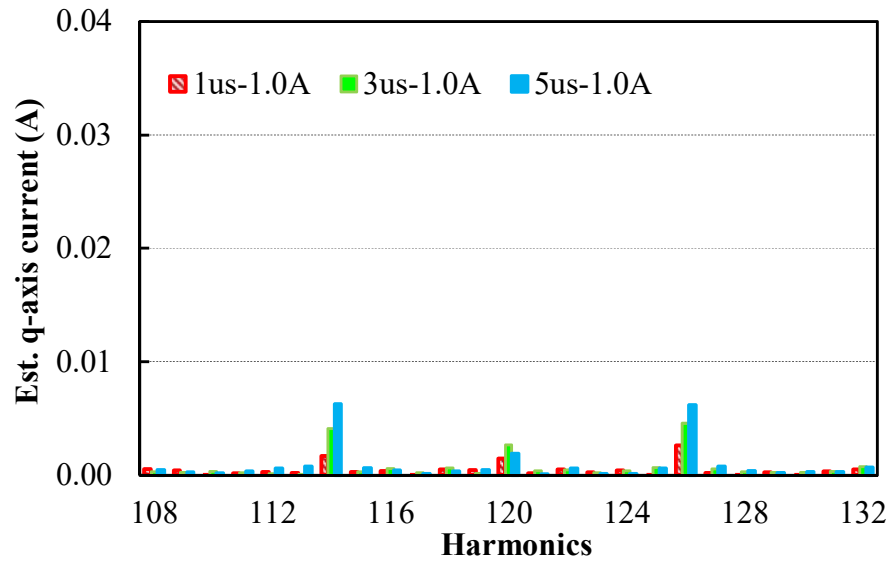
(a) Carrier current, I_q=1.0 A
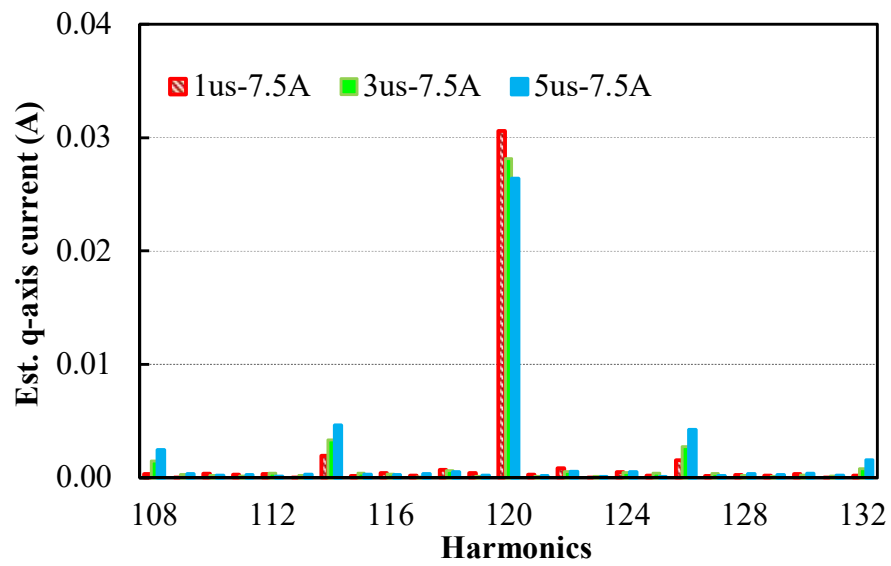
(b) Carrier current, I_q=7.5 A

Fig. 8.11 Measured carrier responses with dead-time for the synchronous pulsating injection.
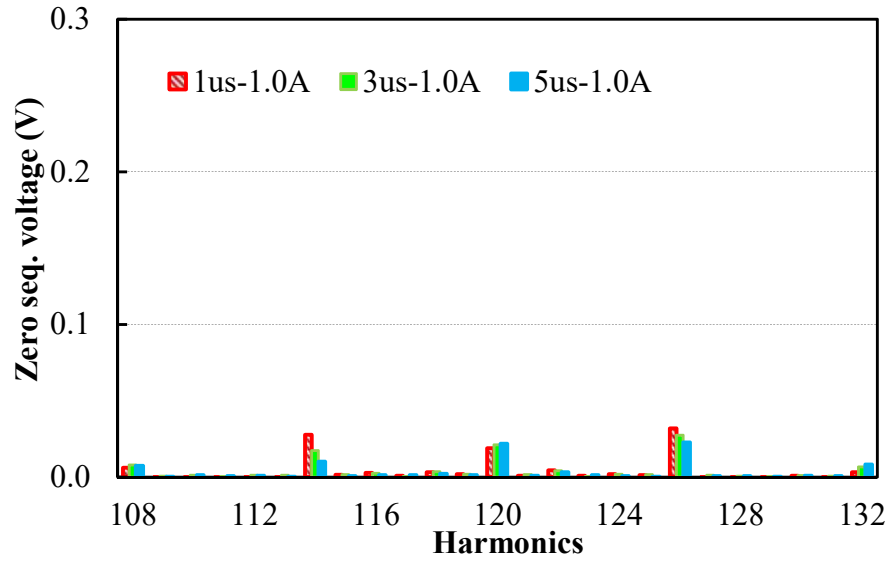
(a) Zero sequence voltage, $I_q=1.0$ A
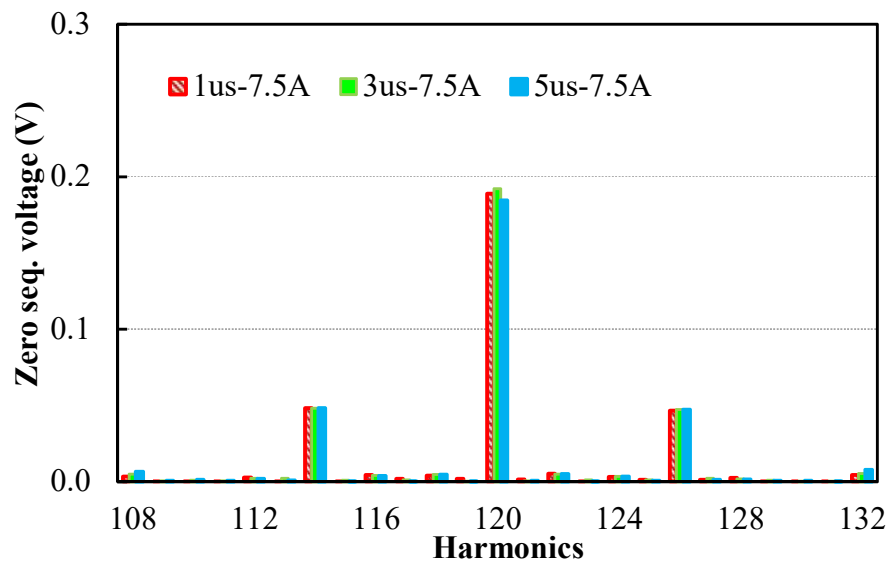
(b) Zero sequence voltage, $I_q=7.5$ A

Fig. 8.12 Measured carrier responses with dead time for anti-rotating pulsating injection.

In order to further confirm the derivations above, the sensorless control with dead-time changing online is also performed as shown in Fig. 8.13. It is noted that only the rotating signal injection with two different carrier responses is employed, while it is not fair for the other two pulsating injection methods. This is due to that the two pulsating injections are amplitude-modulated by saliency position as given in (8.4) and (8.5), and the equivalent position observer bandwidth changes significantly with the dead-time settings. Accordingly,

from Fig. 8.13 for rotating signal injection, when the dead time increases from 1 μs to 3 μs, the position estimation with zero sequence responses is less affected than that with the carrier current responses. Specifically, with negative sequence carrier current sensing, as shown in Fig. 8.13(a), the peak to peak position estimation error increases approximately twice (from ~0.2 rad to ~0.4 rad), while it is almost unchanged for the zero sequence method (Fig. 8.13(b)), which verifies the above theoretical analyses.
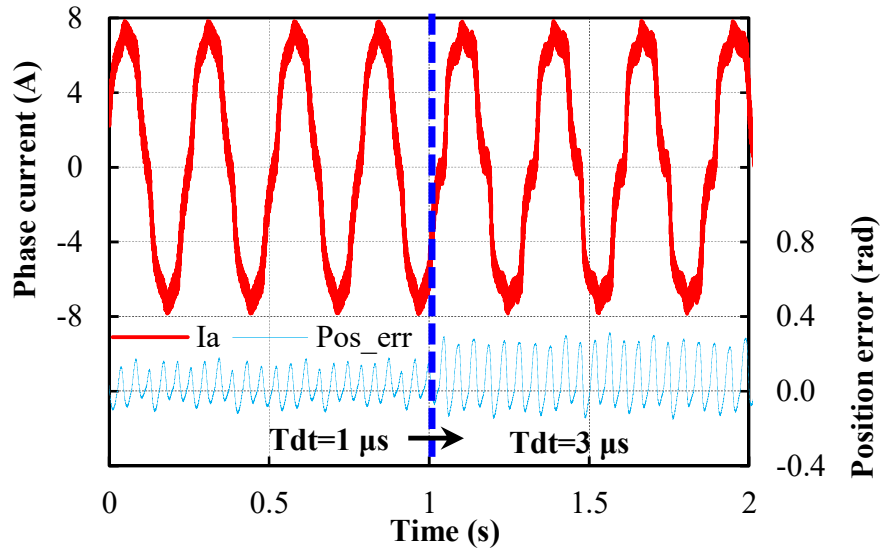
(a) Negative sequence carrier current sensing
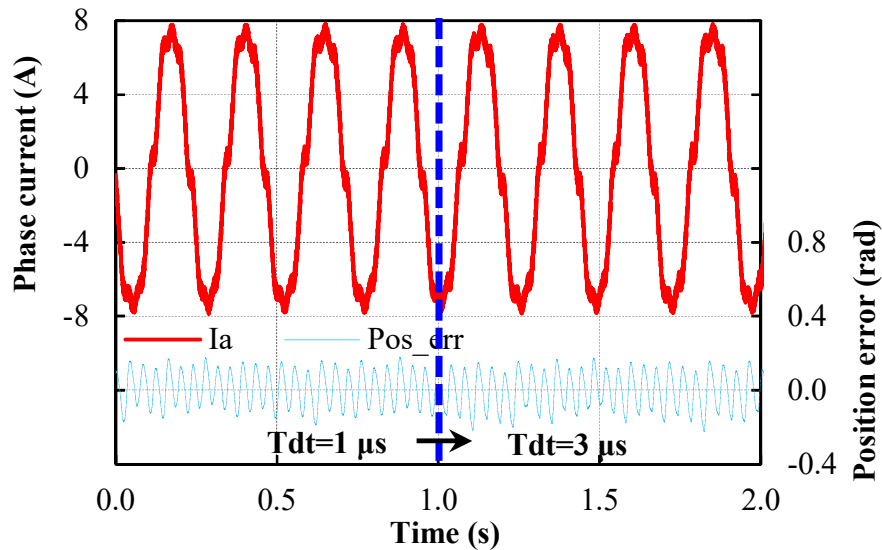
(b) Zero sequence carrier voltage sensing

Fig. 8.13 Position estimation performances for rotating signal injection methods with

alternative sensing signals with the dead-time changing.

8.3.4 Influence of multiple saliency effects

Normally, it is recognized that the inverter nonlinearity and multiple saliency effects (symmetrical conditions) are the main sources for the 6th (or multiple of 6th) oscillating position errors [DEG98] [GON11]. In this section, multiple saliency effects including primary saliency are specifically focused and compared for the above different injection methods. The FE simulation analyses are employed and therefore the inverter nonlinearity effects introduced in the above section 8.3.3 can be eliminated. The detailed modelling and analyses are presented as follows.

To obtain the analytical expressions of phase inductances, Fig. 8.14 gives the spectrum of one phase inductances for the prototype PM machine. It can be seen from Fig. 8.14 that the 2nd harmonic inductance is the primary saliency, while mainly the 4th harmonics exist as the multiple saliency. Hence, the phase inductances can be further described as

$$
\begin{aligned}
L_{aa} &= L_0 - L_2 \cos(2\theta_e) - L_4 \cos(4\theta_e) \\
L_{bb} &= L_0 - L_2 \cos(2\theta_e + \frac{2\pi}{3}) - L_4 \cos(4\theta_e - \frac{2\pi}{3}) \\
L_{cc} &= L_0 - L_2 \cos(2\theta_e - \frac{2\pi}{3}) - L_4 \cos(4\theta_e + \frac{2\pi}{3})
\end{aligned}
\tag{8.34}
$$

Accordingly, the d-/q-axis inductances can be expressed

$$
\begin{aligned}
L_d &= L_0 - \frac{L_2}{2} - \frac{L_4 \cos 6\theta_e}{2} \\
L_q &= L_0 + \frac{L_2}{2} + \frac{L_4 \cos 6\theta_e}{2} \\
L_{dq} &= \frac{L_4 \sin 6\theta_e}{2}
\end{aligned}
\tag{8.35}
$$

It can be seen from (8.34)-(8.35), the 4th phase inductance harmonics are transformed to be the 6th harmonics of d-/q-axis inductances. Consequently, the carrier currents for the three injection methods can be derived as

$$
i_{\alpha\beta}^h = \frac{U}{|Z|}[2L_0 e^{j(\omega_h t + \frac{\pi}{2})} + L_2 e^{j(-\omega_h t + 2\theta_e + \frac{\pi}{2})} + L_4 e^{j(-\omega_h t - 4\theta_e + \frac{\pi}{2})}]
\tag{8.36}
$$

$$\hat{i}_{qh} = \frac{U}{|Z|}[L_2 \sin(2\Delta\theta) + L_4 \sin(2\Delta\theta + 6\theta_e)]\sin\omega_h t \tag{8.37}$$

where |Z| presents the total impedance. Then, according to [RAC08c], the oscillating position error due to the multiple saliency effect can be expressed as

$$\Delta\theta = -\frac{1}{2}\arcsin(\frac{L_4}{L_2}\sin(6\theta_e + \varphi_m)) \tag{8.38}$$

for both rotating and synchronous pulsating injection, and φ_m is the phase angle of the 6th harmonic position error.

Similarly, considering the phase inductance harmonics, zero sequence carrier voltages for rotating and anti-rotating pulsating injection can be expressed as

$$U_{RN} \approx \frac{U}{\sum L_u L_v}[L_0 L_2 \cos(\omega_h t + 2\theta_e) - (\frac{L_2^2}{2} + L_0 L_4)\cos(\omega_h t - 4\theta_e)] \tag{8.39}$$

$$U_{RN} \approx \frac{U}{\sum L_u L_v}[L_0 L_2 \cos\omega_h t \sin(2\Delta\theta) - (\frac{L_2^2}{2} + L_0 L_4)\cos\omega_h t \sin(4\theta_e + 2\hat{\theta}_e)] \tag{8.40}$$

From (8.39)-(8.40), the resultant oscillating position error with zero sequence carrier voltage sensing due to the multiple saliency effect can be expressed as

$$\Delta\theta = -\frac{1}{2}\arcsin((\frac{L_4}{L_2} + \frac{L_2}{2L_0})\sin(6\theta_e + \varphi_{m1})) \tag{8.41}$$

Compared with (8.38), it can be seen that the 6th oscillating error in (8.41) caused by multiple saliency with zero sequence carrier sensing is larger than that with carrier current sensing. This is due to that the ratio of 2nd harmonics to dc components of phase inductance also contributes to the 6th position errors as give in (8.41).

The above analyses on the multiple saliency effects can be verified by FE simulation for the different carrier injection methods as shown in Fig. 8.15. All the carrier injection signals are set as 600 Hz and fundamental frequency is 2.5 Hz. As mentioned above, the influence of inverter nonlinearity effect is eliminated and therefore all the subsidiary harmonics of the carrier signals can be attributed to the machine multiple saliencies. From Fig. 8.15, by way of example, for the synchronous pulsating injection method with carrier current sensing, the

main distortions due to the multiple saliency effect (e.g., the 234th and 246th harmonics) are much smaller than those for the anti-rotating pulsating injection method with zero sequence voltage sensing. Similarly, for rotating signal injection, the carrier current response also has smaller distortions as shown in Fig. 8.15. Therefore, the carrier current sensing based methods are less sensitive to the multiple saliencies compared to the zero sequence carrier voltage based methods, as verified above.
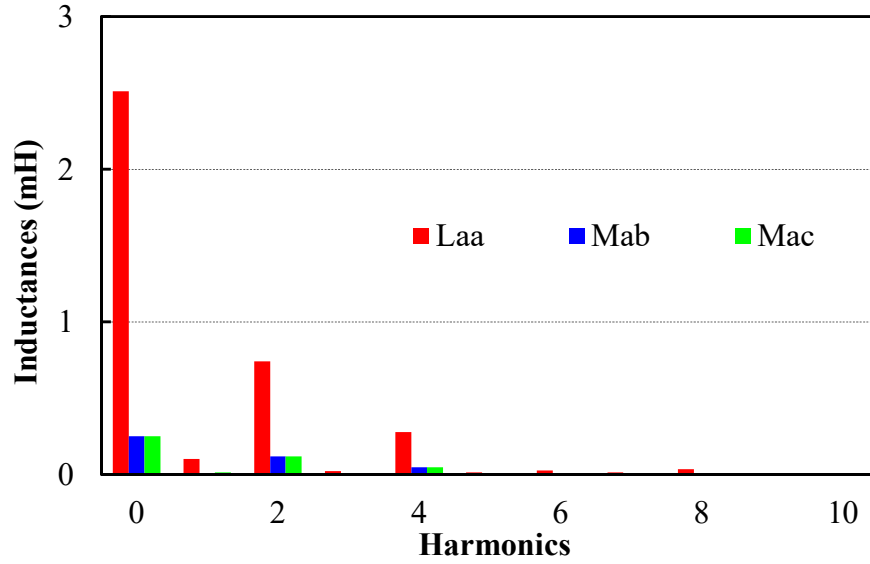
Fig. 8.14 Spectra of phase inductances for the prototype PM machine.
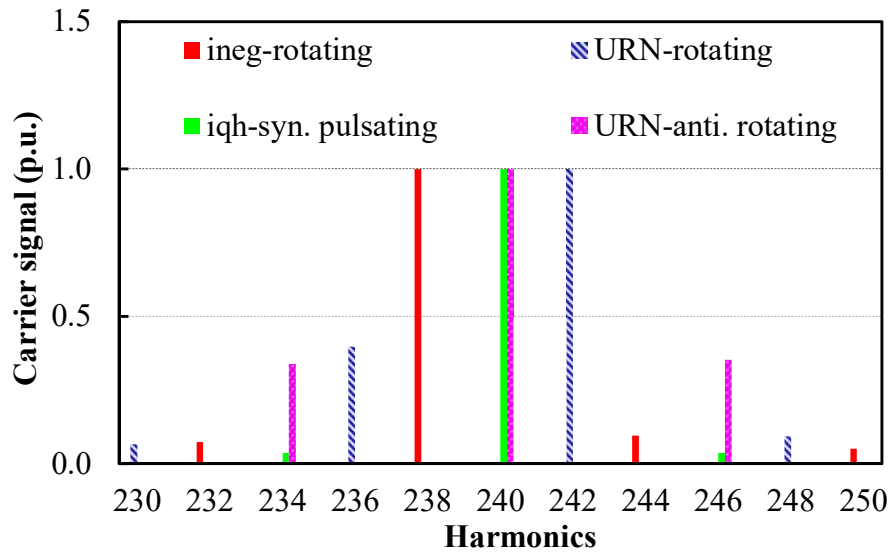
Fig. 8.15 Spectra of carrier signals for different injection methods by FE analyses.

8.3.5   Influence of carrier signal injection on iron and PM losses

The HF injection based sensorless control methods inevitably cause the parasitic losses both in the stator and rotor [YAN12]. Thus, in this part, the iron and PM losses due to HF signal injection are investigated and compared for the above different injection methods by FE simulation. Accordingly, the FE-predicted losses are shown in Fig. 8.16(a)-(c) and Table 8.3, under no-load and full-load conditions, respectively. For the simple and quick FE simulation, all the carrier injection methods adopt the carrier current injection [YAN12]. The HF injection frequency and amplitude for the three methods is all set as 600Hz and 0.5A, and the fundamental frequency as 5 Hz. Then, from Fig. 8.16 and Table 8.3, several interesting observations can be obtained as follows.

1)   The rotating signal injection has relatively larger PM and iron losses, while the other two have similar losses. Since the injection current amplitude on each axis is kept the same, the resultant flux density for rotating injection is increased, resulting in increased losses both on the stator and rotor [REI11].

2)   Compared to the parasitic losses with no HF signal injection, the PM eddy-current losses with HF injection are observed to have the most significant increase, Fig. 8.16(a). This is mainly because the spatial fundamental harmonic (in the electrical period) also contributes to the PM losses if the HF signal is injected, while at no injection condition, the PM losses will not be induced by the spatial fundamental harmonic, which rotates at the same speed with rotor [ISH05].

3)   The influence of load on HF losses is also investigated and can be approximately evaluated by P_{HF} ($P_{HF}=P_{inj}-P_{no\_inj}$, P_{inj} and P_{no_inj} are the losses with and without HF injection as given in Table 8.3) at different load conditions. By way of example, in Table 8.3, for rotating injection, P_{HF} of the stator losses are 55.8 mW at no-load condition, and 39.4 mW at full-load. The decrease of losses with load (from 55.8 mW to 39.4 mW) can be explained by that the variation of main flux-density harmonics is reduced at full-load (e.g., point 'a' in Fig. 8.17(a)-(b)) due to the magnetic saturation (i.e., reduced relative permeability μ), when the HF current with same amplitude is injected (i.e., ΔH is the same, and $\Delta B=\mu \cdot \Delta H$). The same decreasing trend with the load can also be observed for the rotor iron and PM losses, irrespective of injection methods, Table 8.3.

Therefore, from all the above analyses and also the discussions in the previous chapters, the comparative results for the different types of carrier injection methods in terms of signal

processing delays, magnetic saturation, inverter nonlinearity, and multiple saliency effects, etc. are summarized in Table 8.4. Clearly, those comprehensive comparative results can provide useful hints for selecting the proper carrier injection strategies according to the sensorless control applications.

Table 8.3 HF Losses for Different Injection Methods

Losses (mW)		Stator iron	PM	Rotor iron	Total
No inj.	No-load	309.12	0.37	0.19	309.68
	Full-load	332.98	1.44	0.71	335.13
Rotating	No-load	364.96	20.35	0.60	385.90
	Full-load	372.41	18.60	1.03	392.04
Syn. pulsating	No-load	330.68	12.02	0.40	343.10
	Full-load	347.97	12.29	0.87	361.13
Anti. rotating	No-load	336.83	12.48	0.49	349.80
	Full-load	351.00	10.90	0.88	362.79
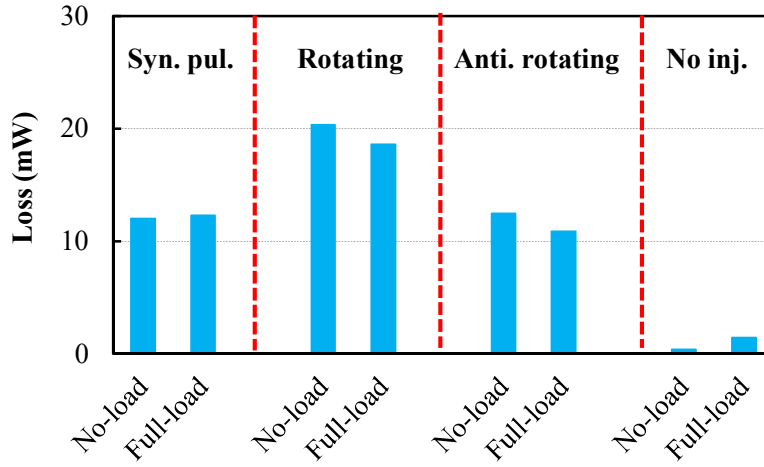
(a) PM losses
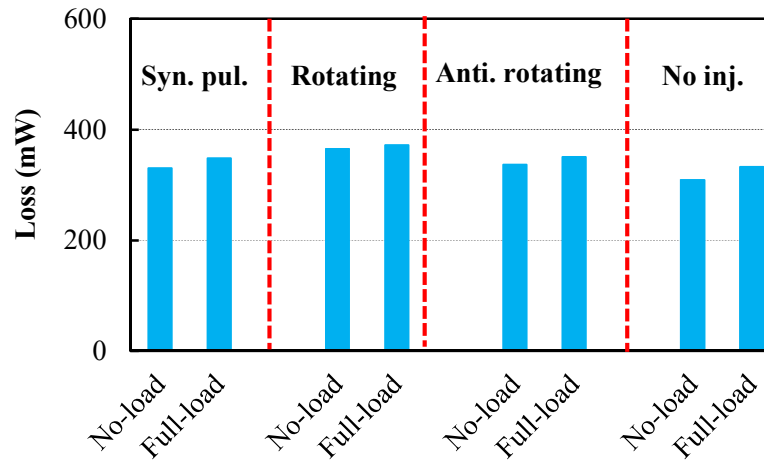
(b) Stator iron losses
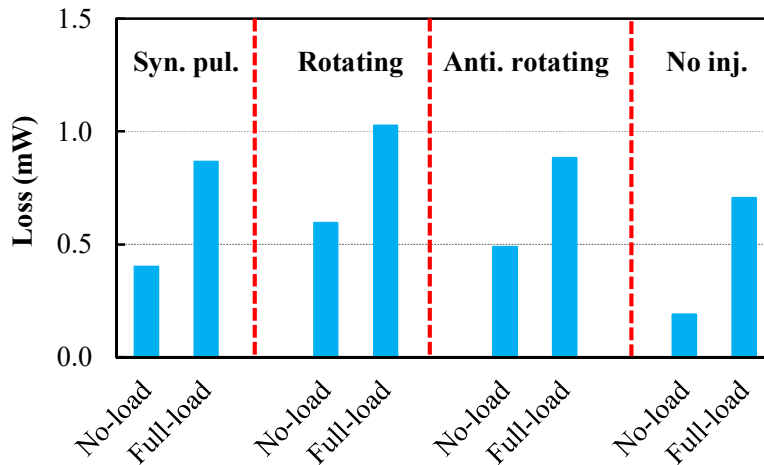
(c) Rotor iron losses

Fig. 8.16 PM and iron losses due to carrier signal injection by FE simulation.
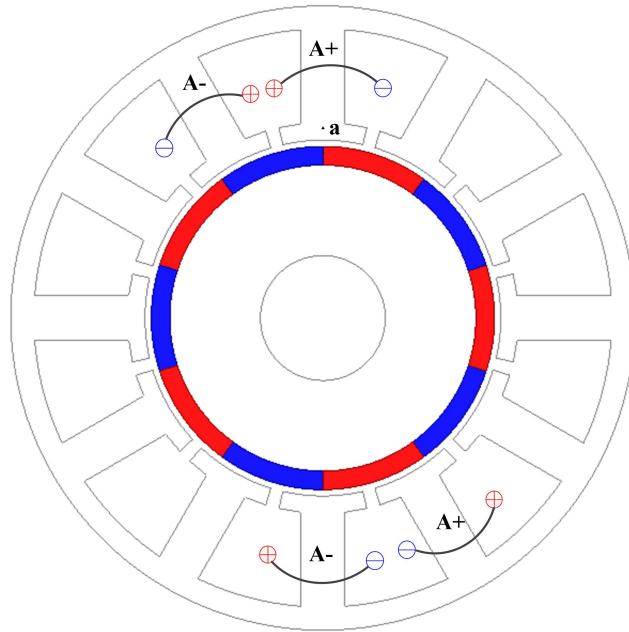
(a) Point 'a' in the stator tooth
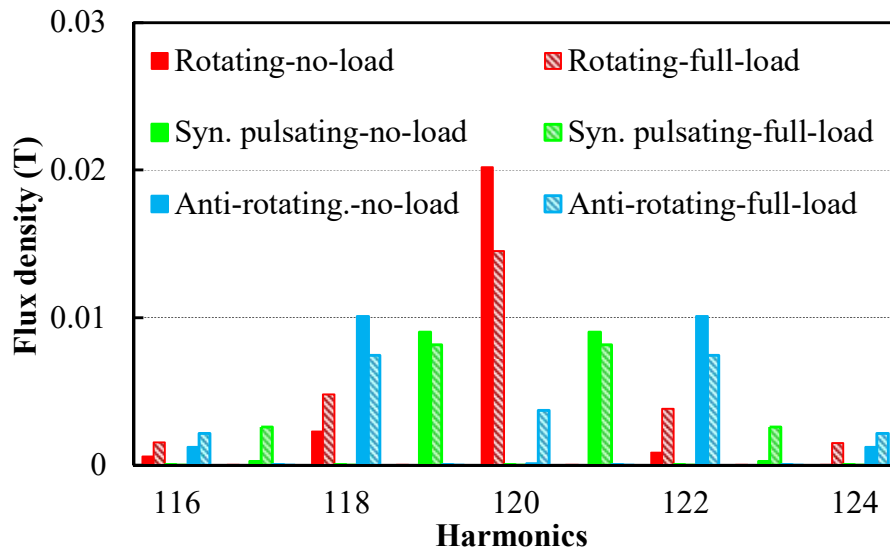
(b)Spectra of flux density at point 'a'

Fig. 8.17 Spectra of flux density (B) for point 'a' in the stator tooth for different injection
methods around the carrier injection frequency.

Table 8.4 Summary of the Comparative Results for Different Carrier Injection Methods

Sensorless Method	*A	*B	*C	*D
Reference frame	Stationary	Stationary	Estimated synchronous	Estimated anti-rotating
Implementation	Easy	Medium	Easy	Medium
Carrier response	Phase-modulated	Phase-modulated	Amplitude-modulated	Amplitude-modulated
Signal demodulation	Medium	Medium	Simple	Simple
Signal processing delay	Sensitive	Sensitive	Insensitive	Insensitive
Accuracy	Medium	Medium	High	High
Bandwidth	Medium	High	Medium	High
Reliability	Medium	High	Medium	High
Cross-coupling	Same	Same	Same	Same
Multiple-saliency	Small	Medium	Small	Medium
Inverter nonlinearity	Sensitive	Insensitive	Medium	Insensitive
Losses	Medium	Medium	Small	Small

*A-Rotating injection with carrier current sensing, *B-Rotating injection with zero sequence voltage sensing, *C-Synchronous pulsating injection with carrier current sensing, *D-Anti-rotating pulsating injection with zero sequence voltage sensing.

8.4 Conclusions

This chapter has compared three different carrier signal injection methods with alternative sensing signals for the sensorless control of PMSMs. FE simulation and experiments have been carried out to verify the theoretical analyses, and the main conclusions can be obtained as follows.

1) The synchronous pulsating signal injection with carrier current sensing and anti-rotating pulsating injection with zero sequence carrier voltage sensing are insensitive to signal processing delays, while other types of methods shows the more sensitivity.

2) The magnetic saturation is observed to have similar effects on carrier responses for different injection methods, and the cross coupling saturation effects cause the same position estimation error regardless of injection and sensing types.

3) The saliency ratio and the inherent characteristics of semiconductor devices significantly influence the inverter nonlinearity effects on different carrier injection strategies with alternative sensing types, and generally the zero sequence voltage sensing based methods are less sensitive to the inverter nonlinearity effects.

4) Machine multiple saliencies have more influence on zero sequence carrier voltage sensing based methods than the carrier current sensing methods.

5) The rotating signal injection has relatively larger total iron and PM losses. The PM losses are observed to be the most sensitive to the HF injection. Besides, the increase of load could result in the reduced HF losses under HF current injection condition.

9 General Conclusions and Future Work

In this thesis, the carrier signal injection methods are investigated for the sensorless control of permanent magnet synchronous machines (PMSMs), utilising alternative types of carrier responses, i.e., the carrier current and zero sequence carrier voltage.

For the carrier current sensing based carrier injection methods, mainly two aspects of research work have been in focus. One is to investigate the combined effects of signal processing delays and HF resistance effects, while the other the influence of machine parameter asymmetry on the sensorless control. It is found that at higher injection frequency, the synthesis of signal processing delays and HF resistance effects can give rise to large position errors, especially for the pulsating signal injection in the estimated synchronous reference frame. As to the influence of machine parameter asymmetry, it is found that the 2nd harmonic position estimation errors arise irrespective of carrier injection methods. Accordingly, the position error compensation strategies are also proposed to suppress the above detrimental effects.

For the zero sequence carrier voltage sensing based carrier injection methods, firstly, a novel sinusoidal-wave signal injection strategy (i.e., the anti-rotating pulsating injection) is proposed utilising the synergies of both zero sequence voltage sensing and pulsating injection. It is shown that the proposed injection strategy has the advantages of simple signal demodulation, high accuracy, fast dynamic response, high bandwidth and stability. Then, the anti-rotating injection strategy is further applied for the square-wave signal injection to combine the merits of both square-wave injection and zero sequence voltage sensing, which also has shown great capability for rotor position estimation. The magnetic polarity detection using the zero sequence voltage responses is also studied. It is found that for the amplitude variation based detection method, the zero sequence voltage response has much higher detection sensitivity. Besides, for the secondary harmonic based detection method, it is also found that the zero sequence voltage response has the advantages of simple signal demodulation, fast response, and large S/N ratio. Considering that the secondary harmonics of the zero sequence carrier voltage contain the real magnetic polarity information and have less distortion, they are directly utilised for the rotor position estimation for the PM machines. It is shown that the secondary harmonic based position estimation strategy not only removes

the time-consuming process of polarity detection, it also enhances the estimation robustness and stability.

The full comparisons for the carrier signal injection methods considering alternative carrier responses (carrier current and zero sequence carrier voltage) are also presented, in terms of signal processing delays, magnetic saturation effects, inverter nonlinearity effects, multiple saliency effects, etc. The comparative results can provide more physical understandings about how the carrier injection method works and how it is affected by the nonlinear behaviours of the PM machine or the inverter.

9.1 Carrier Current Sensing Based Sensorless Control

9.1.1 Analysis of signal processing delays and HF resistance effect

For carrier current sensing based carrier signal injection methods, in the case of high precision A/D converter, higher injection frequency (>1/10 PWM switching frequency) can be adopted. Accordingly, the filters for signal separation can be selected weaker, leading to enhanced system bandwidths. However, at the same time, the signal processing delay effects (e.g., PWM duty ratio updating delay, etc.) become prominent, and the high frequency (HF) resistance effects may also be enlarged. Consequently, for the pulsating signal injection method, it is shown that the position estimation errors become unacceptable due to the combined effects of signal processing delays and HF resistance. In order to suppress the undesirable position errors, in this thesis, a new compensation strategy with a PI regulator is proposed. For the proposed strategy, by modifying the phase angle of the demodulation signal, the amplitude of the useful inductive saliency part is significantly increased while the HF resistance part is suppressed, leading to significantly enhanced position estimation performances. The similar compensation strategy is also applied for the rotating signal injection method, which also shows great compensation effectiveness.

9.1.2 Analysis of machine parameter asymmetry effects

The parameter asymmetries of PM machines are frequently present in the practical applications and may come from the poor mechanical manufacturing, machine eccentricity, stator winding, etc. The influence of machine parameter asymmetries on the carrier signal injection based rotor position estimation is also investigated in this thesis. It is found that with either phase resistance or inductance asymmetry, the 2nd harmonic position errors arise

regardless of carrier injection methods. It is also found that for the traditional two carrier signal injection methods (i.e., the rotating injection and synchronous pulsating injection), the 2nd harmonic errors are different for resistance asymmetry but the same for inductance asymmetry. In order to suppress the position errors for resistance asymmetry, the guidelines for the injection frequency selection are derived. For inductance asymmetry, a new online compensation strategy with dual frequency injection is also presented in this thesis. These compensation strategies all have shown great effectiveness as verified experimentally.

9.2 Zero Sequence Carrier Voltage Sensing Based Sensorless Control

9.2.1 Anti-rotating sinusoidal-wave signal injection

The zero sequence carrier voltage response for carrier signal injection methods is shown to have the advantages of less injection distortions, enhanced estimation bandwidth and stability, etc. However, the conventional zero sequence voltage response is phase-modulated by machine saliency, easily resulting in the position estimation errors. To combine the merits of zero sequence method with the amplitude-modulation technique, a novel anti-rotating signal injection strategy is proposed in this thesis. This injection strategy is performed on the estimated reference frame, anti-rotating at twice the rotor's estimated electrical speed. It is shown that compared to the conventional zero sequence voltage method, the proposed strategy is easier for signal processing and less sensitive to signal processing delays because it is amplitude-modulated by saliency position and the phase shifts due to signal processing delays are intrinsically cancelled. Therefore, the proposed method perfectly combines the synergies of the zero sequence method (i.e., high bandwidth and stability) and the amplitude-modulation technique (i.e., increased accuracy), and shows great rotor position estimation performances. The comparison of the conventional and proposed carrier signal injection methods all with zero sequence carrier voltage sensing is also summarized in Table 9.1.

Table 9.1 Comparative Results of Zero Sequence Voltage Sensing Based Sinusoidal-Wave Signal Injection Methods

Sensorless method	Rotating injection	Synchronous pulsating injection	Proposed anti-rotating pulsating injection
Signal injection			
Reference frame	Stationary	Estimated synchronous	Estimated anti-rotating
Sensing response	Zero sequence voltage	Zero sequence voltage	Zero sequence voltage
Carrier response	Phase-modulated	Amplitude-modulated	Amplitude-modulated
Signal demodulation	Medium	Complex	Simple
Signal processing delay	Sensitive	Sensitive	Insensitive
Cross-coupling	Same	Same	Same
Accuracy	Medium	Low	High

9.2.2 Anti-rotating square-wave signal injection
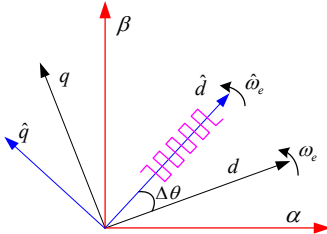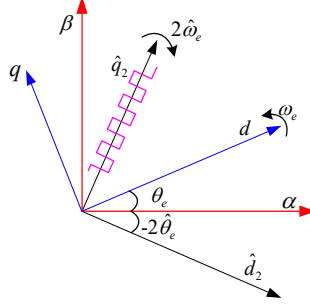
The anti-rotating signal injection strategy is further applied for the square-wave signal injection in this thesis. It is found that the anti-rotating square-wave injection with zero sequence voltage sensing has two main advantages:

- The carrier response amplitude is not related to the injection frequency, i.e., higher injection voltage is not required.

- The carrier response does not need signal differentiation processing, which significantly simplifies the signal demodulation process and increases the position estimation robustness.

Hence, the synergies of the square-wave injection and zero sequence voltage sensing have been perfectly combined with the anti-rotating signal injection strategy. The comparison results of the conventional and proposed square-wave injection methods with different sensing responses are shown in Table 9.2.

Table 9.2 Comparison of Square-Wave Signal Injection Methods with Different Carrier Responses

Sensorless method	Synchronous pulsating injection	Proposed anti-rotating pulsating injection
Signal injection		
Reference frame	Estimated synchronous	Estimated anti-rotating
Sensing response	Carrier current	Zero sequence carrier voltage
Carrier response	Amplitude-modulated	Amplitude-modulated
Signal demodulation	Complex	Simple
Injection voltage	High	Medium
Robustness	Medium	High
Cross-coupling	Same	Same
Accuracy	High	High

9.2.3 Initial rotor position estimation and magnetic polarity identification

The initial rotor position estimation and magnetic polarity identification using the zero sequence carrier voltage response is also investigated in this thesis. Two types of the polarity detection methods, i.e., the amplitude variation based method and the secondary harmonic based method, have been investigated, respectively. It is found that the amplitude variation method using the zero sequence voltage has higher detection sensitivity compared to the conventional method using the carrier current. Besides, for rotating signal injection, the secondary harmonic based detection method using the zero sequence voltage has the advantage of simple signal demodulation, fast response, and moreover has large signal amplitude and less distortion compared to the conventional secondary carrier current harmonics. However, the secondary harmonics of the zero sequence carrier voltage cannot be applied for the anti-rotating signal injection method since two dominant secondary harmonics exist and could severely deteriorate the polarity identification at different rotor positions. In addition, it is also shown that the zero sequence voltage responses cannot be applied for the polarity detection of the conventional pulsating injection method performed in the estimated synchronous reference frame. The magnetic polarity detection strategies for the different carrier signal injection methods are also summarized in Table 9.3.

9.2.4 Rotor position estimation without the need of magnetic polarity detection

For the carrier signal injection methods exploiting the inherent 2nd harmonic saliencies, the estimated rotor position has the angle ambiguity of π, due to the lack of magnetic polarity information in these saliencies. Accordingly, in this thesis, the modulated HF saliency containing the real magnetic polarity information is utilised for rotor position estimation. It is found that the carrier responses (i.e., the secondary harmonics) from the interaction between the HF field and the HF saliency can be used for the actual rotor position estimation without any ambiguity of machine polarity. It is also found that the secondary harmonics of the zero sequence voltage response demonstrate better position estimation performances than those of carrier current. In summary, the modulated HF saliency based position estimation method has the advantages of

- The magnetic polarity ambiguity is totally eliminated, and thus the time-consuming process for the magnetic polarity identification is removed.

- The estimation robustness and stability is significantly enhanced, due to that the estimated position will converge at one rotor position only.

9.3   Comparison of Different Carrier Signal Injection Methods

The different carrier signal injection methods with either carrier current or zero sequence voltage sensing are also compared in this thesis. The existing comparison efforts primarily focused on the two injection methods, i.e., the rotating injection and synchronous pulsating injection. Therefore, the contribution for the comparative research work in this thesis is that the systematic comparisons between three injection methods (i.e., the two existing injection methods plus the proposed anti-rotating pulsating injection method) have been performed. The comparison results on the inverter nonlinearity, cross-coupling saturation, multiple saliency, etc., provide better physical understandings about how the carrier injection method works and how it is affected by the nonlinear behaviours of the PM machine or inverter. Moreover, those comprehensive comparative results can provide useful hints for selecting the proper carrier injection strategies according to the sensorless control applications. The comparative results in terms of signal processing delays, magnetic saturation, inverter nonlinearity, multiple saliency, initial rotor position estimation, and etc., are all summarized in Table 9.3.

Table 9.3 Comparison for Different Carrier Injection Methods with Alternative Carrier Responses

Sensorless Method	*A	*B	*C	*D
Reference frame	Stationary	Stationary	Estimated synchronous	Estimated anti-rotating
Implementation	Easy	Medium	Easy	Medium
Carrier response	Phase-modulated	Phase-modulated	Amplitude-modulated	Amplitude-modulated
Signal demodulation	Medium	Medium	Simple	Simple
Signal processing delay	Sensitive	Sensitive	Insensitive	Insensitive
Cross-coupling	Same	Same	Same	Same
Multiple-saliency	Small	Medium	Small	Medium
Inverter nonlinearity	Sensitive	Insensitive	Medium	Insensitive
Losses	Medium	Medium	Small	Small
Accuracy	Medium	Medium	High	High
Bandwidth	Medium	High	Medium	High
Stability	Medium	High	Medium	High
Amplitude variation based polarity detection	Low Sensitivity	High Sensitivity	Low Sensitivity	High Sensitivity
Secondary harmonic based polarity detection	Low S/N ratio	High S/N ratio	Not applicable	Not applicable
Position estimation without polarity ambiguity	Degraded	Good	Not possible	Not possible

*A-Rotating injection with carrier current sensing, *B-Rotating injection with zero sequence voltage sensing, *C-Synchronous pulsating injection with carrier current sensing, *D-Anti-rotating pulsating injection with zero sequence voltage sensing.

9.4   Future Work: Machine Design for Sensorless Performance Enhancement

From the research work in this thesis, the sensorless control performances are inevitably affected by the nonlinear behaviours of the PM machines. Thus, it requires the PM machine to be properly designed for improved position estimation performances. Specifically, when designing the PM machine for sensorless control, the targets, e.g., how to increase the machine saliency, how to reduce the cross-coupling magnetic saturation effect, how to suppress the multiple saliency effect, etc., should be comprehensively considered. It should be noted that these design targets may conflict with each other. By way of example, by incorporating the air flux-barrier in the spoke-type IPM machine, the d- and q-axis cross-coupling saturation effect can be effectively reduced. However, the saliency ratio may be also reduced at the same time, affecting the S/N ratio of the carrier responses used for position estimation. Clearly, there will be a lot of research work to investigate for the sensorless oriented machine design in the future.

References

[ACA06]   P. P. Acarnley and J. F. Watson, "Review of position-sensorless operation of brushless permanent-magnet machines," *IEEE Trans. Ind. Electron.*, vol. 53, no. 2, pp. 352–362, Apr. 2006.

[ALB13]   L. Alberti, L., N. Bianchi, "Theory and design of fractional-slot multilayer windings," *IEEE Trans. Ind. Appl.*, vol.49, no.2, pp.841, 849, Mar./Apr. 2013.

[ALB15]   L. Alberti, O. Bottesi, and S. Bolognani, "Computation and measurement of high frequency parameters in a synchronous machine," *in 2015 IEEE Energy Conversion Congress and Exposition* (*ECCE*), 2015, pp. 845–852.

[BAE03a]   B.H. Bae, S.K. Sul, J.H. Kwon, and J.S. Byeon, "Implementation of sensorless vector control for super high speed PMSM of turbo compressor," *IEEE Trans. Ind. Appl.*, vol. 39, no. 3, pp. 811-818, 2003.

[BAE03b]   B. H. Bae and S. K. Sul, "A compensation method for time delay of full-digital synchronous frame current regulator of PWM ac drive," *IEEE Trans. Ind. Appl.*, vol. 39, no. 3, pp. 802–810, May/Jun. 2003.

[BET14]   F. Betin et al., "Trends in electrical machines control: samples for classical, sensorless, and fault-tolerant techniques," *IEEE Ind. Electron. Mag.*, vol. 8, no. 2, pp. 43–55, Jun. 2014.

[BIA06]   N. Bianchi, S. Bolognani, M. D. Pr´e, and G. Grezzani, "Design considerations for fractional-slot winding configurations of synchronous machines," *IEEE Trans. Ind. Appl.*, vol. 42, no. 4, pp. 997–1006, Jul./Aug. 2006.

[BIA07]   N. Bianchi, S. Bolognami, J. H. Jang, and S. K. Sul, "Comparison of PM motor structures and sensorless control techniques for zero-speed rotor position detection," *IEEE Trans. Power Electron.*, vol. 22, no. 6, pp. 2466-2475, 2007.

[BIA09]   N. Bianchi and S. Bolognani, "Sensorless-oriented-design of PM motors," *IEEE Trans. Ind. Appl.*, vol. 45, no. 4, pp. 1249–1257, Jul./Aug. 2009

[BIA13]   N. Bianchi, E. Fornasiero, and S. Bolognani, "Effect of stator and rotor saturation on sensorless rotor position detection," *IEEE Trans. Ind. Appl.*, vol.

49, no. 3, pp. 1333–1342, May 2013.

[BIA15]   N. Bianchi, S. Bolognani, A. Faggion, and E. Fornasiero, "Analysis and experimental tests of the sensorless capability of a fractional-slot inset PM motor," *IEEE Trans. Ind. Appl.*, vol. 51, no. 1, pp. 224–231, Jan. 2015.

[BOL09]   I. Boldea, M. C. Paicu, G. D. Andreescu, and F. Blaabjerg, "Active flux DTFC-SVM sensorless control of IPMSM," *IEEE Trans. Energy Convers.*, vol. 24, no. 2, pp. 314-322, 2009.

[BOL11]   S. Bolognani, S. Calligaro, R. Petrella, and M. Sterpellone, "Sensorless control for IPMSM using PWM excitation: analytical developments and implementation issues," *Symposium on Sensorless Control for Electrical Drives*, 2011, pp. 64-73.

[BRI01]   F. Briz, M. W. Degner, J. M. Guerrero, A. Zamarron, and R. D. Lorenz, "Implementation issues affecting the performance of carrier signal injection based sensorless controlled AC drives," *in Conf. Rec. IEEE-IAS Annu. Meeting*, vol. 4, 2001, pp. 2645-2652.

[BRI02]   F. Briz, M. W. Degner, A. Diez, and R. D. Lorenz, "Static and dynamic behavior of saturation-induced saliencies and their effect on carrier-signal-based sensorless AC drives," *IEEE Trans. Ind. Appl.*, vol. 38, no. 3, pp. 670–678, May 2002.

[BRI04]   F. Briz, M. W. Degner, P. García, and R. D. Lorenz, "Comparison of saliency-based sensorless control techniques for AC machines," *IEEE Trans. Ind. Appl.*, vol. 40, no. 4, pp. 1107–1115, Jul./Aug. 2004.

[BRI05]   F. Briz, M. W. Degner, P. García, and J. M. Guerrero, "Rotor position estimation of AC machines using the zero sequence carrier signal voltage," *IEEE Trans. Ind. Appl.*, vol. 41, no. 6, pp. 1637–1646, Nov./Dec. 2005.

[BRI11]   F. Briz and M. W. Degner, "Rotor Position Estimation," *IEEE Ind. Electron. Mag.*, vol. 5, no. 2, pp. 24–36, Jun. 2011.

[CHE03]   Z. Chen, M. Tomita, S. Doki, and S. Okuma, "An extended electromotive force model for sensorless control of interior permanent-magnet synchronous

motors," *IEEE Trans. Ind. Electron.*, vol. 50, no. 2, pp. 288-295, 2003.

[CHE14]   Z. Chen, J. Gao, F. Wang, Z. Ma, Z. Zhang, and R. Kennel, "Sensorless control for spmsm with concentrated windings using multisignal injection method," *IEEE Trans. Ind. Electron.*, vol. 61, no. 12, pp. 6624–6634, Dec. 2014.

[CHE16a]   X. Chen, J. Wang, V. I. Patel, and P. Lazari, "A nine-phase 18-slot 14-pole interior permanent magnet machine with low space harmonics for electric vehicle applications," *IEEE Trans. Energy Convers.*, vol. 31, no. 3, pp. 860–871, Sep. 2016.

[CHE16b]   Z. Chen, F. Wang, G. Luo, Z. Zhang, and R. Kennel, "Secondary saliency tracking-based sensorless control for concentrated winding SPMSM," *IEEE Trans. Ind. Inform.*, vol. 12, no. 1, pp. 201–210, Feb. 2016.

[CHE16c]   Z. Chen, X. Cai, R. Kennel, and F. Wang, "Enhanced sensorless control of SPMSM based on stationary reference frame high-frequency pulsating signal injection," *in 2016 IEEE 8th International Power Electronics and Motion Control Conference* (*IPEMC-ECCE Asia*), 2016, pp. 885–890.

[CHI09]   S. Chi, Z. Zhang, and L. Xu, "Sliding-mode sensorless control of direct drive PM synchronous motors for washing machine applications," *IEEE Trans. Ind. Appl.,* vol. 45, no. 2, pp. 582-590, 2009.

[CHO06]   C. H. Choi and J. K. Seouk, "Compensation of zero-current clamping effects for sensorless drives based on high-frequency signal injection," *in Conf. Rec. 41st IEEE IAS Annu. Meeting*, 2006, pp. 2466–2471.

[CHO08]   C. H. Choi and J. K. Seok, "Pulsating signal injection-based axis switching sensorless control of surface-mounted permanent-magnet motors for minimal zero-current clamping effects," *IEEE Trans. Ind. Appl.*, vol. 44, no. 6, pp. 1741–1748, Nov./Dec. 2008.

[CHU13]   W. Q. Chu and Z. Q. Zhu, "Average torque separation in permanent magnet synchronous machines using frozen permeability," *IEEE Trans. Magn.*, vol. 49, no. 3, pp. 1202–1210, Mar. 2013.

[CON00]   A. Consoli, G. Scarcella, and A. Testa, "A new zero-frequency flux position detection approach for direct-field-oriented-control drives," *IEEE Trans. Ind. Appl.*, vol. 36, no. 3, pp. 797–804, May./Jun. 2000.

[CON06]   A. Consoli, G. Scarcella, G. Bottiglieri, and A. Testa, "Harmonic analysis of voltage zero-sequence-based encoderless techniques," *IEEE Trans. Ind. Appl.*, vol. 42, no. 6, pp. 1548–1557, Nov./Dec. 2006.

[CON09]   A. Consoli, G. Bottiglieri, G. Scarcella, and G. Scelba, "Flux and voltage calculations of induction motors supplied by low- and high-frequency currents," *IEEE Trans. Ind. Appl.*, vol. 45, no. 2, pp. 737–746, Mar. 2009.

[CUP12]   F. Cupertino, A. Guagnano, A. Altomare, and G. Pellegrino, "Position estimation delays in signal injection-based sensorless PMSM drives", *Proc. of IEEE SLED 2012 Symposium*, pp.1-6,2012.

[DAJ14]   G. Dajaku, W. Xie, and D. Gerling, "Reduction of low space harmonics for the fractional slot concentrated windings using a novel stator design," *IEEE Trans. Magn.*, vol. 50, no. 5, pp. 1–12, May 2014.

[DEG98]   M.W. Degner, and R.D Lorenz, "Using multiple saliencies for the estimation of flux, position, and velocity in AC machines," *IEEE Trans. Ind. Appl.*, vol. 34, no. 5, pp. 1097–1104, 1998.

[FOO10]   G. Foo, and M.F. Rahman, "Sensorless sliding-mode MTPA control of an IPM synchronous motor drive using a sliding-mode observer and HF signal injection," *IEEE Trans. Ind. Electron.*, vol. 57, no. 4, pp. 1270 – 1278, 2010

[FUE11]   E. Fuentes, and R. Kennel, "Sensorless-predictive torque control of the PMSM using a reduced order extended Kalman filter," *Symposium on Sensorless Control for Electrical Drives*, 2011, pp. 123-128.

[GAO07]   Q. Gao, G. M. Asher, M. Sumner, and P. Makys, "Position estimation of AC machines over a wide frequency range based on space vector PWM excitation," *IEEE Trans. Ind. Appl.*, vol. 43, no. 4, pp. 1001-1011, 2007.

[GAR07]   P. Garcia, F. Briz, M.W. Degner, and D. Diaz-Reigosa, "Accuracy, bandwidth, and stability limits of carrier-signal-injection-based sensorless control

methods," IEEE Trans. Ind. Appl., vol. 43, no. 4, pp. 990-1000, 2007.

[GON11]   L. M. Gong and Z. Q. Zhu, "A novel method for compensating inverter nonlinearity effects in carrier signal injection-based sensorless control from positive-sequence carrier current distortion," *IEEE Trans. Ind. Appl*., vol. 47, no. 3, pp. 557–565, May/Jun. 2011.

[GON12]   L. Gong, "Carrier signal injection based sensorless control ofpermanent magnet brushless ac machines", PhD Thesis, Research Group of Electric Machines and Drives, Department of Electronic and Electrical Engineering, University of Sheffield, 2012.

[GON13]   L. Gong, and Z.Q. Zhu, "Robust initial rotor position estimation of permanent magnet brushless AC machines with carrier signal injection-based sensorless control" *IEEE Trans. Ind. Appl.,* vol. 49, no. 6, pp. 2602-2609, Nov./Dec., 2013.

[GRA15]   J. Graus and I. Hahn, "Improved accuracy of sensorless position estimation by combining resistance- and inductance-based saliency tracking," *in IECON 2015 - 41st Annual Conference of the IEEE Industrial Electronics Society*, 2015, pp. 002886–002891.

[GUE05]   J.M. Guerrero, M. Leetmaa, F. Briz, A. Zamarron, and R.D. Lorenz, "Inverter nonlinearity effects in high-frequency signal-injection-based sensorless control methods," *IEEE Trans. Trans. Ind. Appl*., vol. 41, no. 2, pp. 618-626, Mar./Apr. 2005.

[GUG06]   P. Guglielmi, M. Pastorelli, and A. Vagati, "Impact of cross-saturation in sensorless control of transverse-laminated synchronous reluctance motors," *IEEE Trans. Ind. Electron*., vol. 53, no. 2, pp. 429-439, Apr. 2006.

[GUO06]   Y. Guo, J. G. Zhu, P. A. Watterson, and W. Wu, "Development of a PM transverse flux motor with soft magnetic composite core," *IEEE Trans. Energy Convers*., vol. 21, no. 2, pp. 426–434, Jun. 2006.

[HA03]   J. I. Ha, K. Ide, T. Sawa, and S. K. Sul, "Sensorless rotor position estimation of an interior permanent-magnet motor from initial states," *IEEE Trans. Ind.*

Appl., vol. 39, no. 3, pp. 761–767, May 2003.

[HAM10]   W. Hammel and R. M. Kennel, "Position sensorless control of PMSM by synchronous injection and demodulation of alternating carrier voltage," *in Proc. 1st Symp. SLED*, Jul. 2010, pp. 56–63.

[HAQ03]   M.E. Haque, L. Zhong, M.F. Rahman, "A sensorless initial rotor position estimation scheme for a direct torque controlled interior permanent magnet synchronous motor drive," *IEEE Trans. Power Electron.*, vol. 18, no. 6, pp.1376–1383, 2003.

[HAR05]   M.C. Harke, D. Raca, and R.D. Lorenz, "Implementation issues for fast initial position and magnet polarity identification of PM synchronous machines with near zero saliency," *in Conf. on Power Electron. and Appl.*, 2005, pp. 1–10.

[HOL05]   J. Holtz, and J. Juliet, "Sensorless acquisition of the rotor position angle of induction motors with arbitrary stator windings," *IEEE Trans.Ind. Appl.*, vol. 41, no. 6, pp. 1675-1682, 2005.

[HOL08]   J. Holtz, "Acquisition of position error and magnet polarity for sensorless control of PM synchronous machines," *IEEE Trans. Ind. Appl.*, vol. 44, no. 4, pp. 1172–1180, 2008.

[HOL98]   J. Holtz, "Sensorless position control of induction motors – an emerging technology," *IEEE Trans. Ind. Electron.*, vol. 45, No. 6, pp.840–852, 1998.

[HU98]   J. Hu, and B. Wu, "New integration algorithms for estimating motor flux over a wide speed range," *IEEE Trans. Power Electron.*, vol. 13, no. 5, pp. 969 – 977, 1998.

[HUA11]   Y. Hua, M. Sumner, G. Asher, Q. Gao, and K. Saleh, "Improved sensorless control of a permanent magnet machine using fundamental pulse width modulation excitation," *IET Electric Power Appl.*, vol. 5, no. 4, pp. 359-370, 2011.

[ISH05]   D. Ishak, Z. Q. Zhu, and D. Howe, "Eddy-current loss in the rotor magnets of permanent-magnet brushless machines having a fractional number of slots per

pole," *IEEE Trans. Magn.*, vol. 41, no. 9, pp. 2462–2469,Sep. 2005.

[ISH06]   D. Ishak, Z. Q. Zhu, and D. Howe, "Comparison of PM brushless motors, having either all teeth or alternate teeth wound," *IEEE Trans. Energy Convers.*, vol. 21, no. 1, pp. 95–106, Mar. 2006.

[IWA16]   Y. Iwaji, R. Takahata, T. Suzuki, and S. Aoyagi, "Position sensorless control method at zero-speed region for permanent magnet synchronous motors using the neutral point voltage of stator windings," *IEEE Trans. Ind. Appl.*, vol. 52, no. 5, pp. 4020–4028, Sep. 2016.

[JAH96]   T. M. Jahns and W. L. Soong, "Pulsating torque minimization techniques for permanent magnet AC motor drives-a review," *IEEE Trans. Ind. Electron.*, vol. 43, no. 2, pp. 321–330, Apr. 1996.

[JAN03]   J.H. Jang, S.K. Sul, J.I. Ha, K. Ide, and M. Sawamura, ''Sensorless drive of surface-mounted permanent-magnet motor by high-frequency signal injection based on magnetic saliency,'' *IEEE Trans. Ind. Appl.*, vol. 39, no. 4, pp. 1031-1039, Jul./Aug. 2003.

[JAN95]   P.L. Jansen, and R.D. Lorenz, "Transducerless position and velocity estimation in induction and salient AC machines," *IEEE Trans., Ind. Appl.*, vol. 31, no. 2, pp. 240 – 247, 1995.

[JEO05]   Y.S. Jeong, R.D. Lorenz, T.M. Jahns, and S.K. Sul, "Initial rotor position estimation of an interior permanent-magnet synchronous machine using carrier-frequency injection methods," *IEEE Trans. Ind. Appl*, vol. 41, no. 1, pp. 38–45, 2005.

[KAN10]   J. Kang, "Sensorless control of permanent magnet motors," *Control Engineering*, vol. 57, no. 4, pp. 1-4, 2010.

[KIM04a]   H. Kim and R.D. Lorenz, "Carrier signal injection based sensorless control methods for IPM synchronous machine drives," *in Proc. of IEEEIAS Annual Meeting*, Vol. 2, pp.977 – 984, Oct. 2004.

[KIM04b]   H. Kim, K.K. Huh, and R.D. Lorenz, "A novel method for initial rotor position estimation for IPM synchronous machine drives," *IEEE Trans. Ind. Appl*, vol.

40, no. 5, pp. 1369–1378, 2004.

[KIM11]   H. Kim, J. Son, and J. Lee, "A high-speed sliding-mode observer for the sensorless speed control of a PMSM," *IEEE Trans. Ind. Electron*., vol. 58, no. 9, pp. 4069–4077, Sep. 2011.

[KIM16]   D. Kim, Y. C. Kwon, S.-K. Sul, J. H. Kim, and R.-S. Yu, "Suppression of injection voltage disturbance for high-frequency square-wave injection sensorless drive with regulation of induced high-frequency current ripple," *IEEE Trans. Ind. Appl.*, vol. 52, no. 1, pp. 302–312, Jan. 2016.

[KOC09]   H. W. De Kock, M. J. Kamper, and R. M. Kennel, "Anisotropy comparison of reluctance and PM synchronous machines for position sensorless control using HF carrier injection," *IEEE Trans. Power Electron*., vol. 24, no. 8, pp. 1905-1913, Aug. 2009.

[KWO15]   Y. C. Kwon and S.-K. Sul, "Reduction of injection voltage in signal injection sensorless drives using capacitor-integrated inverter," *in 2015 IEEE Energy Conversion Congress and Exposition (ECCE)*, 2015, pp. 2941–2948.

[LEE15]   Y. Lee, Y. C. Kwon, and S. K. Sul, "Comparison of rotor position estimation performance in fundamental-model-based sensorless control of PMSM," *in 2015 IEEE Energy Conversion Congress and Exposition (ECCE)*, 2015, pp. 5624–5633.

[LEI08]   R. Leidhold and P. Mutschler, "Improved method for higher dynamics in sensorless position detection," *in 34th Annual Conference of IEEE Ind. Electron*., IECON 2008, 2008, pp. 1240–1245.

[LEI11]   R. Leidhold, "Position sensorless control of PM synchronous motors based on zero-sequence carrier injection," *IEEE Trans. Ind. Electron*.,vol. 58, no. 12, pp. 5371-5379, 2011.

[LEV02]   E. Levi and M. Wang, "A speed estimator for high performance sensorless control of induction motors in the field weakening region," *IEEE Trans. Power Electron.*, vol. 17, no. 3, pp. 365–378, May 2002.

[LEV08]   E. Levi, "Multiphase electric machines for variable-speed applications," *IEEE Trans. Ind. Electron.*, vol. 55, no. 5, pp. 1893–1909, May 2008.

[LI07]   Y. Li, Z. Q. Zhu, D. Howe, and C. M. Bingham, "Improved rotor position estimation in extended back-EMF based sensorless PM brushless ac drives with magnetic saliency," *in 2007 IEEE International Electric Machines Drives Conference*, 2007, vol. 1, pp. 214–219.

[LI09]   Y. Li, Z.Q. Zhu, D. Howe, C.M. Bingham, and D. Stone, ''Improved rotor position estimation by signal injection in brushless AC motors, accounting for cross-coupling magnetic saturation,'' *IEEE Trans. Ind. Appl.*, vol.45, no.5, pp.1843-1849, Sep./Oct. 2009.

[LIM11]   N. Limsuwan, T. Kato, C.Y. Yu, J. Tamura, D.D. Reigosa, K. Akatsu, and R.D. Lorenz, "Secondary resistive losses with high-frequency injection-based self-sensing in IPM machines," *Conf. Rec. IEEE ECCE*, 2011, pp. 622-629.

[LIN14]   T.C. Lin, L.M. Gong, J.M. Liu and Z.Q. Zhu, "Investigation of saliency in switched-flux permanent magnet machine using high-frequency signal injection," *IEEE Trans. Ind. Electron.*, no.99, pp.5094-5104, Sep. 2014.

[LIN15]   T. C. Lin and Z. Q. Zhu, "Sensorless operation capability of surface-mounted permanent-magnet machine based on high-frequency signal injection methods," *IEEE Trans. Ind. Appl.*, vol. 51, no. 3, pp. 2161–2171, May 2015.

[LIU13]   J. M. Liu, "Novel sensorless control of permanent magnet synchronous machines", PhD Thesis, Research Group of Electric Machines and Drives, Department of Electronic and Electrical Engineering, University of Sheffield, 2013.

[LIU14a]   J. M. Liu and Z. Q. Zhu, "Improved sensorless control of permanent magnet synchronous machine based on third-harmonic back-EMF," *IEEE Trans. Ind. Appl.*, vol.50, no.3, pp.1861-1870, May-June 2014.

[LIU14b]   J. M. Liu and Z. Q. Zhu, "Novel sensorless control strategy with injection of high-frequency pulsating carrier signal into stationary reference frame," *IEEE Trans. Ind. Appl.*, vol. 50, no. 4, pp. 2574–2583, Jul. 2014.

[LIU14c] J. M. Liu and Z. Q. Zhu, "Sensorless control strategy by square-waveform high-frequency pulsating signal injection into stationary reference frame," *IEEE J. Emerg. Sel. Top. Power Electron.*, vol. 2, no. 2, pp. 171–180, Jun. 2014.

[LIU16] C. Liu, J. Zhu, Y. Wang, G. Lei, and Y. Guo, "Cogging torque minimization of smc pm transverse flux machines using shifted and unequal-width stator teeth," *IEEE Trans. Appl. Supercond.*, vol. 26, no. 4, pp. 1–4, Jun. 2016.

[MAT96] N. Matsui, "Sensorless PM brushless DC motor drives," *IEEE Trans. Ind. Electron.*, vol. 43, no. 2, pp. 300–308, Apr. 1996.

[MOG13] M. A. G. Moghadam and F. Tahami, "Sensorless control of PMSMs with tolerance for delays and stator resistance uncertainties," *IEEE Trans. Power Electron.*, vol. 28, no. 3, pp. 1391–1399, Mar. 2013.

[MOR02] S. Morimoto, K. Kawamoto, M. Sanada, and Y. Takeda, "Sensorless control strategy for salient-pole PMSM based on extended EMF in rotating reference frame," *IEEE Trans. Ind. Appl.*, vol. 38, no. 4, pp. 1054-1061, 2002.

[MOR96] J. C. Moreira, "Indirect sensing for rotor flux position of permanent magnet AC motors operating over a wide speed range," *IEEE Trans. Ind. Appl.*, vol. 32, no. 6, pp. 1394-1401, 1996.

[NI16] R. Ni, D. G. Xu, F. Blaabjerg, K. Lu, G. Wang, and G. Zhang, "Square-wave voltage injection algorithm for PMSM position sensorless control with high robustness to voltage errors," *IEEE Trans. Power Electron.*, vol. pp, no. 99, pp. 1–1, 2016.

[NOG98] T. Noguchi, K. Yamada, S. Kondo, and I. Takahashi, "Initial rotor position estimation method of sensorless PM synchronous motor with no sensitivity to armature resistance," *Trans. Ind. Electron.*, vol. 45, pp. 118–125, 1998.

[PAR14] Y. Park and S. K. Sul, "Sensorless control method for PMSM based on frequency-adaptive disturbance observer," *IEEE J. Emerg. Sel. Top. Power Electron.*, vol. 2, no. 2, pp. 143–151, Jun. 2014.

[PEL10] G. Pellegrino, P. Guglielmi, E. Armando, and R. I. Bojoi, "Self-commissioning algorithm for inverter nonlinearity compensation in sensorless induction motor

drives," *IEEE Trans. Ind. Appl.*, vol. 46, no. 4, pp. 1416–1424, Jul. 2010.

[QUA14]   N. K. Quang, N. T. Hieu, and Q. P. Ha, "FPGA-Based sensorless PMSM speed control using reduced-order extended kalman filters," *IEEE Trans. Ind. Electron.*, vol. 61, no. 12, pp. 6574–6582, Dec. 2014.

[RAC08a]   D. Raca, P. Garcia, D. Reigosa, F. Briz, and R. Lorenz, "A comparative analysis of pulsating vs. rotating vector carrier signal injection-based sensorless control," *in Proc. 23rd Annu. IEEE APEC*, 2008, pp. 879–885.

[RAC08b]   D. Raca, M.C. Harke, and R.D. Lorenz, "Robust magnet polarity estimation for initialization of PM synchronous machines with near-zero saliency," *IEEE Trans. Ind. Appl*, vol. 44, no. 4, pp. 1199-1209, 2008.

[RAC08c]   D. Raca, P. Garcia, D. Reigosa, F. Briz, and R. D. Lorenz, "Carrier signal selection for sensorless control of PM synchronous machines at zero and very low speeds," *in Conf. Rec. 43rd IEEE IAS Annu. Meeting*, 2008, pp. 1–8.

[RAU07]   R. Raute, C. Caruana, J. Cilia, C. S. Staines, and M. Sumner, "A zero speed operation sensorless PMSM drive without additional test signal injection," *in European Conference on Power Electronics and Applications*, pp. 1-10, 2007.

[RAU10]   R. Raute, C. Caruana, C. S. Staines, J. Cilia, M. Sumner, and G. M. Asher, "Analysis and compensation of inverter nonlinearity effect on a sensorless PMSM drive at very low and zero speed operation," *IEEE Trans. Ind. Electron.*, vol. 57, no. 12, pp. 4065–4074, Dec. 2010.

[REF10]   A. M. EL-Refaie, "Fractional-slot concentrated-windings synchronous permanent magnet machines: Opportunities and challenges," *IEEE Trans. Ind. Electron.*, vol. 57, no. 1, pp. 107–121, Jan. 2010.

[REI08]   D. Reigosa, P. Garcia, D. Raca, F. Briz, and R.D. Lorenz, "Measurement and adaptive decoupling of cross-saturation effects and secondary saliencies in sensorless-controlled IPM synchronous machines," *IEEE Trans. Ind. Appl.*, vol. 44, no. 6, pp. 1758–1767, Nov./Dec. 2008.

[REI10]   D. Reigosa, P. Garcia., F. Briz, D. Raca, and Lorenz. R. D, "Modeling and adaptive decoupling of high-frequency resistance and temperature effects in

carrier-based sensorless control of PM synchronous machines," *IEEE Trans. Ind. Appl.*, vol. 46, no. 1, pp. 139-149, Jan./Feb. 2010.

[REI11] D. D. Reigosa, F. Briz, M. W. Degner, P. Garcia, and J. M. Guerrero, "Temperature issues in saliency-tracking-based sensorless methods for PM Synchronous Machines," *IEEE Trans. Ind. Appl.*, vol. 47, no. 3, pp. 1352–1360, May 2011.

[ROB04] E. Robeischl, and M. Schroedl, "Optimized INFORM measurement sequence for sensorless PM synchronous motor drives with respect to minimum current distortion," *IEEE Trans. Ind. Appl.*, vol. 40, no. 2, pp. 591–598, 2004.

[SAL11] D. E. Salt, D. Drury, D. Holliday, A. Griffo, P. Sangha, and A. Dinu, "Compensation of inverter nonlinear distortion effects for signal-injection-based sensorless control," *IEEE Trans. Ind. Appl.*, vol. 47, no. 5, pp. 2084–2092, Sep. 2011.

[SAT11] S. Sato, H. Iura, K. Ide, and S. K. Sul, "Three years of industrial experience with sensorless IPMSM drive based on high frequency injection method," *in 2011 Symposium on Sensorless Control for Electrical Drives (SLED)*, 2011, pp. 74–79.

[SCH96] M. Schroedl, "Sensorless control of AC machines at low speed and standstill based on the 'INFORM' method," *Conf. Rec. IEEE-IAS Annual Meeting*, 1996, pp. 270–277.

[SEN95] T. Senjyu, M. Tomita, S. Doki, and S. Okuma, "Sensorless vector control of brushless DC motors using disturbance observer," *in 26th Annual IEEE Power Electronics Specialists Conference*, 1995. PESC '95 Record, 1995, vol. 2, pp. 772–777 vol.2.

[SER12] P. Sergeant, F. D. Belie, and J. Melkebeek, "Rotor geometry design of interior PMSMs with and without flux barriers for more accurate sensorless control," *IEEE Trans. Ind. Electron.*, vol. 59, no. 6, pp. 2457–2465, Jun. 2012.

[SHE02] J.X. Shen, Z.Q. Zhu, and D, Howe, "Improved speed estimation in sensorless PM brushless AC drives," *IEEE Trans. Ind. Appl.*, vol. 38, no. 4, pp. 1072-

1080, 2002.

[SHE04]   J.X. Shen, Z. Q. Zhu, and D. Howe, "Sensorless flux-weakening control of permanent-magnet brushless machines using third harmonic back EMF," *IEEE Trans. Ind. Appl.*, vol. 40, no. 6, pp. 1629-1636, 2004.

[SHE06]   J.X. Shen, Z. Q. Zhu, and D. Howe, "Practical issues in sensorless control of PM brushless machines using third-harmonic back-EMF," *IEEE 5th International Power Electronics and Motion Control Conference*, IPEMC2006, pp.1-5, 2006.

[SIT01]   K. Sitapati and R. Krishnan, "Performance comparisons of radial and axial field, permanent-magnet, brushless machines," *IEEE Trans. Ind. Appl.*, vol. 37, no. 5, pp. 1219–1226, Sep. 2001.

[SON16]   X. Song, J. Fang, B. Han, and S. Zheng, "Adaptive compensation method for high-speed surface PMSM sensorless drives of EMF-based position estimation error," *IEEE Trans. Power Electron.*, vol. 31, no. 2, pp. 1438–1449, Feb. 2016.

[SUN11]   K. Sungmin, and S.K. Sul, ''Sensorless control of AC motor—where are we now? ," *Proc. Int. Conf. Elec. Machines and Systems, (ICEMS2011*), 2011, pp. 1-6.

[TAN16]   Q. Tang, A. Shen, X. Luo, and J. Xu, "PMSM sensorless control by injecting HF pulsating carrier signal into ABC frame," *IEEE Trans. Power Electron.*, vol. pp, no. 99, pp. 1–1, 2016.

[VER14]   R. Verma, V. Verma, and C. Chakraborty, "ANN based sensorless vector controlled induction motor drive suitable for four quadrant operation," *in 2014 IEEE Students' Technology Symposium (TechSym)*, 2014, pp. 182–187.

[WAN12]   G. Wang, G. Zhang, R. Yang, and D. Xu, "Robust low-cost control scheme of direct-drive gearless traction machine for elevators without a weight transducer," *IEEE Trans. Ind. Appl*, vol. 48, no. 3, pp. 996-1005, 2012.

[WAN14a]   K. Wang, Z. Q. Zhu, and G. Ombach, "Synthesis of high performance fractional-slot permanent-magnet machines with coil-pitch of two slot-pitches,"

IEEE Trans. Energy Convers., vol. 29, no. 3, pp. 758–770, Sep. 2014.

[WAN14b] K. Wang, Z. Q. Zhu, and G. Ombach, "Torque enhancement of surface-mounted permanent magnet machine using third-order harmonic," *IEEE Trans. Magn.*, vol. 50, no. 3, pp. 104–113, Mar. 2014.

[WAN14c] G. Wang, H. Zhan, G. Zhang, X. Gui, and D. Xu, "Adaptive compensation method of position estimation harmonic error for EMF-based observer in sensorless IPMSM drives," *IEEE Trans. Power Electron*., vol. 29, no. 6, pp. 3055–3064, Jun. 2014.

[WAN14d] G.L. Wang, L.Z. Qu, H.L. Zhan, J. Xu, L. Ding, G.Q. Zhang, and D. G. Xu, "Self-commissioning of permanent magnet synchronous machine drives at standstill considering inverter nonlinearities," *IEEE Trans. Power Electron*., vol.29, no. 12, pp.6615-6627, Dec. 2014.

[WAN14e] X. Wang, W. Xie, G. Dajaku, R.M. Kennel, and R. D. Lorenz, "Position self-sensing evaluation of novel CW-IPMSMS with an HF injection method," *IEEE Trans. Ind. Appl*., vol. 50, no. 5, pp. 3325–3334, Sep./Oct. 2014.

[WAN16a] G. Wang, L. Yang, B. Yuan, B. Wang, G. Zhang, and D. Xu, "Pseudo-random high-frequency square-wave voltage injection based sensorless control of IPMSM drives for audible noise reduction," *IEEE Trans. Ind. Electron*., vol. 63, no. 12, pp. 7423–7433, Dec. 2016.

[WAN16b] G. Wang, L. Yang, G. Zhang, X. Zhang, and D. Xu, "Comparative investigation of pseudo-random high-frequency signal injection schemes for sensorless IPMSM drives," *IEEE Trans. Power Electron*., vol. 32, no. 3, pp. 2123–2132, Mar. 2017.

[WU91] R. Wu, and G.R. Slemon, "A permanent magnet motor drive without a shaft sensor," *IEEE Trans. Ind. Appl.*, vol.27, no.5, pp. 1005–1011, 1991.

[XIA16] L. Xiaoquan, L. Heyun, and H. Junlin, "Load disturbance observer-based control method for sensorless PMSM drive," *IET Electr. Power Appl*., vol. 10, no. 8, pp. 735–743, 2016.

[XIE15]   G. Xie, K. Lu, S. K. Dwivedi, and J. R. Rosholm, "Improved INFORM method by minimizing the inverter nonlinear voltage error effects," *in 2015 IEEE Workshop on Electrical Machines Design, Control and Diagnosis* (WEMDCD), 2015, pp. 188–194.

[XIE16]   G. Xie, K. Lu, S. Dwivedi, R. Riber, and F. Blaabjerg, "Minimum voltage vector injection method for sensorless control of pmsm for low-speed operations," *IEEE Trans. Power Electron.*, vol. 31, no. 2, pp. 1785–1794, 2016.

[XU16a]   P. L. Xu and Z. Q. Zhu, "Carrier signal injection-based sensorless control for permanent-magnet synchronous machine drives considering machine parameter asymmetry," *IEEE Trans. Ind. Electron.*, vol. 63, no. 5, pp. 2813-2824, May 2016.

[XU16b]   P. L. Xu, and Z. Q. Zhu, "Novel carrier signal injection method using zero sequence voltage for sensorless control of PMSM drives," *IEEE Trans. Ind. Electron.*, vol. 63, no. 4, pp. 2053-2061, Apr. 2016.

[XU16c]   P. L. Xu, and Z. Q. Zhu, "Novel square-wave signal injection method using zero sequence voltage for sensorless control of PMSM drives," *IEEE Trans. Ind. Electron.*, vol. 63, no. 12, Dec. 2016..

[XU16d]   P. L. Xu, Z. Q. Zhu, and D. Wu, "Carrier signal injection based sensorless control of permanent magnet synchronous machines without the need of magnetic polarity identification," *IEEE Trans. Ind. Appl.*, vol. 52, no. 5, Sep./Oct. 2016.

[XU17a]   P. L. Xu, and Z. Q. Zhu, "Carrier signal injection based sensorless control for PMSM drives with tolerance of signal processing delays and high frequency resistances," *IET Proc. Electr. Power Appl.*, accepted, 2017.

[XU17b]   P. L. Xu, and Z. Q. Zhu, "Initial rotor position estimation using zero sequence carrier voltage for permanent magnet synchronous machines," *IEEE Trans. Ind. Electron.*, vol. 64, no. 1, Jan. 2017.

[YAN06]   Y. Yan, J. Zhu, H. Lu, Y. Guo, and S. Wang, "Study of a PMSM model incorporating structural and saturation saliencies," *in Conf. Rec. Power*

Electronics and Drives Systems, vol. 1, pp. 575-580, Jan. 2006.

[YAN11]   S. C. Yang, T. Suzuki, R. D. Lorenz, and T.M. Jahns, "Surface permanent magnet synchronous machine design for saliency-tracking self-sensing position estimation at zero and low speeds," *IEEE Trans. Ind. Appl.*, vol. 47, no. 5, pp. 2013–2116, Sep./Oct. 2011.

[YAN12a]   S. C. Yang, and R. D. Lorenz, ''Surface permanent magnet synchronous machine position estimation at low speed using eddy-current-reflected asymmetric resistance,'' *IEEE Trans. Power Electron.*, vol. 27, no. 5, pp. 2595-2604, 2012.

[YAN12b]   S. C. Yang, and R. D. Lorenz, "Comparison of resistance-based and inductance-based self-sensing controls for surface permanent-magnet machines using high-frequency signal injection," *IEEE Trans. Ind. Appl*, vol. 48, no. 3, pp. 977-986, 2012.

[YOO09]   A. Yoo, and S.K. Sul, "Design of flux observer robust to interior permanent-magnet synchronous motor flux variation," *IEEE Trans. Ind. Appl.*, vol. 45, no. 5, pp. 1670-1677, 2009.

[YOO11]   Y. D. Yoon, S.-K. Sul, S. Morimoto, and K. Ide, "High-bandwidth sensorless algorithm for ac machines based on square-wave-type voltage injection," *IEEE Trans. Ind. Appl.*, vol. 47, no. 3, pp. 1361–1370, May. 2011.

[YOO14]   Y. D. Yoon and S.-K. Sul, "Sensorless control for induction machines based on square-wave voltage injection," *IEEE Trans. Power Electron.*, vol. 29, no. 7, pp. 3637–3645, Jul. 2014.

[YU13]   C. Y. Yu, J. Tamura, D. D. Reigosa, and R. D. Lorenz, "Position self-sensing evaluation of a FI-IPMSM based on high-frequency signal injection methods," *IEEE Trans. Ind. Appl.*, vol. 49, no. 2, pp. 880–888, Mar. 2013.

[ZHA14]   H. Zhaobin, Y. Linru, and W. Zhaodong, "Sensorless initial rotor position identification for non-salient permanent magnet synchronous motors based on dynamic reluctance difference," *IET Power Electron.*, vol. 7, no. 9, pp. 2336–2346, Sep. 2014.

[ZHA15]   Y. Zhao, Z. Zhang, W. Qiao, and L. Wu, "An extended flux model-based rotor position estimator for sensorless control of salient-pole permanent-magnet synchronous machines," *IEEE Trans. Power Electron*., vol. 30, no. 8, pp. 4412–4422, Aug. 2015.

[ZHU07]   Z. Q. Zhu and D. Howe, "Electrical machines and drives for electric, hybrid, and fuel cell vehicles," *Proc. IEEE*, vol. 95, no. 4, pp. 746–765, Apr. 2007.

[ZHU11]   Z.Q. Zhu, and L. M. Gong, "Investigation of effectiveness of sensorless operation in carrier-signal-injection-based sensorless-control methods," *IEEE Trans. Ind. Electron*., vol. 58, no. 8, pp. 3431-3439, 2011.

Appendix A Papers and Patents from This PhD Study

Papers

Journal Papers:

1. **P. L. Xu**, and Z. Q. Zhu, "Novel carrier signal injection method using zero sequence voltage for sensorless control of PMSM drives," *IEEE Trans. Ind. Electron.*, vol. 63, no. 4, pp. 2053-2061, Apr. 2016.
2. **P. L. Xu** and Z. Q. Zhu, "Carrier signal injection-based sensorless control for permanent-magnet synchronous machine drives considering machine parameter asymmetry," *IEEE Trans. Ind. Electron.*, vol. 63, no. 5, pp. 2813-2824, May 2016.
3. **P. L. Xu**, Z. Q. Zhu, and D. Wu, "Carrier signal injection based sensorless control of permanent magnet synchronous machines without the need of magnetic polarity identification," *IEEE Trans. Ind. Appl.*, vol. 52, no. 5, Sep./Oct. 2016.
4. **P. L. Xu**, and Z. Q. Zhu, "Novel square-wave signal injection method using zero sequence voltage for sensorless control of PMSM drives," *IEEE Trans. Ind. Electron.*, vol. 63, no. 12, Dec. 2016..
5. **P. L. Xu**, and Z. Q. Zhu, "Initial rotor position estimation using zero sequence carrier voltage for permanent magnet synchronous machines," *IEEE Trans. Ind. Electron.*, vol. 64, no. 1, Jan. 2017.
6. **P. L. Xu,** and Z. Q. Zhu, "Carrier signal injection based sensorless control for PMSM drives with tolerance of signal processing delays and high frequency resistances*," IET Proc. Electr. Power Appl.*, accepted.

Conference Papers:

7. **P. L. Xu**, and Z. Q. Zhu," Analysis of carrier signal injection based sensorlesscontrol of PMSM drives under limited inverter switching frequency condition", *IEEE Energy Conversion Congress and Exposition (ECCE)*, pp. 4131-4138, 2014.
8. **P. L. Xu**, and Z. Q. Zhu," Carrier signal injection based sensorless control of permanent magnet synchronous machines without the need of magnetic polarity identification," *IEEE Energy Conversion Congress and Exposition (ECCE)*, pp.5616–5623, 2015.
9. **P. L. Xu**, and Z. Q. Zhu," Comparison of carrier signal injection methods for sensorless control of PMSM drives," *IEEE Energy Conversion Congress and Exposition (ECCE)*, pp.5616–5623, 2015.

Patents

1. Z. Q. Zhu, **P. L. Xu**, J. Sun, L. M., Gong, "The rotor magnetic polarity identification method and the experimental setup", Guangdong Welling Motor Manufacturing Co., Ltd., CN104506105A, 2015.
2. Z. Q. Zhu, **P. L. Xu**, J. Sun, and L. M. Gong, "A kind of motor control method (zero sequence based position estimation", MIDEA WEILING MOTOR TECHNOLOGY SHANGHAI CO LTD), Chinese invention patent application,CN104579085A, 2015.